

FUNDAMENTAL STUDIES ON THE REMOVAL OF COPPER IN
HYDROXYLAMINE BASED CHEMISTRIES OF INTEREST TO COPPER
CHEMICAL-MECHANICAL PLANARIZATION

by

Wayne Hai-Wei Huang

A Dissertation Submitted to the Faculty of the
DEPARTMENT OF MATERIALS SCIENCE AND ENGINEERING
In Partial Fulfillment of the Requirements
For the Degree of
DOCTOR OF PHILOSOPHY
In the Graduate College
THE UNIVERSITY OF ARIZONA

2003

UMI Number: 3108914

INFORMATION TO USERS

The quality of this reproduction is dependent upon the quality of the copy submitted. Broken or indistinct print, colored or poor quality illustrations and photographs, print bleed-through, substandard margins, and improper alignment can adversely affect reproduction.

In the unlikely event that the author did not send a complete manuscript and there are missing pages, these will be noted. Also, if unauthorized copyright material had to be removed, a note will indicate the deletion.

UMI[®]

UMI Microform 3108914

Copyright 2004 by ProQuest Information and Learning Company.

All rights reserved. This microform edition is protected against unauthorized copying under Title 17, United States Code.

ProQuest Information and Learning Company
300 North Zeeb Road
P.O. Box 1346
Ann Arbor, MI 48106-1346

THE UNIVERSITY OF ARIZONA ®
GRADUATE COLLEGE

As members of the Final Examination Committee, we certify that we have read the dissertation prepared by Wayne Hai-Wei Huang entitled Fundamental Studies on the Removal of Copper in Hydroxylamine Based Chemistries of Interest to Copper Chemical-Mechanical Planarization

and recommend that it be accepted as fulfilling the dissertation requirement for the Degree of Doctor of Philosophy

S. R.
Srini Raghavan

11/24/03
Date

J. Brent Hiskey
J. Brent Hiskey

24 Nov 2003
Date

William G. Davenport
William G. Davenport

24 Nov 2003
Date

John F. O'Hanlon
John F. O'Hanlon

24 Nov 2003
Date

Robert J. Small
Robert J. Small

24 Nov 2003
Date

Final approval and acceptance of this dissertation is contingent upon the candidate's submission of the final copy of the dissertation to the Graduate College.

I hereby certify that I have read this dissertation prepared under my direction and recommend that it be accepted as fulfilling the dissertation requirement.

S. R.
Dissertation Director Srini Raghavan

11/26/03
Date

STATEMENT BY AUTHOR

This dissertation has been submitted in partial fulfillment of requirements for an advanced degree at The University of Arizona and is deposited in the University Library to be made available to borrowers under rules of the Library.

Brief quotations from this dissertation are allowable without special permission, provided that accurate acknowledgment of source is made. Requests for permission for extended quotation from or reproduction of this manuscript in whole or in part may be granted by the head of the major department or the Dean of the Graduate College when in his or her judgment the proposed use of the material is in the interests of scholarship. In all other instances, however, permission must be obtained from the author.

SIGNED: A handwritten signature in cursive script, appearing to read "Wayne Hines", is written over a horizontal line. The signature is fluid and stylized, with a large loop at the end of the last name.

ACKNOWLEDGMENTS

First, I want to send my deepest appreciation to Professor Srini Raghavan for his teachings and guidance. He has been a good friend and I have learned much from him. Second, I want to thank my committee members: Prof. William Davenport, Prof. John O'Hanlon, Dean J. Brent Hiskey, and Dr. Robert Small. Thank you for being on my committee and taking the time to read my dissertation. Third, I want to thank all my current and past research colleagues: Dr. A. Marcia Almanza-Workman, Dr. Yan Fang, Dr. Phil Haworth, Dr. Guangming Li, Tawei Lin, Viral Lowaleker, Subramanian Tamilmani, Dr. Liming Zhang, and many others that I did not mention but not forgotten. I also want to thank all the fellow graduate students that have made my graduate experience a memorable one. I also want to thank Wallace Clark for helping me with the capillary electrophoresis chromatography measurements. Especially, I also want to thank EKC Technology and NSF/SRC Engineering Research Center for Environmentally Benign Semiconductor Manufacturing for providing financial support. Fourth, I want to thank my parents Robert and Julia Huang and my siblings (Sonia, Tina, and Keven). Thanks for encouraging me to pursuit my goals and always support me in my endeavors. Last but not least, I want to send my love to my wife, Jennifer. Thanks for believing in me.

TABLE OF CONTENTS

LIST OF ILLUSTRATIONS.....	7
LIST OF TABLES.....	15
ABSTRACT.....	16
CHAPTER 1. INTRODUCTION.....	18
1.1. Introduction.....	18
1.2. Research Objectives.....	23
CHAPTER 2. BACKGROUND AND LITERATURE REVIEW.....	24
2.1. Chemical-Mechanical Planarization.....	24
2.1.1. CMP Tools.....	28
2.1.2. CMP Consumables (Pads).....	29
2.1.3. CMP Consumables (Slurries).....	32
2.1.4. CMP Mechanical Models.....	33
2.1.5. CMP Chemical Models.....	37
2.1.5.1. Oxide CMP.....	37
2.1.5.2. Metal CMP.....	38
2.1.5.2.1. Tungsten CMP.....	38
2.1.5.2.2. Copper CMP.....	42
2.2. Hydroxylamine.....	48
2.2.1. Chemical and Electrochemical Properties of Hydroxylamine.....	49
CHAPTER 3. EXPERIMENTAL SETUP AND METHODS.....	59
3.1. Industrial Size CMP Polisher.....	59
3.2. Laboratory Scale Electrochemical Abrasion Cell (EC-AC).....	59
3.2.1. Removal of Copper with Abrasion.....	62
3.2.2. Removal of Copper without Abrasion.....	65
3.2.3. Mechanical Variability of EC-AC.....	66
3.3. Electrochemical Measurements.....	72
3.3.1. Potentiodynamic Polarization.....	72
3.3.2. Corrosion Potential (E_{corr}) versus Time.....	81
3.3.3. Voltammetry with Rotating Disc Electrode ^[85, 90, 91]	81
3.4. Chemical and Physical Analysis.....	88
3.4.1. Capillary Electrophoresis Chromatography (CEC).....	88
3.4.2. Atomic Absorption Spectroscopy (AAS).....	90
3.4.3. Surface Profile Measurements.....	91
3.5. pH, Redox, and Oxygen Measurements.....	93
3.6. Potential-pH Diagrams.....	93

TABLE OF CONTENTS - *Continued*

CHAPTER 4. RESULTS AND DISCUSSION.....	95
4.1. Copper CMP Results.....	95
4.2. Electrochemical Abrasion Cell (EC-AC) Experimental Results	102
4.2.1. Mechanical Effects of Copper Abrasion from Using the EC-AC Tool	102
4.2.2. Chemical Effects of Copper Abrasion from Using the EC-AC Tool	108
4.2.3. Removal Rate of Copper without Abrasion Using the EC-AC Tool.....	110
4.2.3.1. Effect of pH on Copper Removal Rates	110
4.2.3.2. Effects of Rotation Speed on Copper Removal Rate without Abrasion	114
4.2.3.3. Effects of Hydroxylamine Concentration on Copper Removal Rate without Abrasion	117
4.3. Potential-pH Diagrams and Redox Potential Measurements.....	121
4.4. Oxygen Concentration Measurements.....	129
4.5. Electrochemical Analysis.....	131
4.5.1. Tafel and Corrosion Rate Analysis without Abrasion	131
4.5.1.1. Effects of pH.....	131
4.5.1.2. Concentration Effects.....	137
4.5.2. Electrochemical Analysis under Abrasion.....	142
4.5.2.1. E_{corr} versus Time	142
4.5.2.2. Tafel and Corrosion Rate Analysis under Abrasion	144
4.5.3. Voltammetry Analysis	153
4.6. Results from Capillary Electrophoresis Chromatography (CEC)	173
CHAPTER 5. PROPOSED MECHANISM	182
5.1. Proposed Mechanism for Copper Removal at pH Value of 6	185
5.2. Proposed Mechanism for Copper Removal at pH Value of 9	186
5.3. Proposed Mechanism for Copper Removal at pH Value of 3	187
CHAPTER 6. CONCLUSIONS AND FUTURE WORK.....	189
6.1. Conclusions.....	189
6.2. Future Work	190
APPENDIX.....	192
REFERENCES	194

LIST OF ILLUSTRATIONS

Figure 1.1.	Cross-sectional view of a MOS transistor with multilevel interconnect structure: (a) Surface topography without planarization, and (b) showing the reduction of the problematic surface topography with planarization. ^[3]	20
Figure 2.1.	Formation of copper interconnect structures. (1) Electrodeposition of copper to fill vias and trenches. (2) Bulk copper removal, Phase I of copper CMP. (3) Barrier/adhesion metal removal and overpolish, Phase II of copper CMP.	26
Figure 2.2.	(a) Measurement of planarity. ^[6] (b). The effect of pattern density on topography defects. At low pattern density, dishing is severe. With increasing pattern density, dishing becomes minimal but erosion becomes more evident. ^[2]	27
Figure 2.3.	Schematic diagrams of the traditional rotary, orbital, and linear driven CMP tools. ^[8-10]	30
Figure 2.4.	Potential-pH diagram of a W-H ₂ O system. ^[32] [Activities of dissolved tungsten species = 10 ⁻⁴ .].....	40
Figure 2.5.	Proposed mechanism for planarization of patterned tungsten metal during CMP. (1). Abrasion of the passive WO ₃ film, exposing tungsten metal to the slurry chemistry. (2). Repassivation of the exposed tungsten metal. (3). Re-abrading the freshly formed WO ₃ film. Steps (1) through (3) are repeated until surface planarization is achieved in step (4). ^[29]	41
Figure 2.6.	Potential-pH diagrams. (a). Cu-H ₂ O system with [Cu] = 0.1, 10 ⁻³ , and 10 ⁻⁶ . (b). Cu-NH ₃ -H ₂ O system with [Cu] = 10 ⁻⁶ and [NH ₃] = 0.1.	44
Figure 2.7.	Calculated equilibrium potentials of redox reactions of nitrogen based species in volts (V) with respect to standard hydrogen electrode (SHE). ^[41, 67, 70] The “acidic” region assumed pH value of 1 for the calculations. The “basic” region assumed pH value of 14 for the calculations.	51
Figure 2.8.	Schematic flow chart of the mechanisms that have been proposed for the decomposition of hydroxylamine (NH ₂ OH).	58

LIST OF ILLUSTRATIONS - *Continued*

Figure 3.1.	Schematic diagram (top) and a photograph (bottom) of the electrochemical abrasion cell that was designed and fabricated for measuring and collecting electrochemical information during abrasion conditions.....	60
Figure 3.2.	Removal rates of copper in 0.5M hydroxylamine based (HNO ₃) slurry as function of pH. Copper removal rates between photoresist covered sample (■) and no photoresist sample (●) were compared. Results obtained from analysis using a P-2 profiler (●) and an atomic absorption spectrophotometer (▲) were compared.....	64
Figure 3.3.	Calculated average relative velocity (mm/min) between pad and sample as a function of the difference in actual rotational speed of pad and sample ($\Delta\omega$). Dashed lines are one standard deviation from the average. Pad speed = 240 rpm. Sample speed = pad speed - $\Delta\omega$. Off-set distance = 0.25 cm (Abrasion area = 1.65 cm ²).....	68
Figure 3.4.	Examples of copper samples showing the off-set distance between the pad and the sample affecting the abrasion area.	69
Figure 3.5.	Calculated average relative velocity (mm/min) as a function of the off-set distance (cm) between pad and sample. Dashed lines are one standard deviation from the average. Pad speed = 240 rpm. Sample speed = 222 rpm. [0.1 cm (off-set) = 1.03 cm ² (abrasion area), 0.5 cm (off-set) = 2.97 cm ² (abrasion area)].....	70
Figure 3.6.	Plot of Butler-Volmer relationship, from Equation (3.3). Assuming $i_o = 10^{-5}$ A/cm ² , $\alpha = 0.5$, $n = 1$, and $T = 298$ K.	74
Figure 3.7.	Semi-log plot of Figure 3.6 and showing Tafel relationships, Equations (3.4) and (3.5), at overpotential (η) larger than ± 0.05 V.	75
Figure 3.8.	Tafel plot of mixed electrode system of hydrogen and zinc electrodes. ^[87]	77
Figure 3.9.	Linear region of a polarization plot, showing polarization resistance (R_p). Assuming $i_o = 10^{-5}$ A/cm ² , $\alpha = 0.5$, $n = 1$, and $T = 298$ K.....	80
Figure 3.10.	A voltammogram of a redox system according to Equations (3.26), (3.29), and (3.36).	87

LIST OF ILLUSTRATIONS - *Continued*

- Figure 3.11. Schematic diagram of the capillary electrophoresis instrument used for detecting cationic and anionic species in solution.89
- Figure 3.12. Schematic diagram of atomic absorption spectrophotometer used for determining dissolved copper concentration in solution.89
- Figure 3.13. Schematic diagram of the P-2 profiler used for surface profile measurements (top). A plot of an actual profile scan of a copper sample that has been abraded (bottom).92
- Figure 4.1. Removal rates of electrodeposited copper film as function of slurry pH. [Strausbaugh 6EC tool, 3 psi, 4% SiO₂ slurry containing 0.5 M hydroxylamine, pH adjusted with H₂SO₄]96
- Figure 4.2. Removal rates of electrodeposited copper film as function of the product of polishing pressure and relative velocity ($P \times R_v$). Preston's model (- - -) and best linear fit (---).97
- Figure 4.3. Replots of Figure 4.2 showing RR with respect to $P^{0.1} \times R_v^{0.1}$ (top) and to $P^{0.9} \times R_v^{0.4}$ (bottom). The linear regression for each plot is drawn as a dashed line (---).100
- Figure 4.4. Contour plot of the R^2 values determined by using Equation (4.2) with the experimental results of Figure 4.2. [The combination of 'a' and 'b' values in Equation (4.2) ranged from 0.1 to 1. Three models from Section 2.1.4 were also plotted. The dashed line represents 'a' = 'b'.]101
- Figure 4.5. Contour plot of the R^2 values determined by using Equation (4.2) with the experimental results obtained using EC-AC tool in 0.5M hydroxylamine based slurry at pH 8.3. [The combination of 'a' and 'b' values in Equation (4.2) ranged from 0.1 to 1. Three models from Section 2.1.4 were also plotted. The dashed line represents 'a' = 'b'.]103
- Figure 4.6. Contour plot of the R^2 values determined by using Equation (4.2) with the experimental results obtained using EC-AC tool in 0.5M hydroxylamine based slurry at pH 6. [The combination of 'a' and 'b' values in Equation (4.2) ranged from 0.1 to 1. Three models from Section 2.1.4 were also plotted. The dashed line represents 'a' = 'b'.]104

LIST OF ILLUSTRATIONS - *Continued*

- Figure 4.7. Contour plot of the R^2 values determined by using Equation (4.2) with the experimental results obtained using EC-AC tool in 0.5M hydroxylamine based slurry at pH 3.5. [The combination of 'a' and 'b' values in Equation (4.2) ranged from 0.1 to 1. Three models from Section 2.1.4 were also plotted. The dashed line represents 'a' = 'b'.]105
- Figure 4.8. Copper removal rates normalized with respect to their mean as a function of pH. [Mean values of CMP tool (H_2SO_4) = 1,858.7 Å/min, EC-AC tool (H_2SO_4) = 897.8 Å/min, EC-AC tool (HNO_3) = 632.5 Å/min.]109
- Figure 4.9. Removal rates of copper in 0.5M hydroxylamine based slurry as function of pH. [Removal rates of copper without abrasion (○ and □) and with abrasion (● and ■). pH adjustment using H_2SO_4 (○ and ●) and HNO_3 (□ and ■).]111
- Figure 4.10. Variations $RR_{Mechanical}$ and the ratio of $RR_{Mechanical}/RR_{Chemical}$ plotted as function of pH.112
- Figure 4.11. Inverse removal rate of copper as function of inverse square root of rotation speed in 0.5M hydroxylamine based chemistry at pH 6. [No abrasion].....115
- Figure 4.12. Removal rate of copper as function of hydroxylamine concentration at pH around 6 using the EC-AC tool that was rotating at 222 rpm (23.25 rad/s).119
- Figure 4.13. Log-Log plot of equation (4.16) as function of hydroxylamine concentration at pH 6. A linear fit is drawn as the dashed line.120
- Figure 4.14. E-pH diagram of copper-water system. [Species considered: [Cu, CuO, Cu_2O] = 1 (solids), [Cu^{2+} , Cu^+ , $Cu(OH)_2$, $HCuO_2^-$, CuO_2^{2-}] = 0.1 (—), = 10^{-3} (- - -), = 10^{-6} (- - -). Dotted lines are the water stability region. Redox potentials of DI water containing sulfate anions (■) and nitrate anions (□).]122
- Figure 4.15. E-pH diagram of nitrogen-water system with NH_2OH as base compound. [The following species and their activities were considered: [NH_2OH , NH_3OH^+] = 10^{-6} (- - -), = 10^{-3} (- · · -), = 0.5 (—) and [NO_3^- , HNO_3 , NO_2^- , HNO_2 , $H_2N_2O_2$, $HN_2O_2^-$, $N_2O_2^{2-}$, NO] = 10^{-6} . Redox potential of DI water with sulfate anions (■) and addition of 0.5M hydroxylamine (●).]124

LIST OF ILLUSTRATIONS - *Continued*

- Figure 4.16. E-pH diagram of copper-hydroxylamine-water system with Cu as base metal. [The following species were considered: $[\text{Cu}, \text{CuO}, \text{Cu}_2\text{O}] = 1$ (solids), $[\text{Cu}^{2+}, \text{Cu}^+, \text{Cu}(\text{OH})_2, \text{HCuO}_2^-, \text{CuO}_2^{2-}, \text{Cu}(\text{NH}_2\text{OH})^{2+}, \text{Cu}(\text{NH}_2\text{OH})_2^{2+}] = 0.1$ (—), $= 10^{-3}$ (- - -), $= 10^{-6}$ (- - -), $[\text{NH}_2\text{OH}, \text{NH}_3\text{OH}^+] = 0.5$. Redox potential of DI water with sulfate anions (■), 0.5M hydroxylamine (●), and 0.5M hydroxylamine + 0.001M copper sulfate (○).].....126
- Figure 4.17. E-pH diagrams of copper-hydroxylamine-water system superimposed together with nitrogen-water system. Stability lines of $\text{NH}_2\text{OH}/\text{NH}_4^+$ (- · -) and $\text{NH}_3\text{OH}^+/\text{NH}_4^+$ (- · -). Redox potentials of 0.5M hydroxylamine solution (●).128
- Figure 4.18. Oxygen levels (ppm) in solution containing 0.5M hydroxylamine (■) and solution without any hydroxylamine (□) with respect to pH. [Sulfuric acid was used to acidify the solutions from pH values of 13 to 1]130
- Figure 4.19. Potentiodynamic polarizations of electrodeposited copper film in 0.5M hydroxylamine base chemistry at different pH values without abrasion. pH 8.8 (☆), pH 8.05 (◇), pH 7.58 (▽), pH 6.99 (□), pH 6.53 (△), and pH 5.98 (○).132
- Figure 4.20. Potentiodynamic polarizations of electrodeposited copper film in 0.5M hydroxylamine base chemistry at different pH values without abrasion. pH 2.95 (☆), pH 3.96 (◇), pH 4.48 (▽), pH 4.98 (□), pH 5.5 (△), and pH 5.98 (○).133
- Figure 4.21. Copper removal rates normalized over their mean in 0.5M hydroxylamine based slurry without any abrasion with respect to pH. The mean value for EC RR ($2e^-$) was 108.9 Å/min. The mean value for actual RR was 327.4 Å/min.136
- Figure 4.22. Tafel polarizations of electrodeposited copper film at pH 6 in varying concentration of hydroxylamine. 1M (□), 0.75M (◇), 0.5M (○), 0.4M (▽), 0.3M (△), 0.2M (☆), 0.1M (◁), 0.05M (◊), and 0.01M (▷).138
- Figure 4.23. Copper removal rates normalized to their mean value with respect to hydroxylamine concentration at pH 6. The mean value for actual RR was 565.9 Å/min and the mean value for EC RR ($2e^-$) was 306.5 Å/min. .140

LIST OF ILLUSTRATIONS - *Continued*

- Figure 4.24. E_{corr} vs time of copper film that was abraded using 0.5M hydroxylamine based slurries. Sulfuric acid was used to adjust the pH.143
- Figure 4.25. Potentiodynamic polarizations of electrodeposited copper film in 0.5M hydroxylamine base slurry at different pH values under abrasion. pH 8.47 (\star), pH 7.99 (\diamond), pH 7.51 (∇), pH 7.0 (\square), pH 6.5 (\triangle), and pH 6.06 (\circ).145
- Figure 4.26. Potentiodynamic polarizations of electrodeposited copper film in 0.5M hydroxylamine base slurry at different pH values under abrasion. pH 3.46 (\triangle), pH 4.01 (\square), pH 4.58 (∇), pH 4.99 (\diamond), pH 5.55 (\circ), pH 5.78 (\star), and pH 6.06 (\circ).146
- Figure 4.27. Polarizations curves of copper in 0.5M hydroxylamine based slurry with and without abrasion at pH values around 8.148
- Figure 4.28. Polarizations curves of copper in 0.5M hydroxylamine based slurry with and without abrasion at pH values around 6.149
- Figure 4.29. Polarizations curves of copper in 0.5M hydroxylamine based slurry with and without abrasion at pH values around 4.150
- Figure 4.30. Electrochemical removal rate ($\text{\AA}/\text{min}$) of copper in 0.5M hydroxylamine based chemistry as function of pH. The EC RR of copper under abrasion (\blacklozenge) and copper without any abrasion (\blacksquare).151
- Figure 4.31. Voltammograms of copper film in phosphate-sulfate buffer solution at pH values of 8, 6, and 3. Scan rate of 50 mV/s from -1.5V to +1V and rotation speed of 50 rpm.154
- Figure 4.32. Voltammograms of copper film in pH 8 solutions with and without 0.01M hydroxylamine. [Scan rate of 50 mV/s from -1.5V to +1V and rotation speed of 50 rpm.]158
- Figure 4.33. Voltammograms of copper film in pH 6 solutions with and without 0.01M hydroxylamine. [Scan rate of 50 mV/s from -1.5V to +1V and rotation speed of 50 rpm.]159
- Figure 4.34. Voltammograms of copper film in pH 3 solutions with and without 0.01M hydroxylamine. [Scan rate of 50 mV/s from -1.5V to +1V and rotation speed of 50 rpm.]160

LIST OF ILLUSTRATIONS - *Continued*

- Figure 4.35. Voltammograms of copper film in 0.01M hydroxylamine based chemistries at pH values of 8, 6, and 3. [Scan rate of 50 mV/s from -1.5V to +1V and rotation speed of 50 rpm.]161
- Figure 4.36. Voltammograms of copper film in pH 6 solutions containing only sulfate-phosphate buffers (- - -), buffers + 0.01M hydroxylamine (-----), buffers + 0.01M KNO₂ (—), and 0.01M hydroxylamine + 0.01M KNO₂ (·····). Scan rate of 50 mV/s from -1.5V to +1V and rotation speed of 50 rpm.166
- Figure 4.37. Voltammogram of copper in 0.01M hydroxylamine solution at pH 8. A linear fit of the cathodic portion of the curve determines the cathodic pseudo-resistance value (- - -). A linear fit of the anodic portion of the curve determines the anodic pseudo-resistance value (·····). A linear fit near the OCP determines the value for R_p (—).171
- Figure 4.38. Chromatograph of ion analysis using CEC. Chromatogram 'a' is of equal concentrations of Cl⁻, NO₂⁻, SO₄²⁻, and NO₃⁻ at 0.01 M. Chromatogram 'b' is of 0.01 M NH₄Cl. Chromatogram 'c' is 0.002 M Cu(NO₃)₂. Chromatogram 'd' is of 0.1 M NH₄OH + 0.001 M CuSO₄ + HNO₃. [Electrokinetic injection for 5 second at 1kV. Applied voltage of 15kV (anions) and 30kV (cations). Capillary column was 75 μm in diameter, and 70 cm in length.]175
- Figure 4.39. Chromatograph of anionic analysis using CEC. Analyte is 0.5 M hydroxylamine based solution prior to copper removal experiments. The solution also contains sulfuric acid for pH adjustments. [Electrokinetic injection for 5 second at 1 kV. Applied voltage of 15 kV. Capillary column was 75 μm in diameter, and 70 cm in length.]176
- Figure 4.40. Chromatograph of cationic analysis using CEC. Analyte is 0.5 M hydroxylamine based solution prior to copper removal experiments. The solution also contains sulfuric acid for pH adjustments. [Electrokinetic injection for 5 second at 1 kV. Applied voltage of 30 kV. Capillary column was 75 μm in diameter, and 70 cm in length.]177
- Figure 4.41. Chromatograph of cationic analysis using CEC. Analyte is 0.5 M hydroxylamine based solution after copper removal experiments. The solution also contains sulfuric acid for pH adjustments. [Electrokinetic injection for 5 second at 1 kV. Applied voltage of 30 kV. Capillary column was 75 μm in diameter, and 70 cm in length.]178

LIST OF ILLUSTRATIONS - *Continued*

- Figure 4.42. Integrated peak areas of NH_3OH^+ and NH_2OH species from chromatograms of cationic analysis (shown in Figure 4.40 and Figure 4.41) plotted with respect to pH.....180
- Figure 5.1. Summary diagram on the decomposition mechanisms of hydroxylamine at pH values of 9, 6, and 3. [“red” – reduction reactions and “oxid” – oxidation reactions.].....184

LIST OF TABLES

Table 2.1. Polyurethane pad properties. ^[11, 12]	29
Table 2.2. Standard reduction potentials of various oxidants. ^[41]	45
Table 2.3. Physical properties of hydroxylamine. ^[55]	48
Table 2.4. Oxidation states of nitrogen based compounds. ^[66, 67]	50
Table 3.1. Parameters used for voltammetry experiments.....	86
Table 3.2. Thermodynamic data used to calculate the E-pH diagrams. ^[41, 66, 67, 94-96]	94
Table 4.1. Values of 'a' and 'b' with highest R ² value and the corresponding K values with respect to three slurry pH conditions.	102
Table 4.2. Electrochemical properties of the polarization curves in Figure 4.19 and Figure 4.20.	135
Table 4.3. Electrochemical properties of the polarization curves in Figure 4.22.	139
Table 4.4. Electrochemical properties of the polarization curves in Figure 4.25 and Figure 4.26.	152
Table 4.5. Calculated equilibrium potentials (in volts vs SHE) for Reactions (4.19) through (4.24) at different pH values and copper ion activities.	156
Table 4.6. Calculated R _p and OCP values from the voltammograms of copper in solutions with pH values of 8, 6, and 3.....	163
Table 4.7. Calculated equilibrium potentials of reactions (4.27) and (4.28) in volts (vs SHE) at the corresponding pH values and ion activity ratios.	164
Table 4.8. Calculated equilibrium potentials for reactions (4.31) and (4.32) in volts (vs SHE) at the corresponding pH values and ion activity ratios.	169
Table 4.9. Calculated pseudo-resistance values from the voltammograms of copper in 0.01M hydroxylamine based solution shown in Figure 4.35.	170

ABSTRACT

The advancement of IC technology has led to an increasing demand for faster and cheaper microelectronic devices. One of the key processing steps in fabricating ultra-large scale integration devices is copper chemical-mechanical planarization (CMP). Traditional copper CMP slurries use hydrogen peroxide as an oxidant. A novel copper CMP slurry based on hydroxylamine chemistry is being considered as an alternative to hydrogen peroxide based slurries.

The main goal of the research reported in this dissertation is to understand the removal of copper in hydroxylamine based chemistries. Copper removal experiments were performed on a regular CMP tool and a specially designed electrochemical abrasion cell (EC-AC). The effects of applied pressure and abrasion speed were investigated on both tools. The electrochemistry of copper in hydroxylamine based chemistry was investigated using electrochemical techniques on the EC-AC tool. The techniques include electrochemical polarization and voltammetry. The effects of solution pH and hydroxylamine concentration on the polarization of copper were systematically investigated. The fate of hydroxylamine and other nitrogen-based species were studied using capillary electrophoresis chromatography.

The removal rates of copper obtained from a regular CMP tool were twice as much as the rates obtained from the EC-AC tool. However, the removal rates from both tools showed the same trend with respect to pH. Interestingly, a maximum peak in copper removal rates occurs at a pH value of 6, and a significant decrease in rates occur at pH values deviating from 6. The copper removal results obtained from the EC-AC tool with

and without abrasion showed that the high removal rate at pH 6 is largely due to chemical attack. The reactions involved in the oxidation of copper are dependent on the decomposition and complexation behaviors of hydroxylamine. Electrochemical analysis showed the removal of copper may be dependent on the reduction of nitric oxide (NO) to hyponitrous specie ($\text{H}_2\text{N}_2\text{O}_2$). Capillary electrophoresis chromatography analyses showed the consumption of hydroxylamine and species generated from the auto-oxidation/reduction of hydroxylamine.

In slightly alkaline pH conditions, the removal of copper was predominantly due to mechanical abrasion of the surface oxide. This was supported by the potential-pH diagrams and the analysis of applied pressure and relative velocity. At pH values ranging from 3 to 5, the removal of copper was due to oxidation of Cu to Cu^{2+} .

CHAPTER 1. INTRODUCTION

1.1. Introduction

The development of integrated circuits (IC) on silicon substrate has evolved from 2,250 transistors per chip in 1971 to 42 million transistors in 2000. This increase in the number of transistors has been fueled by the fierce competition among the IC manufacturers for faster and lower-cost devices. In order for an IC manufacturer to stay competitive, the number of transistors must double every two years. This was first predicted by Gordon Moore and appropriately named “Moore’s Law.”^[1]

Earlier devices with feature sizes of 1 μm and larger have utilized aluminum-based alloys (resistivity $\sim 2.5 \mu\Omega\cdot\text{cm}$) as the interconnect metallization quite effectively. As the need for faster devices increase, interconnect metallization with lower resistance than aluminum-alloys is required to reduce signal delay. Copper metal with resistivity of about $1.67 \mu\Omega\cdot\text{cm}$ has become the metallization of choice for fabricating sub-micron devices. To reduce the resistance-capacitance (RC) delay, a dielectric material with a lower dielectric constant than SiO_2 is necessary.

In order to lower the cost of chip manufacturing, high density ICs, also known as ultra-large scale integration (ULSI) are necessary. New processes will be required for the manufacturing of these ULSI devices, and as a result new challenges will occur. In anticipation of these challenges, a handbook has been compiled and published by Semiconductor Industry Association (SIA)^[2] every few years. The handbook lays out a roadmap of various technologies that currently pose problems or that need to be developed by a certain time in order for manufacturing future generations of ULSI

devices to be possible. According to the 2001 SIA roadmap^[2], a continuation of copper metallization and low- κ dielectrics is still adequate for the 22 nm (DRAM $\frac{1}{2}$ Pitch) technology node in 2016 without significant RC delays while maintaining optimal IC performance.

The increase in device density requires a multileveled interconnect structure consisting of metal/dielectric layers. A cross-sectional view of a metal-oxide-semiconductor field effect transistor (MOSFET) with three metal layer structure is shown in Figure 1.1. The metal layers provide electrical power and signals to the MOSFET. In Figure 1.1(a), the metal/dielectric layers were fabricated without any planarization, and Figure 1.1(b) shows the metal/dielectric layers fabricated with planarization. The unplanarized metal/dielectric layers have a surface topography which may be problematic during photolithography. In the fabrication of 1 μm devices, the unplanarized interconnect structure may not be a concern. However in the fabrication of devices less than 0.1 μm , an unplanarized interconnect structure will make photolithography extremely difficult.

Chemical-mechanical planarization (CMP) has emerged as a technique of choice for planarizing metal and dielectric layers. In a CMP process, the surface topography of metal/dielectric layers are removed by polishing (with applied pressure) the surface using a slurry that contains chemicals and abrasive particles.

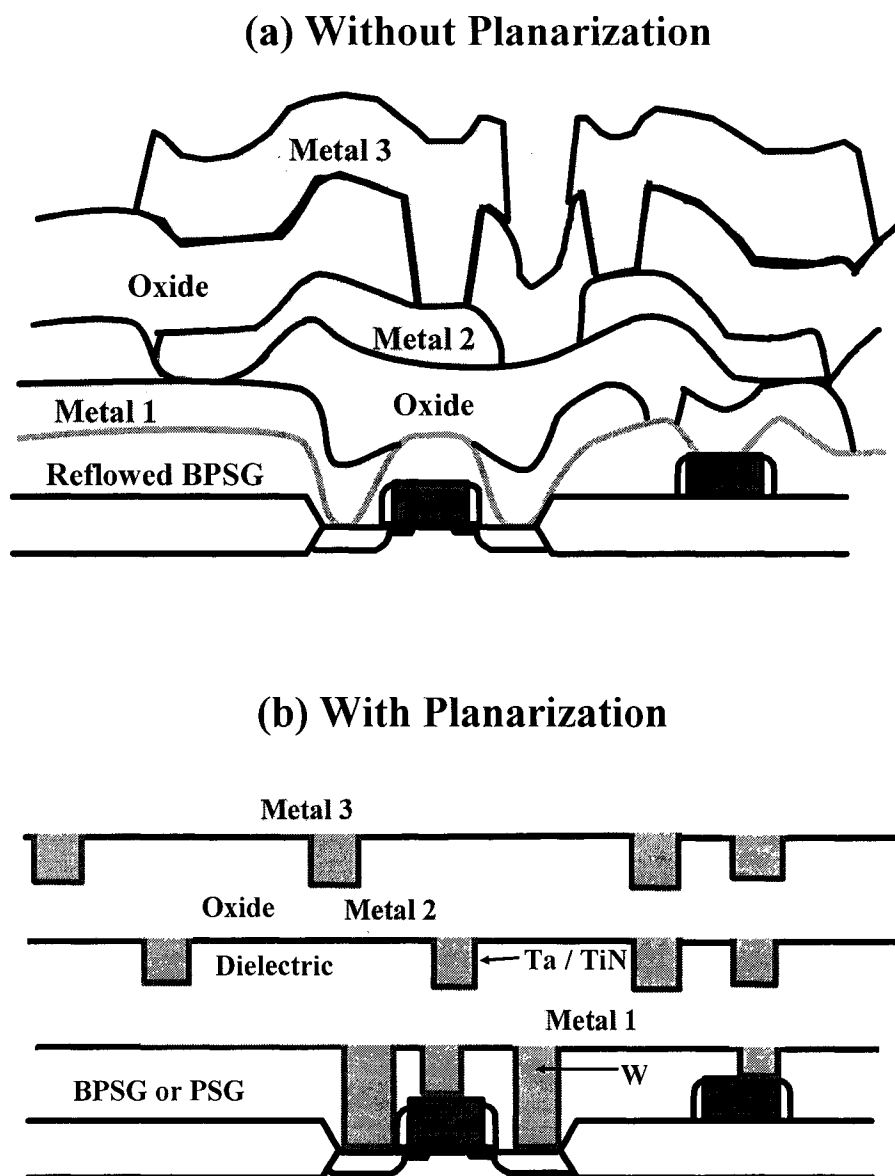


Figure 1.1. Cross-sectional view of a MOSFET with multilevel interconnect structure: (a) Surface topography without planarization, and (b) showing the reduction of the problematic surface topography with planarization.^[3]

Traditional copper CMP slurries use hydrogen peroxide as an oxidant and the silica particles as abrasives. In addition to these constituents, other chemicals such as complexing agents, corrosion inhibitors, and buffers are typically present in copper CMP slurries. Hydrogen peroxide is unstable in the presence of certain metal ions and systems with large surface area. Hence, fabrication plants have to install equipments that can monitor the concentration of hydrogen peroxide in the slurry. This has become prohibitively expensive.

A novel chemical system based on hydroxylamine (NH_2OH), first developed by EKC Technology of Hayward, CA (a subsidiary of DuPont Electronic Technologies), has properties that can benefit the copper/barrier metal CMP process in many ways. Hydroxylamine complexes copper ions effectively and hence eliminates the need for additional complexing chemicals in slurries. It also provides higher removal rates for barrier metals, such as tantalum, than hydrogen peroxide based chemistries.

Copper CMP processes is routinely carried out in fabrication of 130 nm devices. As the device size shrinks below 100 nm, the integration of copper with low- κ dielectrics is coming into the forefront. These low- κ materials are very soft and porous, and cannot withstand the pressures typically applied during a traditional CMP process. Hence, many alternatives to the traditional CMP processes are being evaluated. In these processes there is more emphasis on the 'chemical' aspects of CMP than 'mechanical' aspects. Some of these alternative planarization techniques are electrochemical-mechanical deposition and spin-etch planarization. In a process known as electrochemical-mechanical deposition, partial planarization of the copper surface is achieved during the electrochemical

deposition of copper. Spin-etch planarization is achieved purely based on a chemical system.^[4, 5]

In spite of the heavy use of CMP methods for fabrication of copper interconnect structures, the mechanism of copper CMP is far from understood. In the removal of copper using hydroxylamine based slurries, the process is fraught with challenges. The main goal of this research reported in this dissertation was to understand the removal of copper in hydroxylamine based chemistries. The objectives include performing electrochemical experiments under abrasion and actual CMP experiments. Due to the multivalent nature of nitrogen, the hydroxylamine chemistry is very rich and complicated. Using capillary electrophoresis chromatography, an understanding of the hydroxylamine redox chemistry during removal of copper has also been attempted.

1.2. Research Objectives

The main goal of this research is to carry out fundamental studies to understand the effect of hydroxylamine on removal of electrodeposited copper thin film under simulated CMP conditions. Specific objectives are as follow:

1. To construct potential-pH diagrams, and to understand the redox reactions in aqueous hydroxylamine solutions that can control the dissolution of copper.
2. To design and build an electrochemical abrasion cell (EC-AC), and to simulate CMP on a small scale and carry out electrochemical investigation during abrasion.
3. To conduct chemical analysis using capillary electrophoresis chromatography (CEC), to identify chemical species in reaction products, and to understand the mechanisms of copper-hydroxylamine redox chemistry.
4. To propose mechanisms for the removal process of copper in hydroxylamine based chemistries.

CHAPTER 2. BACKGROUND AND LITERATURE REVIEW

2.1. Chemical-Mechanical Planarization

Chemical-mechanical planarization (also referred to as chemical-mechanical polishing or CMP) is currently the most cost-effective technique in removing electrodeposited copper and reducing topography by planarizing copper metal plugs and lines. The procedures in removing copper and planarizing the topography is schematically shown in Figure 2.1. In step (1), the copper was electrodeposited into the vias and the trenches. After filling and overfilling the vias and trenches, severe topography forms on the metal surface.

Copper CMP is typically performed in two phases. The first phase is bulk copper removal, shown in Figure 2.1 step (2). This is usually achieved with a slurry chemistry that will have a high copper removal rate. The removal rate of copper during Phase I is typically around 3,000 to 5,000 Å/min. Phase I planarization usually ends with a small amount of copper remaining without exposing the barrier/adhesion metal. Phase II consists of removing the remaining copper and barrier/adhesion metal, shown in Figure 2.1 step (3). The slurry chemistry for Phase II CMP usually focuses on removal of the barrier/adhesion metal. The selectivity between copper and barrier metal ideally is one-to-one, but often it is around two-to-one and the overall removal rate is usually around 500 Å/min. The overpolish of the dielectric material, which occurs at the end of Phase II, is to ensure that no remaining copper or barrier/adhesion metals are left on the dielectric surface that may lead to shorting of the conducting lines.

The characteristics of surface topography are often placed in two categories: local and global planarity.^[6, 7] In Figure 2.2(a), a quantitative perspective on the surface topography is schematically shown. After deposition, the surface topography is largely due to the step coverage over the inter-level dielectrics (ILD). Severity of the topography can be easily defined by the topography angle, θ .

$$\theta = \tan^{-1}\left(\frac{D_2}{R}\right) \quad (2.1)$$

In areas of high pattern density, R (step coverage distance) will decrease in relation to D_2 (step height of deposited metal or depth of focus); θ then will be high. In areas of low pattern density, θ will be low. The goal of CMP is to reduce topography and obtain global planarity, $\theta < 0.5^\circ$. During CMP, in order to decrease D_2 , the reduction of M_1 must be greater than M_2 . This is referred to as step-height reduction (SHR):

$$\text{SHR} = 1 - \frac{D_2(\text{post-planarization})}{D_2(\text{pre-planarization})} \quad (2.2)$$

Ideally, perfect planarity is $\text{SHR} = 1$ and $\theta = 0^\circ$.

With copper CMP, the goal is not only to achieve planarity but also to remove M_1 completely and reduce D_2 to zero. In areas of different pattern density, trying to achieve optimal SHR without introducing additional defects has become the biggest challenge. As seen in Figure 2.2(b), defects such as dishing and erosion are common and can be detrimental to the IC performance. At low pattern density, the effects of dishing are typically more severe than at high pattern density. On the contrary, erosion effects are more evident at high pattern density than low.^[2]

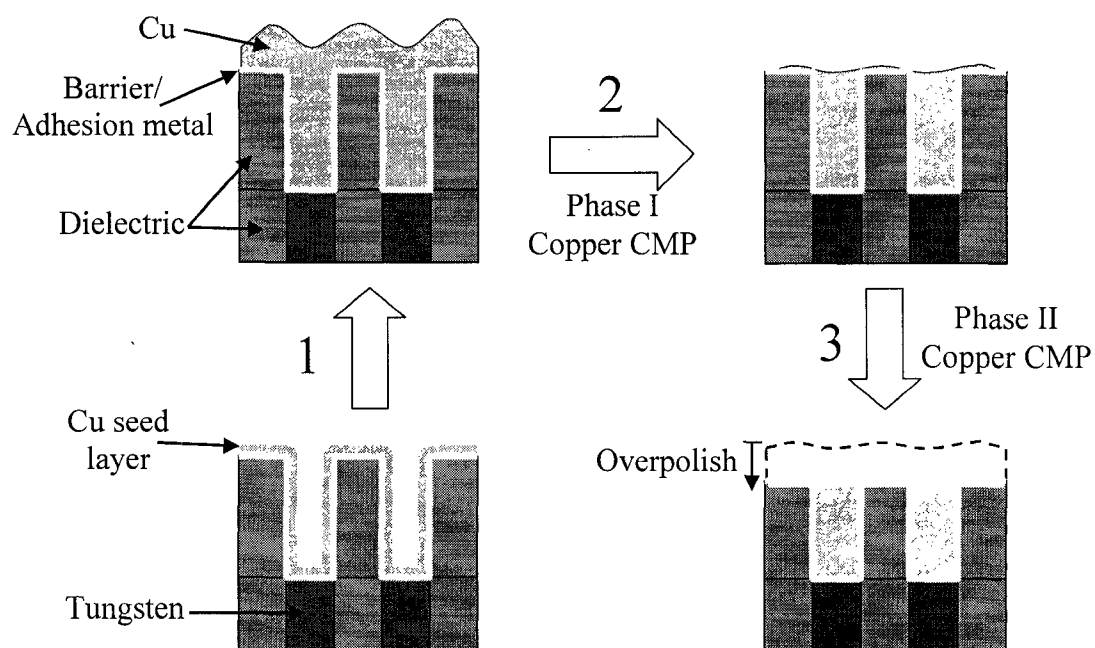
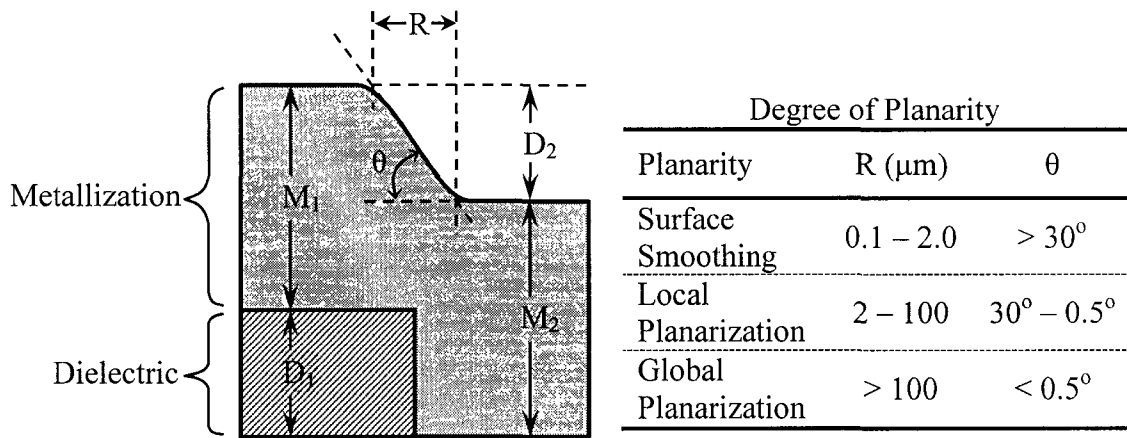


Figure 2.1. Formation of copper interconnect structures. (1) Electrodeposition of copper to fill vias and trenches. (2) Bulk copper removal, Phase I of copper CMP. (3) Barrier/adhesion metal removal and overpolish, Phase II of copper CMP.

(a)



(b)

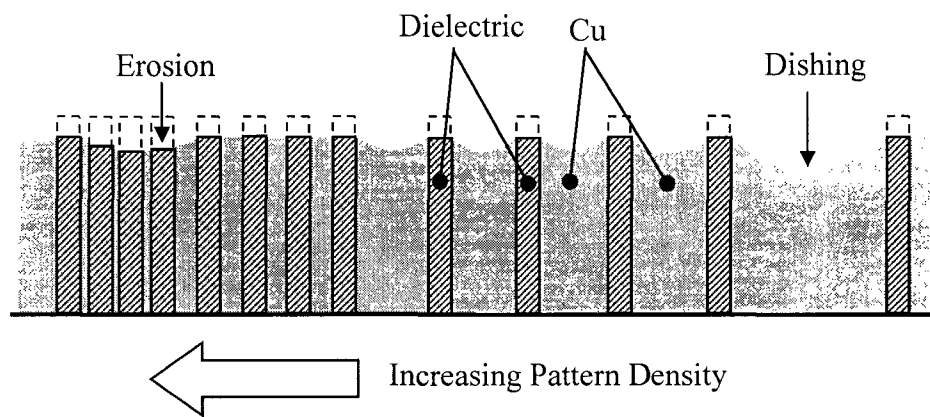


Figure 2.2. (a) Measurement of planarity.^[6] (b). The effect of pattern density on topography defects. At low pattern density, dishing is severe. With increasing pattern density, dishing becomes minimal but erosion becomes more evident.^[2]

2.1.1. CMP Tools

A CMP tool is usually composed of a wafer carrier and a platen. The role of the wafer carrier is to carry the silicon wafer onto the polishing pad/platen and to apply a down force against the polishing pad/platen. There are currently three distinct CMP tool designs:

1. Traditional polisher - carrier and platen both move in rotary motion;^[8]
2. Orbital polisher - the wafer carrier moves in rotary motion in respect to the polishing pad, which moves in an orbital fashion;^[9]
3. Linear polisher - the wafer carrier moves in a rotary motion while the pad moves in linear fashion, much like a belt sander.^[10]

The schematic diagrams of all three CMP tools are shown in Figure 2.3. Each tool has its own advantages and disadvantages. For example, the advantage of the traditional rotary tool is that the design is several decades old and has been researched and developed quite extensively. The rotary tool typically gives consistent and reproducible results in both removal rate and surface planarity. Mechanics of the rotary tool are also simple and easy to maintain. The disadvantage of the rotary tool is large variations in relative velocity between wafer and pad, especially with increasing wafer size. On the other hand, the linear polisher has small variations in relative velocity across the wafer.

The second disadvantage of the rotary tool is its inefficient slurry distribution. This is usually done by dripping the slurry on the polishing pad. Typically, less than 20% of the dispensed slurry is actually used for planarization. The rest of the slurry runs off the pad

and into the waste stream. The orbital tool, in contrast, effectively reduces the amount of unused slurry by dispensing the slurry through the pad directly underneath the wafer.

2.1.2. CMP Consumables (Pads)

The role of the CMP pad is to provide mechanical support and deliver appropriate amounts of slurry chemicals to the wafer surface. The most commonly used CMP pads are made of polyurethane. During the casting and polymerization process, the final properties of the polyurethane pad can be adjusted and engineered for specific application. For example, Rodel[®] (a polyurethane pad manufacturer) categorizes the polyurethane pad based on its density, hardness, and compressibility.^[11, 12] Rodel's IC1000[™] pads are cast and polymerized with micropores to give the pad high rigidity as well as compressibility. Rodel's Suba[™] pads are formed with polyurethane impregnated polyester felt. The Suba pads usually have higher compressibility and lower density than the IC1000 pads. The properties of Rodel's polyurethane pads are tabulated in Table 2.1.

Table 2.1. Polyurethane pad properties.^[11, 12]

Pad Name	Pad Density (g/cm ³)	Compressibility (%)	Hardness
IC1000 - A1	0.63 – 0.80	2.25	57 (Shore D)
- A2	0.74 – 0.83	2.25	57 (Shore D)
Suba 550	~ 0.34	6	73 (Shore A)
Suba 500	0.34	7	72 (Shore A)
Suba X	~ 0.3	10	66 (Shore A)
Suba IV	0.3	15	61 (Shore A)
Politex [®] Supreme	N/A	High	Soft

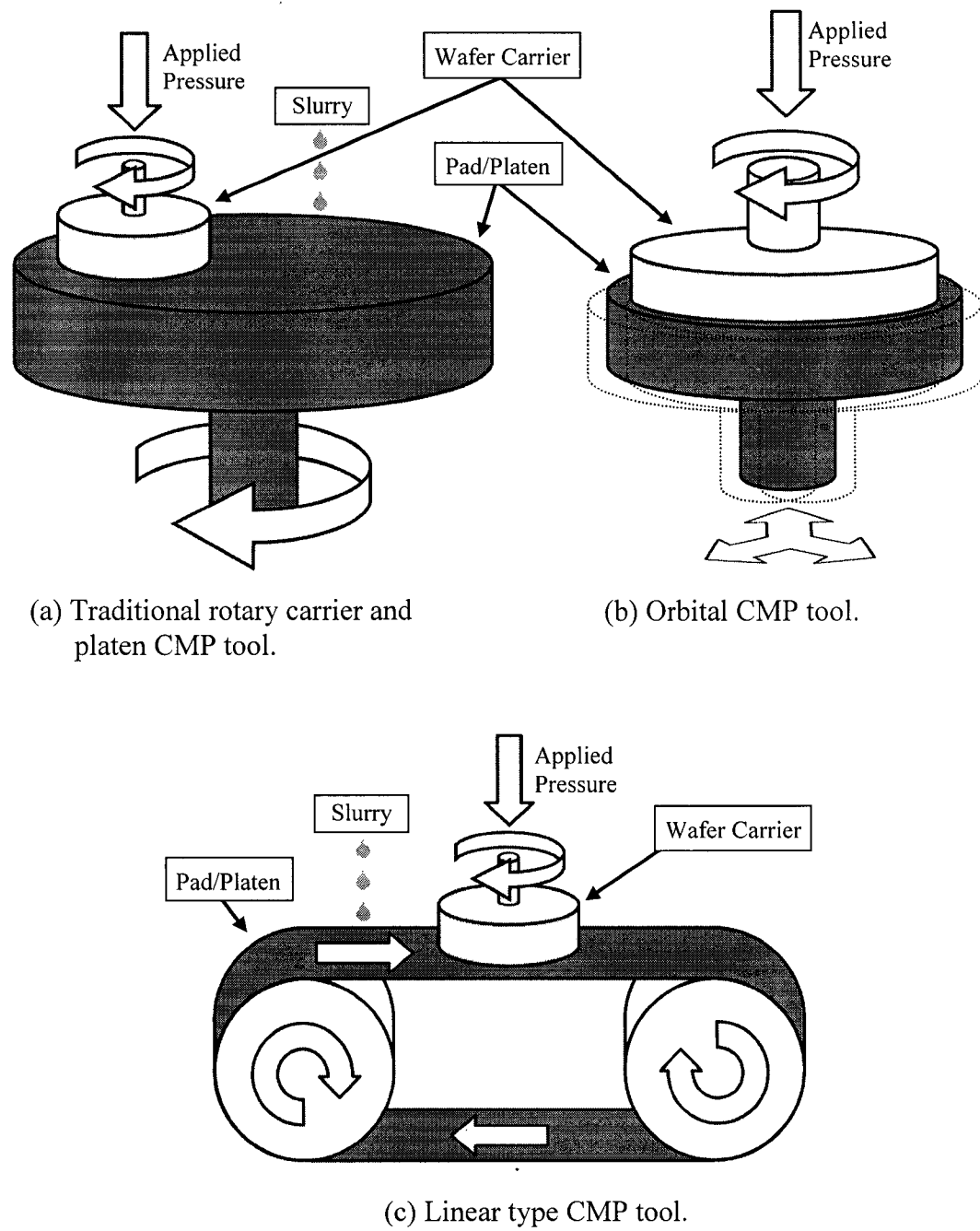


Figure 2.3. Schematic diagrams of the traditional rotary, orbital, and linear driven CMP tools.^[8-10]

Rodel's IC1000 pad is the hardest of all Rodel pads and commonly used to obtain optimal removal rates and local uniformity. Due to the rigidity of IC1000 pads, it proved difficult in conforming to the wafer surface. A stack of IC1000 and Suba IV pads forms a more conformal single pad to obtain better global planarity.

Suba pads and Politex Supreme pads (Rodel softest) are often used for the final buffing steps of the CMP process. The final buffing steps polish the wafers with DI water and sometimes mild chemistries. The goals are to reduce the amount of particulate contaminates on the wafer surface and also to smooth out any scratches that were formed during earlier CMP process steps. The high compressibility and soft properties of Suba and Politex Supreme pads make them ideal for transporting the chemical to and particulate contaminates away from the wafer surface.

A new generation of pads with abrasive particles embedded as part of the pad matrix is slowly emerging as a potential replacement for traditional polyurethane pad and slurry CMP. The new pad is commonly referred to as "fixed abrasive pad" (FAP). The pad surface has micro-replicated post structures that contain the abrasive particles evenly dispersed in a composite binder. The abrasive posts are bonded to a rigid polycarbonate layer that is itself adhered to a resilient foam layer (urethane impregnated felt) similar to the IC1000/Suba IV stack pads.^[13] The biggest advantage of using FAP is eliminating the use of abrasive particles in the slurry. Since abrasive particles are already embedded into the pad, during CMP the particles dislodge from the pad at point of use so no excess abrasive particles are introduced onto the wafer surface. Because only a small amount of

particulate contaminates is introduced onto the wafer surface, the number of defects after CMP are decreased.

2.1.3. CMP Consumables (Slurries)

The role of a CMP slurry is to chemically modify a material's surface which effectively removes layers of material and reduces surface roughness. The composition of a typical CMP slurry has an oxidant and abrasive particles. The concentration of each individual component and the slurry's pH will contribute to CMP removal rates, selectivity between different materials, and generation of defects. Common defects are those that result in loss of uniformity and planarity, as shown in Figure 2.2(b). Other defects are surface scratches and particulate contamination.

In oxide CMP, the pH of the slurry is typically alkaline, around 9 to 11. The bases used to adjust the pH are usually potassium hydroxide (KOH), ammonium hydroxide (NH₄OH), or tetramethylammonium hydroxide (TMAH).^[14] If ionic contaminates, such as K⁺ from KOH, is of concern during CMP, NH₄OH or TMAH are used instead. The abrasive particles used for oxide CMP are usually colloidal silica (SiO₂) and ceria (CeO₂). The abrasive concentration in the slurry is 5 to 30 weight percent. The average size of the abrasive particles is 50 to 400 nm. Both the abrasive concentration and particle size can have significant effects on removal rate and defect generation. An increase in abrasive concentration usually results in increasing removal rates during oxide CMP. However, increasing abrasive concentration tends to form some agglomeration between the particles. The increase in overall particle size usually results in larger and deeper

surface scratches. The increasing abrasive concentration also leads to higher particulate contamination after CMP.

In metal CMP, the slurry composition becomes considerably more complicated. The oxidants currently being used are hydrogen peroxide (H_2O_2), potassium iodate (KIO_3), ferric nitrate ($\text{Fe}(\text{NO}_3)_3$), potassium ferricyanide ($\text{K}_3\text{Fe}(\text{CN})_6$), and hydroxylamine (NH_2OH).^[14] The pH of the slurry for metal CMP is largely dependant on the metal itself. For tungsten, the slurry pH is usually acidic, from 2 to 4. For copper, the slurry pH ranges from 3 to 9. Additives such as complexing or chelating agents are often used to ensure the solubility of metal ion in solution. The combination of an oxidant and a complexant based chemistry are known to form a fairly strong etchant. High etch rates are beneficial during the bulk metal removal, Figure 2.1(1). For final polish, Figure 2.1(3), the high etch rate will contribute to a significant recession in the metal plugs and lines. To prevent the effect of recession during CMP, a corrosion inhibitor is added into the slurry. For example, with copper metal, benzotriazole (BTA) is commonly used as a corrosion inhibitor.

2.1.4. CMP Mechanical Models

In the pursuit of understanding CMP processes, empirical formulations and models based on mechanical parameters, such as applied pressure and relative velocity, have been established. One of the earliest polishing models was proposed by Preston, Equation (2.3).^[15]

$$\text{RR} = K_p P R_v \quad (2.3)$$

$$\text{Removal Rate (RR)} = \frac{\Delta H}{\Delta t} = K_p \frac{\text{Load}}{\text{Area}} \frac{\Delta s}{\Delta t}, \text{ where } P = \frac{\text{Load}}{\text{Area}} \text{ and } R_v = \frac{\Delta s}{\Delta t}$$

Removal rate is defined as the reduction in film thickness after polishing, ΔH , with the polishing time being Δt . Relative velocity (R_v) is the relative distance traveled between wafer and pad, Δs , per polishing time. Applied pressure (P) is the load per unit area and K_p is the Preston coefficient. It is obvious that K_p is a proportionality factor between RR and $P \times R_v$. Also from Equation (2.3), the RR is linearly related to both P and R_v . Because this Equation (2.3) was originally developed based on empirical formulation for polishing of plate glass material, it lacked fundamental concepts. Utilizing concepts such as Young's modulus, film and pad hardness, and localized pressures, allowed polishing models to become more fundamentally sound. By doing this, Brown and Cook found that K_p had an inverse relationship with the modulus of polished glass material.^[16-18]

Considering that CMP of oxide material for shallow trench isolation (STI) and inter-level dielectrics (ILD) applications is similar to glass polishing, not only did Preston's empirical model quickly gain acceptance for oxide CMP but many have used it as a basis for developing new CMP models. For example, Tseng and Wang^[19] used Runnels and Eyman's traveling indenter tribology model,^[20] where the RR is based on the normal stress (σ_n) and the shear stress (τ) applied to the substrate during polishing, Equation (2.4).

$$RR = K_p \sigma_n \tau \quad (2.4)$$

From Brown and Cook, Tseng and Wang used the force (F) acting on the particle/wafer contact area, shown in Equation (2.5).^[18, 21]

$$F = \frac{\sqrt{3} P d^2}{2 k} \quad (2.5)$$

where P is the applied pressure, d is the particle diameter, and k is the fraction of wafer covered by particles. If the wafer surface is completely covered by particles, then $k = 1$.

The normal stress (σ_n) is expressed as Equation (2.6).

$$\sigma_n = \frac{\text{Force}}{\text{Contact Area}} = \frac{F}{\pi r_c^2} \quad (2.6)$$

The radius of the contact area, r_c , is defined by contact mechanics, Equation (2.7).^[22]

$$r_c = \left\{ \frac{3}{4} F \left(\frac{d}{2} \right) \left[\frac{(1-\nu^2)}{E} + \frac{(1-\nu'^2)}{E'} \right] \right\}^{1/3} \quad (2.7)$$

where ν and ν' are the Poisson's ratios of the substrate and particle, and E and E' are the elastic moduli of the substrate and particle, respectively. The shear stress (τ), from Equation (2.4) can be approximated as Equation (2.8).^[23]

$$\tau = C \sqrt{\mu R_v P A} \quad (2.8)$$

where C is a stress-assisted chemical constant, μ is the slurry dynamic viscosity, and A is the polished area. By combining Equations (2.4) through (2.8), Tseng and Wang developed an analytical model, shown in Equation (2.9).^[19]

$$RR = K_{TW} P^{5/6} R_v^{1/2} \quad (2.9)$$

According to Tseng and Wang's model, the $R_v^{1/2}$ term contributes to only shear stresses during polishing, but $P^{5/6}$ term is actually contributing to both normal and shear stresses during polishing. By expanding Equation (2.6), one finds that $\sigma_n \propto P^{1/3}$, and from Equation (2.8), $\tau \propto P^{1/2}$. The K_{TW} from Equation (2.9), would contain all the physical

properties and parameters of the polishing system, such as the particle diameter, Poission's ratios, elastic moduli, polished area, and the slurry's dynamic viscosity.

Another CMP model suggested by Zhao and Shi, also utilizing a particle indenter model, gave a different equation than the one proposed by Tseng and Wang.^[24] The CMP model by Zhao and Shi gave the following equations,

$$RR = K_{ZS} P_{ZS}^{2/3} R_v, \text{ where } P_{ZS}^{2/3} = P^{2/3} - P_{th}^{2/3} \quad (2.10)$$

The threshold pressure (P_{th}) was the minimum pressure required for the particle to become fixed into the pad forming an indenter that acts on the wafer surface. When the applied pressure (P) was less than the threshold pressure (P_{th}), the slurry particles started to roll like ball bearings. This resulted in minimal removal of the substrate material. The main difference between the models of Zhao-Shi and Tseng-Wang is that Zhao-Shi did not consider any relationship between the dependence of R_v and P on RR , as Tseng-Wang did.

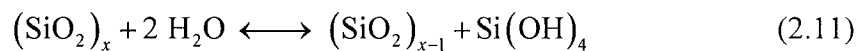
To test how well the oxide CMP models predicted oxide RR , Stein and Hetherington performed a series of CMP studies using different slurry chemistries and oxide films.^[25] Among the models tested were Preston, Tseng-Wang, and Zhao-Shi. The slurries used during oxide CMP were either SiO_2 or CeO_2 based slurries. Stein and Hetherington concluded that when using SiO_2 based slurries, all models, including Preston, predicted the oxide RR equally well. As for CeO_2 based slurries, only Tseng-Wang and Zhao-Shi had adequate prediction. Among all the oxide CMP results, it seemed that the Tseng-Wang's model fit better than Zhao-Shi's model, in terms of their R^2 (coefficient of determination) value.

2.1.5. CMP Chemical Models

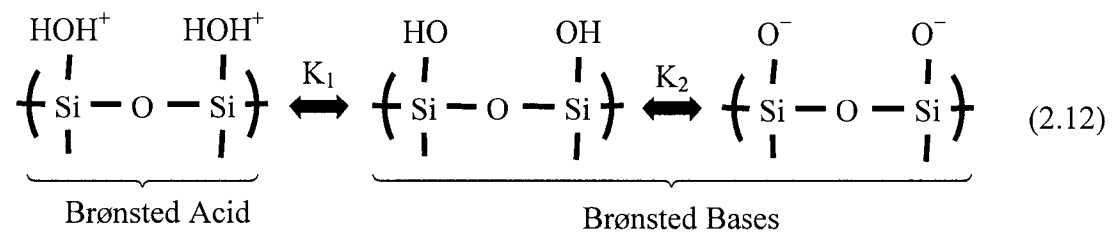
2.1.5.1. Oxide CMP

Chemical effects during CMP are important but difficult to predict and requires a better understanding than currently available. The majority of chemical mechanisms and models applied for oxide CMP were originally proposed and developed for the polishing of glass. The hydrolysis of the oxide surface was found to be an important factor during glass polishing. Izumitani found that glass polishing in non-aqueous environments decreased the polishing performance considerably.^[26] Izumitani polished glass with oil and kerosene and found that removal rates of glass were nearly zero, and there was also a significant decrease in surface quality. The glass surface hardness decreased in aqueous environment, making the surface softer and resulting in a higher glass removal rate.

The chemical reactions occurring at the SiO₂-water interface has been described as a reversible depolymerization of the (SiO₂)_x polymer/matrix, expressed in Reaction (2.11).^[27]



During hydrolysis, the SiO₂-water interface has a surface hydroxyl equilibrium shown in Reaction (2.12).^[27]



The constant (pK_1) between the Brønsted acid (proton acceptor) and the Brønsted bases (proton donor) is about -0.7. Among the Brønsted bases, there is another constant (pK_2) of about 3.9.^[21, 28]

Besides pH, the type of abrasive used can also increase the polish rate. For example, CeO_2 based slurries tend to have higher polish rates than SiO_2 based slurries. Cook proposed a removal mechanism based on a “chemical tooth” effect between the abrasive particle and the SiO_2 surface. At high pH values, the hydrolysis of SiO_2 surface forms $\equiv Si-O^-$ species. The $\equiv Si-O^-$ reacts with the $\equiv Ce-OH$ sites forming a $\equiv Si-O-Ce\equiv$ linkage and releasing an OH^- ion. Between the $\equiv Si-O-Ce\equiv$ linkage, a partial strain on the silicon tetrahedron bonds make the bonds susceptible to an OH^- attack. Once all four tetrahedron bonds are attacked, a $Si(OH)_4$ specie is formed, and thus the Si is carried away from the glass surface.^[21]

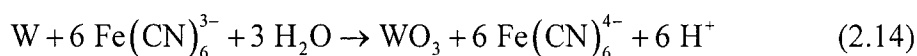
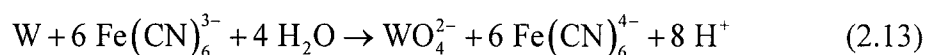
2.1.5.2. Metal CMP

When a metal is in contact with an aqueous solution, the metal surface typically becomes oxidized forming a layer of metal oxide film. Depending on the solution pH and the additives in the solution, the stability of the metal oxide will change as well.

2.1.5.2.1. Tungsten CMP

One of the earlier chemical model proposed for tungsten CMP was in a study by Kaufman *et al* who used ferricyanide ($K_3Fe(CN)_6$) as an based oxidant.^[29] From the stability diagram (E-pH) of a tungsten-water system, shown in Figure 2.4, tungsten forms a stable WO_3 specie at pH below 4. They proposed a mechanism for the planarization

process of tungsten, which is schematically shown in Figure 2.5. Initially, passivation of the tungsten metal occurs by formation of the WO_3 oxide. During CMP, the high feature areas are being abraded and mechanically removing the WO_3 film in those areas, Figure 2.5 step (1). Similar to CMP of SiO_2 , the oxide formed on tungsten surface was softer than tungsten itself; this enabled easy removal of the WO_3 film. The low feature areas are not abraded and they are chemically protected by the passive WO_3 film. The freshly abraded areas are exposed to the oxidizing slurry chemistry forming a fresh layer of WO_3 , Figure 2.5 step (2). The fresh layer of WO_3 is quickly abraded away by the CMP process, Figure 2.5 step (3). Steps (1) through (3) are repeated until the high feature areas are reduced to the same level as the low feature areas, step (4). During the passivation process two competing electrochemical reactions occur on the tungsten surface, Equations (2.13) and (2.14).



The etching of the tungsten metal occurs via Equation (2.13), while the passivating process occurs via Equation (2.14).^[29]

Kaufman's model provided a mechanistic approach to tungsten CMP, but electrochemical measurements during simulated tungsten CMP condition (using oxidants H_2O_2 , $\text{Fe}(\text{NO}_3)_3$, KIO_3 , and $\text{K}_3\text{Fe}(\text{CN})_6$) have shown inconsistencies in Kaufman's model.^[30, 31] Both Kneer *et al* and Stein *et al* showed that formation of the passive WO_x ($x = 2$ to 3) film exist, as predicted by Kaufman, in acidic conditions.^[30, 31]

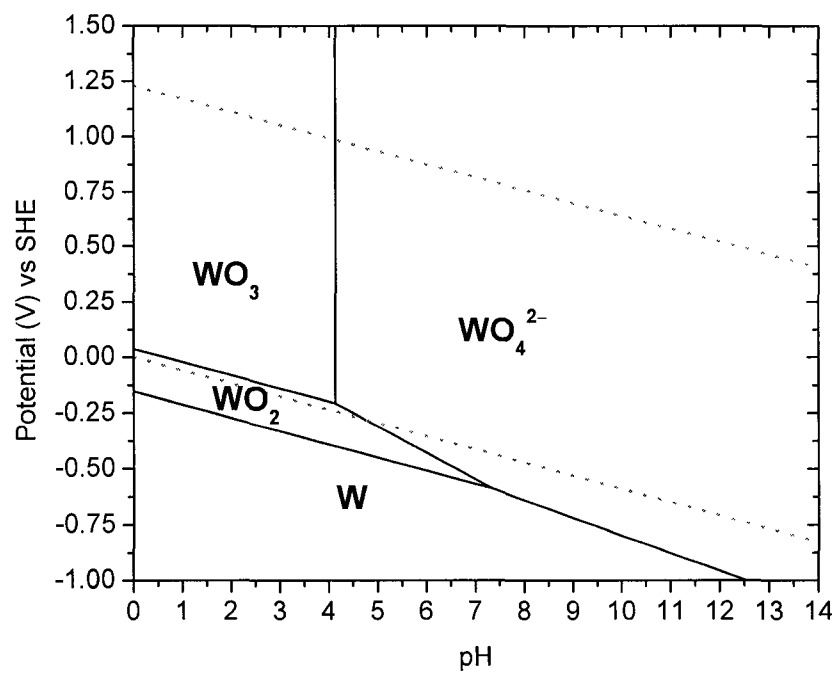


Figure 2.4. Potential-pH diagram of a W-H₂O system.^[32] [Activities of dissolved tungsten species = 10⁻⁴.]

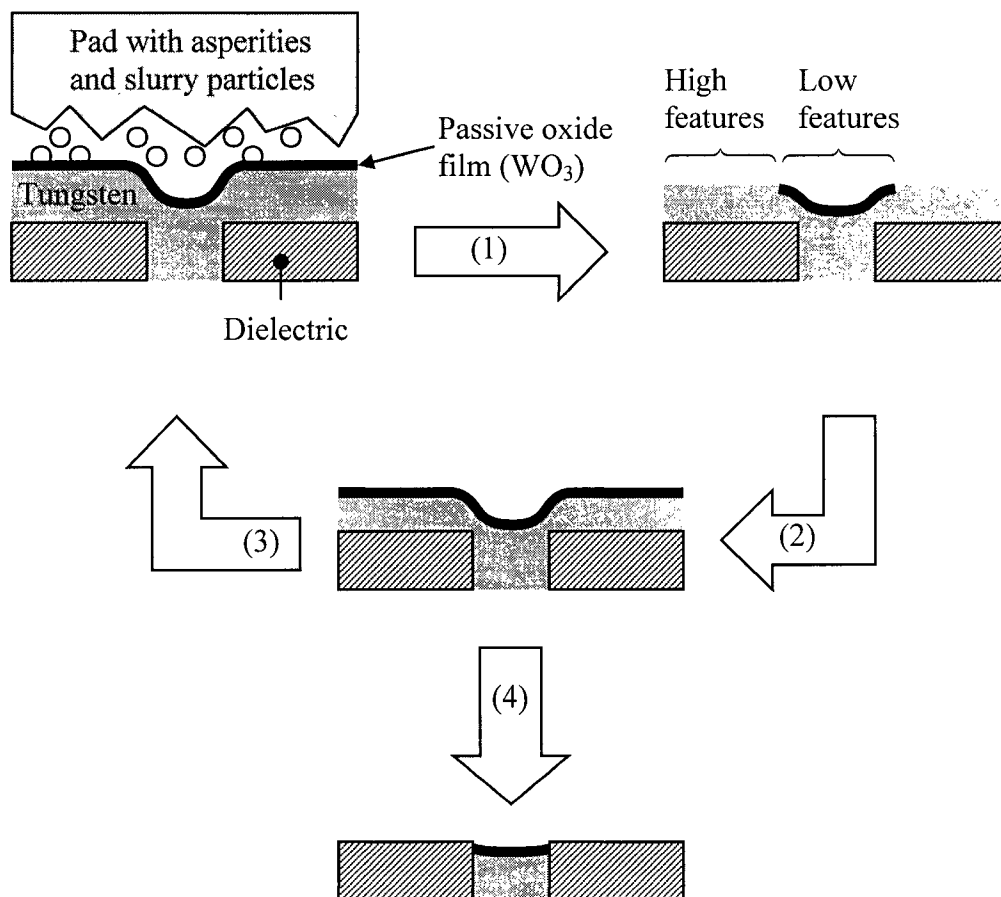


Figure 2.5. Proposed mechanism for planarization of patterned tungsten metal during CMP. (1). Abrasion of the passive WO_3 film, exposing tungsten metal to the slurry chemistry. (2). Repassivation of the exposed tungsten metal. (3). Re-abrading the freshly formed WO_3 film. Steps (1) through (3) are repeated until surface planarization is achieved in step (4).^[29]

However, the thickness of the WO_x film was determined to be 10 to 15Å, and the removal rates were 1,100 to 1,600 Å/min. If Kaufman's mechanism held true, the expected tungsten removal rate based on the model would only be half as much as what was actually measured. This showed that the removal mechanism of tungsten during CMP was not simply due to the removal of a passivating oxide film but to other factors also.

The measurements of corrosion potential (E_{corr}) as function of time have found to be a good technique in observing the effects of passivation. In studies done by Kneer, the E_{corr} versus time was used to observe the passivation behaviors of tungsten film under various chemistries.^[31, 33] It was found that during abrasion, the measured E_{corr} became more negative signifying the removal of a passivating film and exposure of tungsten metal to the chemistry. Once abrasion was stopped, the measured E_{corr} became more positive showing signs of repassivation.

2.1.5.2.2. Copper CMP

The demand for faster microelectronic devices has brought copper as the metallization for interconnect structures. The development of copper CMP processes began in the early 1990s.^[34, 35] Early copper CMP slurry consisted of nitric acid (HNO_3) and ammonia hydroxide (NH_4OH) based chemistries.^[36, 37] Nitric acid has been a well-known copper etchant; therefore, slurry containing HNO_3 was expected to actively dissolve copper. The copper CMP removal rate using nitric acid based slurry was approximately 4,000 Å/min.^[36, 37] To prevent copper from etching out of control,

benzotriazole (BTA), a commonly used copper corrosion inhibitor, was often added into the slurry.

From the copper-water E-pH diagram shown in Figure 2.6(a), the stability of copper in aqueous chemistry shows that copper should be stable in neutral and slight alkaline pH ranges (~4 to ~12) forming a passive metal oxide.^[32, 38] In extreme pH conditions (pH < 3), copper metal is unstable and easily soluble. At pH > 13, copper is unstable in the form of HCuO_2^- and CuO_2^{2-} . The amount of dissolved copper can change the stability of copper species. With increasing dissolved copper concentration, the $\text{Cu}^{2+}/\text{CuO}$ stability line shifts from pH 7 towards ~ 4, and the stability region of CuO expands into the high alkaline pH values.

In a CMP slurry containing NH_4OH , the pH value was typically in the alkaline region, pH ~ 11. The removal rate of copper using this slurry was approximately 1,500 Å/min. In Figure 2.6(b), the E-pH diagram of copper with addition of NH_3 in the system is shown. The diagram has activity of $[\text{Cu}] = 10^{-6}$ and activity of $[\text{NH}_3] = 0.1$. In this copper-ammonia-water system, formation of copper-amine based complexes occurs. The diagram showed that near neutral and alkaline conditions, pH > 4, copper is only stable in the form of copper-amine complexes, $\text{Cu}(\text{NH}_3)_x^{2+}$ (where x = 1 to 4). In more reducing conditions, $\text{Cu}(\text{NH}_3)_2^+$ may exist as well.

Ideally, copper CMP should be done in neutral or acidic conditions. Because high selectivity is required between copper and ILDs (such as SiO_2), alkaline copper CMP is typically not recommended.^[39] This is due to the passivation of copper film and SiO_2 being chemically attacked at high pH values.

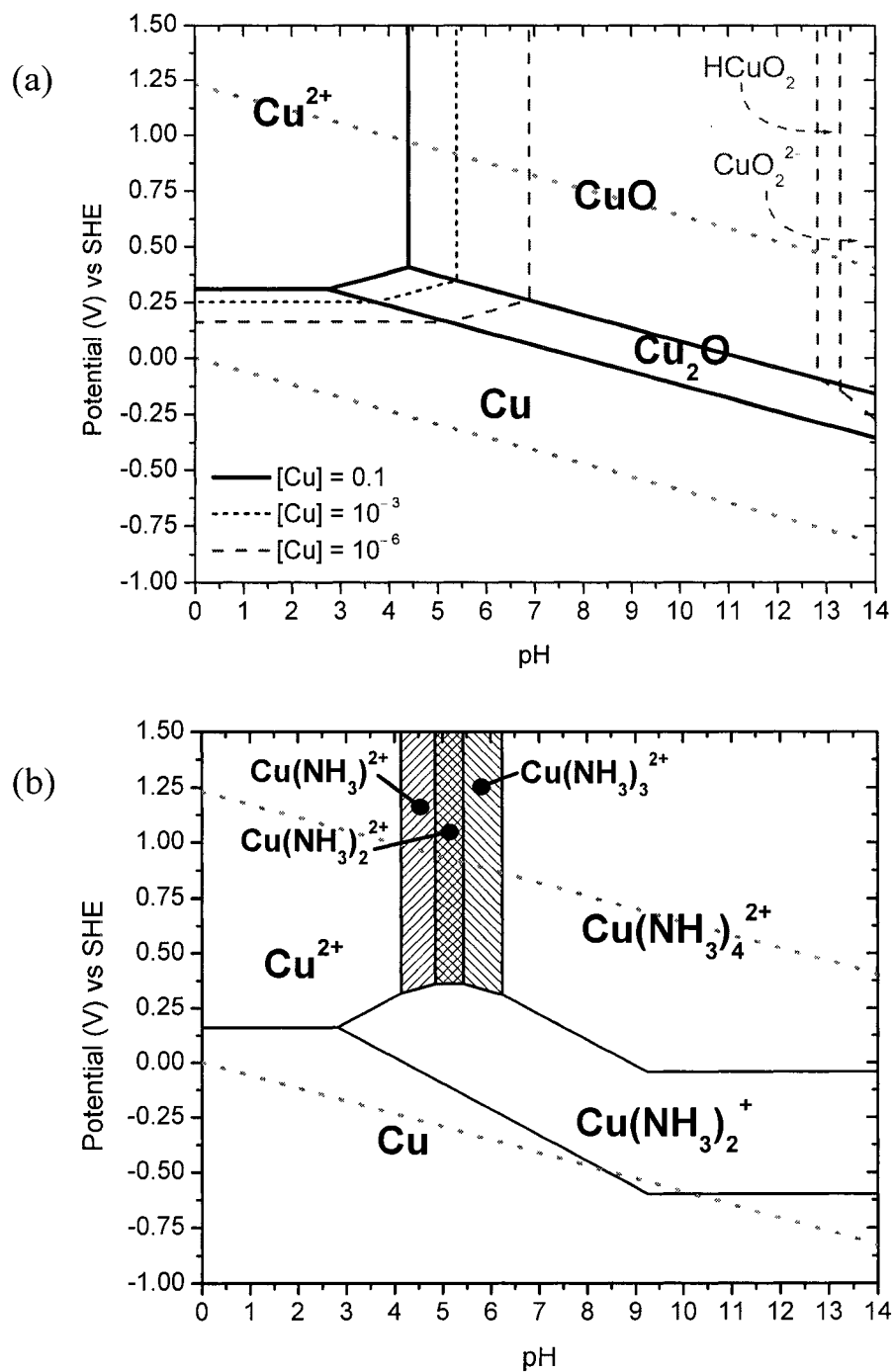


Figure 2.6. Potential-pH diagrams. (a). Cu-H₂O system with [Cu] = 0.1, 10⁻³, and 10⁻⁶. (b). Cu-NH₃-H₂O system with [Cu] = 10⁻⁶ and [NH₃] = 0.1.

It is also possible to polish copper in near neutral conditions by using ammonium salts (NH_4NO_3 and $(\text{NH}_4)_2\text{SO}_4$) rather than ammonium hydroxide.^[40] The advantage of using ammonium salts is that one still can take advantage of the complexing abilities of NH_3 to have optimal removal rate without suffering a loss in Cu/SiO_2 selectivity.

A wide range of oxidants have been tested and evaluated for copper CMP. The various oxidants and its electrochemical potential are tabulated in Table 2.2. The order of the oxidants in Table 2.2 is based on their standard reduction potential (E°). The higher reduction potential reactions are more likely to serve as an oxidant than the lower reduction potential reactions.

Table 2.2. Standard reduction potentials of various oxidants.^[41]

Oxidants	Electrochemical Half-Cell Reactions	E° (V) vs SHE	Ref.
H_2O_2	$\text{H}_2\text{O}_2 + 2 \text{H}^+ + 2 \text{e}^- \leftrightarrow 2 \text{H}_2\text{O}$	1.763	[42, 43]
$(\text{NH}_3\text{OH})_2\text{SO}_4$	$\text{NH}_3\text{OH}^+ + 2 \text{H}^+ + 2 \text{e}^- \leftrightarrow \text{NH}_4^+ + \text{H}_2\text{O}$	1.35	[44]
O_2	$\text{O}_2 + 4 \text{H}^+ + 4 \text{e}^- \leftrightarrow 2 \text{H}_2\text{O}$	1.229	
KIO_3	$2 \text{IO}_3^- + 12 \text{H}^+ + 10 \text{e}^- \leftrightarrow \text{I}_2 + 6 \text{H}_2\text{O}$	1.195	
KIO_3	$\text{IO}_3^- + 6 \text{H}^+ + 6 \text{e}^- \leftrightarrow \text{I}^- + 3 \text{H}_2\text{O}$	1.085	[45]
$\text{Fe}(\text{NO}_3)_3$	$\text{NO}_3^- + 3 \text{H}^+ + 2 \text{e}^- \leftrightarrow \text{HNO}_2 + \text{H}_2\text{O}$	0.94	
$\text{Fe}(\text{NO}_3)_3$	$\text{Fe}^{3+} + \text{e}^- \leftrightarrow \text{Fe}^{2+}$	0.771	
$\text{O}_2/\text{H}_2\text{O}_2$	$\text{O}_2 + 2 \text{H}^+ + 2 \text{e}^- \leftrightarrow \text{H}_2\text{O}_2$	0.695	
$\text{K}_3\text{Fe}(\text{CN})_6$	$\text{Fe}(\text{CN})_6^{3-} + \text{e}^- \leftrightarrow \text{Fe}(\text{CN})_6^{4-}$	0.358	[29]
	$\text{Cu}^{2+} + 2 \text{e}^- \leftrightarrow \text{Cu}$	0.34	

From Table 2.2, it may be seen that H_2O_2 has the highest reduction potential. Other oxidants such as $\text{Fe}(\text{NO}_3)_3$ and KIO_3 are also being used in slurries for copper CMP, because both have higher potentials than Cu^{2+}/Cu . Even though H_2O_2 has a higher reduction potential than $\text{Fe}(\text{NO}_3)_3$, the copper static etch rate in $\text{Fe}(\text{NO}_3)_3$ based chemistries more than doubled compared to H_2O_2 based chemistries.^[46] This may be due to the fact that $\text{Fe}(\text{NO}_3)_3$ has two oxidizing species, Fe^{3+} and NO_3^- , and that H_2O_2 is easily decomposed into oxygen, which has lower reduction potential than $\text{Fe}(\text{NO}_3)_3$. A four-fold increase in copper removal rate can occur when complexing agents, such as glycine, citric acid, phthalate, and others were added into the slurries.^[47, 48] To prevent unwanted etching of copper, corrosion inhibitors are incorporated into the slurry chemistry. The stability of most complexes of copper with complexing agents and corrosion inhibitors often occurs in near neutral pH conditions (pH ~ 4 to 10).^[49]

During copper CMP, the formation of a passive layer is necessary to obtain planarity according to Kaufman's model. The formation of a passive oxide layer on copper in the presence of an oxidant, such as H_2O_2 , is stable and usually prevents additional dissolution of copper. The addition of a complexant, such as glycine, will complex with copper and prevent the formation of a passive oxide, and enhances the removal rate. Without a passive oxide, unwanted dissolution of copper occurs creating defects, such as recession, which result in loss of surface planarity. Adding corrosion inhibitor, such as BTA, will form a $\text{Cu}(\text{BTA})$ passive film and prevent the dissolution of copper. Oxidants, such as KIO_3 , will form a combination of CuO and CuI passive films necessary to obtain surface

planarity. If the added complexant prevents the formation of CuO, enough surface passivation still occurs with CuI to obtain surface planarity.^[45]

A copper CMP slurry using hydroxylamine (NH₂OH) is currently being developed by EKC Technology in Hayward, California (a subsidiary of DuPont Electronic Technologies).^[50-54] Without additional additives, such as complexants or inhibitors, the static etch rate of copper has a very strong dependence on pH. Studies from EKC Technology showed that hydroxylamine based slurries can remove copper film at a rate of ~100 Å/min and ~1000 Å/min at pH 3 and 5, respectively.^[51, 52] This pH dependence on copper removal tends to contradict the pH dependence observed for other oxidants, such as H₂O₂ and KIO₃.^[45, 48] The observed and expected pH dependence on copper removal rate using H₂O₂ and KIO₃ is a decrease in removal rate when the slurry pH increased from ~3 to ~5. The higher copper removal rate at pH ~ 5 when using NH₂OH raised several fundamental questions regarding the mechanism of copper removal and the stability of copper in hydroxylamine chemistry, which will be discussed later.

2.2. Hydroxylamine

Hydroxylamine (HO-NH₂ or NH₂OH) was first discovered in 1865 by Lossen, and later synthesized in 1891 by Lobry de Bruyn.^[55-57] Hydroxylamine forms transparent, colorless, and odorless crystals. The physical properties of hydroxylamine are listed in Table 2.3.

Table 2.3. Physical properties of hydroxylamine.^[55]

Physical properties	Description
Molecular weight	33.03 g/mol
Melting point	32.05 °C
Boiling point (29 kPa)	56 °C
Appearance	Transparent, colorless
Smell	Odorless
Solubility	Complete soluble in water, methanol, and ethanol

The production of caprolactam (2-oxohexamethylenimine or C₆H₁₁ON) largely depends on the use of hydroxylamine to form cyclohexanone oxime from cyclohexanone.^[58] Caprolactam has been used predominately in producing spinnable polymer (such as nylon) through polycondensation process. Currently, as much as 800,000 metric tons a year of hydroxylamine was used to produce caprolactam.^[55]

Hydroxylamine is comparable to a hybrid between hydrazine (H₂N-NH₂ or N₂H₄) and hydrogen peroxide (HO-OH or H₂O₂).^[59] Hydrazine has often been considered a strong reducing agent, and hydrogen peroxide is a well-known oxidant. The behaviors of hydroxylamine as either an oxidant or a reducing agent largely depends on the pH of the

solution. In acidic media, hydroxylamine becomes an oxidant and in alkaline condition, it behaves more as a reducing agent.^[59]

The use of hydroxylamine spans into various industries. Hydroxylamine is used as a reducing agent in the reduction of silver(1+) to silver metal during the development of photographic films.^[60] The US Department of Energy has also used hydroxylamine as a reducing agent for the processing of plutonium(4+) to plutonium(3+). The US Army has also been investigating the use of hydroxylamine as an oxidizer for liquid gun propellant mixture.^[61] Hydroxylamine based chemistries have been used in recent years for the fabrication of microelectronic devices. In particular, hydroxylamine has been found to be an effective chemistry in stripping photoresist and removing etch residues on critical surfaces after plasma etching.^[62-65]

2.2.1. Chemical and Electrochemical Properties of Hydroxylamine

The oxidation states of nitrogen compounds, including hydroxylamine, are listed in Table 2.4. Hydroxylamine has a nitrogen atom with an oxidation state of -1 . For hydroxylamine to behave as an oxidant, the nitrogen atom should reduce into -2 and -3 oxidation states. Hydroxylamine (NH_2OH) can be reduced to hydrazine (N_2H_4) and ammonia (NH_3). When the nitrogen atom in hydroxylamine is oxidized from -1 to either 0 through $+5$, it behaves more like a reducing agent. The numbers of possible oxidation reactions for hydroxylamine are more than its reduction reactions. The majority of the common nitrogen gas species, such as N_2 , N_2O , NO , and NO_2 , could form through oxidation of hydroxylamine.

Table 2.4. Oxidation states of nitrogen based compounds. ^[66, 67]

Oxidation state	Typical compounds
+5	HNO ₃ , NO ₃ ⁻
+4	NO ₂ , N ₂ O ₄
+3	HNO ₂ , NO ₂ ⁻ , NO ⁺ , NCl ₃
+2	NO
+1	N ₂ O, H ₂ N ₂ O ₂ , N ₂ O ₂ ²⁻ , NHCl ₂
0	N ₂
-1/3	HN ₃ , N ₃ ⁻
-1	NH ₃ OH ⁺ , NH ₂ OH, NH ₂ Cl
-2	N ₂ H ₅ ⁺ , N ₂ H ₄
-3	NH ₄ ⁺ , NH ₃

The equilibrium potentials of redox reactions between various nitrogen based species are diagrammed in Figure 2.7. All of the equilibrium potentials calculated in acidic conditions have an assumed pH value of 1, and the equilibrium potentials calculated in alkaline condition have an assumed pH value of 14. The redox equilibrium potentials in Figure 2.7 can be useful in identifying whether the reaction is favorable or not in a given condition. For example, at a pH value of 14, the reduction of N₂ → NH₂OH has an equilibrium potential of -3.04V. Due to the large negative potential value, this reaction shows that NH₂OH can serve as a reducing agent for a majority of the reduction process.

The dissociation reactions for hydroxylamine are as follow:^[68, 69]



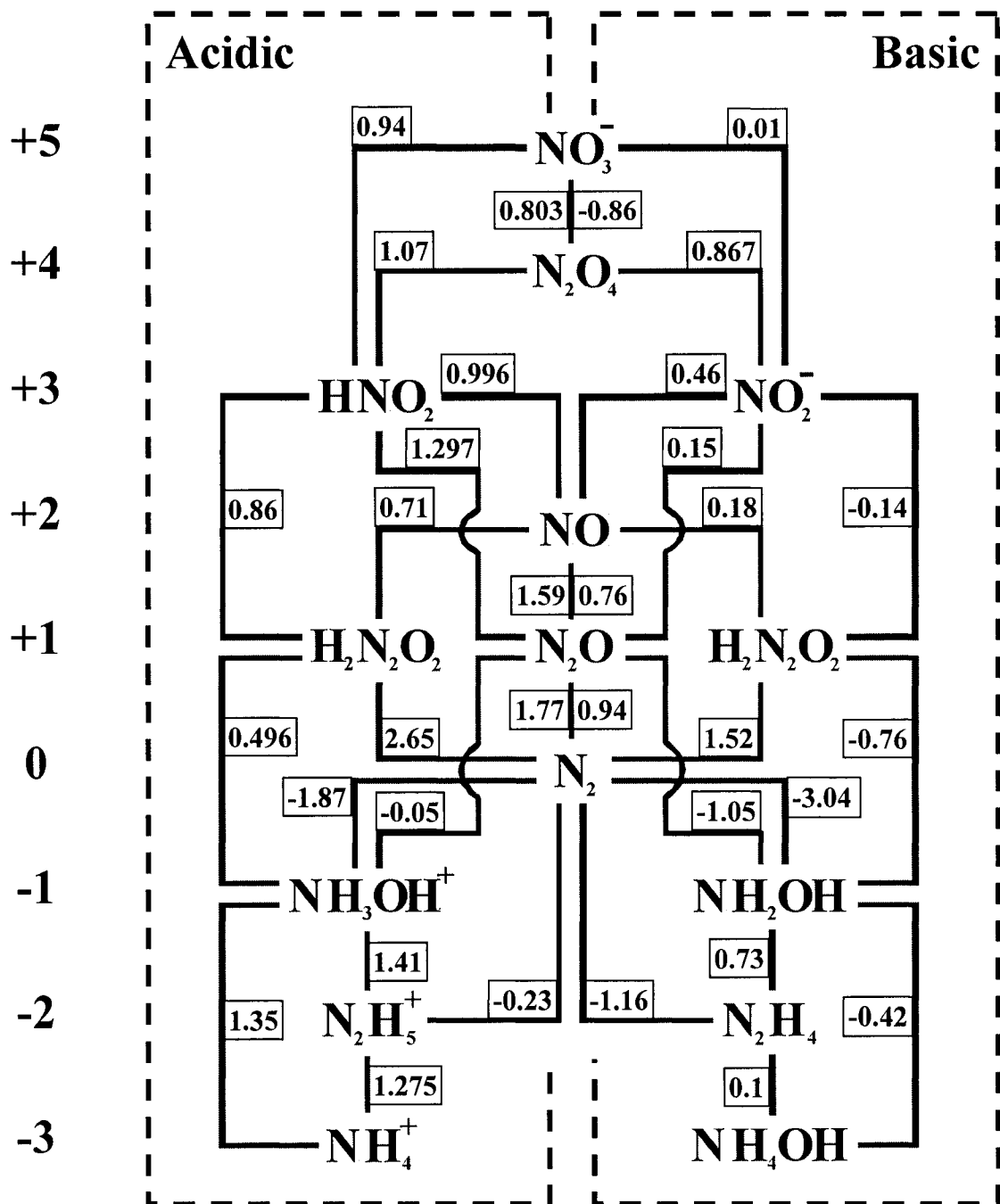
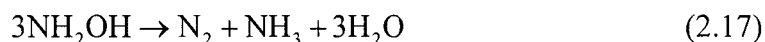


Figure 2.7. Calculated equilibrium potentials of redox reactions of nitrogen based species in volts (V) with respect to standard hydrogen electrode (SHE).^[41, 67, 70] The “acidic” region assumed pH value of 1 for the calculations. The “basic” region assumed pH value of 14 for the calculations.

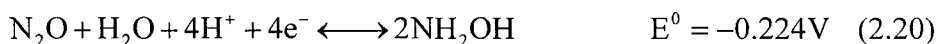
The pK value for Reaction (2.15) is 5.80, which means that at pH values less than 5.8, hydroxylamine exists in NH_3OH^+ form, and at pH values greater than 5.8, hydroxylamine is likely to be in NH_2OH form.

Studies performed on the stability and the decomposition behaviors of hydroxylamine have produced results that may be of interest in understanding the mechanism of hydroxylamine during the copper CMP process. In several studies it was found that in alkaline conditions, the decomposition of hydroxylamine typically proceeded through the chemical reactions shown in Reactions (2.17) and (2.18).^[71, 72]



Depending on the solution pH and varying additives/catalysts, the amount of the decomposition products (N_2 , N_2O , and NH_3) will vary. For example, in a strongly alkaline NH_2OH solution containing copper ions, both Reactions (2.17) and (2.18) occur simultaneously and quickly. The percentages of decomposition products converted from NH_2OH in alkaline condition were 22.4% N_2 , 27.5% N_2O , and 28.2% NH_3 . In a neutral pH, the amount of decomposition product decreased by half, only producing 12.2% N_2 , 7.2% N_2O , and 12% NH_3 . In acidic conditions, NH_3OH^+ was quite stable and produced undetectable decomposition products.^[72] In a technical report from the US Department of Energy on hydroxylammonium nitrate ($\text{NH}_3\text{OH}^+\cdot\text{NO}_3^-$),^[61, 73] the decomposition ratios between $\text{N}_2\text{O}:\text{N}_2$ were in the range of 2:1 to 4:1 under normal conditions. In the presence of iron, the ratio was increased to 36:1. It was proposed that the decomposition Reactions

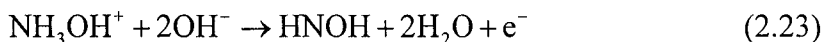
(2.17) and (2.18) are due to oxidation and reduction of NH_2OH . The oxidation of NH_2OH to either N_2 or N_2O is shown below,



The reduction of NH_2OH to NH_3 is shown as follows,



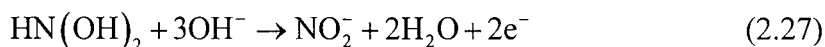
The decomposition of hydroxylamine may be more complicated than the redox reactions shown in Reactions (2.17) and (2.18). Several possible intermediate reactions that may lead to decomposition of hydroxylamine have been extensively investigated. In a study by Rao *et al*, a nitroxyl specie (HNO or HNOH) was proposed to be a rate-determining intermediate to the oxidation steps of NH_2OH to N_2 and N_2O .^[74] The formation of a nitroxyl species in strongly alkaline ($\text{pH} \geq 13$) and acidic conditions are shown as Reactions (2.22) and (2.23), respectively.



Further decomposition of the nitroxyl (HNO and HNOH) to either N_2O or N_2 is shown in Reaction (2.24) and (2.25).



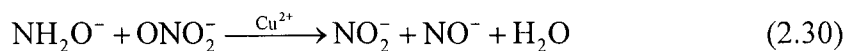
Trace amounts of nitrite ions (NO_2^-) also found in solution were considered as an oxidized product of a dihydroxylammonia ($\text{HN}(\text{OH})_2$) specie, which was formed from the hydrolysis of HNO, shown in Reaction (2.26) and (2.27).^[74]



In a study by Hughes *et al.*,^[75] the proposed formation of NO_2^- from decomposition of hydroxylamine in alkaline conditions was different than the reactions proposed by Rao *et al.* Hughes *et al.* found that in an oxygen-rich atmosphere, about 90% of the decomposition products from hydroxylamine contained NO_2^- and peroxyxynitrite (ONO_2^-). When heavy-metal ions were present, approximately 75% of hydroxylamine was decomposed into NO_2^- . The remaining 30% was detected as ONO_2^- , which acted as a transient intermediate. Hughes *et al.* proposed that the nitroxyl ion (NO^- or HNO) was the intermediate specie in forming ONO_2^- , which is shown in Reactions (2.28) and (2.29).

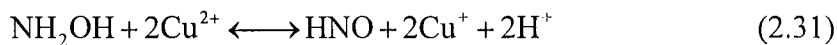


In strongly alkaline conditions (pH ~ 14), NH_2OH de-protonated into NH_2O^- , as shown in Reaction (2.16). If insufficient oxygen was present in the solution, NO^- would dimerize and form N_2O , Reaction (2.24) instead of forming ONO_2^- , shown in Reaction (2.29). The continuing decomposition of NH_2OH occurred when ONO_2^- reacted with NH_2O^- , resulting in the formation of NO_2^- , as shown in Reaction (2.30).



Trace amount of metal ions, such as Cu^{2+} , were likely to catalyze Reaction (2.30). Interestingly, increasing concentrations of Cu^{2+} ions seemed to decrease the formation of NO_2^- . This was probably due to the rapid consumption of ONO_2^- and O_2 forcing NO^- to dimerize, forming N_2O . A similar study by Moews and Audrieth supports with the same conclusion.^[76]

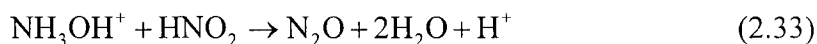
The effects of copper catalyzed oxidation of hydroxylamine were studied by Anderson.^[77] In this study, it was found that the formation of NO_2^- may occur through the following reactions,



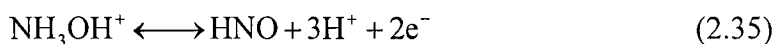
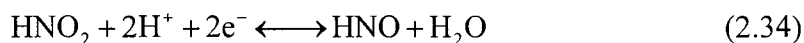
Again, nitroxyl (HNO) was considered as an intermediate in the decomposition of hydroxylamine.

To review, the studies mentioned above seem to agree on the decomposition products of hydroxylamine, which were N_2 , N_2O , NO_2^- , and NH_3 . However, most of the arguments were on the formation of NO_2^- . Rao *et al* proposed an intermediate $\text{HN}(\text{OH})_2$ specie, Reaction (2.27), while Hughes *et al* proposed the catalytic effects of ONO_2^- , Reaction (2.30). Anderson proposed the reaction of HNO and oxygen to form NO_2^- .

In a study by Stedman *et al*, the presence of NO_2^- or HNO_2 in hydroxylamine solution was found to induce additional decomposition of hydroxylamine.^[78, 79] They demonstrated that in acidic conditions, hydroxylamine reacts with HNO_2 forming N_2O , which is shown in Reaction (2.33).

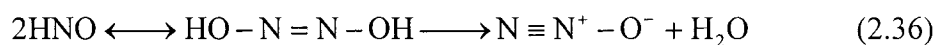


In earlier discussions, the formation of N_2O was proposed to occur through the dimerization of HNO, Reaction (2.24). The formation of HNO can occur either from HNO_2 or NH_3OH^+ , or both. The reactions from both sources are shown below.



To establish whether NH_3OH^+ or HNO_2 was the dominant source of HNO, Stedman *et al* reacted isotopically ^{15}N -hydroxylamine ($^{15}\text{N}-\text{H}_2\text{OH}$) with normal ^{14}N -nitrous acid ($\text{H}-^{14}\text{N}-\text{O}_2$) and found the N_2O that was generated contained both ^{14}N and isotope ^{15}N . If the formation of N_2O was from a single source of HNO, *i.e.* hydroxylamine, then doubly isotopic N_2O would be detected by mass spectrometric measurements. The lack of doubly isotopic N_2O ruled out the single source HNO mechanism. The other logical conclusion was that hydroxylamine may have directly reacted with HNO_2 forming singly isotopic N_2O .

In a similar study, Bothner-By *et al*^[80] used isotopically marked nitrogen reactants and found that the N_2O species produced, have a ratio of 1:1 between $^{14}\text{N}\equiv^{15}\text{N}^+\text{O}^-$ and $^{15}\text{N}\equiv^{14}\text{N}^+\text{O}^-$, at pH value of 7. When the pH value was decreased to 1, the ratio became 2:1. It was then proposed that the intermediate specie in the formation of N_2O via the dimerization process of HNO may be hyponitrous acid ($\text{H}_2\text{N}_2\text{O}_2$). This is shown in Reaction (2.36).



A schematic flow chart in Figure 2.8 was constructed to help in clarifying all of the possible proposed decomposition mechanisms that were discussed earlier. The figure shows nitrogen-based species with increasing oxidation states from bottom to the top and decreasing pH values from right to left. The species circled have been qualitatively identified from the decomposition studies reviewed earlier. The formations of NO_2^- and N_2O from hydroxylamine, as shown in the figure, and the discussions on the decomposition of hydroxylamine (earlier in this section) all seem to indicate a nitroxyl (HNO) intermediate step.

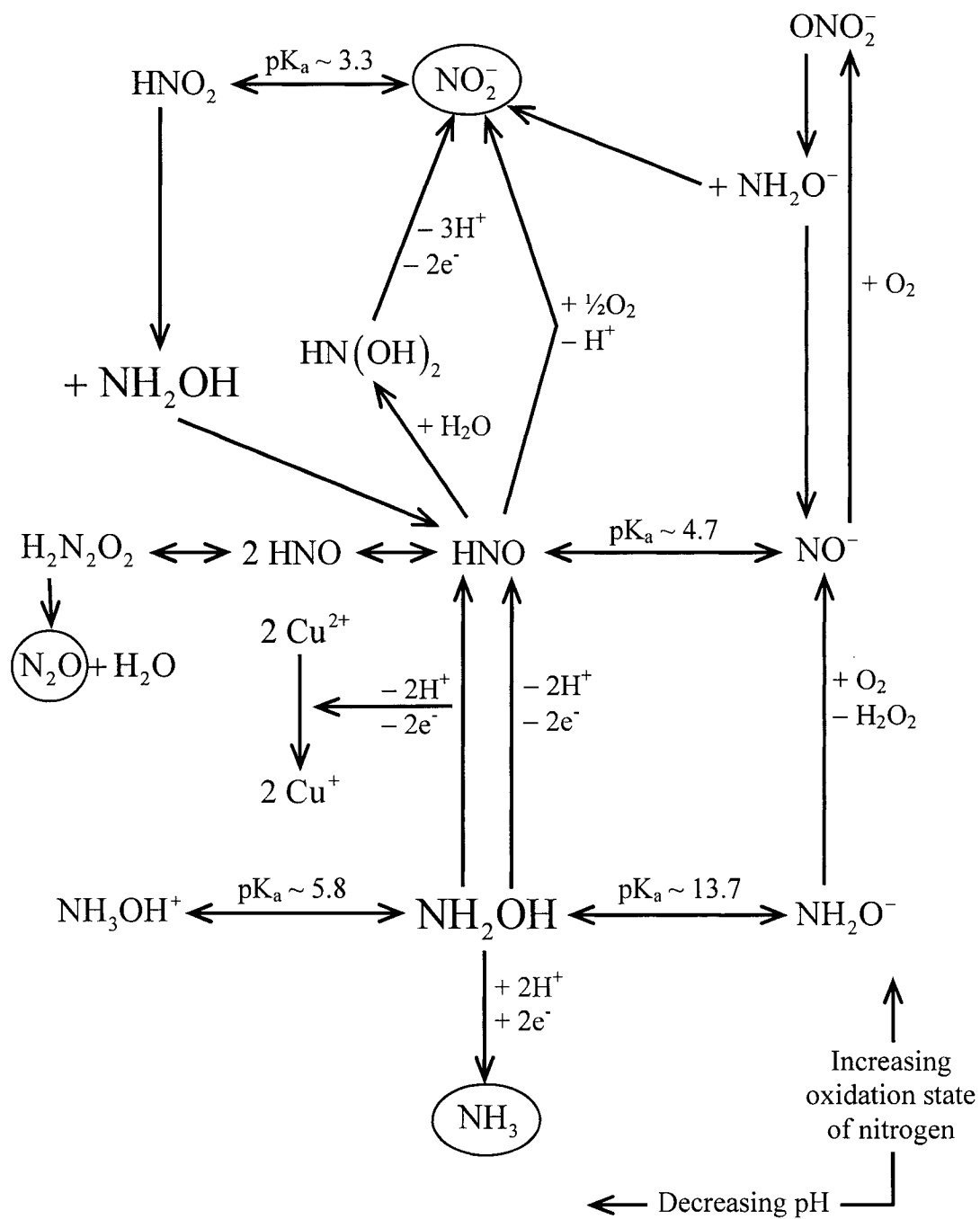


Figure 2.8. Schematic flow chart of the mechanisms that have been proposed for the decomposition of hydroxylamine (NH_2OH).

CHAPTER 3. EXPERIMENTAL SETUP AND METHODS

3.1. Industrial Size CMP Polisher

The CMP of copper wafers in hydroxylamine based slurry was performed on a Strausbaugh Model 6EC 8" wafer polisher. The 6EC polisher performs like a traditional CMP tool, shown in Figure 2.3(a). The slurry used for polishing contained 0.5M hydroxylamine and 4% colloidal SiO₂ (particle size ~70 nm). The pH of the slurry was adjusted using microelectronic grade sulfuric acid. The polishing was done on a single platen system using an IC-1400/Suba IV stacked pad. Between each wafer polishing, the pad was reconditioned using a diamond conditioning pad. The polishing pressure varied between 3, 6, and 9 psi. The polishing speed for the wafer carrier varied between 10, 30, 50, and 75 rpm, while the platen speed was set to ~ 0.93× the wafer carrier speed. The amount of copper removed after polishing was determined by a CDE ResMap 4-point probe film thickness measurement.

3.2. Laboratory Scale Electrochemical Abrasion Cell (EC-AC)

All small scale abrasion/polishing studies were performed on a specially designed "electrochemical" abrasion cell. This research tool is schematically shown in Figure 3.1. The EC-AC tool can be viewed as an upside-down industrial CMP tool, shown in Figure 2.3(a). The advantage of this design was the ability to perform and measure electrochemical data using an electroplated copper film on silicon wafer under abrasion conditions.

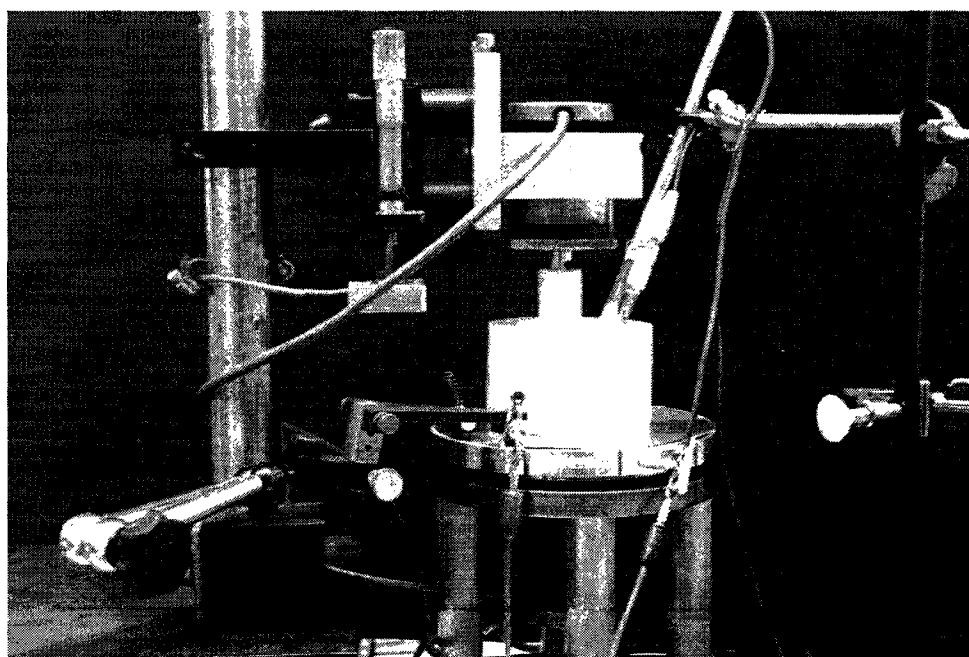
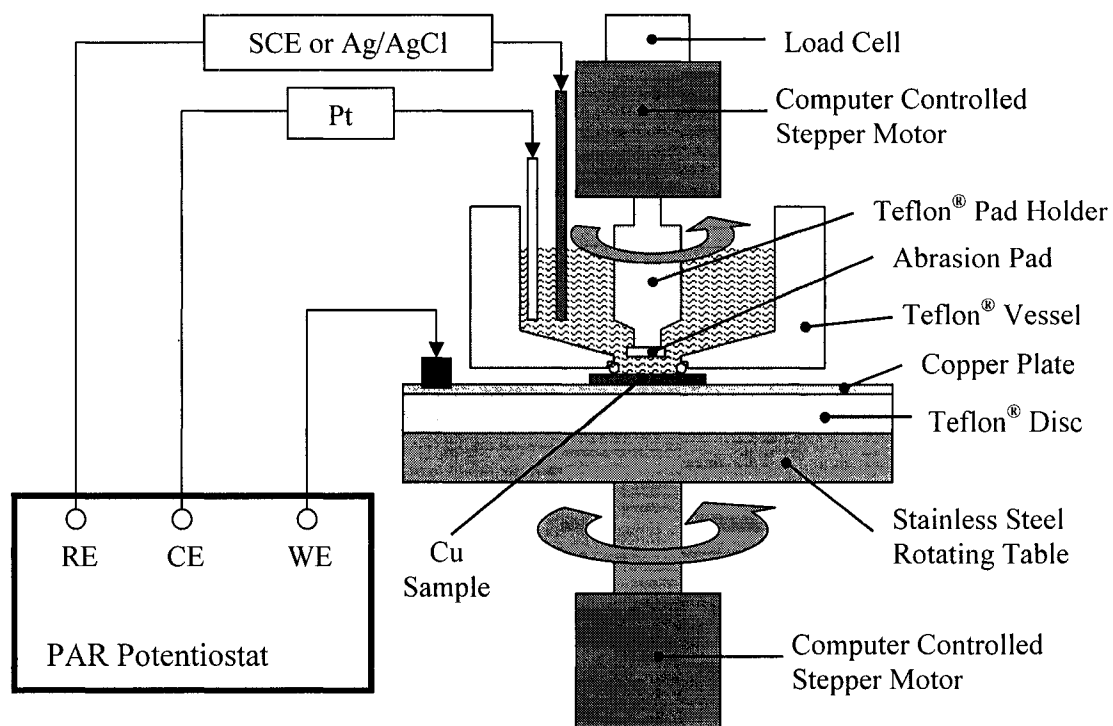


Figure 3.1. Schematic diagram (top) and a photograph (bottom) of the electrochemical abrasion cell that was designed and fabricated for measuring and collecting electrochemical information during abrasion conditions.

Many researchers have used a traditional rotating disc electrode (RDE) setup to simulate copper CMP while performing electrochemical analysis.^[36, 42, 45, 47, 81] When using the RDE setup, bulk copper metal samples are used instead of electroplated copper film on silicon. The bulk copper samples may possess different electrical properties than electroplated copper film on silicon. The upside-down design provides a vessel to hold the solutions or slurries, which can later be collected and chemically analyzed.

The EC-AC tool has of two parts: (1) The top part consists of pad, pad holder, top stepper motor, and the load cell; (2) The bottom part consists of the Teflon vessel, copper sample, and the stainless steel table with the bottom stepper motor. The bottom part was assembled by first placing a conducting plate (usually a 0.063” thick copper metal) on top of the stainless steel table, with a plastic (Teflon) insulating plate in between. The conducting plate allows current to flow from the copper surface that is exposed to solution to the working electrode connection on the potentiostat. Since most of the copper samples are 3 cm × 3 cm square pieces diced from an 8” silicon wafer, current cannot flow to the back side of the silicon wafer. Therefore, the electrical path is created along the edges of the 3 cm × 3 cm square pieces. This is achieved by either coating the edges with nickel or silver pastes, or by wrapping the edges with a conductive foil.

Once the copper sample is placed on top of the conductive plate, the Teflon vessel that holds the solution is placed over the copper sample. A Viton[®] o-ring is used to make the seal between the Teflon vessel and the copper sample surface. The o-ring serves two purposes: (1) To prevent solution from leaking out of the Teflon vessel; and (2) To keep the copper sample in place under rotation. To ensure that the viton o-ring is in place, the

Teflon vessel is securely fastened to the stainless steel table with four screws. After the copper sample has been properly assembled, the electrical continuity between the copper surface and edge of the conducting plate is tested using an ohmmeter.

The complete assembly of the EC-AC tool occurs when the bottom part is placed underneath the top part. With the pad/pad holder in place, the reference (RE) and counter (CE) electrodes are both placed into the Teflon vessel as close to the copper sample as possible. The connections of the RE and the CE to the potentiostat are straightforward. The working electrode (WE) is connected using a graphite rod that is pressed firmly on the conducting plate against the stainless steel table. Electrical continuity is fairly constant even while the graphite rod is sliding on the conducting plate during rotation.

Once the EC-AC tool is completely assembled and the electrodes are in place with all the necessary connections, 100 ml of solution or slurry is poured into the Teflon vessel. While keeping the pad/pad-holder suspended above the copper sample, rotation of the pad/pad-holder and the copper sample is initiated. Abrasion of the copper sample occurs when the pad is lowered and brought into contact with the copper sample.

3.2.1. Removal of Copper with Abrasion

During abrasion experiments, the abrasion pad may not always cover 100% of the area where the sample is in contact with the solution chemistry. This may prove problematic, especially when the solution chemistry has a high static etch rate on the metal film. The unwanted static dissolution of the metal film occurs in the area that is not abraded but is still in contact with the solution chemistry. This will contribute excess

metal ions into the solution. The metal ions in solution, quantified using atomic absorption spectroscopy, may not be a correct representation of the metal removed only by abrasion. During electrochemical measurements, the currents collected could also contain both the abraded and un-abraded region. An answer to these problems is to spin-coat the metal surface with a film of positive photoresist. Once the resist film cures in air, it has a soft polymeric consistency which can be easily removed during abrasion experiments. The un-abraded area retains the resist coverage and prevents any unwanted metal dissolution from occurring throughout the experiment.

Prior to each abrasion experiment, about 50% of the photoresist in the abraded region was removed using a cotton swab and isopropyl alcohol. All of the abrasion experiments used a conditioned Rodel[®] IC1000 pad attached to the pad-holder with Rodel[®] Suba IV and a spongy double-sided adhesive pad. The slurry used for abrasion experiments, unless otherwise specified, typically consisted of 0.5M hydroxylamine, 4% SiO₂ particles, and inorganic acid (H₂SO₄ or HNO₃) for pH adjustments. The metal film area in contact with the solution chemistry was defined by a Viton[®] o-ring seal with an area ~ 3 cm². The pad area was 0.7 cm². The abrasion area typically varied anywhere between 1 to 2 cm².

The copper removal rates from the abrasion experiments between copper samples coated with photoresist and copper samples without photoresist were compared. The copper removal rates are plotted with respect to slurry pH in Figure 3.2. The figure shows that by having photoresist on the copper sample surface does not affect the removal rates of copper from pH 9 through 2.5.

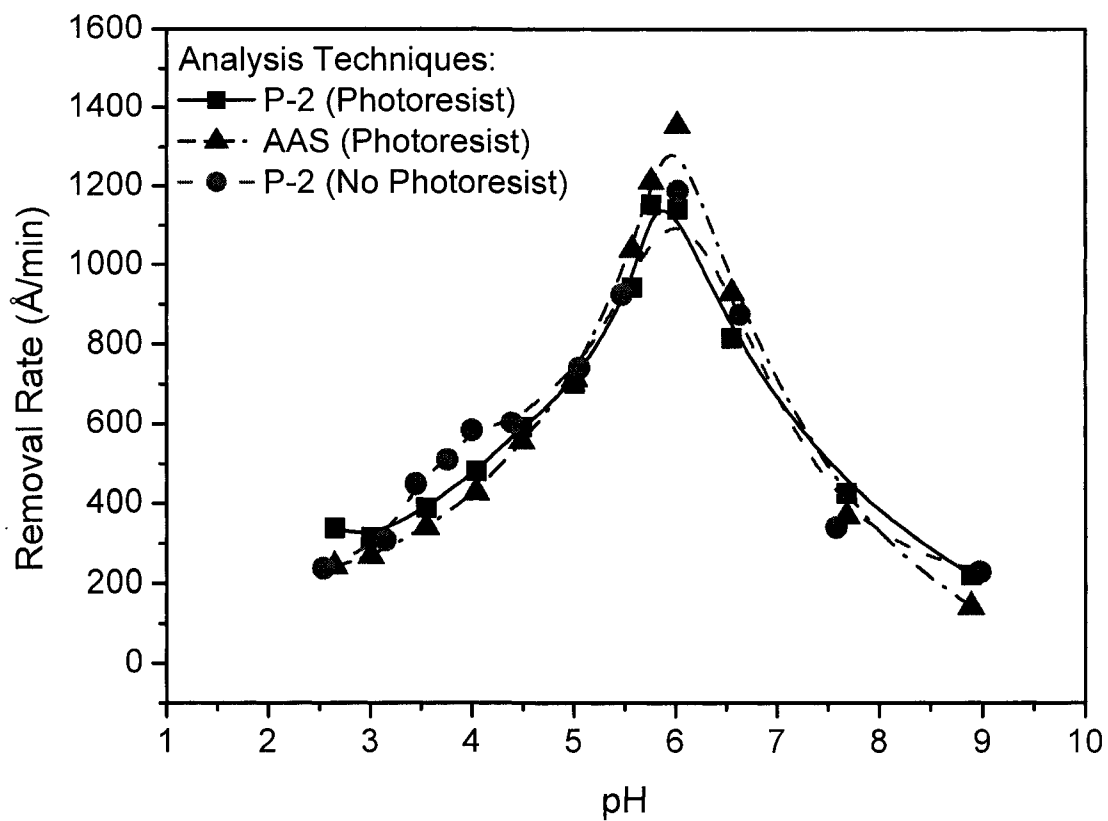


Figure 3.2. Removal rates of copper in 0.5M hydroxylamine based (HNO_3) slurry as function of pH. Copper removal rates between photoresist covered sample (■) and no photoresist sample (●) were compared. Results obtained from analysis using a P-2 profiler (●) and an atomic absorption spectrophotometer (▲) were compared.

The amount of pressure applied to the copper film during abrasion experiments were measured by a load cell that was fastened to the pad-holder/motor assembly. Standard calibrating weights were used to calibrate the digital readout of the load cell. The range of measurable pressure ranged from 0 to 40 pounds per square inch (psi). From experimental work, it was found at low pressure, below 2 psi, that a significant amount of fluctuation from the digital readout occurred during abrasion. This may have been due to the uneven contact between the pad and the sample. Most of the experiments were performed at a pressure of 9 to 10 psi.

3.2.2. Removal of Copper without Abrasion

The effects of a hydroxylamine based chemistry on electrodeposited copper film (16 kÅ) without any abrasion (dynamic etch) were studied. All of the dynamic etch experiments were performed using the EC-AC tool (Figure 3.1). For most of the experiments, the copper sample was set to rotate at 222 rpm, unless stated otherwise. Two chemical systems were setup to study the etch rate of copper film. The first system used a slurry, which contained hydroxylamine, 4% colloidal silica, and either HNO₃ or H₂SO₄ for pH adjustments. To simulate CMP conditions, a Rodel IC1000 pad was held about 5 to 10 mm above the copper sample, which was set to rotate at 240 rpm. The second system simply contained hydroxylamine and buffers without any solid particles. No pad was held above the copper sample throughout the experiment. The buffers used for the second system contained potassium dibasic phosphate (K₂HPO₄) and sulfuric acid. Total etch time for an experiment varied from 10 minutes to 60 minutes depending on the

solution pH and hydroxylamine concentration. The copper area exposed to the solution chemistry is $\sim 3 \text{ cm}^2$. The amount of copper dissolved was determined by using both atomic absorption spectrascopy (AAS) and P-2 profile measurements. The results are shown as removal rate with respect to pH in Figure 3.2. In comparing the values from AAS and P-2, both showed very similar removal rates (within $\pm 50 \text{ \AA}/\text{min}$ variations). The results obtained from both chemical systems showed no significant differences.

3.2.3. Mechanical Variability of EC-AC

The speed at which abrasion or polishing experiments occurred is expressed as relative velocity or linear velocity between the pad and the sample. The details of the relative velocity calculations are shown in the Appendix. Since the rotational speed of the pad and the sample is set independently, and the x-y position between the pad and the sample may not always be the same, the relative velocity across the abraded area may be different from one experiment to the next. The maximum achievable rotation speed for the pad holder is 3,000 rpm, but the maximum speed for the sample is only 600 rpm. The weight of the stainless steel table that the sample sits on limits the sample rotation speed, making it slower. At a higher rotation speed, the momentum of the table would take over and disengage the lower stepper motor. To prevent over-spillage of the solution that is contained by the Teflon vessel, the tolerable sample rotation speed drops to around 300 rpm. If a higher sample rotation speed is required, a cap must be placed on top of the vessel to prevent any over-spillage. The addition of a cap to the vessel, makes

electrochemical measurements impossible, because there is insufficient room to place the electrodes appropriately.

To determine which factors would contribute the largest variations in relative velocity across the abraded area, Figure 3.3 and Figure 3.5 were plotted. Two factors were considered; (1) the difference in rotational speed ($\Delta\omega$) between pad and sample and (2) the off-set distance between the pad and the sample. The off-set is directly related to the final abrasion area. At distance = 0, the abrasion area is equal to the pad area. At larger off-set distances, the abrasion area increases. Examples are shown in Figure 3.4.

For calculations of the relative velocity at various $\Delta\omega$, the pad speed is set to 240 rpm and the off-set distance was set to 0.25 cm (area = 1.65 cm²). For calculations of the relative velocity at various off-set distances, the pad speed is set to 240 rpm and the sample to 222 rpm. Figure 3.3 shows the relative velocity as a function of difference in pad and sample rotational speeds ($\Delta\omega$). Figure 3.5 shows the relative velocity as a function of the off-set distances. The individual solid circles represent the average relative velocity across the abraded area. The dashed lines are one standard deviation from the average. From Figure 3.3, increasing $\Delta\omega$ shows little change in the relative velocity, but the standard deviation to the average relative velocity became significantly large at high $\Delta\omega$. Ideally, it is best to have $\Delta\omega = 0$ because the standard deviation is small. However, problematic phenomena may occur, when $\Delta\omega = 0$, such as rotational harmonics during abrasion. Therefore, the majority of the abrasion experiments were performed with $\Delta\omega = 18$ rpm which eliminated rotational harmonics and minimized the standard deviation.

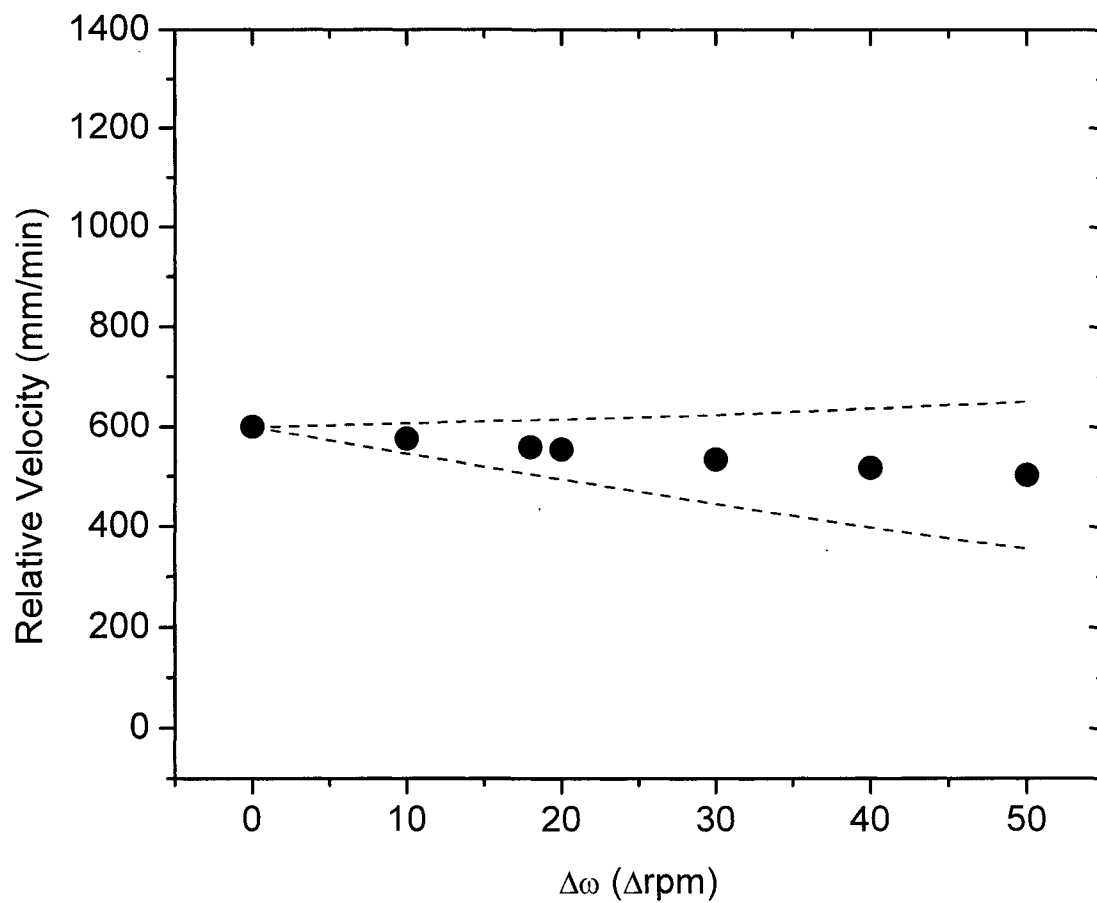


Figure 3.3. Calculated average relative velocity (mm/min) between pad and sample as a function of the difference in actual rotational speed of pad and sample ($\Delta\omega$). Dashed lines are one standard deviation from the average. Pad speed = 240 rpm. Sample speed = pad speed - $\Delta\omega$. Off-set distance = 0.25 cm (Abrasion area = 1.65 cm²).

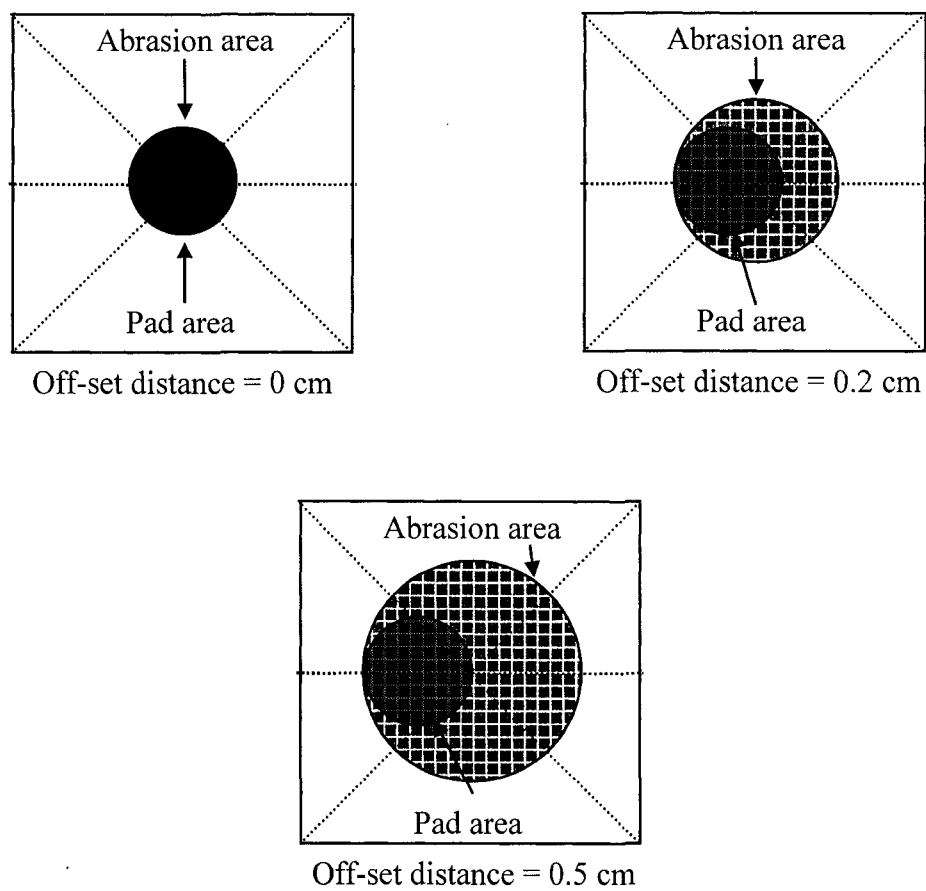


Figure 3.4. Examples of copper samples showing the off-set distance between the pad and the sample affecting the abrasion area.

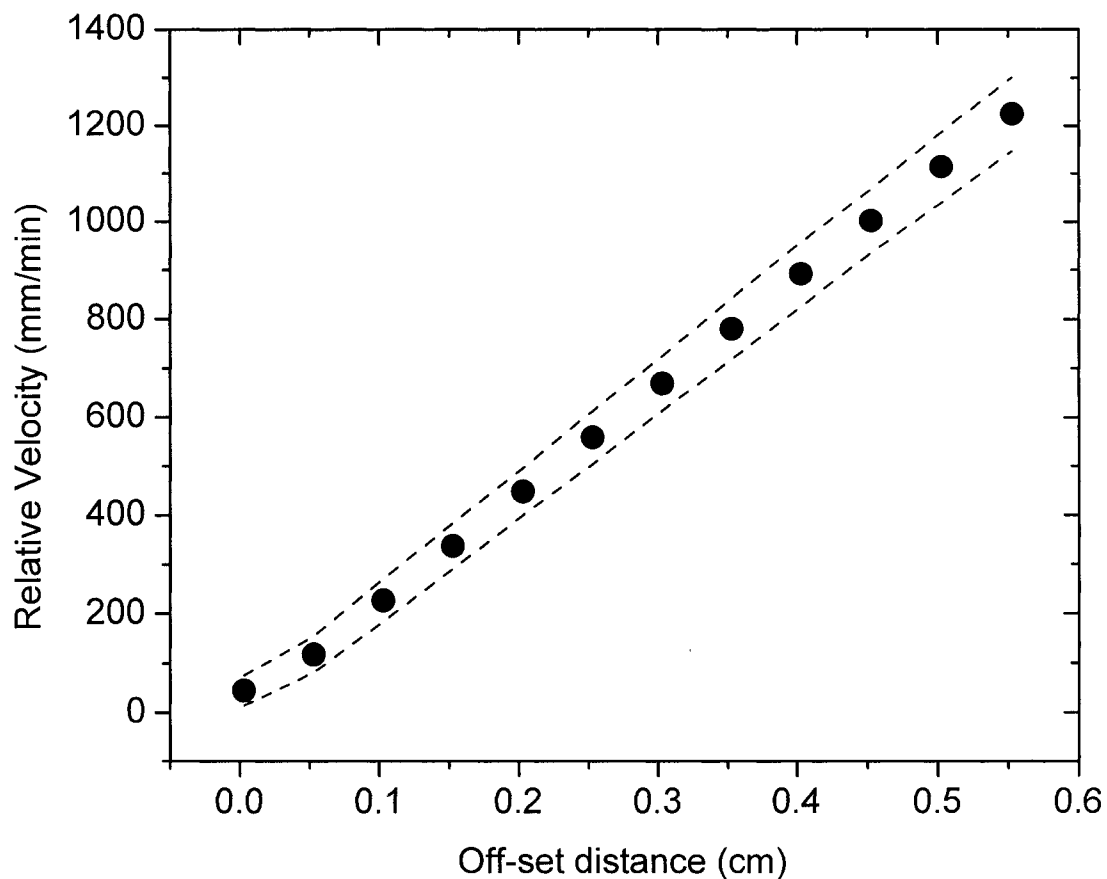


Figure 3.5. Calculated average relative velocity (mm/min) as a function of the off-set distance (cm) between pad and sample. Dashed lines are one standard deviation from the average. Pad speed = 240 rpm. Sample speed = 222 rpm. [0.1 cm (off-set) = 1.03 cm² (abrasion area), 0.5 cm (off-set) = 2.97 cm² (abrasion area)]

In Figure 3.5, the relative velocity varies fairly linear with the off-set distances. Larger off-set distances would result in higher relative velocity. The standard deviation in the averaged relative velocity at large off-set distances is much less significant than the standard deviation observed at high $\Delta\omega$. Even though the standard deviation is small at a given off-set distance, as much as a 500 mm/min (250%) increase in relative velocity occurs when the off-set distance changes from 0.09 cm to 0.33 cm. Because most abrasion experiments focused on chemical effects, the pad rotation speed was set to 240 rpm and the sample to 222 rpm ($\Delta\omega = 18$ rpm). At these values, the relative velocity was between 200 to 800 mm/min. The variation was largely due to the final off-set distance.

On a traditional rotary CMP tool polishing an 8" wafer with the pad rotating at 70 rpm and the wafer rotating at 75 rpm, the calculated relative velocity would be ~10,700 mm/min. Considering that a CMP tool has an order of magnitude higher in relative velocity than the EC-AC tool, it is possible that results obtained using the laboratory scaled EC-AC tool may not equate exactly to the results obtained on a CMP tool. The amount of fundamental information collected from the laboratory scaled polisher was certainly greater than a CMP tool could have generated.

3.3. Electrochemical Measurements

All electrochemical measurements were performed using Princeton Applied Research potentiostats (Models 263, 263A, and 273A). The electrochemical experiments were done using the three-electrode setup. The working electrode was copper. Different types of copper samples were used for electrochemical measurements. These include electrodeposited copper film ($\sim 16 \text{ k}\text{\AA}$) (on a film stack of tantalum ($\sim 2 \text{ k}\text{\AA}$) / SiO_2 /Si), a 99.99% solid copper disc, or a 99.99% 25 μm copper foil. The copper film was obtained from EKC Technology, and the copper disc/foil was purchased from Aldrich Chemicals. The counter electrode was a platinum metal plate. The reference electrode was either saturated calomel (SCE) or silver-silver chloride (Ag/AgCl). Both single-junction and doubled junction reference electrodes were tested. No significant differences were observed between reference electrodes throughout experimental work.

3.3.1. Potentiodynamic Polarization

Potentiodynamic polarization technique is a simple and a quick way to determine the extent of corrosion on metals that may take place in different chemistries and abrasion conditions. The potentiodynamic experiments were performed by polarizing the metal from -0.3 V to $+0.3 \text{ V}$ with respect to E_{corr} . The majority of experiments was performed at a scan rate of 5 mV/s . From the polarization result, information such as corrosion current density (i_{corr}) was calculated. The theories and steps used in the calculations are described in the following paragraphs.

The corrosion of a metal is an electrochemical reaction shown as Equation (3.1). This is often referred to as a “charge-transfer” (CT) reaction.



The amount of current (I , Ampere) or current density (i , Ampere/cm²) produced from Equation (3.1) can be described using the Butler-Volmer relationship, Equations (3.2) and (3.3).^[82-85]

$$i = i_a - i_c = \text{anodic current density} - \text{cathodic current density} \quad (3.2)$$

$$i = i_o \left\{ \exp \left[\frac{\alpha n F \eta}{R T} \right] - \exp \left[- \frac{(1 - \alpha) n F \eta}{R T} \right] \right\} \quad (3.3)$$

i = net or measured current density

i_o = exchange current density

η = overpotential { = applied potential (E) – equilibrium potential (E_{Eqlib}) }

α = anodic transfer coefficient

F = Faraday constant, 96500 C mol⁻¹

n = number of electrons

R = Gas constant, 8.314 J mol⁻¹ K⁻¹

T = Absolute temperature, K

An example of a Butler-Volmer plot is shown in Figure 3.6, assuming $i_o = 10^{-5}$ A/cm², $\alpha = 0.5$, $n = 1$, and $T = 298$ K. A Tafel plot is derived from the Butler-Volmer plot by taking the absolute value of the measured current density (i) and plotting it as a semi-log plot of overpotential (η) as a function of measured current density (i), shown in Figure 3.7.

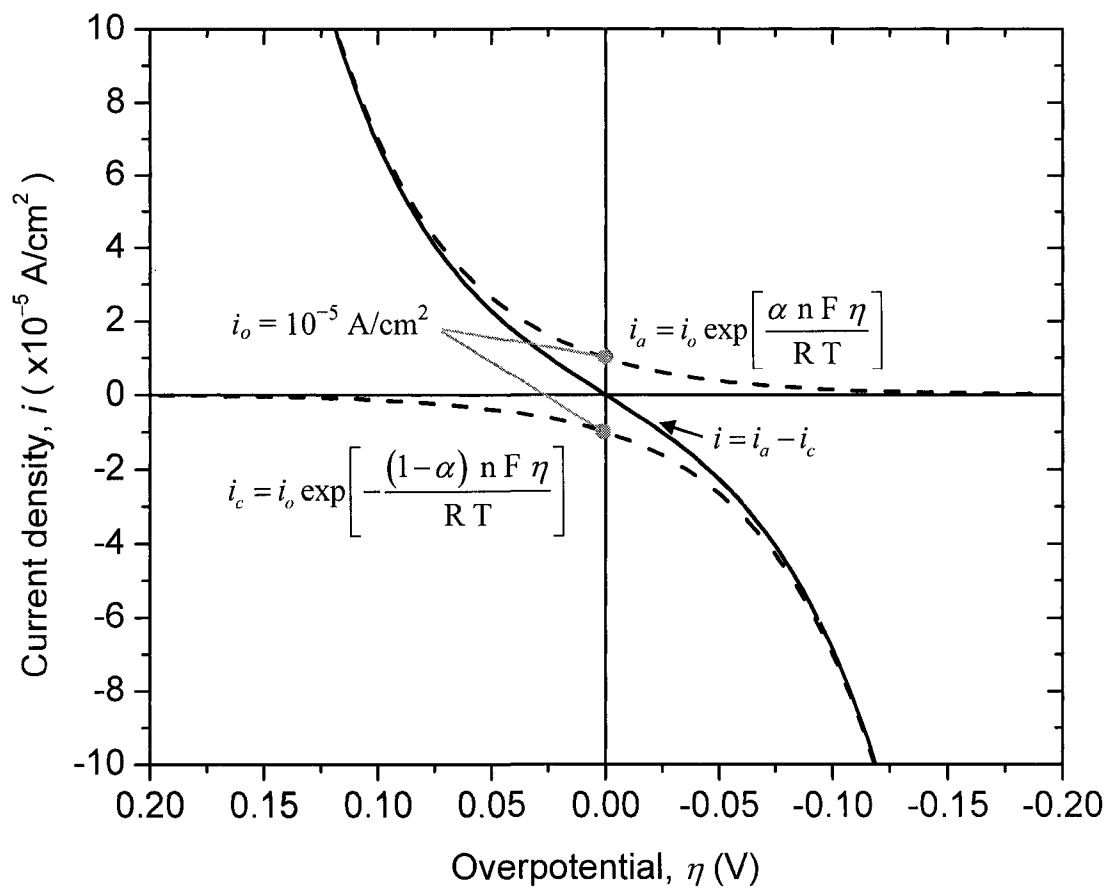


Figure 3.6. Plot of Butler-Volmer relationship, from Equation (3.3). Assuming $i_o = 10^{-5}$ A/cm 2 , $\alpha = 0.5$, $n = 1$, and $T = 298$ K.

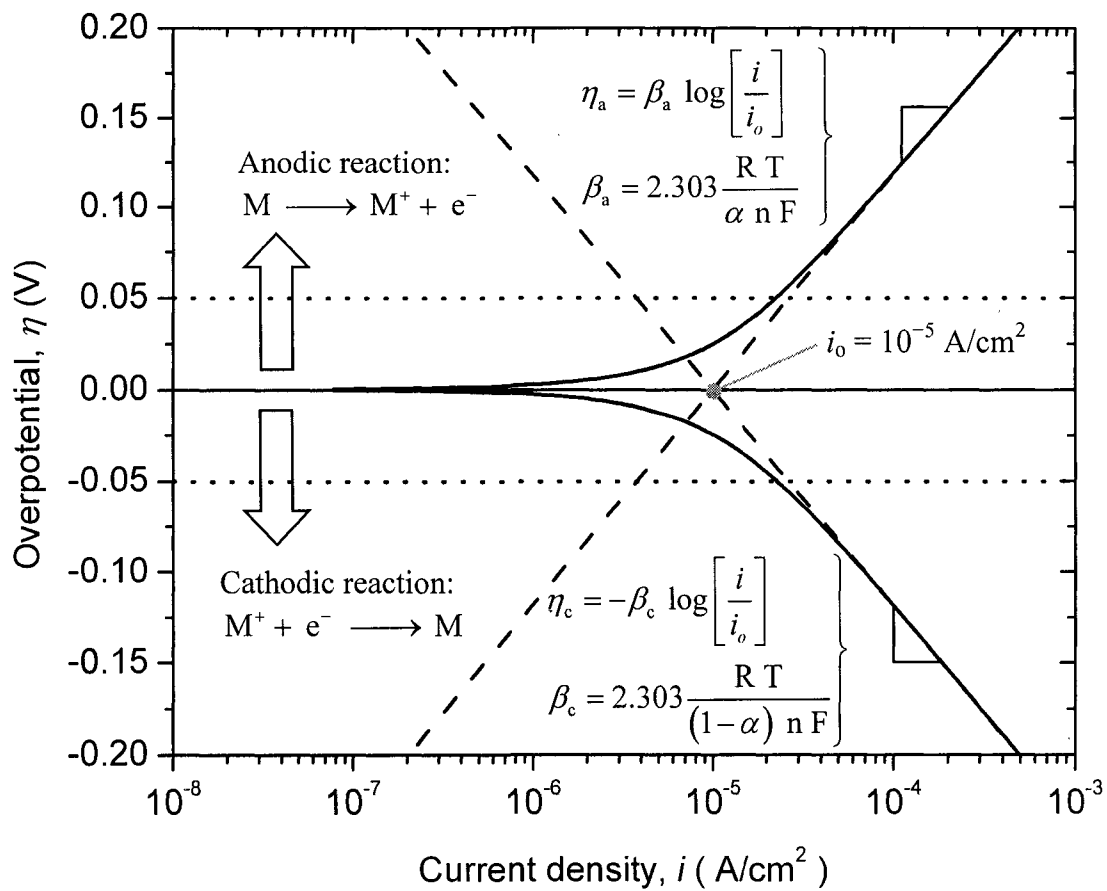


Figure 3.7. Semi-log plot of Figure 3.6 and showing Tafel relationships, Equations (3.4) and (3.5), at overpotential (η) larger than ± 0.05 V.

When the overpotential (η) is larger than ± 0.05 V, a linear relationship can be established between η and $\log(i)$ known as the Tafel relationship, which is shown in Equations (3.4) and (3.5).^[86, 87]

$$\text{Anodic: } \eta_a = \beta_a \log \left[\frac{i}{i_o} \right], \text{ where } \beta_a = 2.303 \frac{R T}{\alpha n F} \quad (3.4)$$

$$\text{Cathodic: } \eta_c = -\beta_c \log \left[\frac{i}{i_o} \right], \text{ where } \beta_c = 2.303 \frac{R T}{(1-\alpha) n F} \quad (3.5)$$

The anodic and cathodic current densities in Figure 3.7 look symmetrical because of the transfer coefficient (α) = 0.5. If α deviates from 0.5, the slope of the anodic and cathodic curves will change according to Equations (3.4) and (3.5). Larger α will decrease the anodic slope (β_a) and increase the cathodic slope (β_c).

During actual experimentation, conditions are far from ideal and plotted data rarely resembles Figure 3.7. In a typical corrosion system, the anodic reaction and the cathodic reaction may not be the same. For example, a piece of zinc metal immersed in acid solution would have a corrosion behavior diagrammed in Figure 3.8. The curve representing evolution of hydrogen is plotted with $i_o(\text{H}^+/\text{H}_2) = 10^{-10}$ A/cm², $E(\text{H}^+/\text{H}_2) = 0$ V vs SHE, $n(\text{H}^+/\text{H}_2) = 2$, and $\alpha(\text{H}^+/\text{H}_2) = 0.5$. The curve representing zinc is plotted with $i_o(\text{Zn}^{2+}/\text{Zn}) = 10^{-7}$ A/cm², $E(\text{Zn}^{2+}/\text{Zn}) = -0.76$ V vs SHE, $n(\text{Zn}^{2+}/\text{Zn}) = 2$, and $\alpha(\text{Zn}^{2+}/\text{Zn}) = 0.5$. Figure 3.8 is referred to as a mixed potential plot.^[88] The intersection of H^+/H_2 cathodic curve and Zn^{2+}/Zn anodic curve is where both anodic and cathodic current densities are equal.

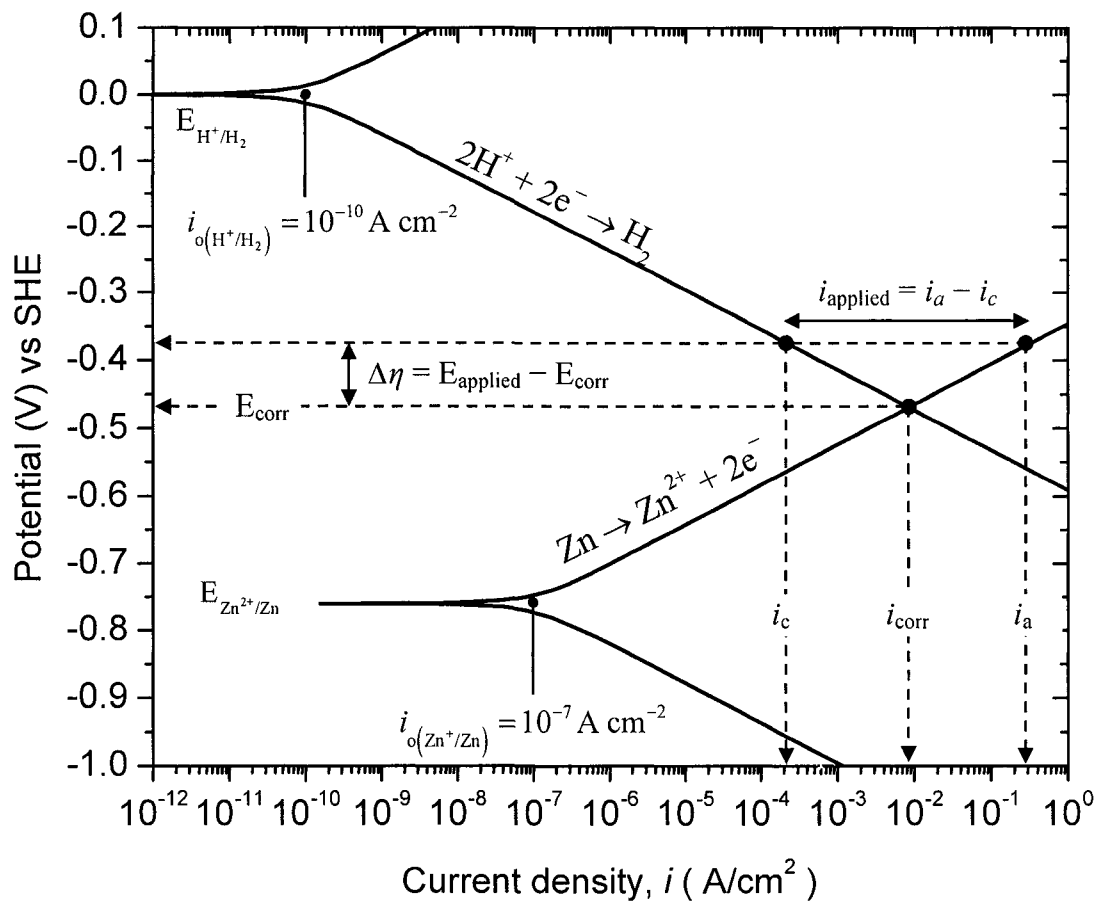


Figure 3.8. Tafel plot of mixed electrode system of hydrogen and zinc electrodes.^[87]

This is often the point where corrosion takes place. The corresponding current density is labeled as the corrosion current density (i_{corr}) and the potential is labeled as corrosion potential (E_{corr}). The E_{corr} is measurable from experiments, but i_{corr} is calculated from Tafel plots. In Figure 3.8, the point of E_{corr} and i_{corr} is well into the Tafel region of both anodic and cathodic reactions. Equations (3.4) and (3.5) are valid representations of the perturbation away from E_{corr} and i_{corr} . The $\Delta\eta$ in Figure 3.8 represents anodic perturbation applied from equilibrium (E_{corr}). The amount of perturbation is shown in Equation (3.6).

$$\Delta\eta = \eta_{\text{applied}} - \eta_{\text{corr}} = (E_{\text{applied}} - E_{\text{Zn}^{2+}/\text{Zn}}) - (E_{\text{corr}} - E_{\text{Zn}^{2+}/\text{Zn}}) = E_{\text{applied}} - E_{\text{corr}} \quad (3.6)$$

Using the Tafel relationship of Equation (3.4), the anodic and cathodic current densities (i_a & i_c) generated due to the perturbation may be calculated using Equations (3.7) and (3.8).

$$\Delta\eta = \beta_a \log \left[\frac{i_a}{i_{a(\text{Zn}^{2+}/\text{Zn})}} \right] - \beta_a \log \left[\frac{i_{\text{corr}}}{i_{a(\text{Zn}^{2+}/\text{Zn})}} \right] = \beta_a \log \left[\frac{i_a}{i_{\text{corr}}} \right] \quad (3.7)$$

$$i_a = i_{\text{corr}} 10^{\Delta\eta/\beta_a} \quad \text{and} \quad i_c = i_{\text{corr}} 10^{-\Delta\eta/\beta_c} \quad (3.8)$$

The anodic and cathodic currents produced from the perturbation are shown in Equation (3.8). The net current is i_{applied} , shown in Equation (3.9).

$$i_{\text{applied}} = i_a - i_c = i_{\text{corr}} 10^{\Delta\eta/\beta_a} - i_{\text{corr}} 10^{-\Delta\eta/\beta_c} = i_{\text{corr}} \left(10^{\Delta\eta/\beta_a} - 10^{-\Delta\eta/\beta_c} \right) \quad (3.9)$$

Using the Maclaurin series shown in Equation (3.10), the i_{applied} of Equation (3.9) is approximated into Equation (3.11).

$$10^x = 1 + 2.303x + \frac{(2.303x)^2}{2!} + \dots + \frac{(2.303x)^n}{n!}, \text{ where } n = 0, 1, 2, \dots, \infty \quad (3.10)$$

$$i_{\text{applied}} = i_{\text{corr}} \left(\left(1 + \frac{2.303 \times \Delta\eta}{\beta_a} \right) - \left(1 - \frac{2.303 \times \Delta\eta}{\beta_c} \right) \right) = i_{\text{corr}} 2.303 \times \Delta\eta \left(\frac{1}{\beta_a} + \frac{1}{\beta_c} \right) \quad (3.11)$$

The corrosion current density (i_{corr}) may be calculated according to Equation (3.12).

$$i_{\text{corr}} = \frac{i_{\text{applied}}}{2.303 \times \Delta\eta} \left(\frac{1}{\beta_a} + \frac{1}{\beta_c} \right)^{-1} = \frac{i_{\text{applied}}}{2.303 \times \Delta\eta} \left(\frac{\beta_a \beta_c}{\beta_a + \beta_c} \right) \quad (3.12)$$

Equation (3.12) is also known as the Stern-Geary equation.^[89]

Small perturbations from equilibrium (± 0.01 V) can be approximated using a linear function. The slope of the linear fit would have units of $\text{A V}^{-1} \text{cm}^{-2}$ or $\Omega^{-1} \text{cm}^{-2}$. The inverse of the slope is the polarization resistance (R_p). This is also schematically demonstrated in Figure 3.9. Substituting the definition of R_p into Equation (3.12), the Stern-Geary equation becomes Equation (3.13).

$$i_{\text{corr}} = \frac{1}{2.303 \times R_p} \left(\frac{\beta_a \beta_c}{\beta_a + \beta_c} \right) \quad (3.13)$$

All of the corrosion current density values were calculated according to Equation (3.13).

The amount of material removed could be estimated from the corrosion current density using Faraday's Law, Equation (3.14).

$$\begin{aligned} \text{Corrosion rate or } J \text{ (flux), } \left(\frac{\text{moles}}{\text{s} \cdot \text{cm}^2} \right) &= \frac{i_{\text{corr}}}{n F} \text{ or} \\ \text{Film removal rate, } \left(\frac{\text{\AA}}{\text{min}} \right) &= \frac{i_{\text{corr}}}{n F} \times \frac{\text{Molecular Weight}}{\rho_M (\text{weight density})} \times \frac{60 \text{ s}}{\text{min}} \times \frac{\text{\AA}}{10^{-8} \text{ cm}} \end{aligned} \quad (3.14)$$

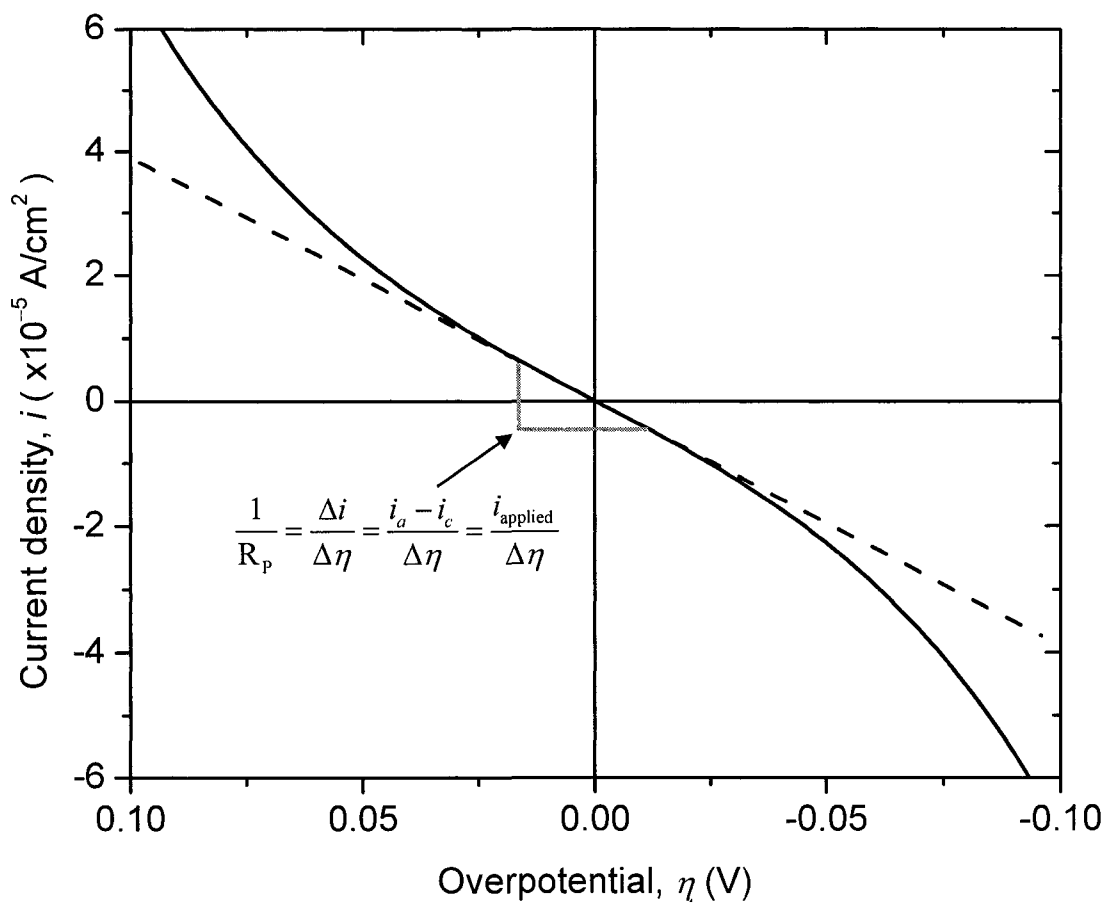


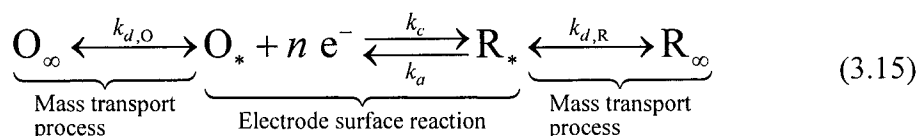
Figure 3.9. Linear region of a polarization plot, showing polarization resistance (R_p). Assuming $i_o = 10^{-5}$ A/cm², $\alpha = 0.5$, $n = 1$, and $T = 298$ K.

3.3.2. Corrosion Potential (E_{corr}) versus Time

From Figure 3.8, the corrosion potential (E_{corr}) occurs when net current density ($i_a - i_c$) = 0. If the metal under analysis is in equilibrium with the solution, the E_{corr} would remain constant as a function of time. If the E_{corr} is not constant as a function of time, then the metal/solution equilibrium has not been established. The E_{corr} vs. time experiments were performed on copper under abrasion to observe the effects of passivation either by oxide formation or adsorption of species on the copper surface that was exposed to hydroxylamine based chemistries.

3.3.3. Voltammetry with Rotating Disc Electrode^[85, 90, 91]

Voltammetry is a potential sweep technique that measures the current with applied potential. This technique is similar to potentiodynamic techniques, except that the overall kinetic processes involve charge-transfer reactions of oxidized (O) and reduced (R) species, as well as the mass transport of these electroactive species (O and R), shown in Reaction (3.15).



$k_{d,O}$ = mass transport coefficient for O

$k_{d,R}$ = mass transport coefficient for R

k_a = anodic electrochemical rate constant

k_c = cathodic electrochemical rate constant

O_* and R_* = species at the electrode surface

O_∞ and R_∞ = species in the bulk solution

The anodic (k_a) and cathodic (k_c) electrochemical rate constants are described using the Butler-Volmer relationship, Equation (3.3). The mass transport process is described using Fick's First Law, shown below,

$$J_i(x) = -D_i \frac{\partial C_i(x)}{\partial x} \quad (3.16)$$

Using Equation (3.16) the flux of the electroactive (J) species can be expressed as follows,

$$J = k_{d,O} ([O]_* - [O]_\infty) = k_{d,R} ([R]_\infty - [R]_*) \quad (3.17)$$

J = flux of the electroactive species

$$k_{d,O} = \frac{D_O}{\delta} \text{ and } k_{d,R} = \frac{D_R}{\delta} = \text{mass transport coefficient}$$

D_O and D_R = diffusion coefficient

δ = diffusion layer thickness

Since the reactions of $[O]_*$ and $[R]_*$ species occur at the electrode surface, the flux of these species involved in the reaction is shown below,

$$J = -k_c [O]_* + k_a [R]_* \quad (3.18)$$

By combining both of the flux equations, (3.17) and (3.18), the overall flux equation then becomes Equation (3.19).

$$J = \frac{-k_c [O]_\infty + k_a [R]_\infty}{1 + \frac{k_c}{k_{d,O}} + \frac{k_a}{k_{d,R}}} \quad (3.19)$$

Using Faraday's Law ($i = n F J$), the flux may be converted to show as current density (i). Limiting current densities ($i_{L,c}$ and $i_{L,a}$) of the electroactive species occur when surface species ($[O]_*$ and $[R]_*$) go to zero, which is shown in the following equations,

$$i_{L,c} = -n F k_{d,O} [O]_{\infty} \text{ and } i_{L,a} = n F k_{d,R} [R]_{\infty} \quad (3.20)$$

By substituting the $[O]_{\infty}$ and $[R]_{\infty}$ in Equation (3.19) with (3.20), a new expression for Equation (3.19) becomes (3.21).

$$i = \frac{-i_{L,c} k_c k_{d,R} + i_{L,a} k_a k_{d,O}}{k_{d,O} k_{d,R} + k_c k_{d,R} + k_a k_{d,O}} \quad (3.21)$$

If only R specie was present in solution then values of k_c and $i_{L,c}$ will go to zero, which would simplify Equation (3.21) to (3.22).

$$i = \frac{i_{L,a} k_a k_{d,O}}{k_{d,O} k_{d,R} + k_a k_{d,O}} = \frac{i_{L,a} k_a}{k_{d,R} + k_a} \Rightarrow \frac{1}{i} = \frac{k_{d,R}}{i_{L,a} k_a} + \frac{1}{i_{L,a}} \quad (3.22)$$

By expanding $i_{L,a}$ in Equation (3.22), the contribution of charge-transfer (i_F , faradic) and mass transfer (i_T , transport) current densities to overall current density (i) is shown below,

$$\frac{1}{i} = \frac{k_{d,R}}{n F k_{d,R} [R]_{\infty} k_a} + \frac{1}{n F k_{d,R} [R]_{\infty}} = \underbrace{\frac{1}{n F k_a [R]_{\infty}}}_{\text{Charge transfer}} + \underbrace{\frac{1}{n F k_{d,R} [R]_{\infty}}}_{\text{Mass transfer}} \quad (3.23)$$

$$\frac{1}{i} = \frac{1}{i_F} + \frac{1}{i_T}$$

If only O specie was present in solution, where k_a and $i_{L,a}$ go to zero, the same relationship between i , i_F , and i_T in Equation (3.23) may be obtained. The i_F in Equation (3.23), behaves according to the Butler-Volmer relationship, and the i_T is the diffusion limiting current density based on the mass transfer coefficient of $k_{d,R}$.

In an ideal condition, the value of $k_{d,R}$ is simply defined as D/δ , Equation (3.17). In a rotating disc electrode (RDE) setup, the hydrodynamics of the system were taken into consideration. The transport coefficient in a RDE setup is shown in Equation (3.24).

$$k_d = \frac{0.620 \pi r^2 D^{2/3} \omega^{1/2}}{\nu^{1/6}} \quad (3.24)$$

where 'r' is radius of the RDE, 'ω' is angular velocity in radian/s, and 'ν' is kinematic viscosity of the solution in cm²/s. The limiting anodic current density ($i_{L,a}$) in a RDE system becomes the following equation,

$$i_{L,a} = n F k_{d,R} [R]_{\infty} = \frac{0.620 \pi r^2 D_R^{2/3} \omega^{1/2} n F [R]_{\infty}}{\nu^{1/6}} \quad (3.25)$$

In order to derive a relationship of the total current density (i) as function of overpotential (η), Equation (3.23) was rearranged into the following equation,

$$i = \frac{i_F i_T}{i_T + i_F} \quad (3.26)$$

The faradic current density (i_F) was expanded to show the dependence of overpotential (η) for both anodic and cathodic current densities.

$$i_F = n F (k_a [R]_{\infty} - k_c [O]_{\infty})$$

where $k_a = k_o \exp\left[\frac{\alpha n F \eta}{R T}\right]$ and $k_c = k_o \exp\left[-\frac{(1-\alpha) n F \eta}{R T}\right]$ (3.27)

$$i_F = n F k_o \left([R]_{\infty} \exp\left[\frac{\alpha n F \eta}{R T}\right] - [O]_{\infty} \exp\left[-\frac{(1-\alpha) n F \eta}{R T}\right] \right) \quad (3.28)$$

$$\text{where } i_o = n F k_o [R]_{\infty}^{1-\alpha} [O]_{\infty}^{\alpha}$$

$$i_F = i_o \left(\exp\left[\frac{\alpha n F \eta}{R T}\right] - \exp\left[-\frac{(1-\alpha) n F \eta}{R T}\right] \right) \quad (3.29)$$

From Equation (3.17) and the Nernst equation, the transport current density (i_T) was derived as the function of overpotential (η). This is shown in the following equations,

$$i_T = n F k_{d,R} ([R]_{\infty} - [R]_*) \quad (3.30)$$

$$i_{L,a} = n F k_{d,R} [R]_{\infty}, \text{ when } [R]_* \text{ specie go to zero} \quad (3.31)$$

$$\frac{i_T}{i_{L,a}} = \frac{n F k_{d,R} ([R]_{\infty} - [R]_*)}{n F k_{d,R} [R]_{\infty}} = \frac{[R]_{\infty} - [R]_*}{[R]_{\infty}} = 1 - \frac{[R]_*}{[R]_{\infty}} \quad (3.32)$$

$$[R]_* = [R]_{\infty} \left(1 - \frac{i_T}{i_{L,a}} \right) \text{ and } [O]_* = [O]_{\infty} \left(1 - \frac{i_T}{i_{L,c}} \right) \quad (3.33)$$

From the Nernst equation, transport of [R] and [O] species to the electrode surface are derived.

$$E = E^0 - \frac{R T}{n F} \ln \left[\frac{[R]_*}{[O]_*} \right] \quad (3.34)$$

Combining Equations (3.33) and (3.34), the overpotential dependence of i_T is shown as Equation (3.36). This equation is sometime referred to as concentration polarization.

$$E = E^0 - \frac{R T}{n F} \ln \left[\left(\frac{i_T - i_{L,a}}{i_{L,c} - i_T} \right) \frac{k_{d,O}}{k_{d,R}} \right] \text{ where } E^0 - \frac{R T}{n F} \ln \left[\frac{k_{d,O}}{k_{d,R}} \right] = E_{1/2} \quad (3.35)$$

$$\eta = E - E_{1/2} = - \frac{R T}{n F} \ln \left[\frac{i_T - i_{L,a}}{i_{L,c} - i_T} \right]$$

$$i_T = \frac{i_{L,a}}{1 + \exp \left[- \frac{n F \eta}{R T} \right]} + \frac{i_{L,c}}{1 + \exp \left[\frac{n F \eta}{R T} \right]} \quad (3.36)$$

A schematic diagram of current density (i) versus overpotential (η) plot using Equations (3.26), (3.29), and (3.36) is shown in Figure 3.10.

From the voltammogram in Figure 3.10, formation of a cathodic or an anodic peak current density occurs when the capacitive current density is generated across the double

layer at high scan rates. The total faradic current density (i_{TF}) can be expressed as the following equation,

$$i_{TF} = i_F + C_{DL} \frac{dE}{dt} \quad (3.37)$$

where i_F is the faradic current density according to Equation (3.29), C_{DL} is the double layer capacitance, and $\frac{dE}{dt}$ is the scan rate. From Equation (3.37) at low scan rate, the capacitive current density is small allowing $i_{TF} = i_F$. As scan rate increases, the capacitive current density increases and thus increases the total faradic current density. At higher overpotentials, the effect of transport current density (i_T) starts to dominate which will lower the overall current density to its limiting current density (i_L) and the formation of a peak current density occurs. This is schematically shown in Figure 3.10.

All voltammetry experiments were performed with the parameters listed in Table 3.1. In comparing traditional RDE setup versus the EC-AC tool for measuring voltammetry, there were no obvious differences between the two voltammograms. The voltammograms in the results section were mostly obtained using the copper film with the EC-AC tool.

Table 3.1. Parameters used for voltammetry experiments.

Experimental Parameters	Materials or Values Used
Electrode Material	99.98% copper foil and 99.99% solid copper 16 kÅ ECD copper film on silicon wafer
Scan rate (mV/s)	5, 10, 50, and 100
Rotation speed (rpm)	0, 55.5, 222, 555.5 rpm

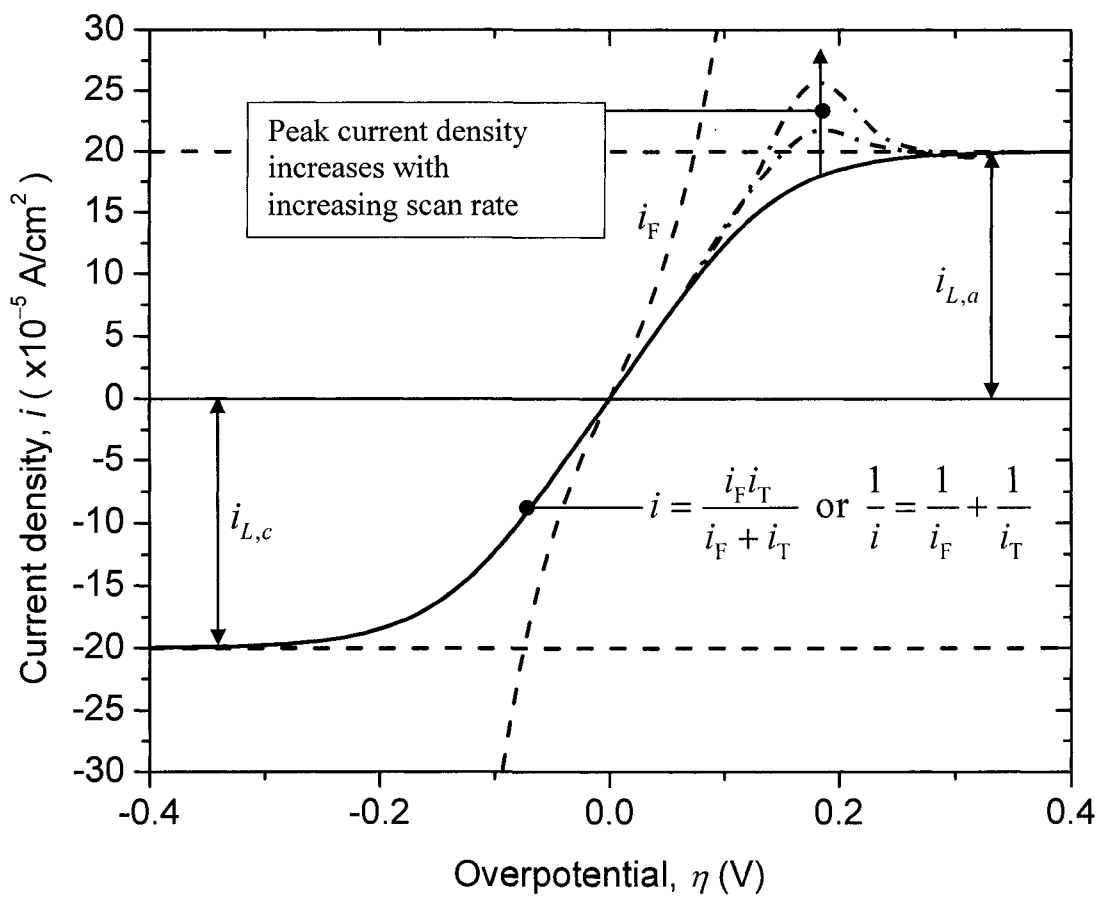


Figure 3.10. A voltammogram of a redox system according to Equations (3.26), (3.29), and (3.36).

3.4. Chemical and Physical Analysis

3.4.1. Capillary Electrophoresis Chromatography (CEC)

The identification and separation of various anions and cations were achieved using a Beckman P/ACE 2000 instrument. The instrument used a hollow capillary column 75 μm in diameter and 70 cm in separation length filled with a buffer electrolyte. The ends of the column were placed into separate buffer reservoirs. Two platinum electrodes were also placed into the buffer reservoirs and connected to a high voltage power supply. A schematic diagram of CEC is shown in Figure 3.11. Samples were injected into the column either by pressure or electrokinetic injection. After injection, the ions were separated by applying a voltage that produced an electric field across the capillary column. The applied voltages for anionic and cationic analyses were 15 kV and 30 kV, respectively. The polarity arrangement of the electrodes determined whether cation or anion analysis was being performed.

The detector was a photomultiplier tube that detected the light intensity through a cross section of the capillary column at wavelengths of 214, 254, and 280 nm. Since most small inorganic ions do not have a high absorption in the UV region, a method known as indirect detection was employed for the detection of small ions. The buffer used for indirect detection contained strong UV absorbing molecules; when a non-absorbing ion passed over the detector, a negative absorption peak was generated. A positive peak formed when a stronger absorbing ion passed over the detector.

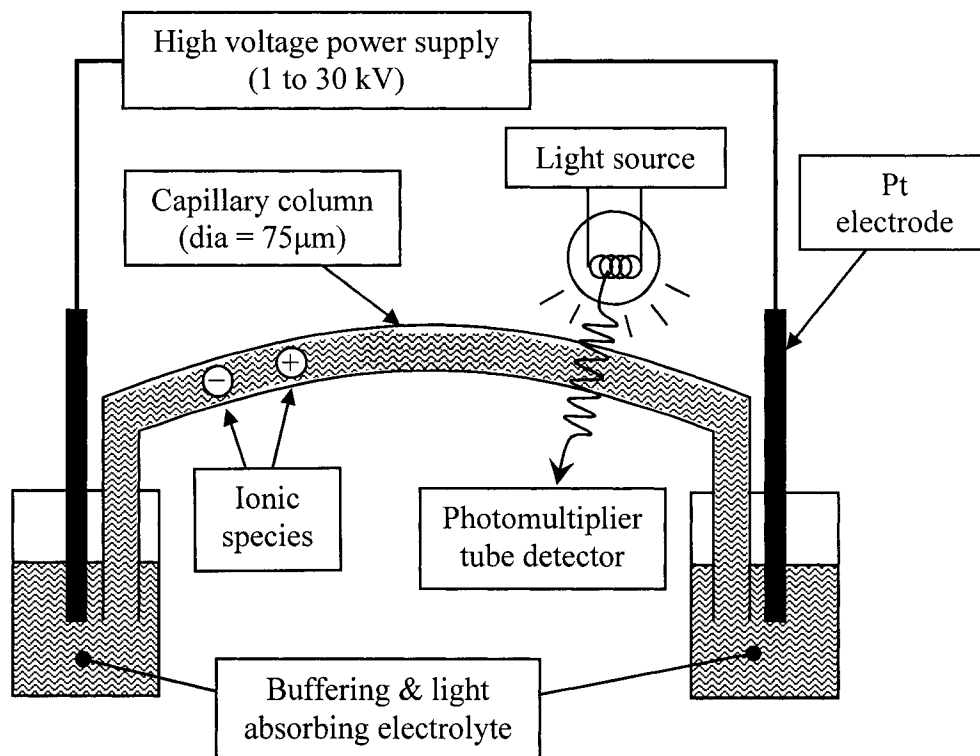


Figure 3.11. Schematic diagram of the capillary electrophoresis instrument used for detecting cationic and anionic species in solution.

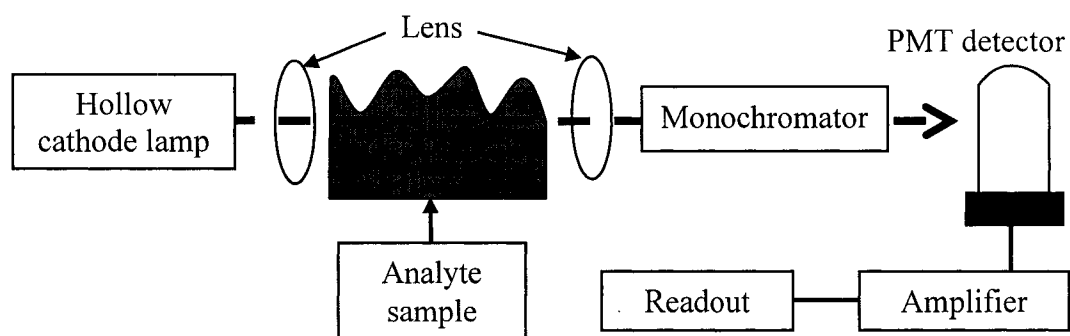


Figure 3.12. Schematic diagram of atomic absorption spectrophotometer used for determining dissolved copper concentration in solution.

The buffer used for anion analysis was prepared by first mixing 0.02 *M* dodecyltrimethylammonium bromide (DTAB) with 0.01 *M* chromium trioxide (CrO_3) in water. Chromium trioxide easily dissolved in water forming chromic acid (H_2CrO_4) which dissociated forming a chromate ion (CrO_4^{2-}), making the solution acidic. The addition of DTAB into chromic acid formed an insoluble precipitate of $(\text{DTA}^+)_2\text{CrO}_4^{2-}$. After mixing, the $(\text{DTA}^+)_2\text{CrO}_4^{2-}$ was filtered and rinsed thoroughly to ensure that no bromide ion remained in the precipitate. The precipitate was then dried in a regular oven at approximately 100°C for 30 minutes. Since the $(\text{DTA}^+)_2\text{CrO}_4^{2-}$ was stable only in acidic conditions, 0.01 *M* $(\text{DTA}^+)_2\text{CrO}_4^{2-}$ was dissolved in water with 0.05 *M* ethanolamine to buffer the solution's pH to above 9. About 1% of polyethyleneglycol (PEG) was also added into the buffer for better peak definition. The solution's final pH was approximately 9.8, and its conductivity was about 3 mS/cm.

The buffer used for cation analysis contained 0.0065 *M* hydroxyisobutyric acid, 0.005 *M* methyl benzyl amine, 0.004 *M* 18-crown-6-ether, and 1% PEG. The pH of the cation buffer was about 4.5, and its conductivity was about 0.314 mS/cm.

3.4.2. Atomic Absorption Spectroscopy (AAS)

The measurement of dissolved copper ions in solution was achieved using a Perkin-Elmer Model 2380 AAS. The technique aspirates a sample of the analyte into the acetylene-air mixture flame. The temperature of the acetylene-air flame is typically 2300°C . At this temperature, ionization of metal ions (including copper) occurred. The detection of copper occurred by passing a light source through the ionizing flame and into

a photomultiplier detector. A schematic diagram of AAS is shown in Figure 3.12. The light source was a hollow cathode lamp (HCL) specially optimized for copper. During ionization, absorption of light occurred at a characteristic wavelength for each element. For copper, the most sensitive wavelength occurred at 324.8 nm. A linear working curve was obtained by measuring the absorption of five known copper concentrations (0.1, 0.5, 1.0, 3.0, and 5.0 ppm) prepared from an AA copper standard solution purchased from Alfa-Aesar Chemicals. The linear working range of copper was 0.1 to 5.0 ppm. All working curves established prior to analysis had a coefficient of determination (R^2) = 0.99.

3.4.3. Surface Profile Measurements

The surface profile was measured using a Tencor P-2 Long Scan Profiler. This instrument used a sharp stylus that was dragged across the surface features. The amount of vertical movement on the stylus was detected by electrical signals produced from the piezo-electric material attached to the stylus assembly. The electrical signals were translated into vertical distance. A schematic diagram of a surface profiler is shown in Figure 3.13. It used a tungsten carbide-tipped stylus with a 5.0 μm tip radius and a shank angle of 60°. The instrument had a minimum horizontal resolution of 0.01 $\mu\text{m}/\text{point}$ and a vertical resolution of 100 Å. If the scan distance was greater than 5 mm, a non-linear baseline was observed.

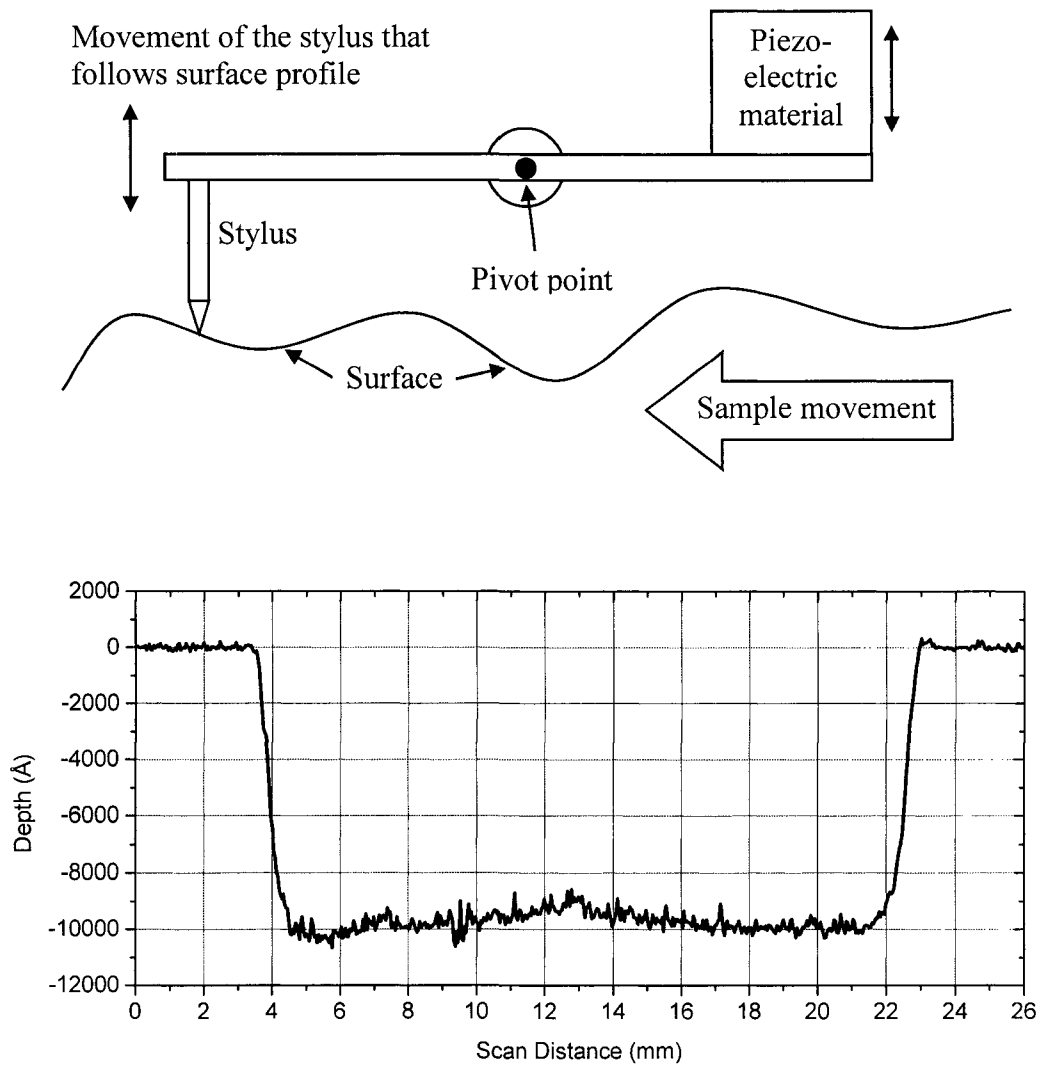


Figure 3.13. Schematic diagram of the P-2 profiler used for surface profile measurements (top). A plot of an actual profile scan of a copper sample that has been abraded (bottom).

For all measurements taken with scan distance greater than 5 mm, a polynomial function was used to level the scanned profile. For determining the amount of copper removed from the sample, two scans perpendicular to each other were performed. The plot of a typical profile scan is shown in Figure 3.13.

3.5. pH, Redox, and Oxygen Measurements

All solution measurements were obtained using Orion Model 920A and Model 1230 meters. For pH measurements, a glass sensing single junction combination (with built-in Ag/AgCl reference electrode) pH probe was used. For redox measurements, a platinum sensing combination electrode (with built-in Ag/AgCl reference electrode) was used. For the measurements of oxygen level in solution, a probe made of two dissimilar metals (a cathode and an anode) encased in an epoxy body was used. The detection occurred when oxygen diffused through a membrane window in the epoxy body and then reduced electrochemically on the cathode. The amount of voltage change between cathode and anode correlates to the amount of oxygen present in solution. The meters and the probes were all purchased from Thermo Orion and were calibrated using freshly prepared buffer solutions on a monthly basis.

3.6. Potential-pH Diagrams

Stability of a metal in aqueous system may be understood by constructing a graph of electrochemical potentials as function of pH, also known as E-pH or Pourbaix diagrams.^[32, 38] The advantage of a potential-pH diagrams is that it enables engineers to

have some fundamental understandings on the stability of a metal in solution prior to any investigations.

The construction of a potential-pH (E-pH) diagram is entirely based on the thermodynamic data of each species involved. Using Gibbs formation energies (ΔG_f^0) of individual species, a line in the E-pH diagram representing the transition from one specie to the other may be calculated. From these transition lines, a region of stability for a specie is formed. The number of transitions becomes more complicated when the total number of species is increased. In facilitating the construction of the E-pH diagrams, two software programs were used. One was a DOS based program named ROSOF^[92], and the other was a windows based program name STABCAL.^[93] The ΔG_f^0 values used for calculation and construction of the E-pH diagrams are tabulated in Table 3.2.

Table 3.2. Thermodynamic data used to calculate the E-pH diagrams.^[41, 66, 67, 94-96]

Species	ΔG_f^0 kcal/mol (298K)	Species	ΔG_f^0 kcal/mol (298K)
Cu	0	NH ₃	-6.36
Cu ²⁺	15.66	NH ₄ ⁺	-18.97
Cu ⁺	12.00	N ₂ H ₄	30.60
CuO (s)	-30.40	N ₂ H ₅ ⁺	19.70
Cu ₂ O (s)	-34.90	NH ₂ OH	-5.59
Cu(OH) ₂ (aq)	-59.53	NH ₃ OH ⁺	-13.54
HCuO ₂ ⁻	-61.42	NO ₂ ⁻	-8.84
CuO ₂ ²⁻	-43.30	HNO ₂	-13.28
N ₂ (g)	0	NO ₃ ⁻	-26.58
N ₂ O (g)	24.82	HNO ₃	-26.58
NO (aq)	20.62	Cu(NH ₂ OH) ²⁺	6.77
NO ₂ (g)	12.22	Cu(NH ₂ OH) ₂ ²⁺	-1.11
N ₂ O ₃ (g)	33.20	H ₂ O ₂	-31.94
H ₂ N ₂ O ₂ (aq)	8.57	HO ₂ ⁻	-16.05
HN ₂ O ₂ ⁻	18.12	O ₂ (aq)	3.88
N ₂ O ₂ ²⁻	33.10	H ₂ O	-56.69
NO ⁻	32.47	HNO (aq)	26.06

CHAPTER 4. RESULTS AND DISCUSSION

4.1. Copper CMP Results

Both the mechanical and chemical parameters that affect the removal rate of copper during CMP in hydroxylamine based slurry were investigated. The mechanical parameters were polishing pressure and relative velocity, and the chemical parameters were slurry pH and hydroxylamine concentration.

The first set of investigations was carried out to determine the effect of slurry pH on copper removal rates (RR). The results are plotted in Figure 4.1. In these tests, hydroxylamine concentration was held at 0.5 *M* and pH adjustments were made using sulfuric acid. The wafer and pad speeds were kept constant at 47 and 50 rpm, respectively, and the polishing pressure was maintained at 3 psi (20.7 kPa). It may be seen from Figure 4.1 that the maximum removal rate of copper occurs in the vicinity of pH 6, a value very close to the pK_a of hydroxylamine. The removal rates of copper dropped off at acidic as well as alkaline conditions.

A slurry pH of 6 was chosen to elucidate the effect of polishing pressure and speed on copper removal rates. When studying the effect of polishing pressure, the wafer and pad rotational speeds were kept constant at 47 and 50 rpm, respectively. At the set wafer and pad rotational speeds, the relative velocity was calculated to be 7.17 m/min. When studying the effect of polishing speed, the polishing pressure was set at 3 psi.

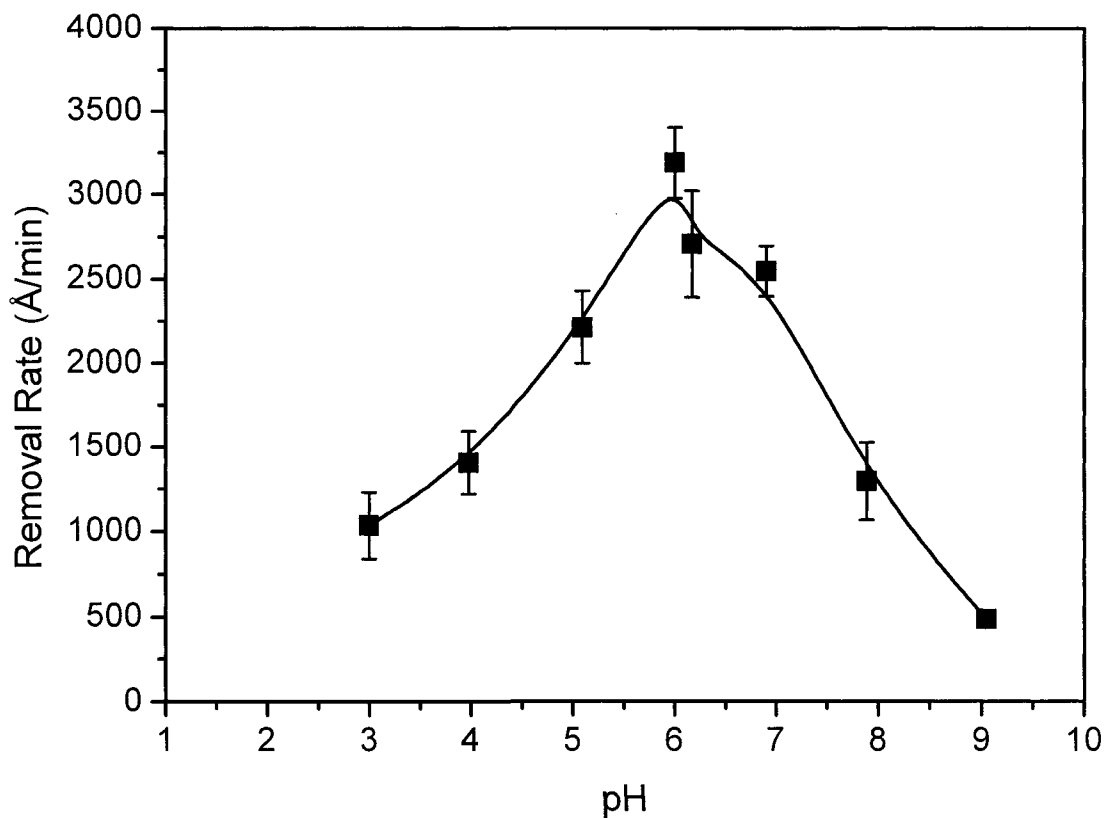


Figure 4.1. Removal rates of electrodeposited copper film as function of slurry pH. [Strausbaugh 6EC tool, 3 psi, 4% SiO₂ slurry containing 0.5 M hydroxylamine, pH adjusted with H₂SO₄]

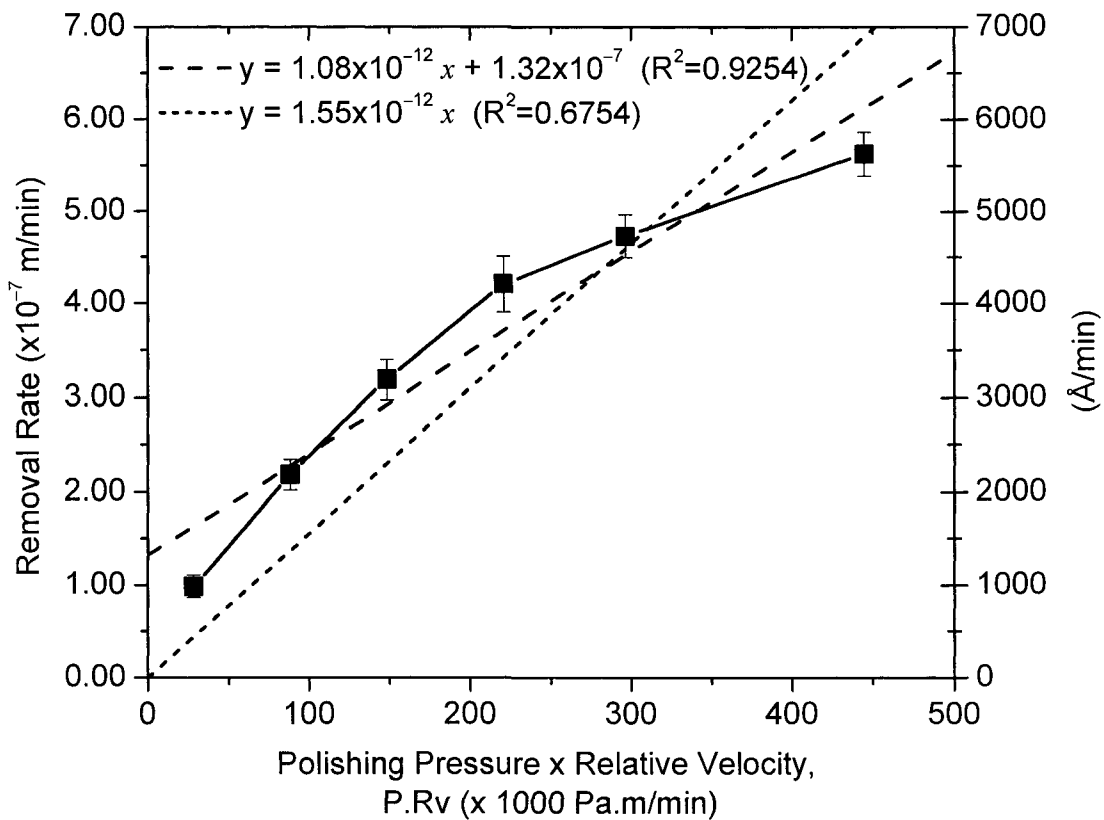


Figure 4.2. Removal rates of electrodeposited copper film as function of the product of polishing pressure and relative velocity ($P \times Rv$). Preston's model (---) and best linear fit (---).

The results from both studies are plotted in Figure 4.2 as removal rates of copper versus the product of polishing pressure and relative velocity ($P \times R_v$). If the CMP of copper followed Preston's equation, the removal rate would be zero at zero pressure or relative velocity. A fit of the experimental data, including origin, to the Prestonian model is shown in the figure. This linear fit has a poor correlation coefficient (R^2) of 0.6754. The best linear fit of the results, excluding the origin, exhibited a much higher R^2 of 0.9254 and yielded a y-axis intercept of $\sim 1,320 \text{ \AA}/\text{min}$ ($\sim 1.32 \times 10^{-7} \text{ m}/\text{min}$). The equation of the best linear fit transformed Preston's equation into the following,

$$RR = K P R_v + RR_0 \quad (4.1)$$

where RR_0 can be interpreted as the static etch rate. As would be shown later, this intercept value corresponds to the etch rate of copper in 0.5M hydroxylamine based slurry. Also from Preston's model, the slope (Preston's constant) has been proposed to have a relationship of $1/(2E)$ to Young's modulus (E) of the substrate. Based on this relationship, a modulus of 323 GPa was calculated from the experimental data. Considering that the modulus of bulk copper is between 110 to 138 GPa, the significance of Preston's constant being equal to $1/(2E)$ was not validated.

Since the experimental data plotted in Figure 4.2 indicated a non-linear behavior, attempts were made to fit the data to an equation of the type shown below.

$$RR = K P^a R_v^b + RR_0 \quad (4.2)$$

In Preston's model, the power factors 'a' and 'b' are both equal to 1. In Tseng-Wang's model, 'a' = 0.83 and 'b' = 0.5, while for Zhao-Shi's model, 'a' = 0.67 and 'b' = 1. All three models were described in detail in the background section.

The CMP results from Figure 4.2 were replotted as RR versus the product of P^a and R_V^b while varying the values of 'a' and 'b' from 0.1 through 1.0. An example of this is shown in Figure 4.3. The figure shows a plot of $P^{0.1} \times R_V^{0.1}$ and another plot of $P^{0.9} \times R_V^{0.4}$. Linear regression was performed on both plots and the R^2 from the regression was recorded. This process was repeated for all combinations of 'a' and 'b'. The linear regression of $P^{0.1} \times R_V^{0.1}$ showed a better R^2 value than $P^{0.9} \times R_V^{0.4}$. This means that there is a combination of 'a' and 'b' values that would yield the highest R^2 value. To achieve this, the resulting regression R^2 from each pair of 'a' and 'b' values was plotted in a contour plot shown in Figure 4.4. Also shown in the figure are the three CMP models discussed earlier.

The highest R^2 value in Figure 4.4 is obtained when 'a' = 0.5 and 'b' = 0.7. Thus the removal of copper in a hydroxylamine based slurry may be expressed as,

$$RR = K^* P^{0.5} R_V^{0.7} + RR_0 \quad (4.3)$$

The constant, K^* , from Equation (4.3) was calculated to be $5.8 \times 10^{-10} \text{ Pa}^{-0.5} (\text{m/min})^{0.3}$. The inverse value for K^* then becomes $1.72 \times 10^9 \text{ Pa}^{0.5} (\text{m/min})^{-0.3}$. The units obtained for K^* made it difficult for a comparison to Preston's constant obtained in Figure 4.2.

Since the optimal value of 'b' was greater than 'a', relative velocity had a slightly larger contribution in the removal rates of copper than applied pressure. Because the mass transport of the active species to copper surface is dependent on relative velocity, it is likely that the removal rates of copper may be controlled by the transport of active species to the surface.

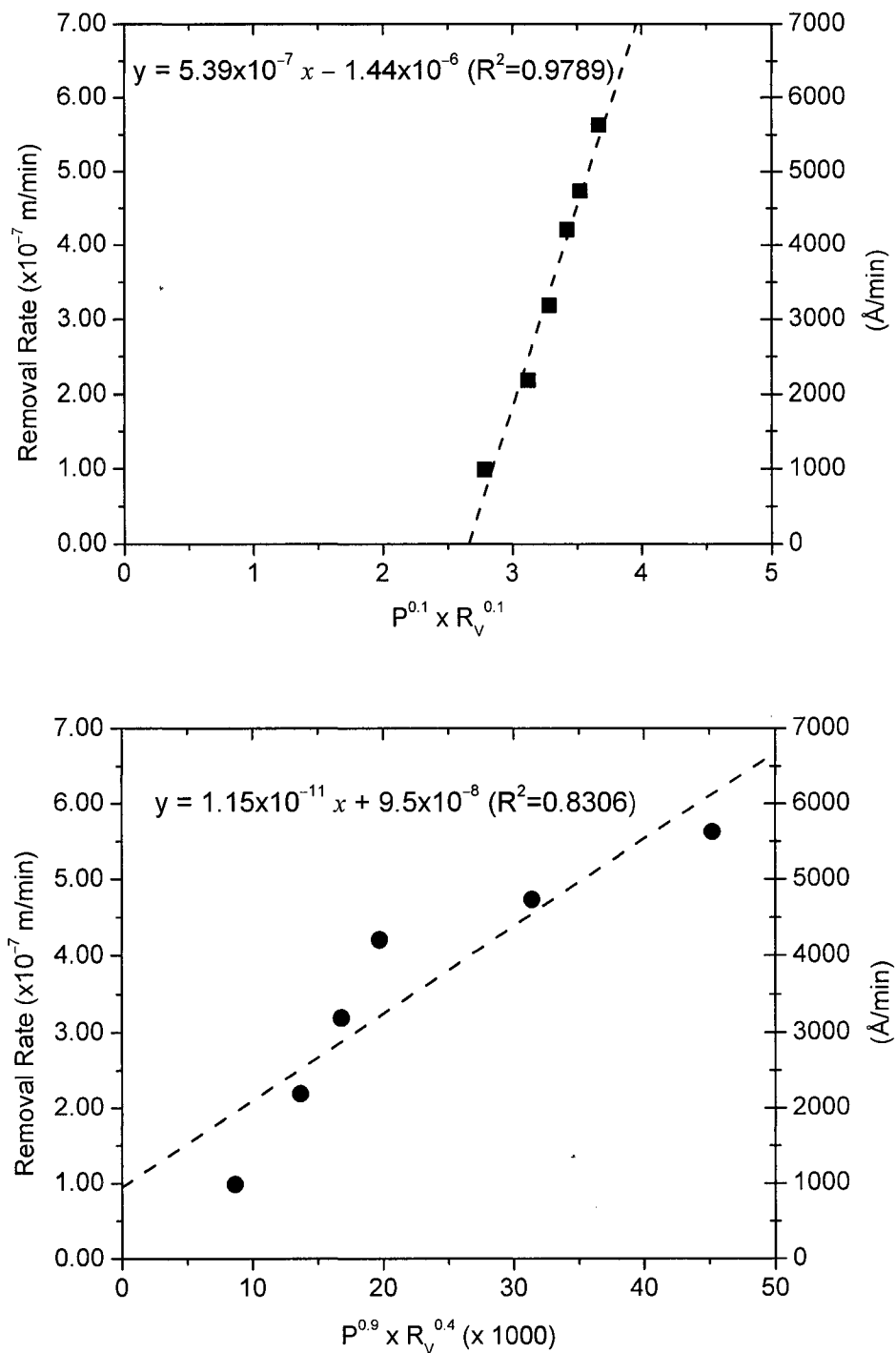


Figure 4.3. Replots of Figure 4.2 showing RR with respect to $P^{0.1} \times R_V^{0.1}$ (top) and to $P^{0.9} \times R_V^{0.4}$ (bottom). The linear regression for each plot is drawn as a dashed line (---).

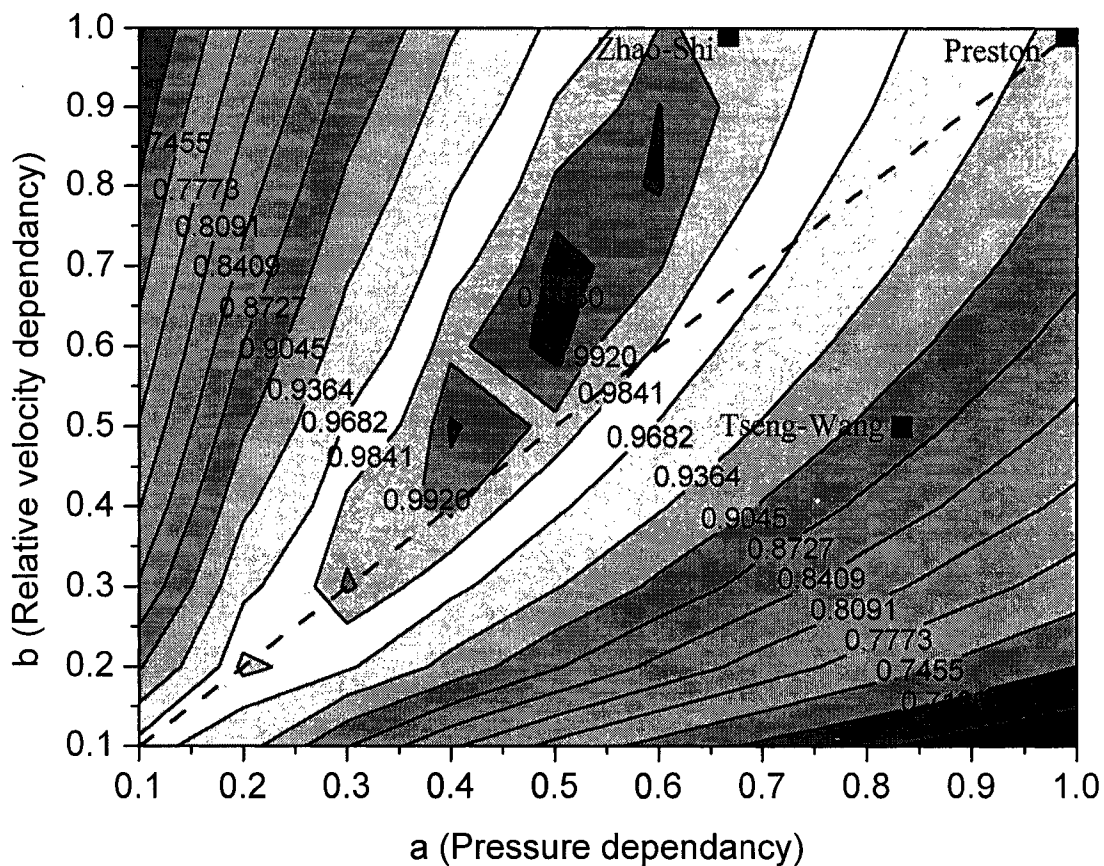


Figure 4.4. Contour plot of the R^2 values determined by using Equation (4.2) with the experimental results of Figure 4.2. [The combination of 'a' and 'b' values in Equation (4.2) ranged from 0.1 to 1. Three models from Section 2.1.4 were also plotted. The dashed line represents 'a' = 'b'.]

4.2. Electrochemical Abrasion Cell (EC-AC) Experimental Results

Electrodeposited copper films were abraded in the EC-AC tool, which is schematically shown in Figure 3.1. Even though the kinematics of the EC-AC tool are significantly different from that of the CMP tool, the copper removal rates obtained from the EC-AC tool are similar to the CMP tool. The main advantages in using the EC-AC tool to study a CMP process are: (1) Fundamental information collected will help in understanding and improving future CMP processes; and (2) The amount of consumables used is minimal which helps to keep cost down.

4.2.1. Mechanical Effects of Copper Abrasion from Using the EC-AC Tool

The abrasion results obtained in 0.5M hydroxylamine based slurry at pH values of 8.3, 6, and 3.5 using the EC-AC tool were subjected to the same analysis as the results from the CMP tool. The regression R^2 values are plotted as contour plots shown in Figure 4.5, Figure 4.6, and Figure 4.7, for pH values of 8.3, 6, and 3.5, respectively. The values of 'a' and 'b' with the highest R^2 value and the corresponding K value are tabulated in the following table.

Table 4.1. Values of 'a' and 'b' with highest R^2 value and the corresponding K values with respect to three slurry pH conditions.

Slurry pH	'a' - P dependency	'b' - R_v dependency	Highest R^2 value	K (constant)
8.3	1	0.1	0.9318	$7.77 \times 10^{-14} \text{ Pa}^{-1} (\text{m/min})^{0.9}$
6	0.1	0.5	0.8117	$2.19 \times 10^{-8} \text{ Pa}^{-0.1} (\text{m/min})^{0.5}$
3.5	0.2	0.1	0.7877	$4.84 \times 10^{-9} \text{ Pa}^{-0.2} (\text{m/min})^{0.9}$

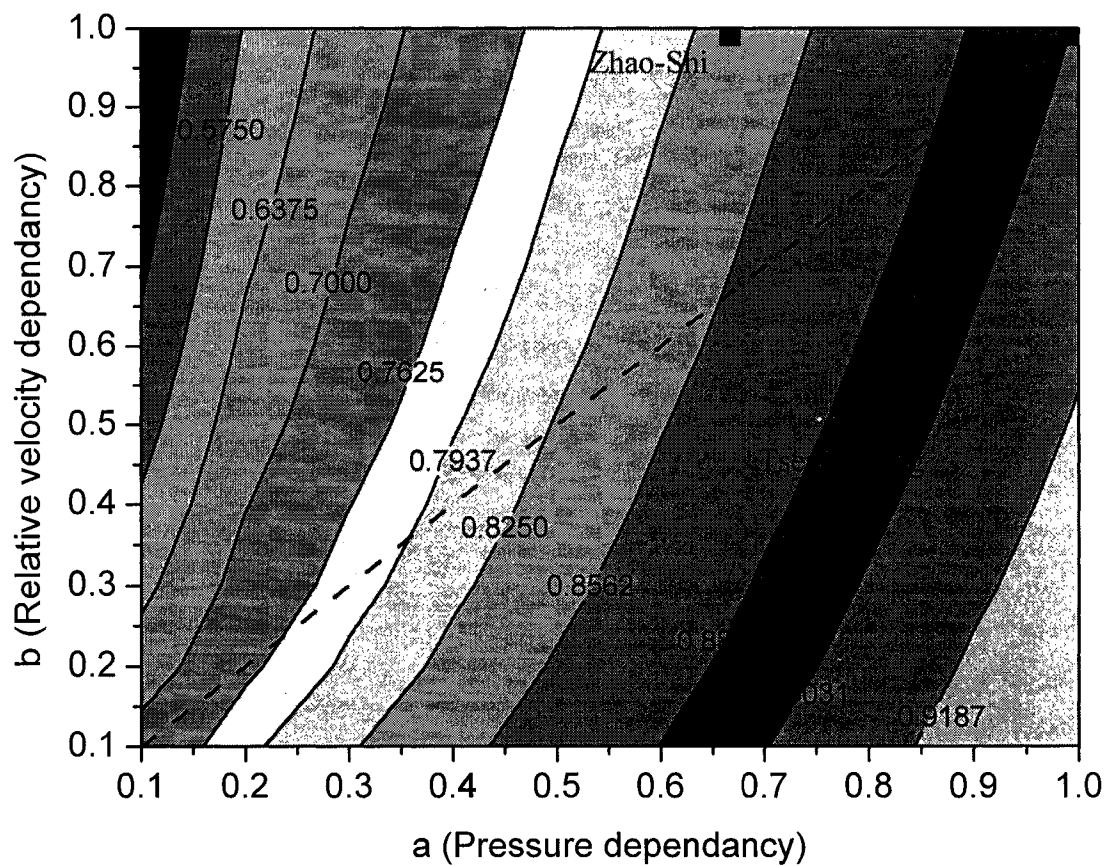


Figure 4.5. Contour plot of the R^2 values determined by using Equation (4.2) with the experimental results obtained using EC-AC tool in 0.5M hydroxylamine based slurry at pH 8.3. [The combination of 'a' and 'b' values in Equation (4.2) ranged from 0.1 to 1. Three models from Section 2.1.4 were also plotted. The dashed line represents 'a' = 'b'.]

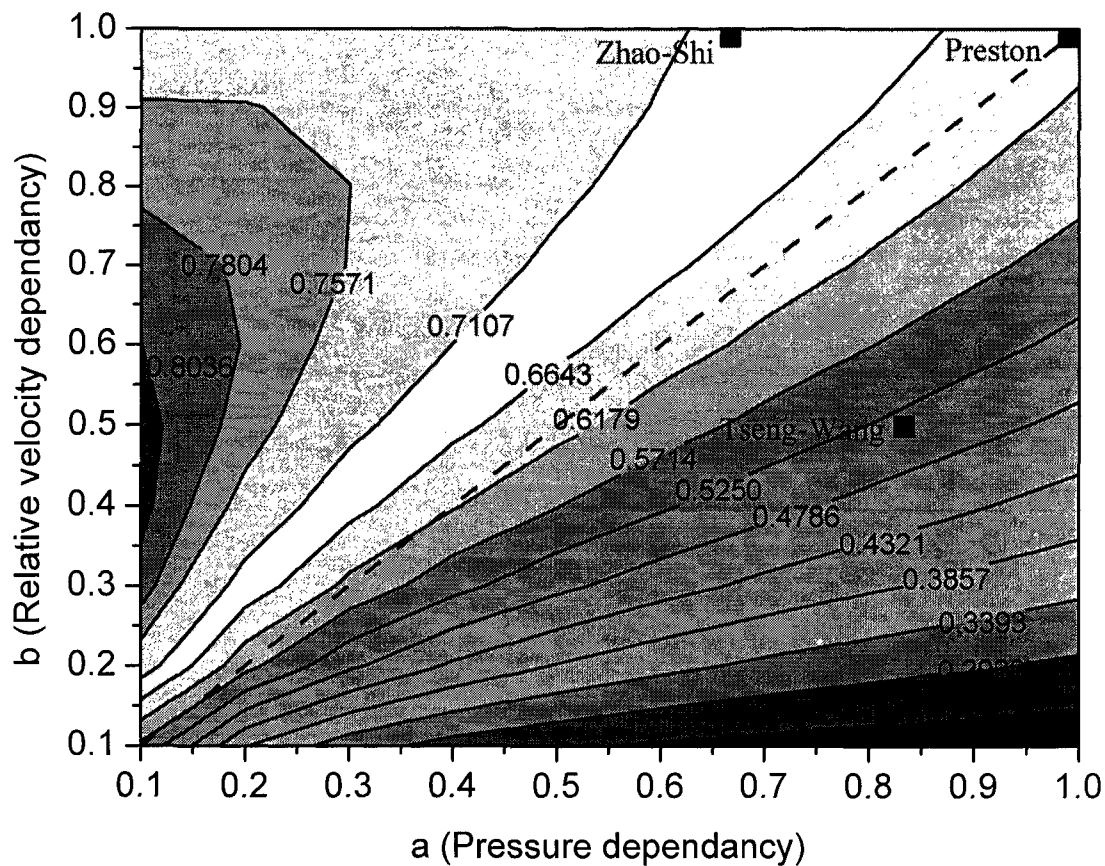


Figure 4.6. Contour plot of the R^2 values determined by using Equation (4.2) with the experimental results obtained using EC-AC tool in 0.5M hydroxylamine based slurry at pH 6. [The combination of 'a' and 'b' values in Equation (4.2) ranged from 0.1 to 1. Three models from Section 2.1.4 were also plotted. The dashed line represents 'a' = 'b'.]

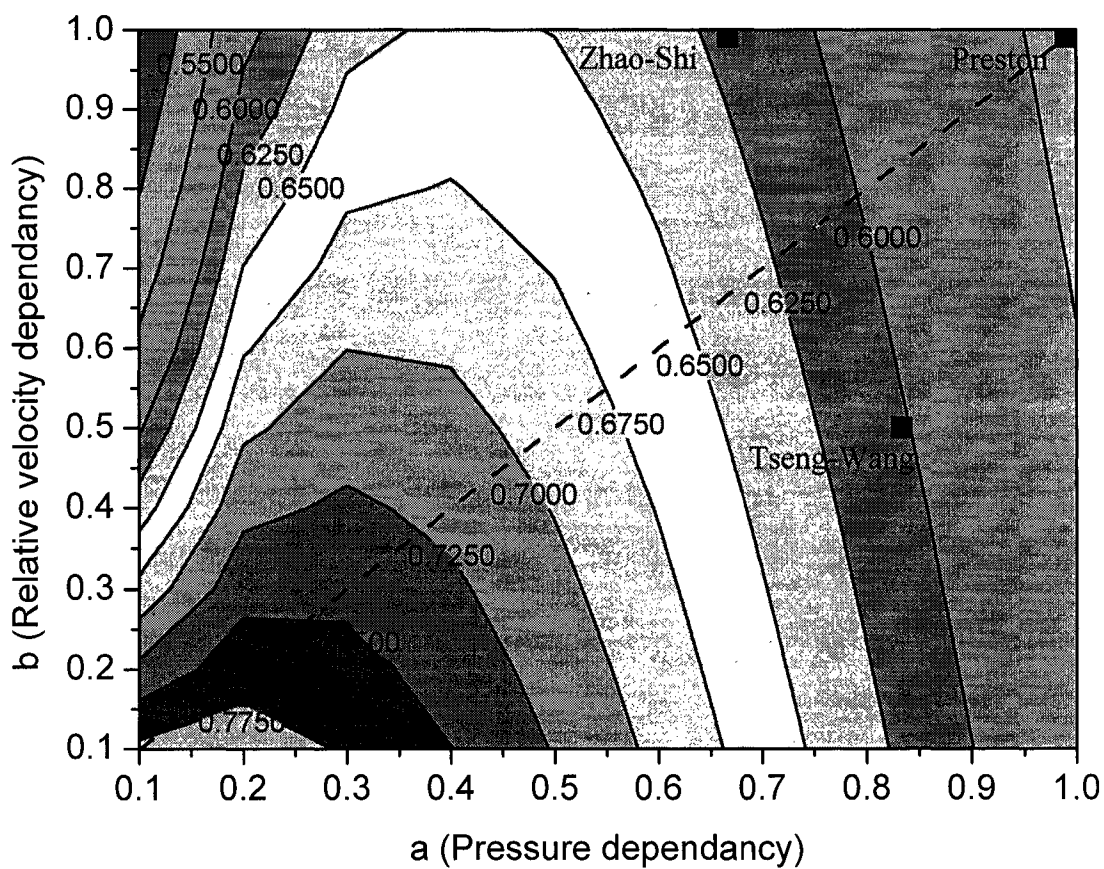


Figure 4.7. Contour plot of the R^2 values determined by using Equation (4.2) with the experimental results obtained using EC-AC tool in 0.5M hydroxylamine based slurry at pH 3.5. [The combination of 'a' and 'b' values in Equation (4.2) ranged from 0.1 to 1. Three models from Section 2.1.4 were also plotted. The dashed line represents 'a' = 'b'.]

The highest R^2 value of 0.9318 at pH \sim 8.3 was obtained when values of 'a' and 'b' were 1 and 0.1, respectively. The larger value of 'a' in comparison to 'b' indicates that the removal rate of copper at this pH is predominantly dependent on applied pressure. This dependence on pressure also indicates that the mechanical effects were more dominant at this pH. The stronger mechanical effect over the weaker chemical effect in removing copper during abrasion may indicate the formation of a passive copper oxide film on the surface.

The highest R^2 value of 0.8117 at pH \sim 6 was obtained when values of 'a' and 'b' were 0.1 and 0.5, respectively. The larger value of 'b' over 'a' indicates that the removal rate of copper at pH \sim 6 is predominantly dependent on relative velocity. Relative velocity contributes to both mechanical and chemical effects in the removal of copper during abrasion. The mechanical effect of relative velocity is the amount of shear stress applied to the copper sample during abrasion. However, the shear stress is also dependent on the amount of pressure applied to the copper sample. Since the smaller value of 'a' indicates that removal of copper is mildly dependent on applied pressure, the majority of the copper removed is due to chemical attack. The dissolution rate of copper that is dependent on relative velocity is due to transport of reactive chemical species to the copper surface.

The values of 'a' and 'b' at pH \sim 6 obtained by using the EC-AC tool are similar to the values obtained by using an industrial CMP tool. As discussed earlier, analysis of the results obtained with the CMP tool also show that 'b' is greater than 'a'. However, the ratio of 'a' to 'b' (ratio = a/b) in the EC-AC tool was 0.2, which was smaller than the 0.7

value obtained using the CMP tool. The difference in ratio from both tools is due to the EC-AC tool being a much smaller scaled version of a regular CMP tool. It is likely that the scaling factor may influence the overall kinematics of the EC-AC tool.

The highest R^2 value of 0.7877 at pH ~ 3.5 was obtained when values of 'a' and 'b' were 0.2 and 0.1, respectively. The slightly larger value of 'a' over 'b' indicates that the removal rate of copper at pH ~ 3.5 is slightly more dependent on applied pressure. This same behavior was also observed for the removal of copper at pH ~ 8.3 , but the best fit value of 'a' was found to be 1. If the value of 'a' = 1 at pH ~ 8.3 signifies a strong passive oxide layer, then a much smaller value of 0.2 at pH ~ 3.5 may indicate lack of a passive oxide layer. This is highly probable considering that copper oxides are not stable at a pH value of ~ 3.5 . The removal rates of copper having slightly larger dependency on applied pressure over relative velocity is likely due to the formation of a fresh copper surface upon abrasion at pH ~ 3.5 .

4.2.2. Chemical Effects of Copper Abrasion from Using the EC-AC Tool

The effect of pH on copper removal rates was studied using slurries containing 0.5M hydroxylamine. The removal rate results obtained using the EC-AC tool showed the same maximum at pH 6 as the results from the CMP tool. To show that both tools behaved similarly with respect to pH, the removal rates obtained from both tools were normalized to their mean values and plotted with respect to pH. This plot is shown in Figure 4.8. The results obtained from both tools show the same trend in copper removal rates with respect to pH. All showed a maximum in removal rates at pH value ~ 6 . This clearly shows that the chemical component of CMP can be effectively studied using the EC-AC tool.

Even though the trend of copper removal rates with pH was the same, the removal rates obtained using the EC-AC tool were considerably lower than the results from the CMP tool. For example, the copper removal rate at pH 6 from the EC-AC tool was 1,300 Å/min, while the removal rate from the CMP tool was 3,200 Å/min. This is likely due to the difference in the relative velocity between the CMP and the EC-AC tool. The relative velocity in the CMP tool was calculated to be 7.17 m/min with wafer and pad rotating at 47 and 50 rpm, respectively. In the EC-AC tool, a much lower relative velocity of 1.0 m/min was calculated even with wafer and pad rotating at 222 and 240 rpm, respectively.

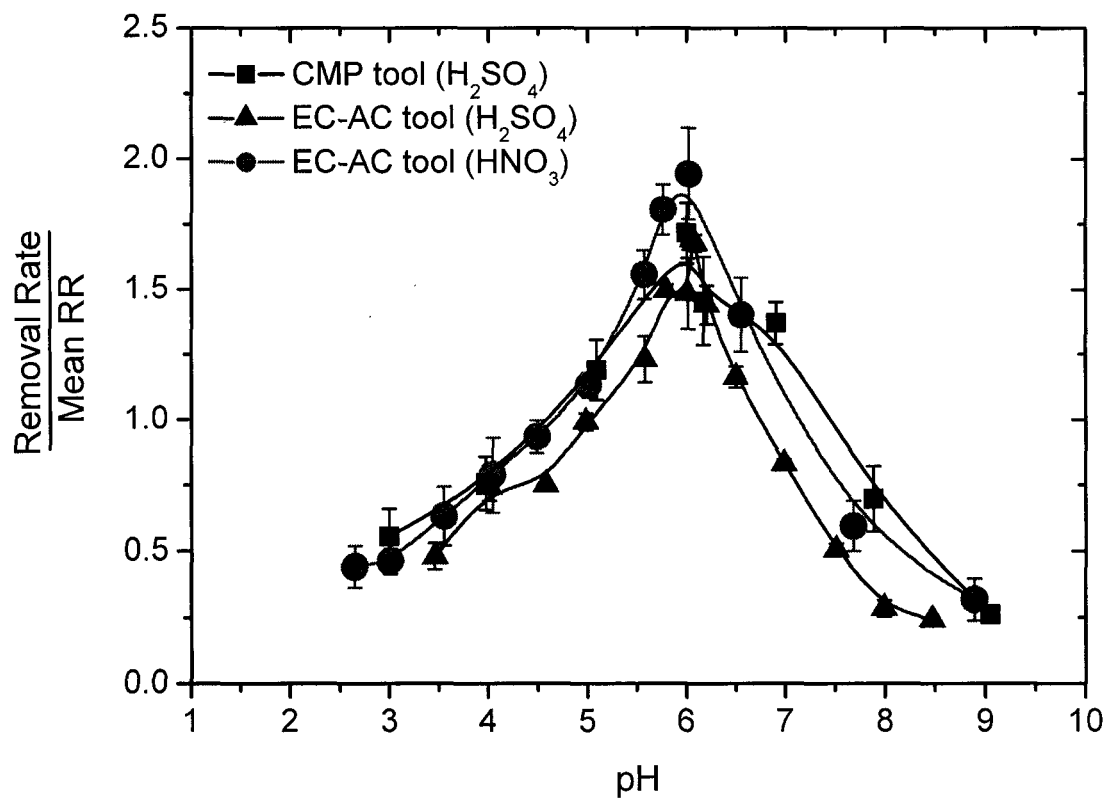


Figure 4.8. Copper removal rates normalized with respect to their mean as a function of pH. [Mean values of CMP tool (H₂SO₄) = 1,858.7 Å/min, EC-AC tool (H₂SO₄) = 897.8 Å/min, EC-AC tool (HNO₃) = 632.5 Å/min.]

4.2.3. Removal Rate of Copper without Abrasion Using the EC-AC Tool

4.2.3.1. Effect of pH on Copper Removal Rates

In order to deconvolute the effect of chemical and mechanical factors during the copper removal process, removal rates of copper were studied in the absence of abrasion. In Figure 4.9, the removal rates of copper with and without abrasion in 0.5M hydroxylamine based slurry are plotted as function of pH. Interestingly, without any abrasion to the copper sample, a maximum in removal rates was also observed at pH 6. This shows that the removal rate of copper in hydroxylamine based chemistry has a strong chemical dependence on slurry pH. At pH values of 4 to 5, the removal rate of copper was significantly increased upon abrasion. However this effect was not observed at pH values of 7 to 8.

The removal rates of copper during abrasion contain both mechanical and chemical factors, and removal rates of copper with no abrasion contain only a chemical factor. The removal rates from abrasion and no abrasion can be expressed as the following equations.

$$RR_{\text{Abrasion}} = RR_{\text{Mechanical}} + RR_{\text{Chemical}} \quad (4.4)$$

$$RR_{\text{No Abrasion}} = RR_{\text{Chemical}} \quad (4.5)$$

The values for $RR_{\text{Mechanical}}$ are the difference in copper removal rates between abrasion and no abrasion conditions. The behavior of $RR_{\text{Mechanical}}$ with respect to pH is shown in Figure 4.10. The ratios of $RR_{\text{Mechanical}}/RR_{\text{Chemical}}$ are also plotted in this figure. If the ratio of $RR_{\text{Mechanical}}/RR_{\text{Chemical}}$ were greater than 1, the removal process would be more influenced by mechanical effects. If the chemical effects were more dominant during the removal process, the ratio would be less than 1.

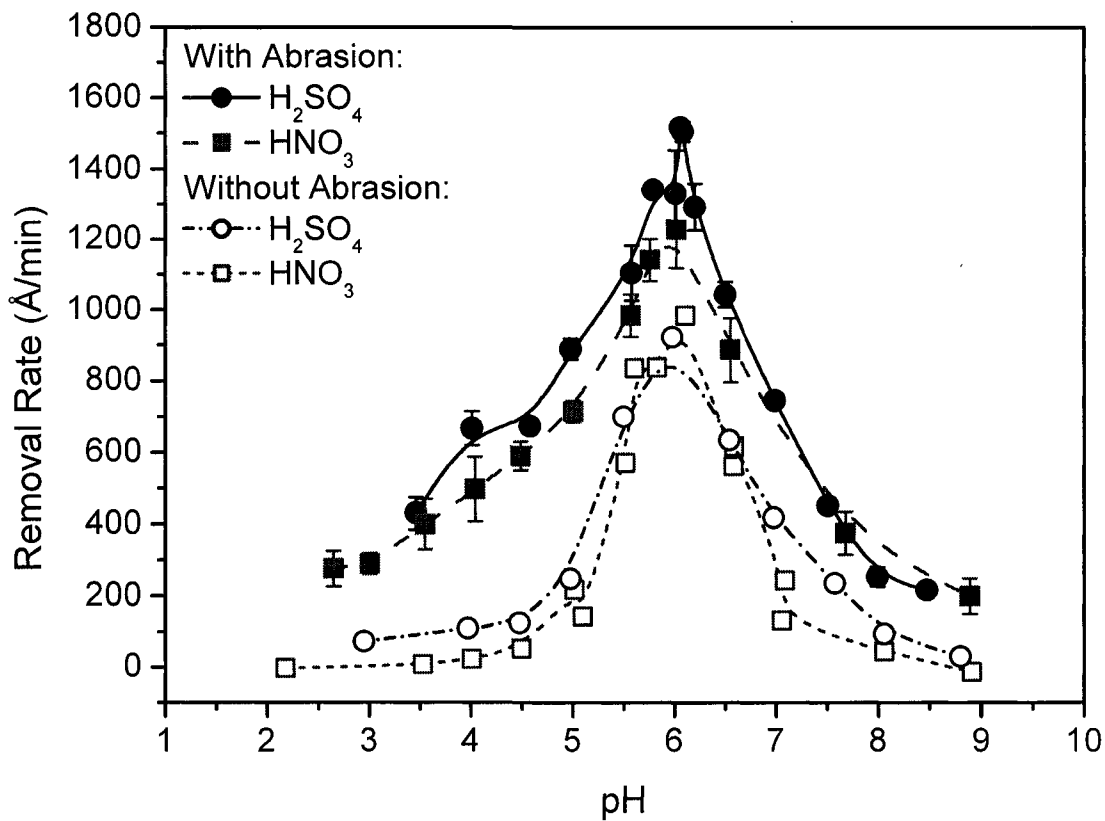


Figure 4.9. Removal rates of copper in 0.5M hydroxylamine based slurry as function of pH. [Removal rates of copper without abrasion (○ and □) and with abrasion (● and ■). pH adjustment using H_2SO_4 (○ and ●) and HNO_3 (□ and ■).]

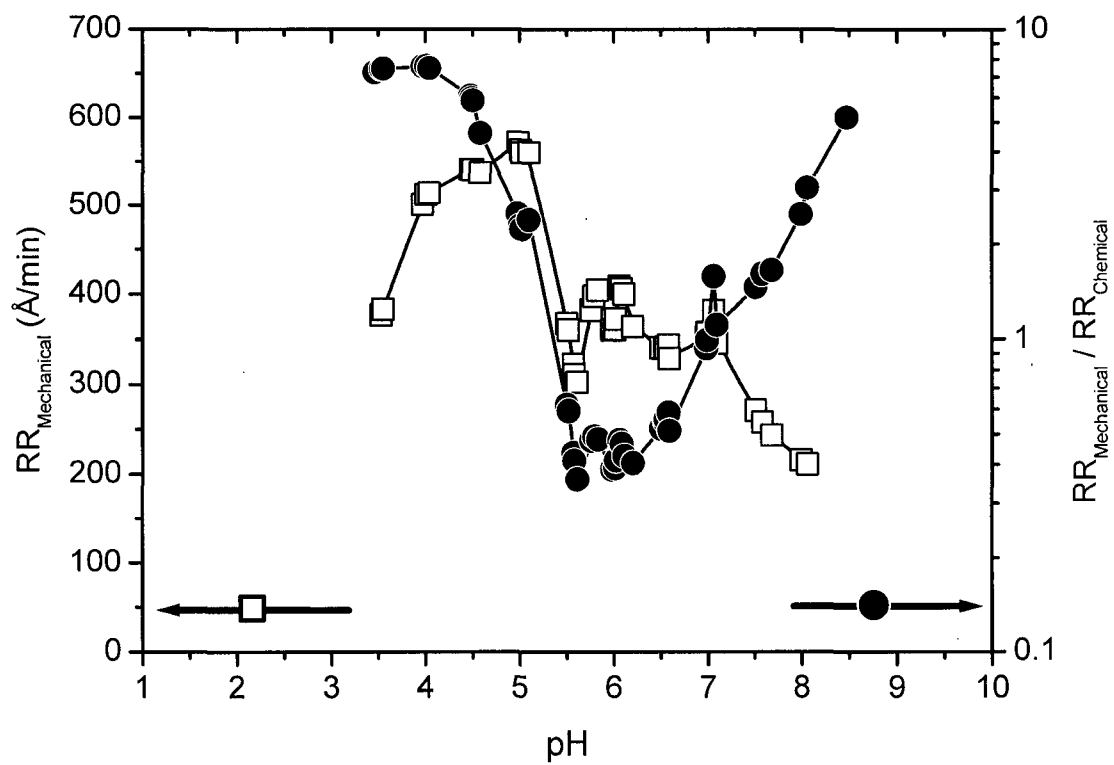


Figure 4.10. Variations $RR_{\text{Mechanical}}$ and the ratio of $RR_{\text{Mechanical}}/RR_{\text{Chemical}}$ plotted as function of pH.

In the near neutral pH range of 5.5 to 7 (Figure 4.10), the $RR_{\text{Mechanical}}/RR_{\text{Chemical}}$ is less than 1. Within this pH range, the chemical effects are more dominant than the mechanical effects. Also within this pH range, $RR_{\text{Mechanical}}$ stayed consistently between ~ 300 and ~ 400 Å/min. At pH values of 7 to 9, the ratio was greater than 1 and showed an increasing trend with respect to pH. The increasing ratio above pH 7 indicates that the mechanical effect is more dominant. Interestingly, the $RR_{\text{Mechanical}}$ shows a decreasing trend with an increase in pH values. The small values of RR_{Chemical} above pH 7, point to the formation of a protective layer (possibly an oxide film).

At pH values less than 5.5, the ratio $RR_{\text{Mechanical}}/RR_{\text{Chemical}}$ is also greater than 1, indicating that mechanical effects are more dominant than chemical effects. The $RR_{\text{Mechanical}}$ reaches a maximum at pH 5 and decreases with pH values below 5. The strong influence of $RR_{\text{Mechanical}}$ in acidic conditions agrees with the effects of abrasion pressure and relative velocity discussed in earlier sections.

The behavior of copper removal rates with respect to pH may be divided into three sections. The first section is pH values below 5, the second section is pH values ranging from 5 to 7, and the third section is pH values greater than 7. These sections were divided according to the $RR_{\text{Mechanical}}$ and RR_{Chemical} behaviors within the pH ranges. In the first and third sections, $RR_{\text{Mechanical}}$ dominates over RR_{Chemical} , while in the second section RR_{Chemical} dominates over $RR_{\text{Mechanical}}$. It is clear that the observed maximum copper removal rate at pH 6 is a chemical-effect-dependant phenomenon.

4.2.3.2. Effects of Rotation Speed on Copper Removal Rate without Abrasion

The RR_{Chemical} can be controlled by the kinetics of the reactions (RR_{Kinetic}) or by mass-transport of the species that moves to and away from the copper surface ($RR_{\text{Transport}}$) or both. This is expressed in the following equations,

$$\frac{1}{RR_{\text{Chemical}}} = \frac{1}{RR_{\text{Kinetic}}} + \frac{1}{RR_{\text{Transport}}} \quad (4.6)$$

$$RR_{\text{Kinetic}} = k' [\text{NH}_2\text{OH}]^a \quad (4.7)$$

$$RR_{\text{Transport}} = k'' [\text{NH}_2\text{OH}] = \frac{0.62 \pi r^2 D^{2/3} [\text{NH}_2\text{OH}]}{v^{1/6}} \omega^{1/2} \quad (4.8)$$

where k' is the rate constant, a is reaction order, and k'' is the transport constant. In Equation (4.8), 'D' is the diffusion coefficient and 'v' is the kinematic viscosity. The $RR_{\text{Transport}}$ is known to be proportional to the square-root of the rotational speed ($\omega^{1/2}$).

To study the effects of rotation speeds on copper removal rate in 0.5M hydroxylamine solutions maintained at pH of 6, rotational speeds ranging from 55.5 rpm (5.81 rad/s) to 555 rpm (58.12 rad/s) were investigated. In Figure 4.11, the experimental results are plotted as inverse copper removal rates ($1/RR_{\text{Chemical}}$) versus the inverse square root of rotational speed ($\omega^{-1/2}$). A linear relationship in Figure 4.11 shows that in the range of rotational speeds investigated, the removal rate of copper is influenced by mass-transfer effects. This could also explain the enhanced removal rate observed at higher relative velocities during the abrasion process discussed earlier.

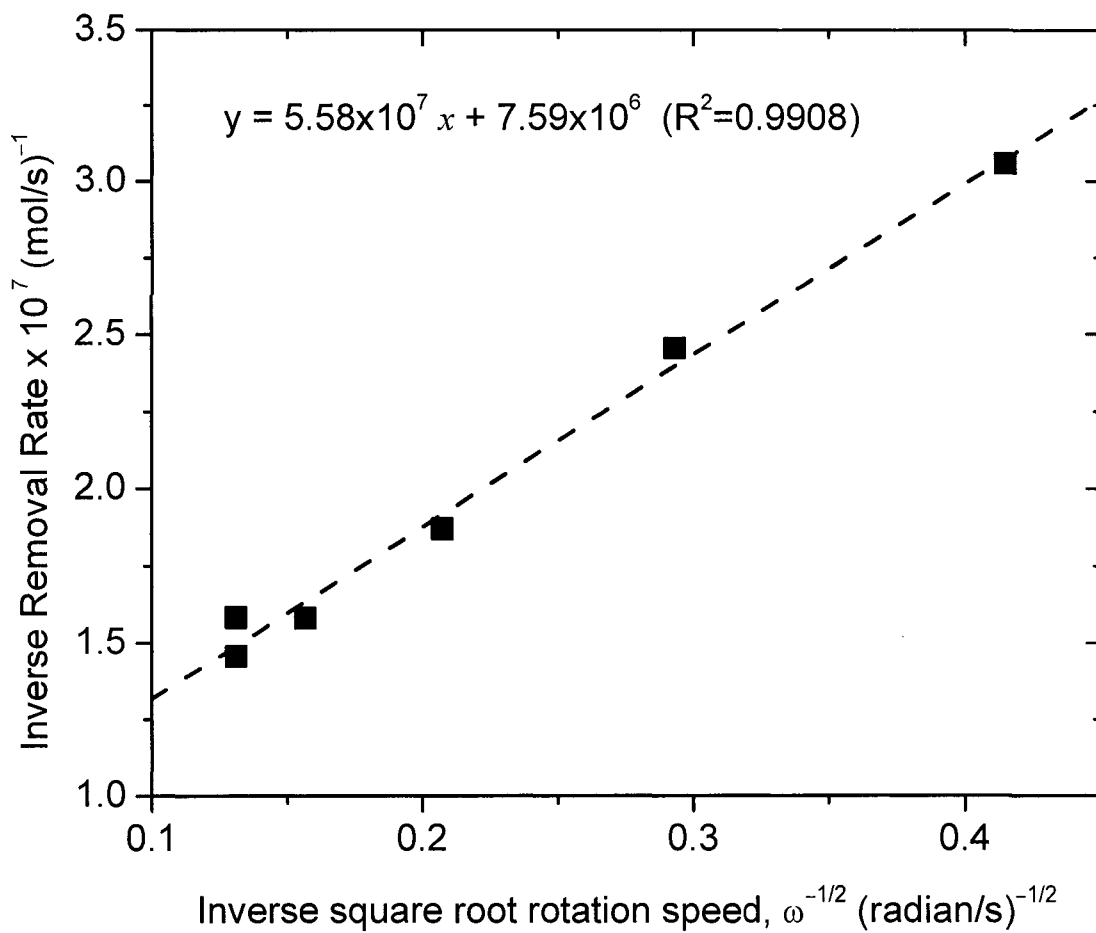


Figure 4.11. Inverse removal rate of copper as function of inverse square root of rotation speed in 0.5M hydroxylamine based chemistry at pH 6. [No abrasion]

The slope of the linear fit are equal to

$$\frac{v^{1/6}}{0.62 \pi r^2 D^{2/3} [\text{NH}_2\text{OH}]} \quad (4.9)$$

At the hydroxylamine concentration of 0.5 M (5×10^{-4} mol/cm³), Equation (4.9) then becomes,

$$\text{slope} \times [\text{NH}_2\text{OH}] = \frac{v^{1/6}}{0.62 \pi r^2 D^{2/3}} = 27918.3 \frac{\text{s}^{1/2}}{\text{cm}^3}. \quad (4.10)$$

$$k'' = \frac{0.62 \pi r^2 D^{2/3} \omega^{1/2}}{v^{1/6}} = \frac{\omega^{1/2}}{27918.3 \frac{\text{s}^{1/2}}{\text{cm}^3}}. \quad (4.11)$$

The determined transport constant (k'') from equation (4.11) can be used to calculate the rate constant (k').

Extrapolation of the linear fit in Figure 4.11 to a zero value of $\omega^{-1/2}$ (i.e., infinite rotational speed) would yield a value of 1,868 Å/min. This means that in the absence of mass-transfer effects a copper removal rate of 1,868 Å/min may be obtained for the chemical system. Also from Equation (4.6), the y-intercept is related to $\text{RR}_{\text{Kinetic}}$. In order to calculate the rate constant (k'), a value for the reaction order (a) is required. By investigating the copper removal rates with respect to hydroxylamine concentration, a value for the reaction order may be determined.

4.2.3.3. Effects of Hydroxylamine Concentration on Copper Removal Rate without Abrasion

The effects of hydroxylamine concentration on copper removal rate were investigated using the EC-AC cell rotating at 222 rpm and at a solution pH of 6. The results are shown in Figure 4.12. The results show that the removal rates of copper increase with increasing hydroxylamine concentrations. The effect of $RR_{Kinetic}$ on $RR_{Chemical}$ shown in Equation (4.6) was investigated further. The kinetics of the reactions are typically known to be dependent on the concentration of the species involved in the reactions. Equation (4.7) assumes that $RR_{Kinetic}$ is dependent only on hydroxylamine concentration and the reaction order (a). With this assumption, Equation (4.6) is rearranged as follows,

$$\frac{1}{RR_{Chemical}} - \frac{1}{RR_{Transport}} = \frac{1}{RR_{Kinetic}} \quad (4.12)$$

$$\frac{1}{RR_{Chemical}} - \frac{1}{k''[NH_2OH]} = \frac{1}{k'[NH_2OH]^a} \quad (4.13)$$

$$\frac{1}{RR_{Chemical}} - \frac{27918.3 s^{1/2} / cm^3}{\omega^{1/2} [NH_2OH]} = \frac{1}{k'[NH_2OH]^a} \quad (4.14)$$

The logarithm of Equation (4.14) results in the following equations.

$$\log \left[\frac{1}{RR_{Chemical}} - \frac{27918.3 s^{1/2} / cm^3}{\omega^{1/2} [NH_2OH]} \right] = \log \left[\frac{1}{k'[NH_2OH]^a} \right] \quad (4.15)$$

$$\log \left[\frac{1}{RR_{Chemical}} - \frac{27918.3 s^{1/2} / cm^3}{\omega^{1/2} [NH_2OH]} \right] = -\log k' - a \log [NH_2OH] \quad (4.16)$$

A log-log plot according to Equation (4.16) is shown in Figure 4.13. The slope is representative of the order of the reaction (a). From the y-intercept, the rate constant (k') can be determined. The linear fit in Figure 4.13 shows a slope of -1.28 and a y-intercept of 2.6799. Therefore, the value of a is 1.28 and k' is $2.09 \times 10^{-3} \text{ cm}^3/\text{s}$.

It would be intuitive to compare the value of the rate constant (k') with that of the transport constant (k''). It may be noted that the value of k'' is a function of rotational speed (ω), shown in Equation (4.11). By considering the highest attainable rotation speed on the EC-AC tool is approximately 600 rpm, this would result in $k'' = 2.84 \times 10^{-4} \text{ cm}^3/\text{s}$. Since the transport constant (k'') is smaller than the chemical rate constant ($k' = 2.09 \times 10^{-3} \text{ cm}^3/\text{s}$), this indicates that the effect of mass transport controls the removal rate of copper without abrasion (RR_{Chemical}). In order for the RR_{Chemical} to be controlled by the chemical rate constant (k'), the rotation speed on the EC-AC tool would have to reach 35,000 rpm.

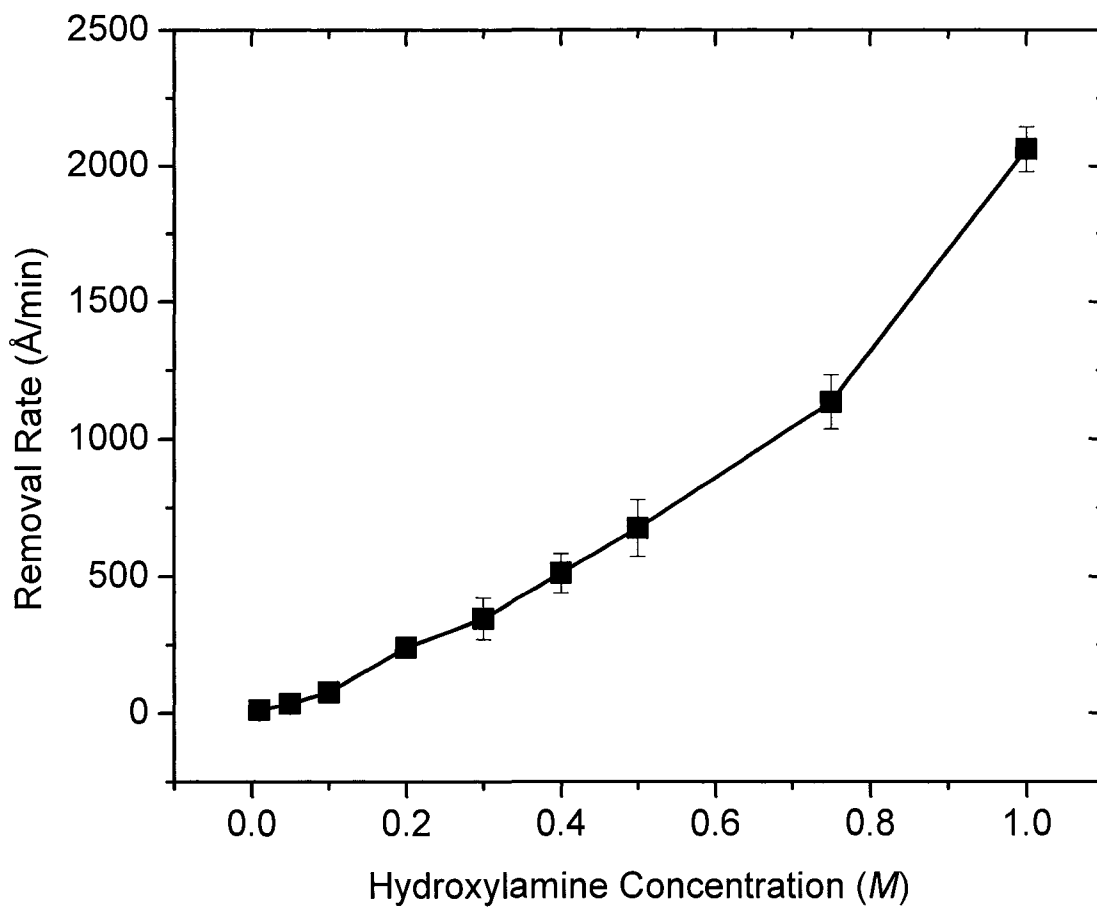


Figure 4.12. Removal rate of copper as function of hydroxylamine concentration at pH around 6 using the EC-AC tool that was rotating at 222 rpm (23.25 rad/s).

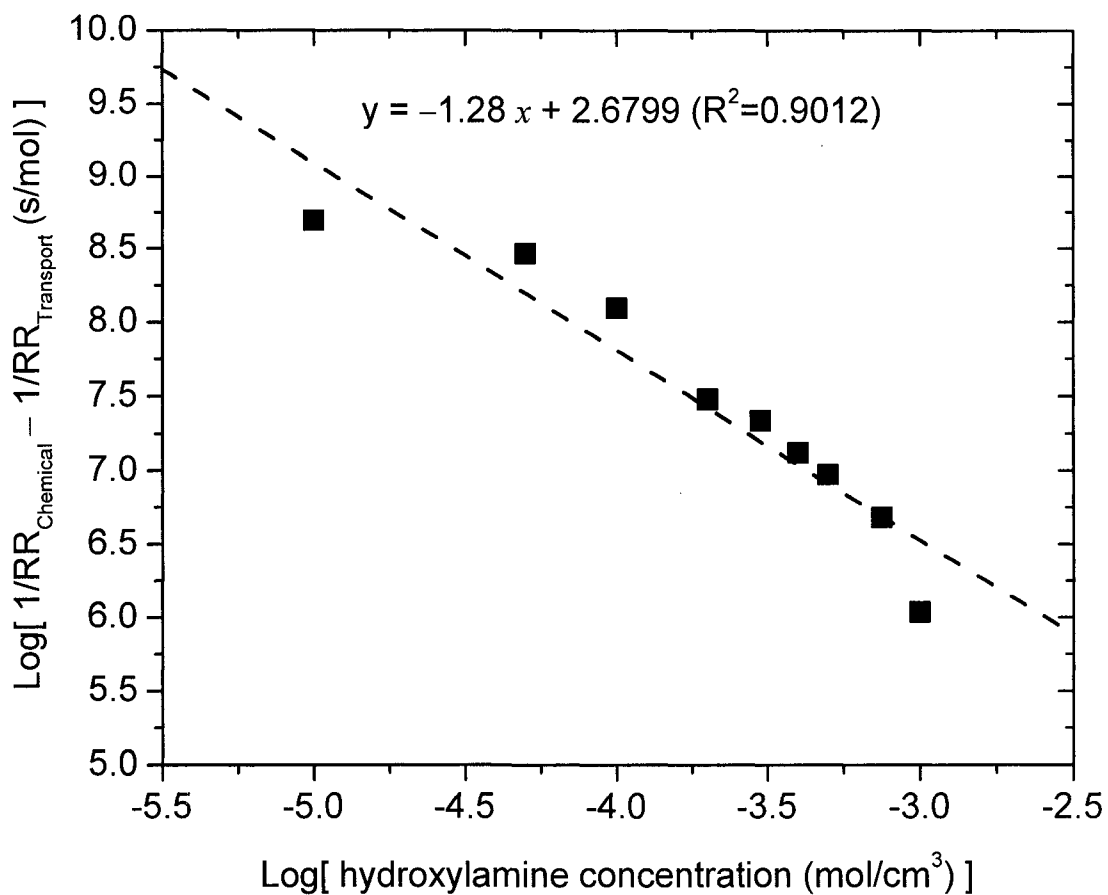


Figure 4.13. Log-Log plot of equation (4.16) as function of hydroxylamine concentration at pH 6. A linear fit is drawn as the dashed line.

4.3. Potential-pH Diagrams and Redox Potential Measurements

Potential-pH (E-pH) diagrams were constructed to understand the observed chemical effects of hydroxylamine on the removal rate (or dissolution rate) of copper. The E-pH diagram of a copper-water system is shown in Figure 4.14. The three copper activities considered were 0.1, 10^{-3} , and 10^{-6} . Stability lines that were most affected by varying activities were $\text{Cu}^{2+}/\text{CuO}$, $\text{Cu}^{2+}/\text{Cu}_2\text{O}$, and Cu^{2+}/Cu . At a dissolved copper activity of 10^{-6} , species such as HCuO_2^- and CuO_2^{2-} are thermodynamically stable in highly alkaline solutions. At higher copper activities, the stability region of HCuO_2^- and CuO_2^{2-} was replaced by CuO . In an acidic solution at pH values below 4, Cu^{2+} is the most stable specie at all dissolved copper activities.

The redox potential of deionized water containing inorganic acids and bases was measured and plotted into the copper-water E-pH diagram. Two different acids, sulfuric and nitric, were used to lower the pH. For both nitrate and sulfate systems, the measured redox potential versus pH line exhibits a slope of -0.054 V/pH , as may be expected for the $\text{O}_2/\text{H}_2\text{O}$ equilibrium. From Figure 4.14, if a copper metal is immersed into water with a pH greater than 7, the formation of CuO is expected. Dissolution of copper metal is expected at a pH lower than 4. Also from the E-pH diagram, one would expect the tendency for dissolution of copper at pH 4 to be greater than at pH 6.

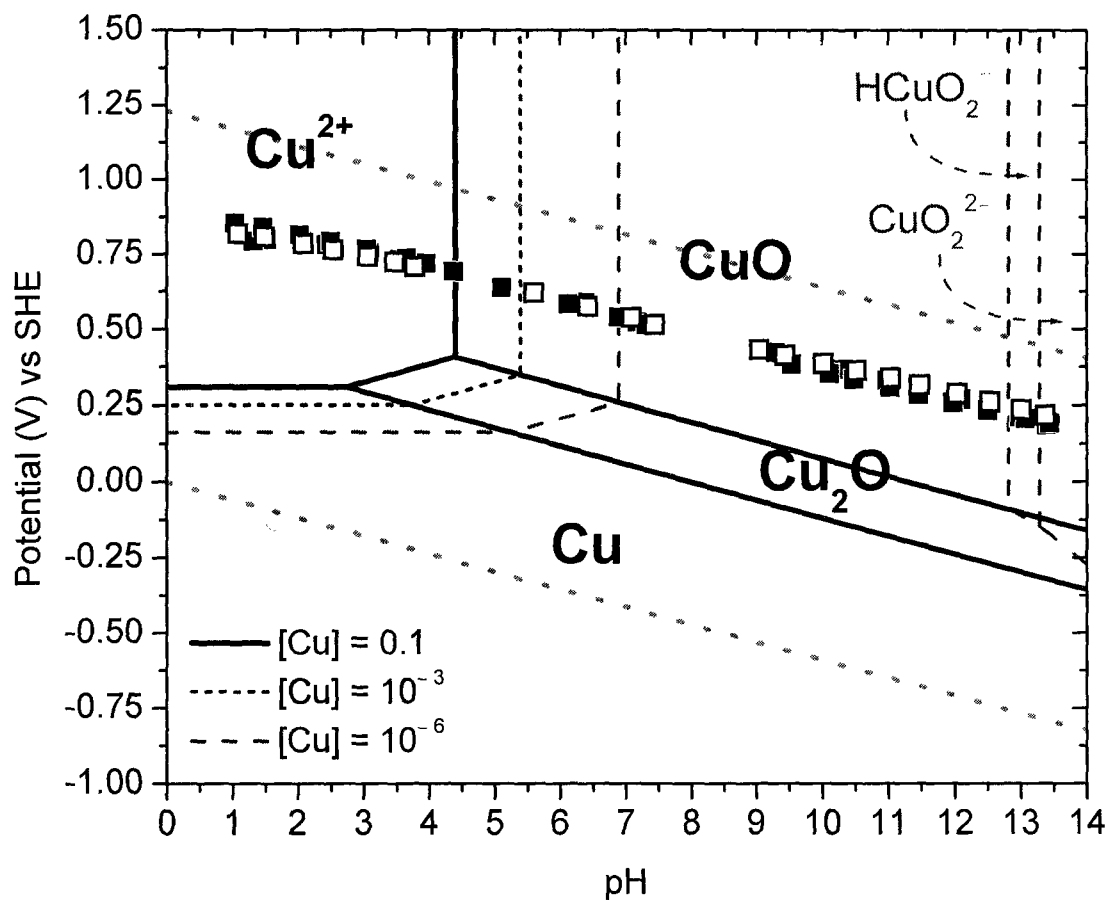


Figure 4.14. E-pH diagram of copper-water system. [Species considered: [Cu, CuO, Cu₂O] = 1 (solids), [Cu²⁺, Cu⁺, Cu(OH)₂, HCuO₂⁻, CuO₂²⁻] = 0.1 (—), = 10⁻³ (- - -), = 10⁻⁶ (- · -). Dotted lines are the water stability region. Redox potentials of DI water containing sulfate anions (■) and nitrate anions (□).]

The E-pH diagram of a nitrogen-water system with emphasis on hydroxylamine is shown in Figure 4.15. If all of the nitrogen based species in Table 3.2 were used in constructing the E-pH diagram, only NO_3^- , N_2 , and ammonia (NH_3 and NH_4^+) would appear in the diagram. In order for hydroxylamine and some intermediate species, such as NO , NO_2^- , and hyponitrous-hyponitrite species ($\text{H}_2\text{N}_2\text{O}_2$, HN_2O_2^- , and $\text{N}_2\text{O}_2^{2-}$), to appear in the diagram, several nitrogen based species had to be excluded from the calculation. These species were ammonia (NH_3 and NH_4^+), hydrazine (N_2H_4 and N_2H_5^+), N_2 , and N_2O . Even though N_2O was excluded from the calculation, a hatched region showing the stability of N_2O in Figure 4.15 was drawn because most of the studies on the decomposition of hydroxylamine found in the literature have claimed that the majority of the decomposition product is N_2O . The hatched region of N_2O was obtained by including N_2O with the other nitrogen species and excluding ammonia, hydrazine, and N_2 .

In order for the nitrogen-water E-pH diagram to be representative of the hydroxylamine based chemistry, the activities of the nitrogen-based species were kept constant at 10^{-6} while only varying the activities of hydroxylamine. By increasing the activities of NH_2OH and NH_3OH^+ from 10^{-6} to 0.5, lines representing the redox couple of hyponitrous-hyponitrite species ($\text{H}_2\text{N}_2\text{O}_2$, HN_2O_2^- , and $\text{N}_2\text{O}_2^{2-}$) with hydroxylamine shifts to a more reducing potential.

The measured redox potentials of the water-sulfate and 0.5M hydroxylamine solution, acidified using sulfuric acid, are plotted in Figure 4.15. The water-sulfate system shows a fairly oxidizing aqueous chemistry. In the presence of 0.5M hydroxylamine, the measured redox potentials lowered, signifying a less oxidizing chemical system.

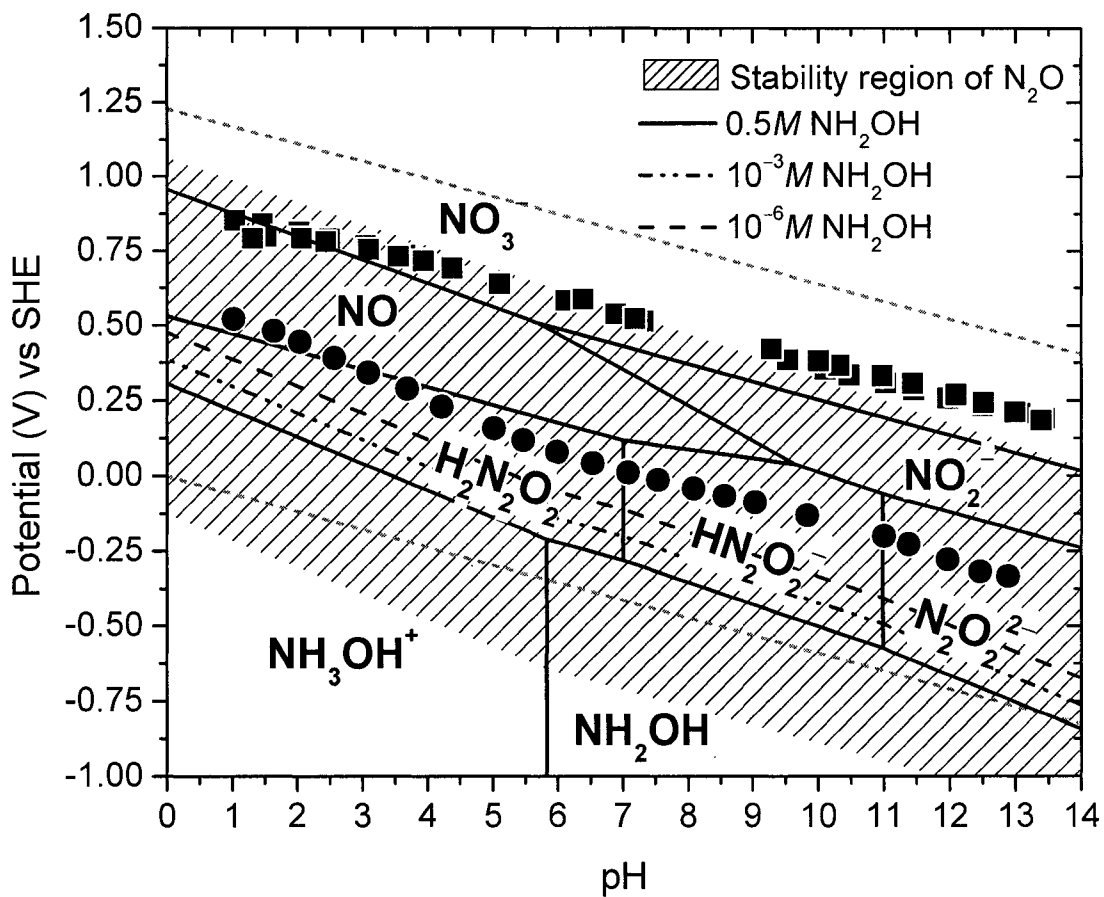


Figure 4.15. E-pH diagram of nitrogen-water system with NH_2OH as base compound. [The following species and their activities were considered: $[NH_2OH, NH_3OH^+] = 10^{-6}$ (— · —), $= 10^{-3}$ (- · · -), $= 0.5$ (—) and $[NO_3^-, HNO_3, NO_2^-, HNO_2, H_2N_2O_2, HN_2O_2^-, N_2O_2^{2-}, NO] = 10^{-6}$. Redox potential of DI water with sulfate anions (■) and addition of 0.5M hydroxylamine (●).]

The measured redox potential of 0.5M hydroxylamine falls in the region of hyponitrous-hyponitrite species. The decomposition of hydroxylamine could produce N₂O possibly through hyponitrous-hyponitrite intermediates. It is also possible that the reduction of NO₂⁻ and NO coupled with oxidation of hydroxylamine forms the intermediate hyponitrous-hyponitrite specie, which eventually evolves to N₂O, reaction (2.36). The presence of NO₂⁻ and NO in solution would come from the decomposition process of hydroxylamine, enhanced by the reduction of O₂.

The potential-pH diagram of copper-hydroxylamine-water is shown in Figure 4.16 for a hydroxylamine activity of 0.5. The dissolved copper activity was varied between 0.1 and 10⁻⁶. The pH region where Cu(NH₂OH)²⁺ and Cu(NH₂OH)₂²⁺ complexes are stable lies between ~3.5 and ~8, depending on the activity of the soluble copper species. With increasing dissolved copper activity, the stability region of Cu(NH₂OH)₂²⁺ complex shrinks.

The measured redox potentials of 0.5M hydroxylamine solution (with and without 0.001 M CuSO₄) are plotted in Figure 4.16. Interestingly, the measured redox potentials of hydroxylamine based chemistries follow Cu₂O/Cu stability line closely except for pH values less than ~4. At a dissolved copper activity of 10⁻⁶, the Cu₂O/Cu equilibrium line does not extend below pH ~7. From pH values of ~7 to ~3.5, the measured redox potentials of hydroxylamine fall within the Cu(NH₂OH)₂²⁺ and Cu(NH₂OH)²⁺ stability region. As the dissolved copper activity is increased to 10⁻³, the Cu₂O/Cu equilibrium line extends all the way to pH ~3.5. At pH values less than 3, the measured redox potentials of hydroxylamine lie in the Cu²⁺ region.

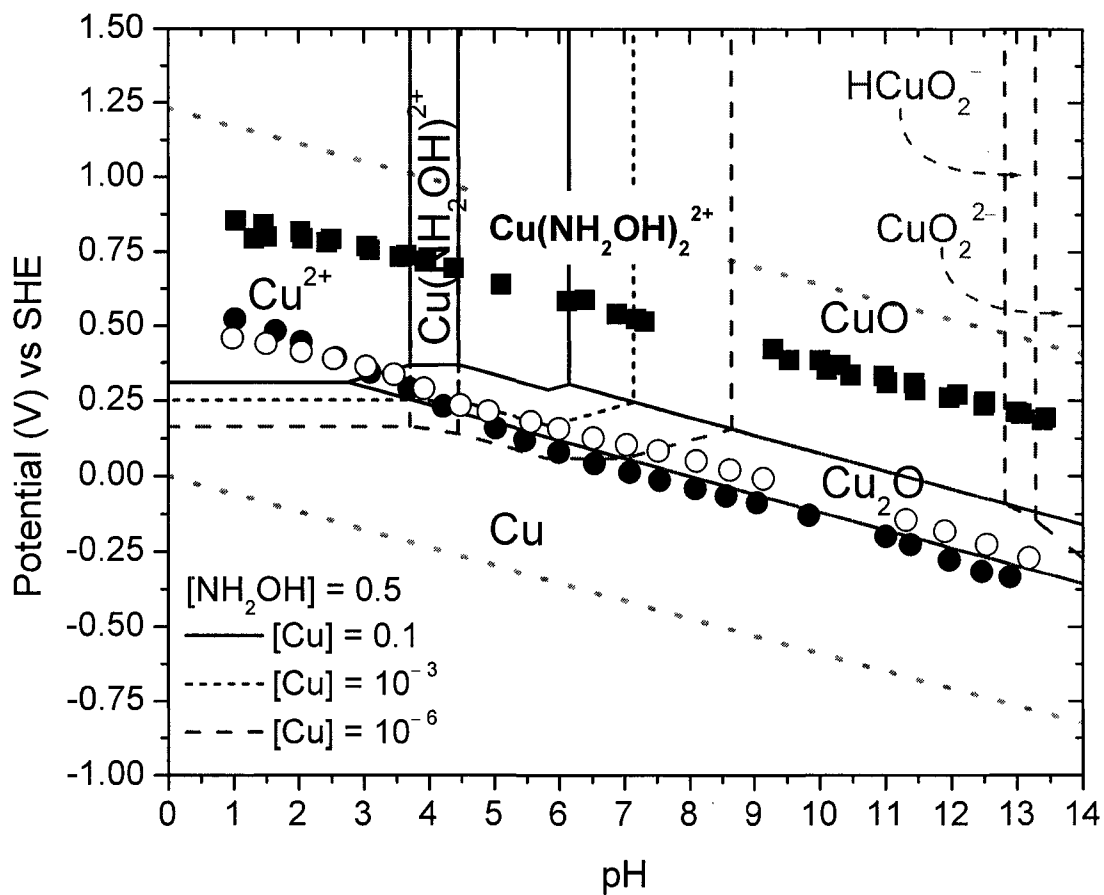


Figure 4.16. E-pH diagram of copper-hydroxylamine-water system with Cu as base metal. [The following species were considered: $[\text{Cu}, \text{CuO}, \text{Cu}_2\text{O}] = 1$ (solids), $[\text{Cu}^{2+}, \text{Cu}^+, \text{Cu}(\text{OH})_2, \text{HCuO}_2^-, \text{CuO}_2^{2-}, \text{Cu}(\text{NH}_2\text{OH})^{2+}, \text{Cu}(\text{NH}_2\text{OH})_2^{2+}] = 0.1$ (—), $= 10^{-3}$ (- - -), $= 10^{-6}$ (- · -), $[\text{NH}_2\text{OH}, \text{NH}_3\text{OH}^+] = 0.5$. Redox potential of DI water with sulfate anions (■), 0.5M hydroxylamine (●), and 0.5M hydroxylamine + 0.001M copper sulfate (○).]

The E-pH diagrams of copper-hydroxylamine-water and nitrogen-water systems are superimposed into a single E-pH diagram shown in Figure 4.17. The measured redox potentials of 0.5M hydroxylamine solution are also plotted in the figure. The reduction equilibrium lines of $\text{NH}_3\text{OH}^+/\text{NH}_4^+$ and $\text{NH}_2\text{OH}/\text{NH}_4^+$ are drawn, even though earlier diagrams did not include NH_3 and NH_4^+ species. The reason for the presence of the hydroxylamine/ammonia equilibrium lines is to show the feasibility of this reduction reaction coupled with oxidation of copper. It may be noted that both $\text{NH}_3\text{OH}^+/\text{NH}_4^+$ and $\text{NH}_2\text{OH}/\text{NH}_4^+$ equilibrium lines are more noble than the Cu^{2+}/Cu equilibrium line; hence, oxidation of Cu by either NH_3OH^+ or NH_2OH with NH_4^+ as the reduction product is thermodynamically favorable.

From Figure 4.17 at pH values about 6, the complexation of hydroxylamine can favor the oxidation of copper provided an oxidizing agent is available. In the figure, the $\text{NO}/\text{H}_2\text{N}_2\text{O}_2$ couple may be seen to be more noble than the $\text{Cu}/\text{Cu}(\text{NH}_2\text{OH})_2^{2+}$ couple at pH 6. The reduction of $\text{NO} \rightarrow \text{H}_2\text{N}_2\text{O}_2$ coupled with the oxidation of $\text{Cu} \rightarrow \text{Cu}(\text{NH}_2\text{OH})_2^{2+}$ is also thermodynamically favorable. The presence of NO in solution would come from the decomposition of hydroxylamine. The measured redox potential of hydroxylamine at pH 6 falls in between the stability lines of $\text{NO}/\text{H}_2\text{N}_2\text{O}_2$ and $\text{Cu}/\text{Cu}(\text{NH}_2\text{OH})_2^{2+}$.

The reduction process of $\text{NH}_2\text{OH} \rightarrow \text{NH}_4^+$ coupled with oxidation of copper are also thermodynamically favorable. The question then becomes which of two reduction processes, $\text{NH}_2\text{OH} \rightarrow \text{NH}_4^+$ or $\text{NO} \rightarrow \text{H}_2\text{N}_2\text{O}_2$, is kinetically faster. The kinetics of the reduction process will be investigated and discussed in later sections.

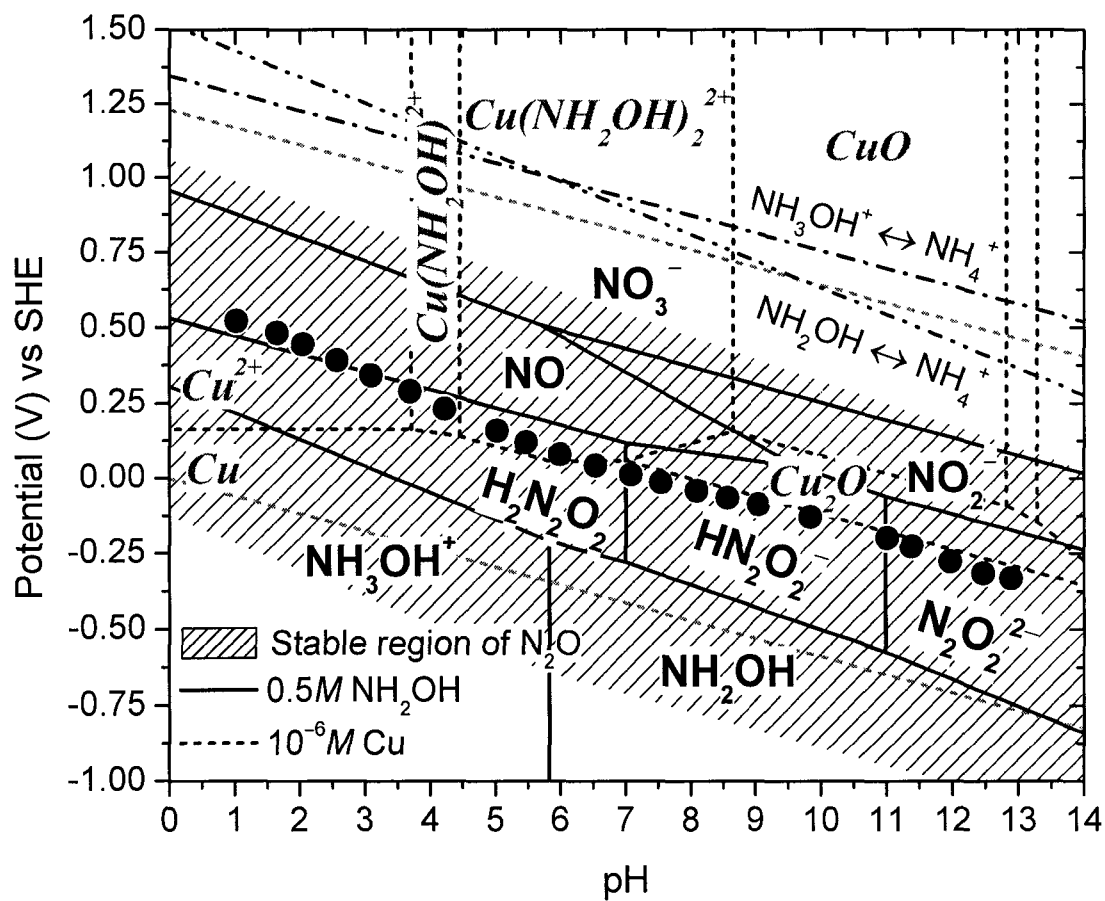
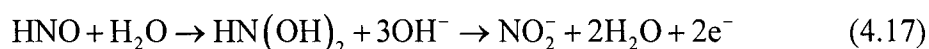


Figure 4.17. E-pH diagrams of copper-hydroxylamine-water system superimposed together with nitrogen-water system. Stability lines of NH_2OH/NH_4^+ ($-\cdot\cdot\cdot-$) and NH_3OH^+/NH_4^+ ($-\cdot-\cdot-$). Redox potentials of $0.5M$ hydroxylamine solution (\bullet).

4.4. Oxygen Concentration Measurements

The oxygen levels in solutions with and without 0.5M hydroxylamine were measured in open air with respect to solution pH. The results are shown in Figure 4.18. The oxygen levels in solution without hydroxylamine showed a constant value of approximately 7.4 ppm in the pH range of 1 to 13. When 0.5 M hydroxylamine was added into the solution at pH values greater than 12, the oxygen level decreased to about 0.5 ppm. As pH values decreased from 12 to 5, the oxygen levels in hydroxylamine containing solution increased linearly at about 1.1 ppm per pH value. At pH values less than 5, the oxygen levels remained constant at about 7.3 ppm. These results indicate that hydroxylamine reacts with oxygen in solution at pH values greater than 5. Thus hydroxylamine appears to be an effective oxygen scavenger in alkaline solutions.

The oxidation of hydroxylamine is likely to occur via the following reactions,



The coupled oxygen reduction reaction is,



The drop in oxygen levels, when hydroxylamine was added into the solution at pH values above 5, is a clear indication of hydroxylamine being oxidized by reducing oxygen. However, at pH values below 5, the saturated oxygen level indicate that either the oxidation of hydroxylamine does not occur, or it occurs at a slower rate than the rate at which oxygen dissolves in solution.

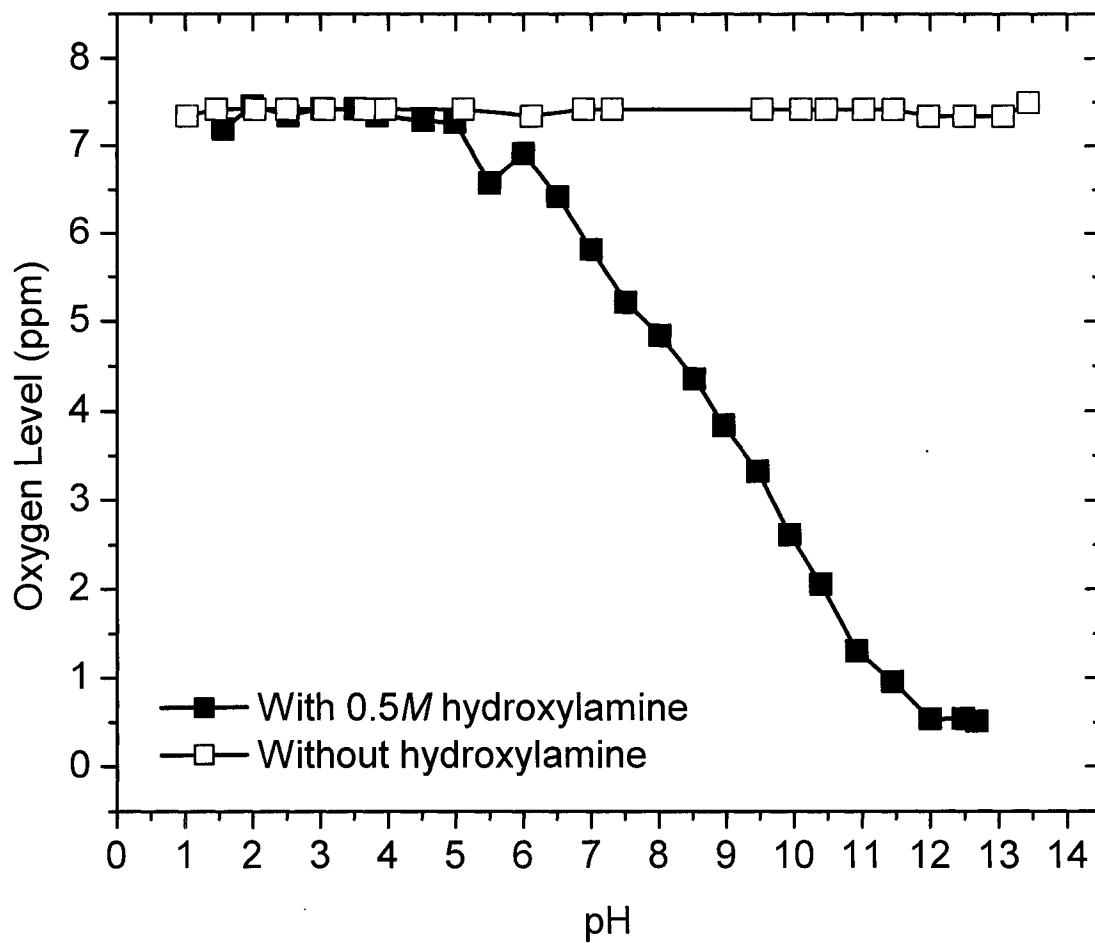


Figure 4.18. Oxygen levels (ppm) in solution containing 0.5M hydroxylamine (■) and solution without any hydroxylamine (□) with respect to pH. [Sulfuric acid was used to acidify the solutions from pH values of 13 to 1]

4.5. Electrochemical Analysis

Electrochemical techniques were used to probe the electrochemical reactions that may occur between copper and hydroxylamine. Earlier experimental results showed that the overall copper removal rate (RR_{Overall}) during CMP is split into two removal effects, mechanical and chemical ($RR_{\text{Mechanical}}$ and RR_{Chemical}). In Figure 4.9, the copper removal rates with respect to pH showed that RR_{Overall} and RR_{Chemical} have the same trend. Therefore, if the mechanisms for RR_{Chemical} during copper CMP in hydroxylamine based chemistry is understood, then the mechanisms for RR_{Overall} during copper CMP can be understood as well. Electrochemical experiments were performed both in the presence and absence of abrasion to probe the electrochemical phenomena that contribute to RR_{Chemical} .

4.5.1. Tafel and Corrosion Rate Analysis without Abrasion

4.5.1.1. Effects of pH

Polarization curves of copper in 0.5M hydroxylamine at pH values greater than and less than 6 are shown in Figure 4.19 and Figure 4.20, respectively. Both figures are plotted as overpotential (η) vs. $\log(i)$. From each polarization curve, the values of Tafel slope (β_a and β_c), polarization resistance (R_p), corrosion potential (E_{corr}), and corrosion current density (i_{corr}) were determined and tabulated in Table 4.2.

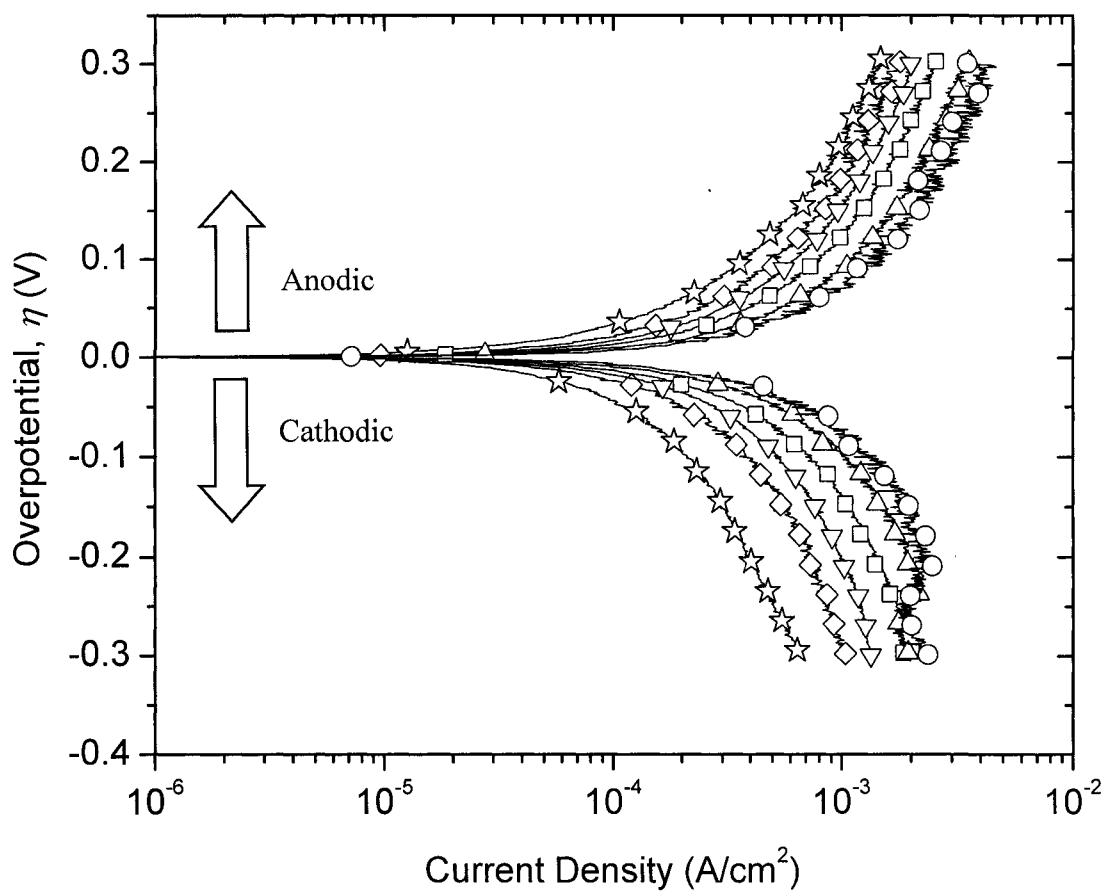


Figure 4.19. Potentiodynamic polarizations of electrodeposited copper film in 0.5M hydroxylamine base chemistry at different pH values without abrasion. pH 8.8 (\star), pH 8.05 (\diamond), pH 7.58 (∇), pH 6.99 (\square), pH 6.53 (\triangle), and pH 5.98 (\circ).

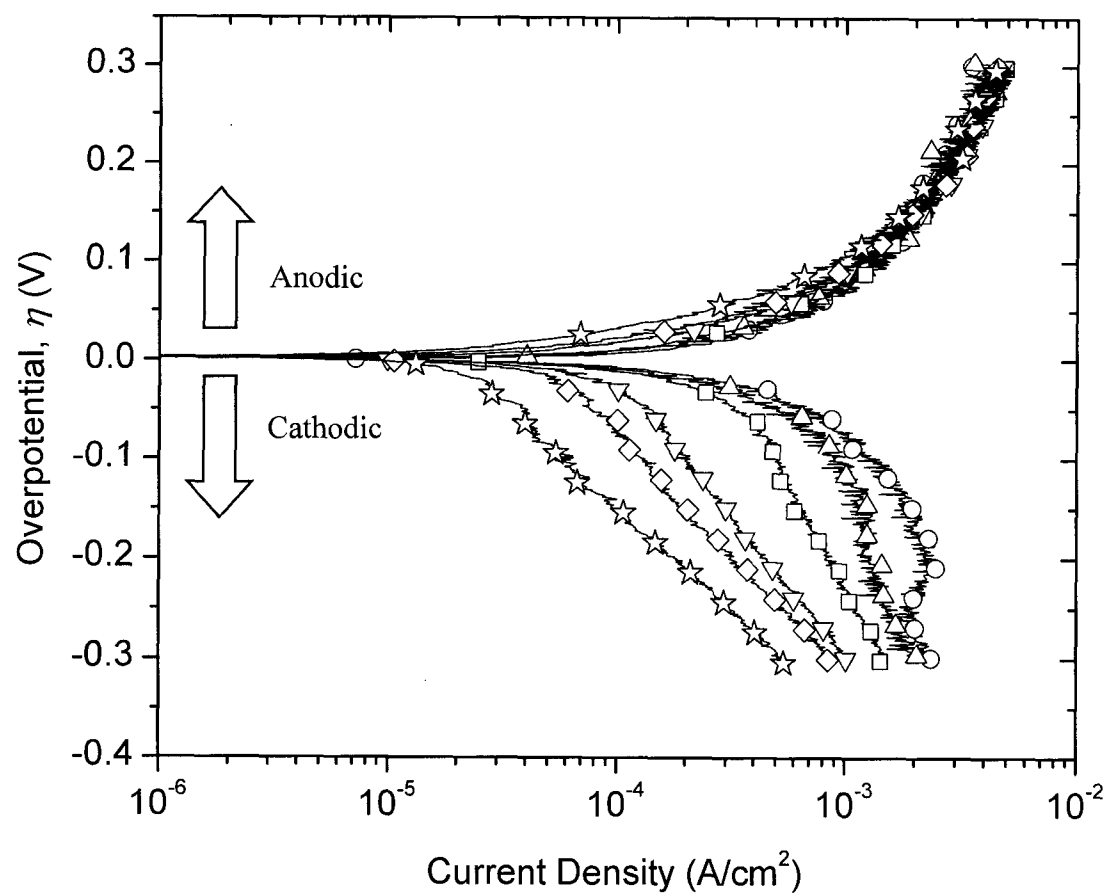


Figure 4.20. Potentiodynamic polarizations of electrodeposited copper film in 0.5M hydroxylamine base chemistry at different pH values without abrasion. pH 2.95 (\star), pH 3.96 (\diamond), pH 4.48 (∇), pH 4.98 (\square), pH 5.5 (\triangle), and pH 5.98 (\circ).

The polarization curves in Figure 4.19 show that both cathodic and anodic curves shift in the direction of increasing current density with decreasing pH values from 8.8 to 5.98. This results in higher corrosion current density (i_{corr}) and likely a higher copper removal rate. The polarization curves in Figure 4.20 show that cathodic polarization curves shift in the direction of decreasing current density with decreasing pH values below 5.98, while the anodic polarization curves showed no change with respect to decreasing pH values. Even though the anodic polarization curves did not change much, the calculated i_{corr} decreased with decreasing pH values from 5.98 to 2.95. This decrease in i_{corr} value corresponded with the shift in cathodic polarization curves below pH 5.98. The shift in cathodic polarization curves with decreasing pH values may be attributed to a reduction reaction that becomes less favorable in acidic condition.

The tabulated results in Table 4.2 show that properties such as R_p and i_{corr} have similar behaviors to actual copper removal rates. In earlier discussions, the removal rates of copper were found to have a maximum pH value of 6. This same maximum was also observed for i_{corr} in Table 4.2. Since R_p is inversely related to i_{corr} , the behavior of R_p with respect to pH is opposite that of i_{corr} showing a minimum at pH value of 6.

To demonstrate that the behavior of i_{corr} is the same as the actual copper removal rates with respect to pH, i_{corr} ($\mu\text{A}/\text{cm}^2$) values were converted to removal rates ($\text{\AA}/\text{min}$) based on 2 electron charge transfer. This will be referred to as electrochemical removal rates (EC-RR). A plot that contains actual copper removal rates and EC-RR normalized to their mean values with respect to pH is shown in Figure 4.21.

Table 4.2. Electrochemical properties of the polarization curves in Figure 4.19 and Figure 4.20.

pH	β_a (V/decade)	β_c (V/decade)	R_p ($\Omega \cdot \text{cm}^2$)	E_{corr} (V vs SHE)	i_{corr} ($\mu\text{A}/\text{cm}^2$)
8.8	0.277 ± 0.004	-0.353 ± 0.004	40.9 ± 1.5	0.035	175.5 ± 0.2
8.05	0.306 ± 0.005	-0.371 ± 0.006	24.7 ± 0.6	0.084	314.4 ± 2.6
7.58	0.316 ± 0.004	-0.374 ± 0.006	18.7 ± 0.3	0.104	424.0 ± 4.3
6.99	0.341 ± 0.005	-0.355 ± 0.006	14.4 ± 0.2	0.118	542.0 ± 6.4
6.53	0.329 ± 0.005	-0.309 ± 0.005	10.1 ± 0.2	0.134	731.2 ± 6.2
5.98	0.323 ± 0.006	-0.419 ± 0.019	7.9 ± 0.3	0.167	$1,070.0 \pm 20.0$
5.5	0.303 ± 0.006	-0.485 ± 0.012	9.7 ± 0.5	0.183	885.5 ± 4.0
4.98	0.279 ± 0.004	-0.415 ± 0.002	11.6 ± 0.4	0.182	667.7 ± 0.6
4.48	0.261 ± 0.004	-0.282 ± 0.001	20.4 ± 1.6	0.187	307.5 ± 4.8
3.96	0.235 ± 0.004	-0.240 ± 0.001	28.0 ± 2.6	0.193	195.9 ± 3.6
2.95	0.221 ± 0.004	-0.207 ± 0.001	53.0 ± 6.2	0.187	93.5 ± 2.6

The figure indicates that the trend of EC-RR with respect to pH is similar to actual RR. However the mean values for EC-RR is 109 $\text{\AA}/\text{min}$ and actual RR is 327 $\text{\AA}/\text{min}$. This indicates that the calculated EC-RR (based on 2 e^- charge transfer) alone cannot accurately predict actual copper rates. Even though EC-RR cannot predict actual copper rates, it still offers useful information in the analysis of copper removal rates with respect to pH in hydroxylamine based chemistry.

The Tafel slopes (β_a and $|\beta_c|$) from Table 4.2 show that all the values are in the range of 0.207 to 0.485 V/decade. Ideally, if the transfer coefficients for anodic (α_a) and cathodic (α_c) reactions are equal to 0.5 and the number of electrons transferred (n) is 2, then the values for β_a and $|\beta_c|$ would be 0.059 V/decade.

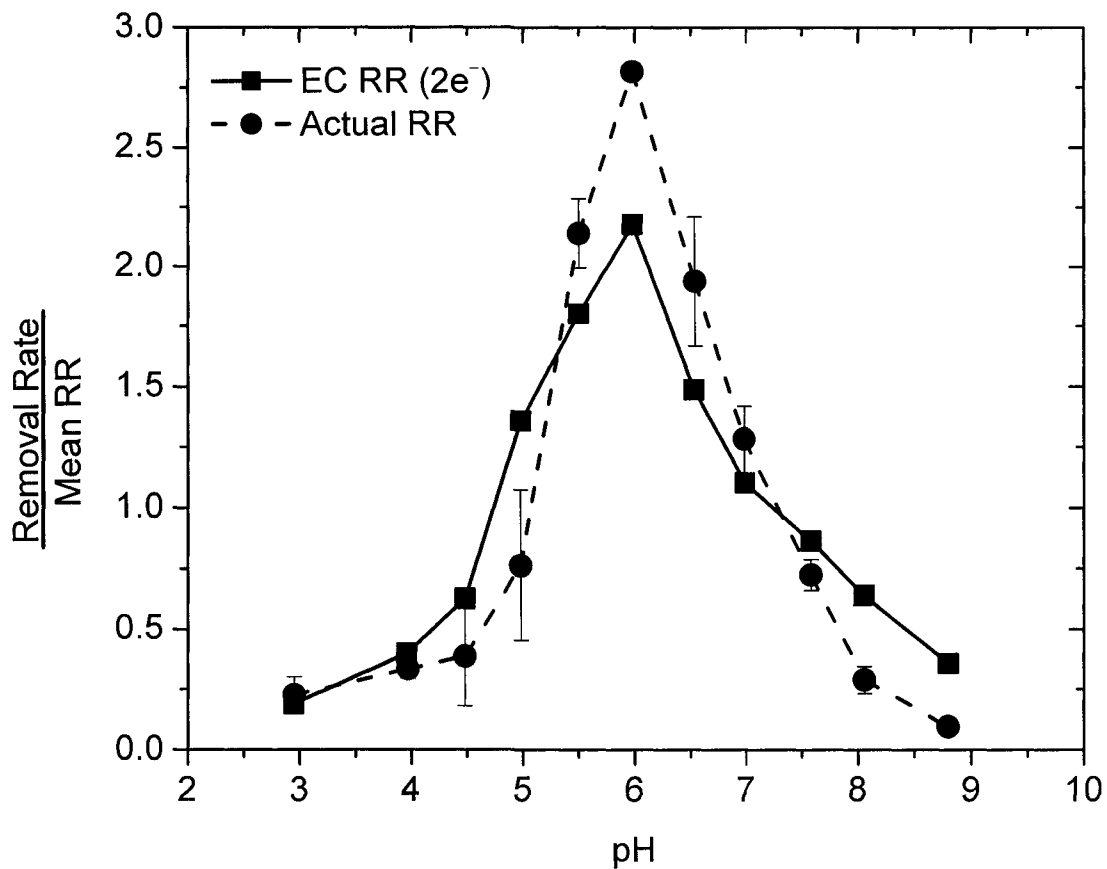


Figure 4.21. Copper removal rates normalized over their mean in 0.5M hydroxylamine based slurry without any abrasion with respect to pH. The mean value for EC RR (2e⁻) was 108.9 Å/min. The mean value for actual RR was 327.4 Å/min.

Considering that the measured values for β_a and $|\beta_c|$ is between 0.207 and 0.485, it is likely that the transfer coefficients (α_a and α_c) are very small. Based on $n = 2$, the α_a and α_c for all pH values tested were between 0.15 and 0.06.

4.5.1.2. Concentration Effects

The effects of hydroxylamine based chemistry on dissolution of copper were studied as a function of concentration at pH value of 6. The polarization curves of copper in solutions of different hydroxylamine concentration maintained at pH 6 are plotted in Figure 4.22 as overpotential (η) versus $\log(i)$. The cathodic polarization curves show subtle changes with respect to hydroxylamine concentration. Beyond -0.1 V overpotential, almost all of the cathodic polarization curves appear to reach limiting current densities ranging from 1×10^{-3} to 3×10^{-3} A/cm². However, the anodic polarization curves change significantly with respect to hydroxylamine concentration. As hydroxylamine concentrations decrease, the anodic polarization curves shift in the direction of lower current densities. Also with decreasing hydroxylamine concentrations, the anodic limiting current densities seem to occur over a larger range of 7×10^{-5} to 4×10^{-3} A/cm² than the cathodic limiting current densities.

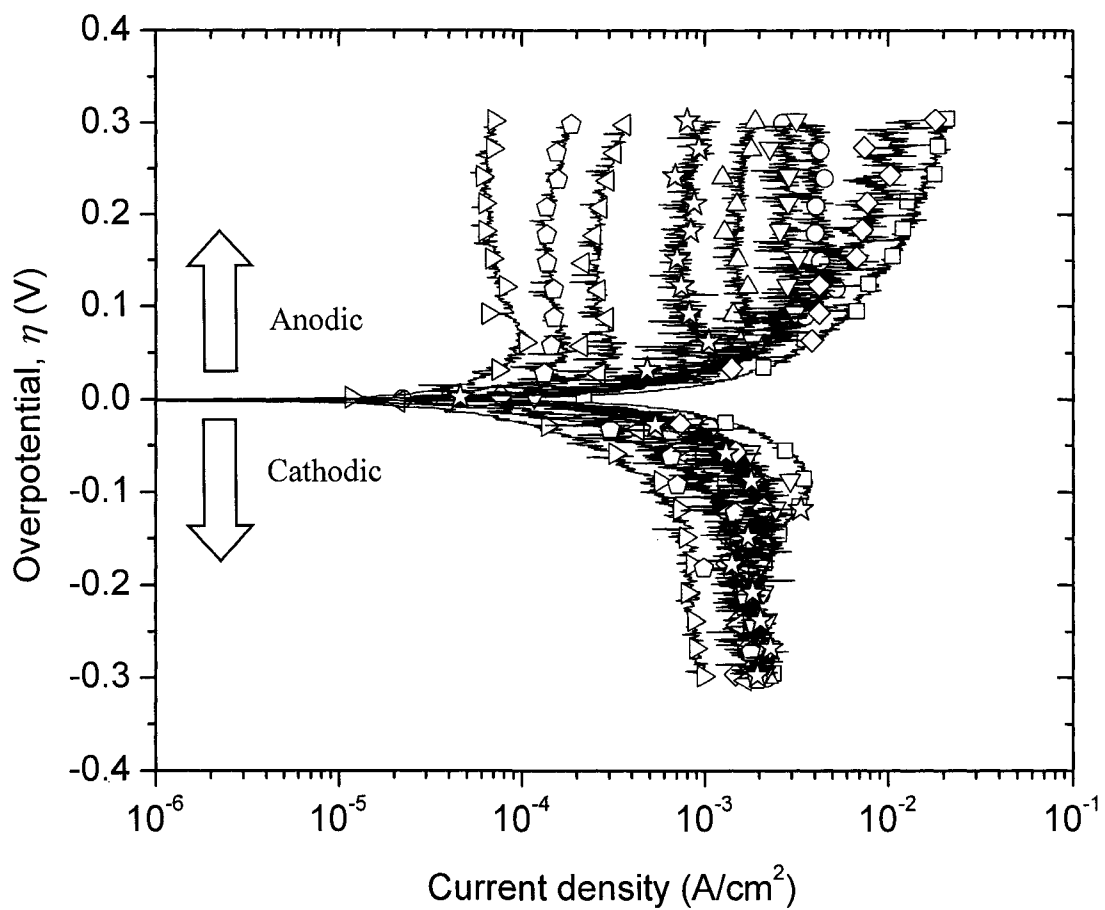


Figure 4.22. Tafel polarizations of electrodeposited copper film at pH 6 in varying concentration of hydroxylamine. 1M (\square), 0.75M (\diamond), 0.5M (\circ), 0.4M (∇), 0.3M (\triangle), 0.2M (\star), 0.1M (\triangleleft), 0.05M (\trianglerightarrow), and 0.01M (\triangleright).

The polarization parameters of β_a , β_c , R_p , E_{corr} , and i_{corr} for each curve are tabulated in Table 4.3. Note that the β_a and β_c data have a significant amount of errors, as much as ± 0.1 V/decade. These errors are due to very limited Tafel regions and the appearance of the Tafel region (± 0.05 to ± 0.3 V overpotential) created by the limiting current density. These errors also affect the calculations of i_{corr} values.

The electrochemical removal rates (EC RR in $\text{\AA}/\text{min}$) calculated from i_{corr} (based on 2 electron charge transfer) and normalized to the mean value are plotted in Figure 4.23. Also plotted in the figure are normalized actual copper removal rates from Figure 4.12. The results in Figure 4.23 show that copper removal rates determined from i_{corr} do not follow the trend of actual copper removal rates. This is likely due to the large amount of errors introduced into the i_{corr} calculation from the polarization curves in Figure 4.22.

Table 4.3. Electrochemical properties of the polarization curves in Figure 4.22.

Conc. (M)	β_a (V/decade)	β_c (V/decade)	R_p ($\Omega \cdot \text{cm}^2$)	E_{corr} (V vs SHE)	i_{corr} ($\mu\text{A}/\text{cm}^2$)
1	0.315 ± 0.006	-0.186 ± 0.014	1.89 ± 0.03	0.145	$2,985 \pm 377$
0.75	0.261 ± 0.009	-0.174 ± 0.028	3.20 ± 0.13	0.140	$1,573 \pm 318$
0.5	0.254 ± 0.033	-0.227 ± 0.086	3.39 ± 0.09	0.149	$1,708 \pm 1,222$
0.4	0.202 ± 0.045	-0.263 ± 0.055	3.70 ± 0.16	0.159	$1,491 \pm 784$
0.3	0.259 ± 0.080	-0.421 ± 0.073	4.07 ± 0.12	0.166	$1,901 \pm 1,315$
0.2	0.229 ± 0.057	-0.335 ± 0.034	5.78 ± 0.24	0.175	$1,137 \pm 505$
0.1	0.488 ± 0.073	-0.418 ± 0.028	10.59 ± 0.41	0.187	$1,026 \pm 206$
0.05	0.289 ± 0.098	-0.383 ± 0.016	16.50 ± 0.51	0.197	481 ± 267
0.01	0.137 ± 0.051	-0.422 ± 0.018	32.40 ± 0.82	0.197	153 ± 124

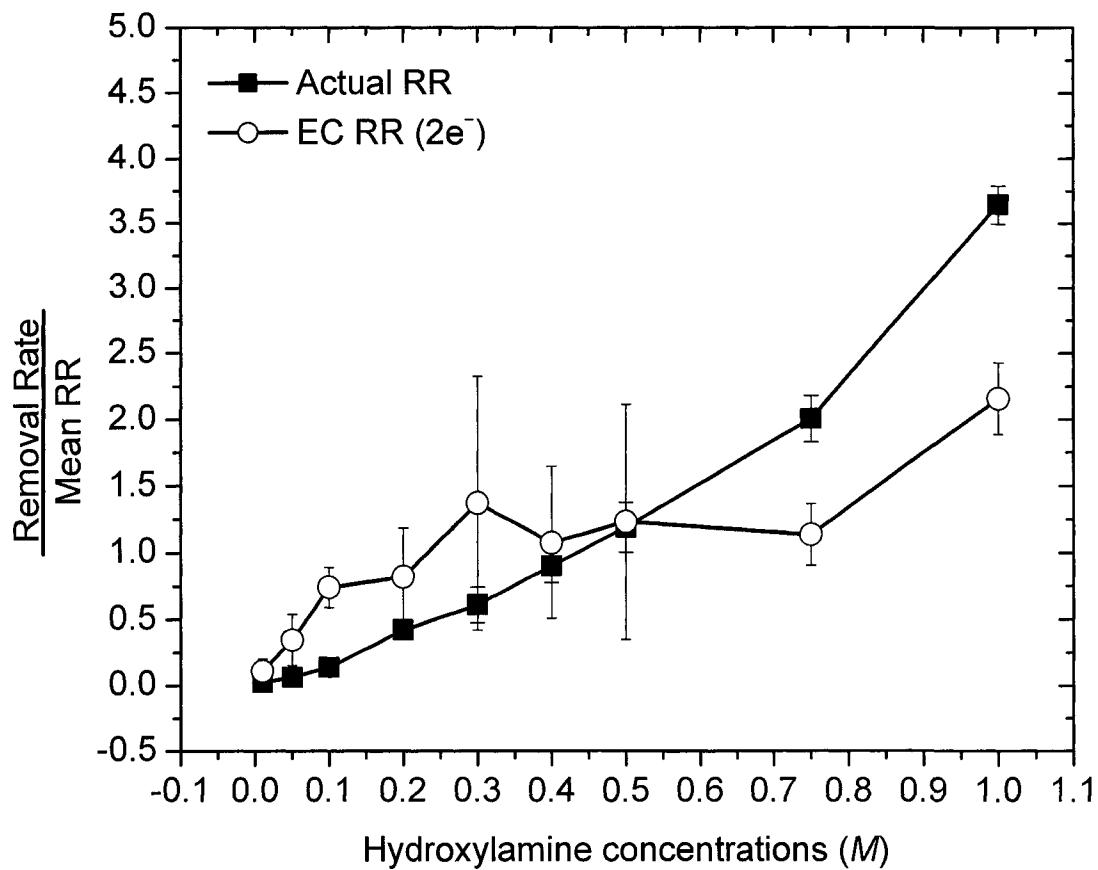


Figure 4.23. Copper removal rates normalized to their mean value with respect to hydroxylamine concentration at pH 6. The mean value for actual RR was 565.9 Å/min and the mean value for EC RR (2e⁻) was 306.5 Å/min.

Earlier discussions have proposed the reduction of hydroxylamine to ammonia as the coupled reaction to oxidation of copper. If the reduction of hydroxylamine to ammonia were true, a significant shift in the cathodic polarization curves with respect to hydroxylamine concentrations would be expected. Instead, the cathodic limiting current density only shifted from 3×10^{-3} to 1×10^{-3} A/cm² with decreasing hydroxylamine concentrations. The lack of dependence in cathodic polarization curves on hydroxylamine concentration is intriguing. This perhaps indicates that some intermediate species in small amounts evolved from hydroxylamine rather than hydroxylamine itself being reduced. The significant shifts in the anodic polarization curves with respect to hydroxylamine concentrations are likely due to the complexation of copper by hydroxylamine.

4.5.2. Electrochemical Analysis under Abrasion

4.5.2.1. E_{corr} versus Time

Corrosion potential (E_{corr}) of copper in 4% silica slurries containing 0.5M hydroxylamine was measured during and following abrasion with an IC1000 pad. The pH of the slurry was adjusted from alkaline to acidic using sulfuric acid. The copper sample was initially abraded in the hydroxylamine based slurry for 1 min to remove any native oxide films that may have formed during exposure to air. Once the contact between the pad and the copper sample was broken, abrasion was stopped and the monitoring of E_{corr} versus time began. After about 50 seconds, the contact between pad and sample was reestablished. After about 100 seconds of abrasion, the abrasion was stopped by breaking the contact between pad and sample. The results of the experiment are shown in Figure 4.24.

In weakly alkaline and neutral conditions (pH values 6 to 9) the E_{corr} of copper decreased upon abrasion. This may be expected due to the removal of CuO or Cu₂O layer on the copper surface. However, at pH values below 6, the E_{corr} of copper increased slightly upon abrasion. Since soluble copper species such as Cu²⁺, Cu(NH₂OH)₂²⁺, and Cu(NH₂OH)_x²⁺ are thermodynamically stable at pH values below 6, the increase in E_{corr} is intriguing. E_{corr} is a mixed potential; therefore, its value is dependent on the equilibrium potential of the oxidation and reduction reactions as well as the slope of the polarization curves. The increase of E_{corr} can be due to an increasing slope of the anodic (Cu → Cu(NH₂OH)_x²⁺) polarization curve or due to the decreasing slope of the cathodic polarization curve.

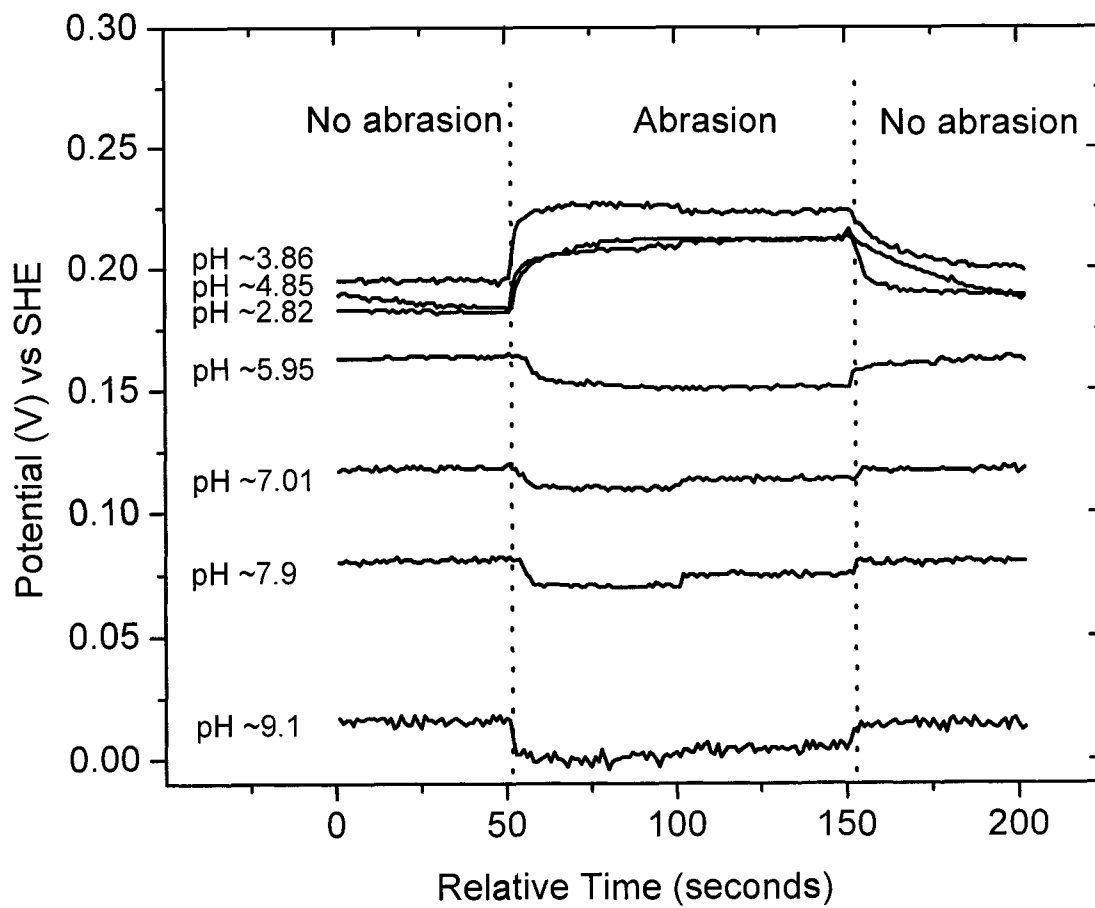


Figure 4.24. E_{corr} vs time of copper film that was abraded using 0.5M hydroxylamine based slurries. Sulfuric acid was used to adjust the pH.

Since abrasion created a fresh copper surface, it is more likely that the cathodic polarization curve shifts toward higher current density values, *i.e.*, cathodic reaction takes place more efficiently.

4.5.2.2. Tafel and Corrosion Rate Analysis under Abrasion

The polarization curves of copper under abrasion at different pH values are plotted as overpotential (η) versus $\log(i)$ shown in Figure 4.25 and Figure 4.26. The polarization curves in Figure 4.25 show that both cathodic and anodic curves shift in the direction of increasing current density with decreasing pH values from 8.47 to 6.06. This results in higher corrosion current density (i_{corr}) and likely a higher copper removal rate. The polarization curves in Figure 4.26 show that cathodic polarization curves shift in the direction of decreasing current density with decreasing pH values below 6.06, while the anodic polarization curves show no change with respect to decreasing pH values. The polarization curves under abrasion are very similar to the polarization curves without abrasion for most of the pH values except in acidic conditions.

The effects of abrasion on polarization curves at pH values of 8 and 6 are shown in Figure 4.27 and Figure 4.28. The curves show subtle shifts toward higher current densities and more negative potentials during abrasion. The shift in potentials of the polarization curves at pH 8 and 6 coincide with the decrease in E_{corr} vs time (Figure 4.24) at similar pH values upon abrasion. The increase in current density of the polarization curves during abrasion indicates that the passive layer formed on the copper surface was removed.

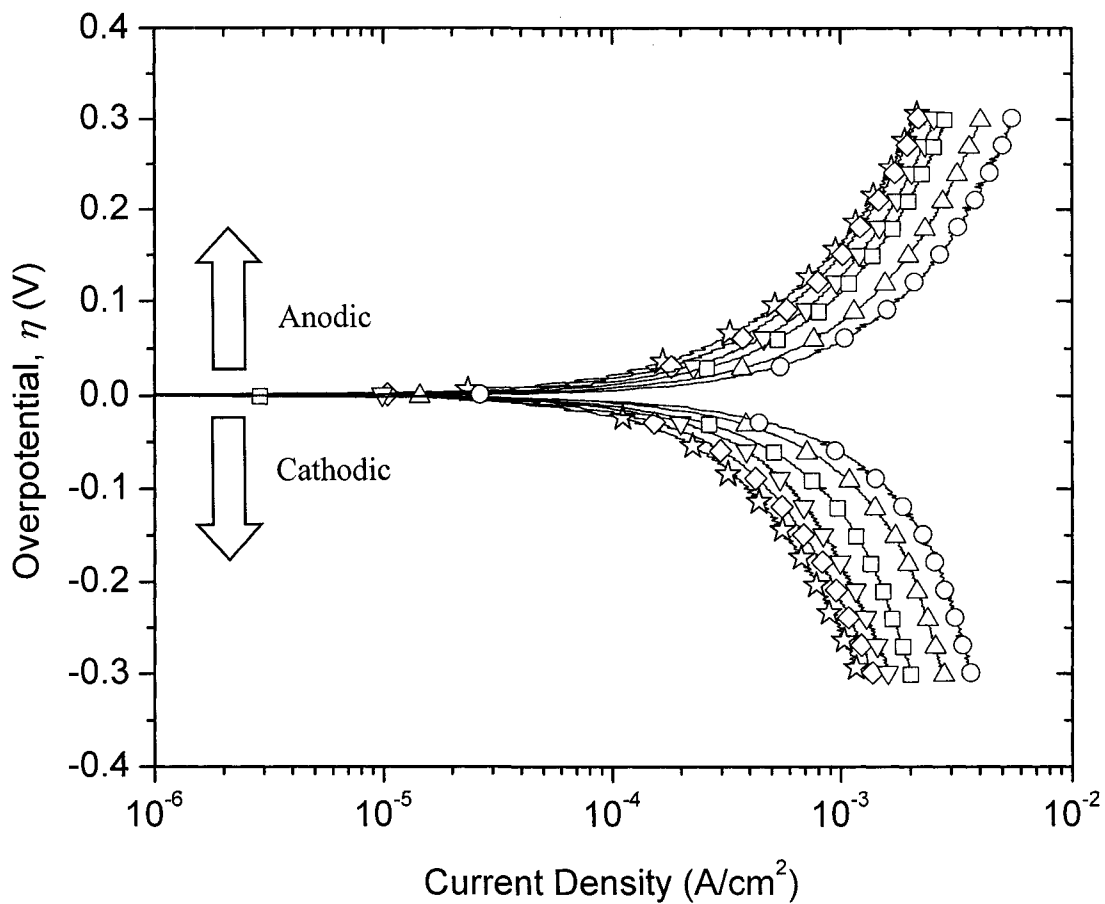


Figure 4.25. Potentiodynamic polarizations of electrodeposited copper film in 0.5M hydroxylamine base slurry at different pH values under abrasion. pH 8.47 (☆), pH 7.99 (◇), pH 7.51 (▽), pH 7.0 (□), pH 6.5 (△), and pH 6.06 (○).

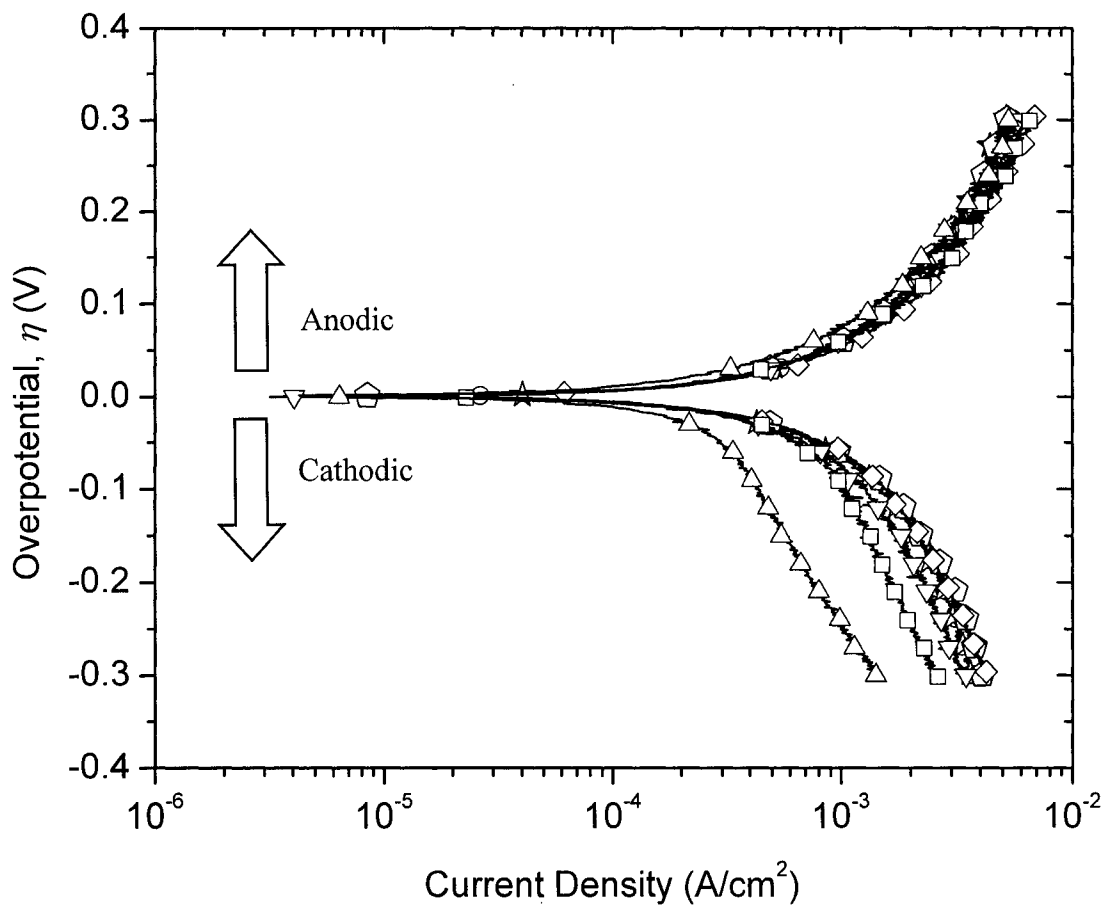


Figure 4.26. Potentiodynamic polarizations of electrodeposited copper film in 0.5M hydroxylamine base slurry at different pH values under abrasion. pH 3.46 (\triangle), pH 4.01 (\square), pH 4.58 (∇), pH 4.99 (\diamond), pH 5.55 (\diamond), pH 5.78 (\star), and pH 6.06 (\circ).

If the magnitude of the increasing current density is small, this may represent the removal of a thin (poorly formed) passive layer. For a more protective passive layer, a large increase in the magnitude would be expected.

The polarization curves at pH 4 in Figure 4.29 show a significant shift towards increasing current density upon abrasion of the copper sample. The cathodic portion of the polarization curve shows about a decade increase in current density upon abrasion, while the anodic portion shows very little changes. The shift of the cathodic polarization curve and changes in cathodic Tafel slope upon abrasion may be the reason for the increase in E_{corr} values around pH 4. The changes in the cathodic polarization curve upon abrasion are likely due to a shift in the exchange current density (i_0). This may be caused by a freshly abraded copper surface that allows the reduction reaction to occur more efficiently.

From each polarization curve in Figure 4.25 and Figure 4.26, the values of Tafel slope (β_a and β_c), polarization resistance (R_p), corrosion potential (E_{corr}), and corrosion current density (i_{corr}) were determined and tabulated in Table 4.4. Electrochemical removal rates (EC RR) based on 2 electron charge-transfer were calculated. The EC RR while the copper was being abraded along with EC RR of copper without abrasion are plotted in Figure 4.30. The EC RR of copper under abrasion does not show a sharp maximum in removal rate at pH 6. This was unexpected considering that overall copper removal rates with respect to pH showed a clear maximum at around a pH value of 6.

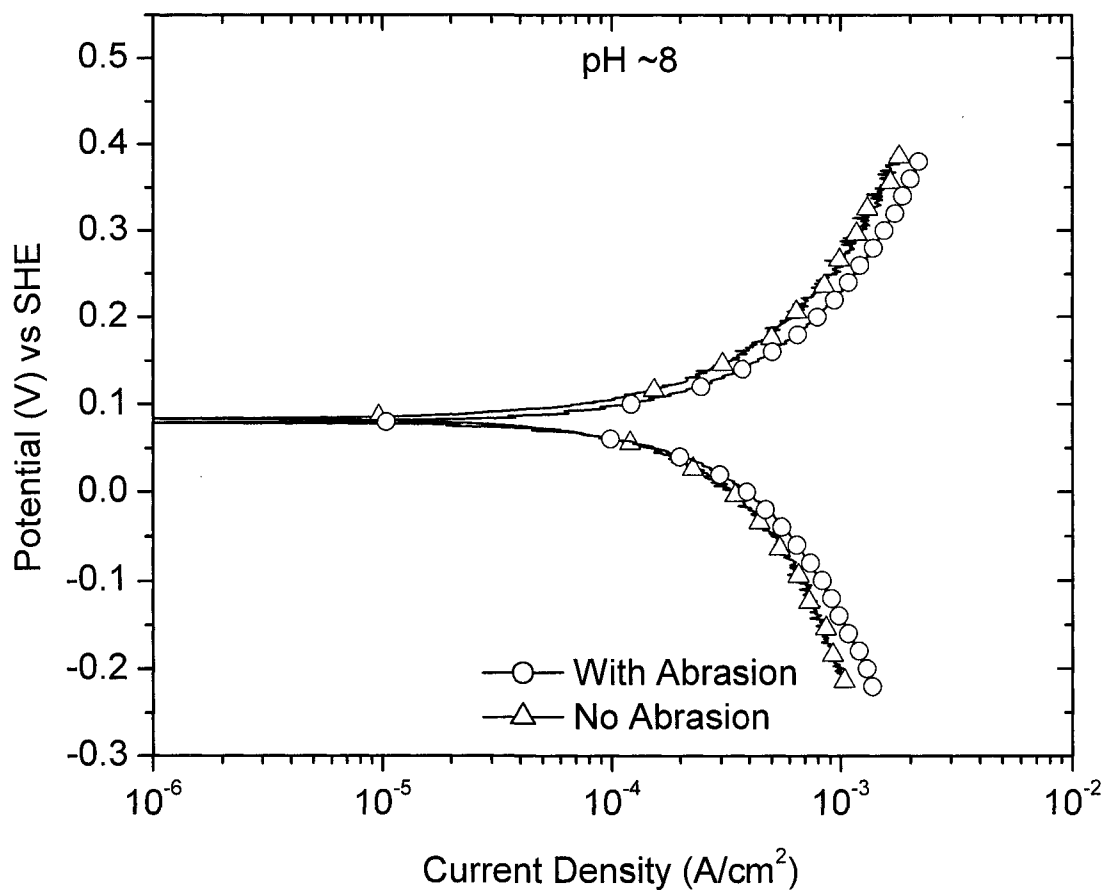


Figure 4.27. Polarizations curves of copper in 0.5M hydroxylamine based slurry with and without abrasion at pH values around 8.

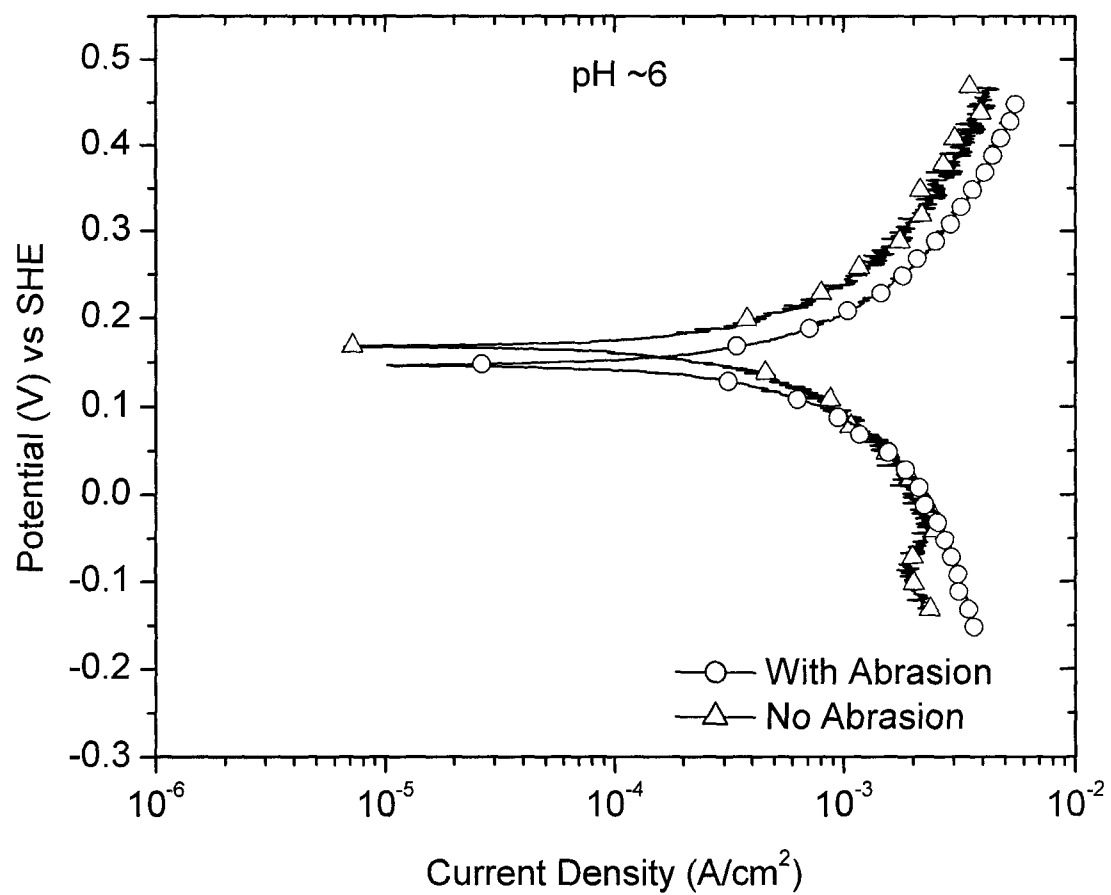


Figure 4.28. Polarizations curves of copper in 0.5M hydroxylamine based slurry with and without abrasion at pH values around 6.

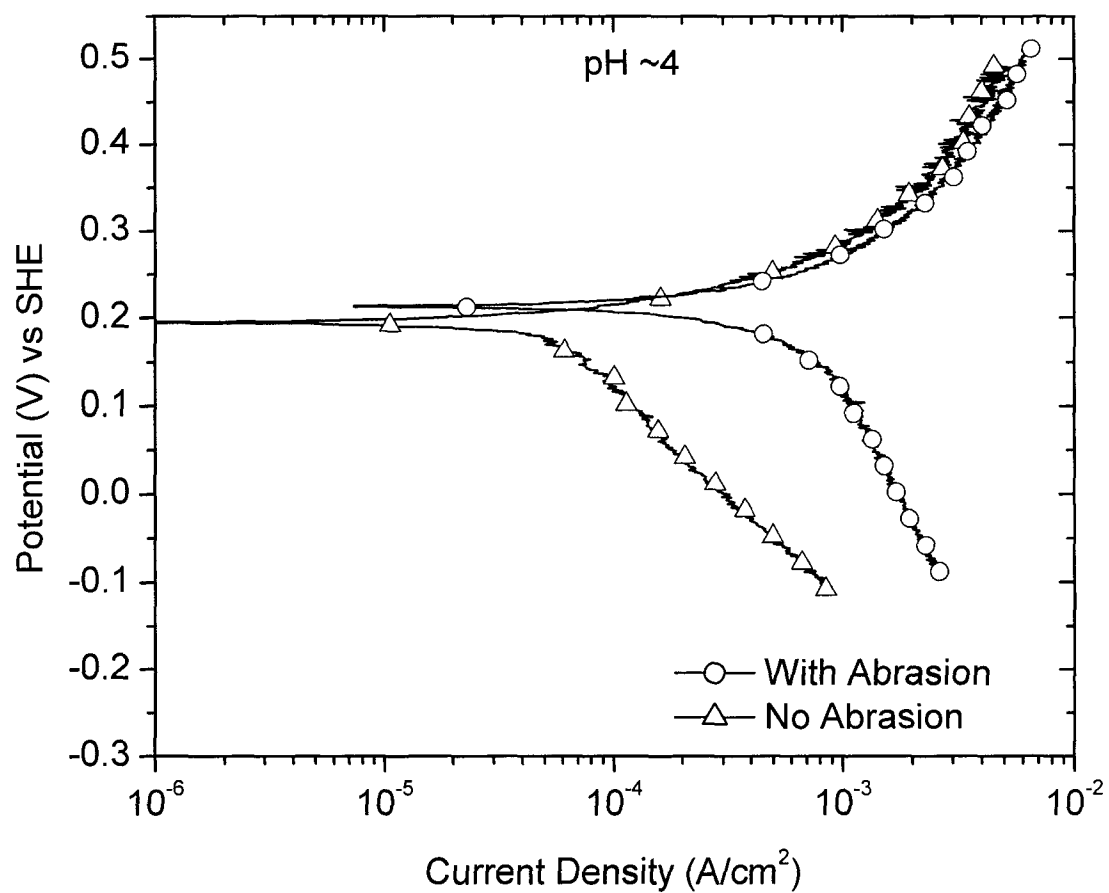


Figure 4.29. Polarizations curves of copper in 0.5M hydroxylamine based slurry with and without abrasion at pH values around 4.

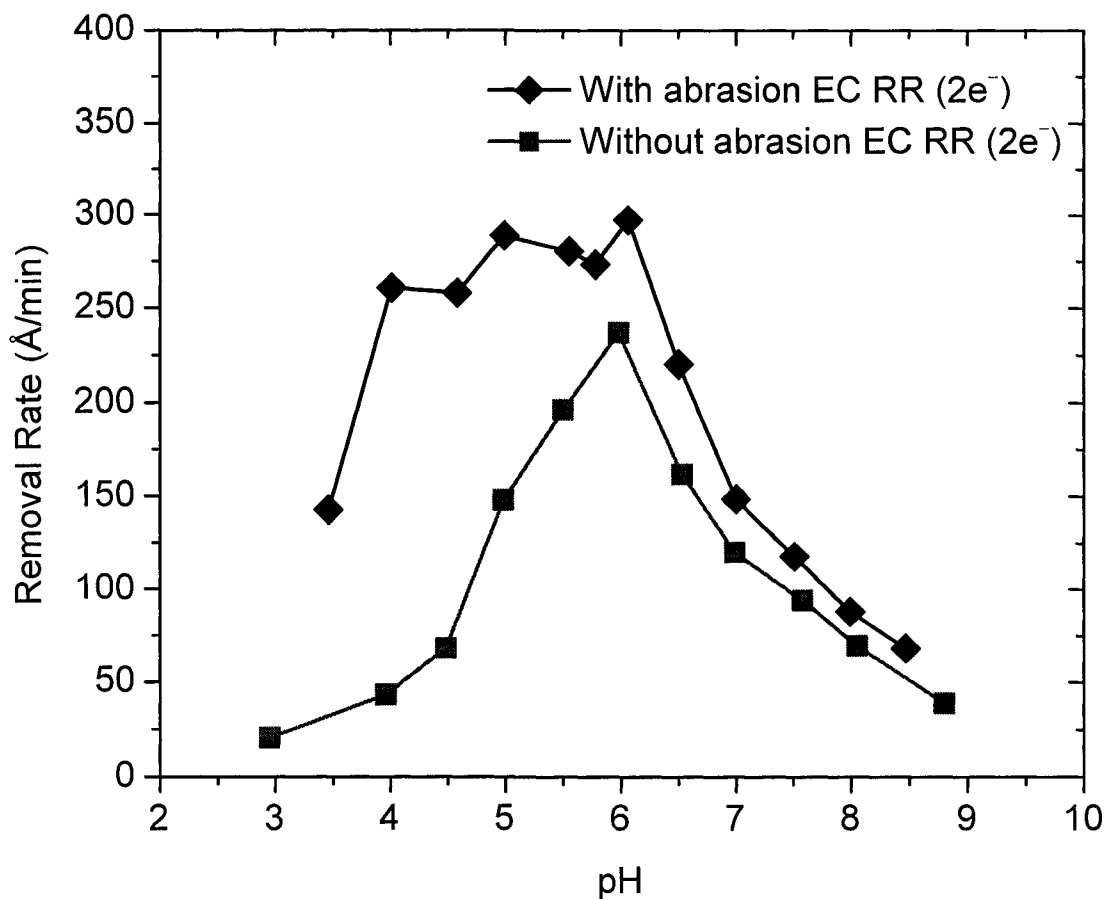


Figure 4.30. Electrochemical removal rate ($\text{\AA}/\text{min}$) of copper in $0.5M$ hydroxylamine based chemistry as function of pH. The EC RR of copper under abrasion (\blacklozenge) and copper without any abrasion (\blacksquare).

Table 4.4. Electrochemical properties of the polarization curves in Figure 4.25 and Figure 4.26.

pH	β_a (V/decade)	β_c (V/decade)	R_p ($\Omega \cdot \text{cm}^2$)	E_{corr} (V vs SHE)	i_{corr} ($\mu\text{A}/\text{cm}^2$)
8.47	0.285 ± 0.004	-0.342 ± 0.004	105.3 ± 1.8	0.040	308.2 ± 0.5
7.99	0.305 ± 0.004	-0.364 ± 0.005	50.8 ± 1.1	0.079	396.8 ± 0.8
7.51	0.312 ± 0.004	-0.391 ± 0.005	50.2 ± 0.5	0.104	531.7 ± 4.0
7.0	0.323 ± 0.005	-0.396 ± 0.007	25.0 ± 0.3	0.121	671.5 ± 7.2
6.5	0.328 ± 0.005	-0.408 ± 0.008	15.1 ± 0.2	0.136	994.3 ± 11.8
6.06	0.327 ± 0.005	-0.410 ± 0.008	16.5 ± 0.2	0.147	$1,343.0 \pm 15.7$
5.78	0.330 ± 0.005	-0.389 ± 0.007	10.3 ± 0.1	0.161	$1,234.0 \pm 13.9$
5.55	0.329 ± 0.005	-0.378 ± 0.006	11.1 ± 0.1	0.181	$1,267.0 \pm 13.7$
4.99	0.309 ± 0.004	-0.382 ± 0.005	18.1 ± 0.2	0.204	$1,304.8 \pm 10.5$
4.58	0.306 ± 0.004	-0.392 ± 0.005	12.7 ± 0.3	0.217	$1,164.8 \pm 5.9$
4.01	0.294 ± 0.004	-0.463 ± 0.004	16.9 ± 0.3	0.213	$1,176.7 \pm 4.3$
3.46	0.274 ± 0.004	-0.385 ± 0.002	32.7 ± 0.9	0.208	644.6 ± 2.5

It is interesting to note that abrasion increased the removal rate mostly in the acidic region. If passive layer removal is the dominant mechanism for CMP then one would expect to see a significant effect of abrasion at alkaline pH values. It appears that the abrasion creates a fresh copper surface on which reduction reaction can occur in a more facile manner.

4.5.3. Voltammetry Analysis

Linear sweep voltammetry was used in an effort to identify various oxidizable and reducible species in the hydroxylamine chemistry. Most of the voltammetry experiments were performed using a copper film as the working electrode. The first set of experiments was carried out in a phosphate-sulfate buffer solution at pH values of 8, 6, and 3. These experiments were conducted to establish the background voltammograms in the hydroxylamine based chemical systems. The results from the phosphate-sulfate buffer system are shown in Figure 4.31. All of the voltammograms were obtained by scanning from -1.25V to +1.0V (vs SHE) at a scan rate of 50 mV/s. In the figure, negative current densities represent reduction reactions and positive current densities represent oxidation reactions.

In Figure 4.31, three regions of interest are marked as 'a', 'b', and 'c'. In region 'a', the voltammograms for all pH values show the cathodic current density plateau of about 1.5×10^{-4} A/cm². At more cathodic potentials beyond region 'a', the current density seems to increase in an almost exponential fashion. The potential at which the cathodic current density increases in an almost exponential fashion is different for each pH value; it is around -0.6V for pH 3, -0.76V for pH 6, and -0.92V for pH 8. The shift in potential is 0.053 V/pH. Region 'b' is where the transition from cathodic to anodic current density occurs. A re-scaled plot of region 'b' is shown as an inset in Figure 4.31. From region 'a' to 'b', the decreasing cathodic current density shows a transition to anodic current density. This transition region has a potential shift with solution pH. This is similar to the potential shift observed at cathodic potentials more negative than -0.6V.

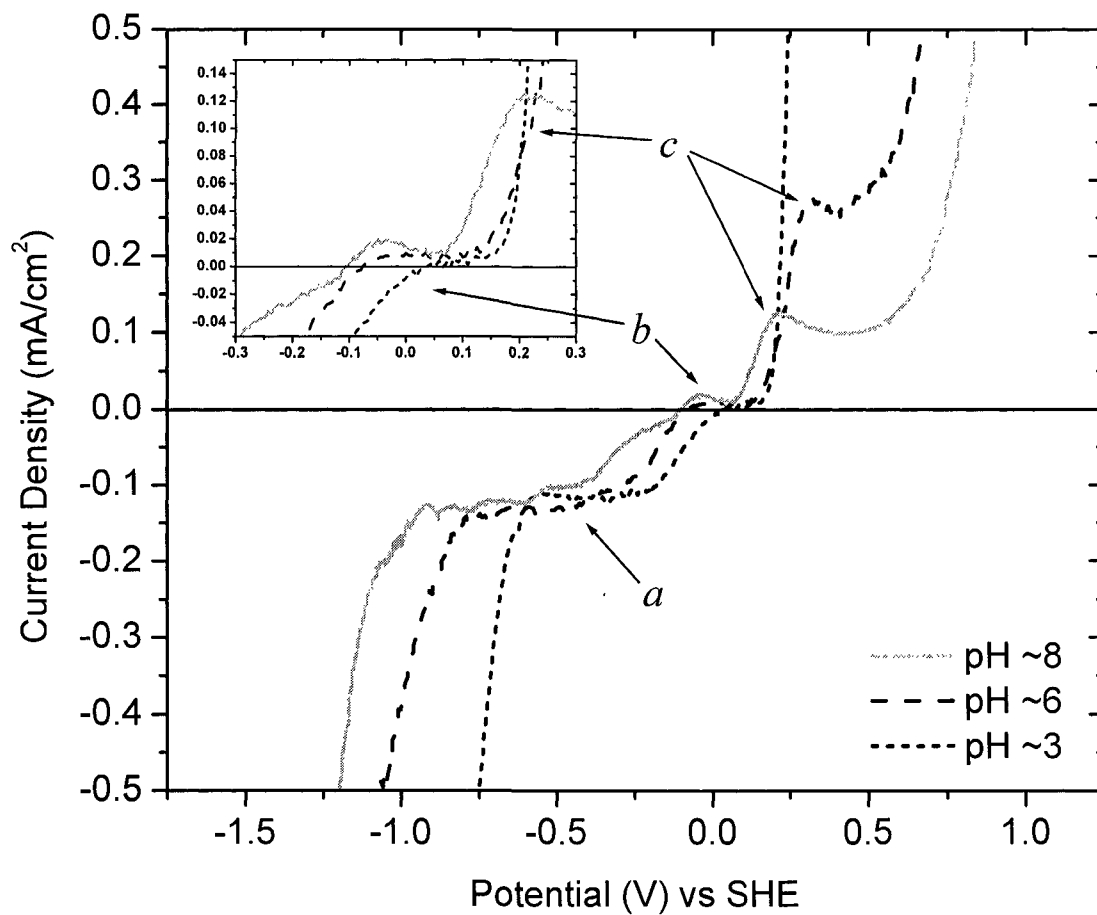
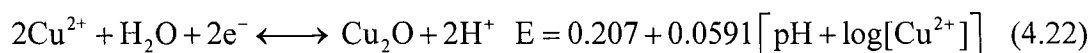
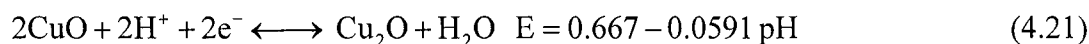
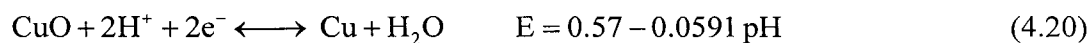
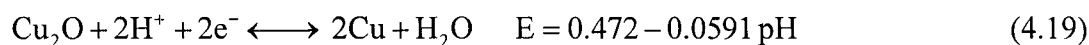


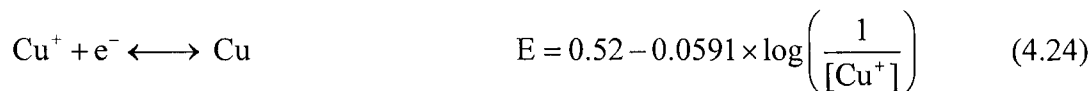
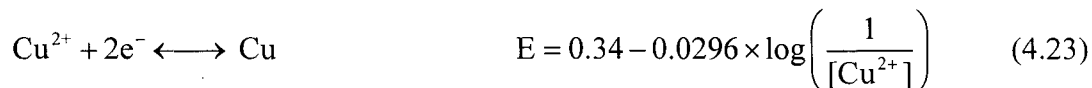
Figure 4.31. Voltammograms of copper film in phosphate-sulfate buffer solution at pH values of 8, 6, and 3. Scan rate of 50 mV/s from -1.5V to +1V and rotation speed of 50 rpm.

In region 'b', from the inset of Figure 4.31, a small anodic peak current density may be seen to occur at pH 8. The magnitude of this anodic current density decreases with decreasing pH. In region 'c', the developed anodic peak current densities are also a function of solution pH. At pH 8, the peak current density is around 0.12 mA/cm². With decreasing pH values from 8 to 6, the peak current density increases to 0.27 mA/cm². At pH 3, the anodic current density increases exponentially without the formation of a peak current density.

The cathodic current density plateau at region 'a' is likely due the reduction of O₂ → H₂O. A typical value for the limiting current density for oxygen reduction in aerated solution is 1×10⁻⁴ A/cm² and the measured cathodic current density plateaus have an approximate value of 1.5×10⁻⁴ A/cm². The rapid increase in cathodic current density at more negative potential is likely due to a hydrogen reduction reaction. The 0.053 V/pH shift in potential is comparable to the theoretical 0.059 V/pH dependence of a hydrogen reduction reaction.

The anodic portion of Figure 4.31 shows dissolution behavior of copper in aqueous solutions. Depending on solution pH, formation of copper based oxides may occur. The E-pH relationship of copper and its oxides are shown in the following reactions.





The equilibrium potentials for Reactions (4.19) through (4.24) at pH values of 8, 6, and 3 for two different dissolved copper activities are tabulated in the following table.

Table 4.5. Calculated equilibrium potentials (in volts vs SHE) for Reactions (4.19) through (4.24) at different pH values and copper ion activities.

pH	Reaction (4.19)	Reaction (4.20)	Reaction (4.21)	[Cu ^{x+}]	Reaction (4.22)	Reaction (4.23)	Reaction (4.24)
8	0.0	0.097	0.194	10 ⁻⁴	0.443	0.222	0.284
				10 ⁻⁶	0.325	0.162	0.165
6	0.117	0.215	0.312	10 ⁻⁴	0.325	0.222	0.284
				10 ⁻⁶	0.207	0.162	0.165
3	0.295	0.393	0.49	10 ⁻⁴	0.148	0.222	0.284
				10 ⁻⁶	0.030	0.162	0.165

From Figure 4.31 at pH 8, the initial anodic peak occurs at -0.05V (SHE) and the second anodic peak current density occurs at +0.21V (SHE). From Table 4.5, the two potentials that most closely predict the observed peak current densities at pH 8 are from Reactions (4.19) and (4.21), which show the transition of Cu to Cu₂O then Cu₂O to CuO. For the pH 6 voltammogram in Figure 4.31, the anodic portion shows an undefined current density peak in the range of -0.03V to +0.116V (SHE) and a second peak current density at +0.311V (SHE). These current density peaks also show the transition of Cu to Cu₂O then Cu₂O to CuO. The voltammogram at pH 3 does not show any clear evidence of current density peaks. There is simply a transition region from the OCP to +0.169V

(SHE), then the current density increases exponentially at potentials greater than +0.169V. From Table 4.5, the exponential increase in current density after +0.169V (SHE) at pH 3 is best represented by Reactions (4.23) and (4.24), which are the dissolution of copper metal to copper ions.

In the second set of experiments, the effects of hydroxylamine on copper voltammogram (Figure 4.31) were investigated. In Figure 4.32, the effect of 0.01M hydroxylamine at pH 8 on the copper voltammogram is shown. It is of interest to note that by having 0.01M hydroxylamine in the solution, the magnitude of the cathodic current density plateau 'a' increased from 0.1 to 0.25 mA/cm². The potential where the onset of hydrogen reduction occurs also shifts from -1.05V to -0.68V (SHE). In region 'b', the transition of cathodic to anodic current densities occurs. In this region, values of open circuit potential (OCP) and polarization resistance (R_p , $\pm 0.01V$ from OCP) were determined. The OCP of copper in a solution without hydroxylamine was around -0.107V (SHE) and with hydroxylamine the OCP shifted to -0.015V (SHE), a difference of 0.092V. The R_p calculated near the OCP for the voltammogram without hydroxylamine was 2,096 $\Omega \cdot \text{cm}^2$ and with hydroxylamine was 510 $\Omega \cdot \text{cm}^2$. In region 'c', both voltammograms in Figure 4.32 show an anodic peak current density at +0.21V (SHE) except that the curve with solution containing hydroxylamine is a bit higher in current density than the solution without hydroxylamine.

The effects of 0.01M hydroxylamine at pH 6 are shown in Figure 4.33. In the cathodic portion of the voltammogram, particularly region 'a', a strong cathodic peak current density occurs around -0.5V (SHE).

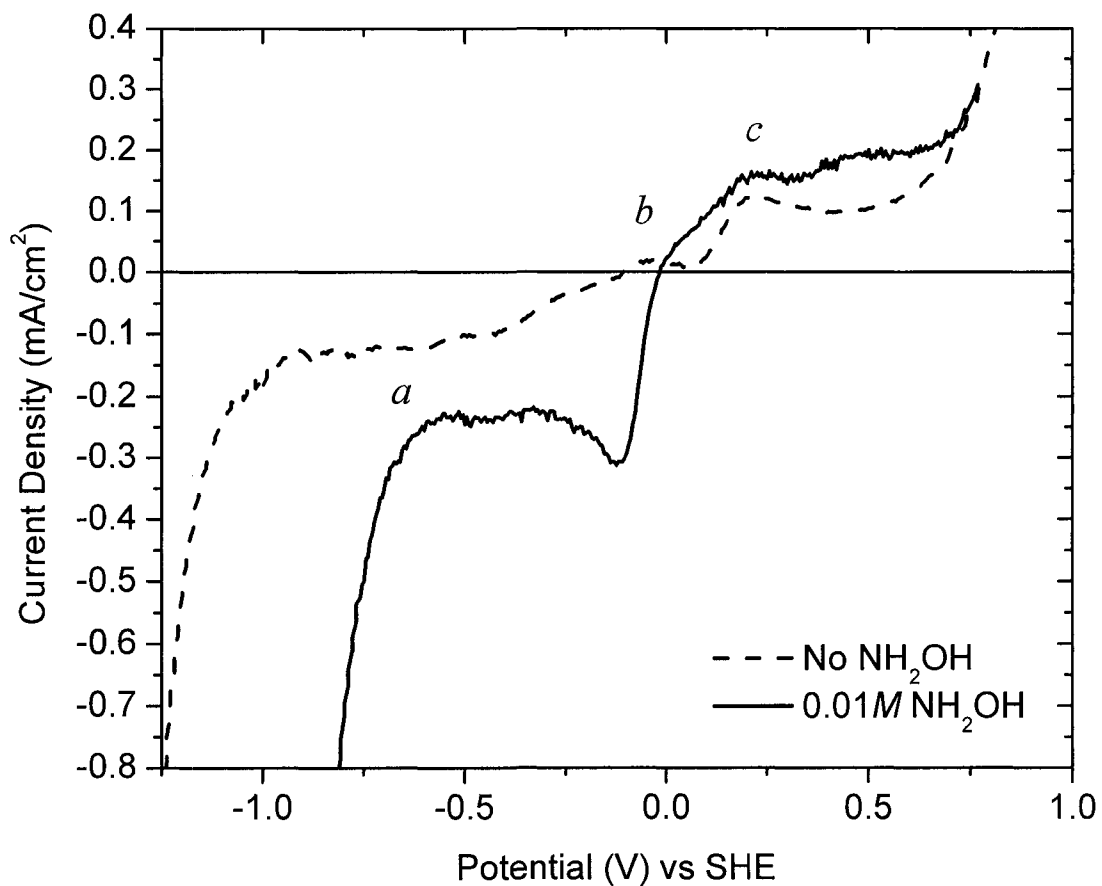


Figure 4.32. Voltammograms of copper film in pH 8 solutions with and without 0.01M hydroxylamine. [Scan rate of 50 mV/s from -1.5V to +1V and rotation speed of 50 rpm.]

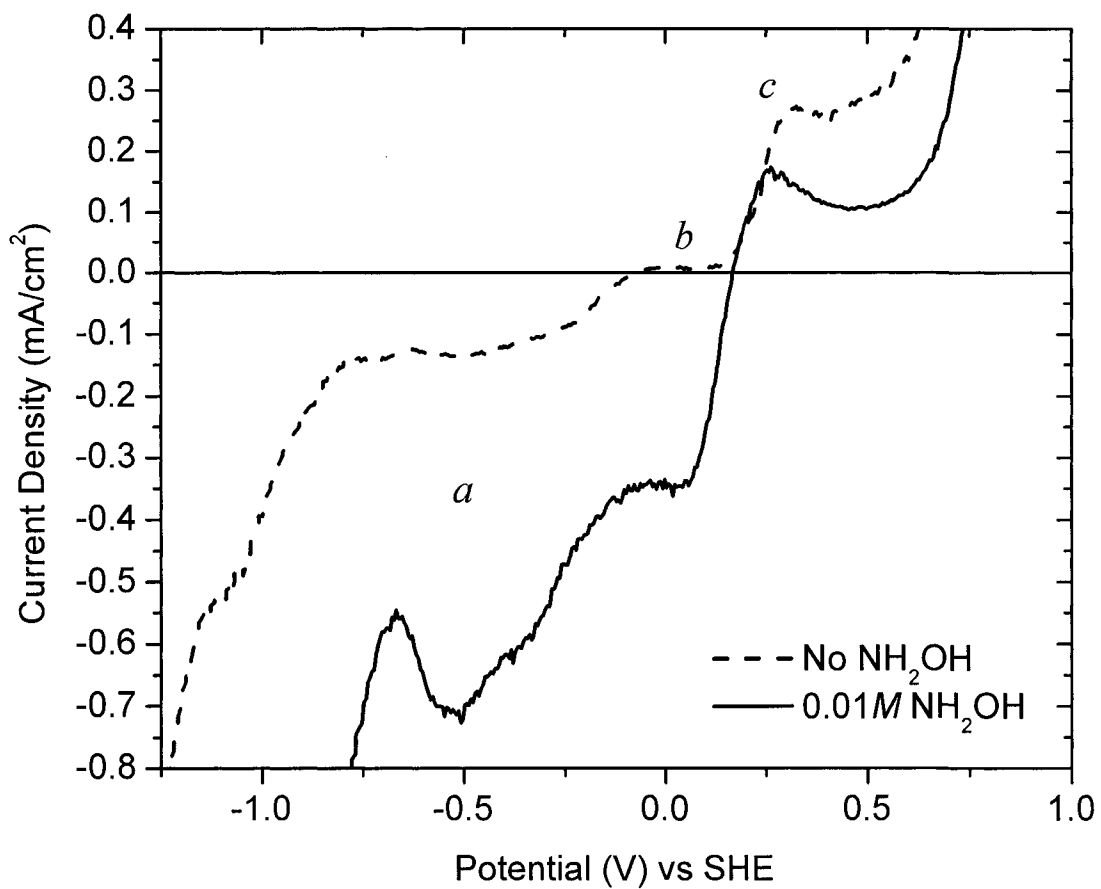


Figure 4.33. Voltammograms of copper film in pH 6 solutions with and without 0.01M hydroxylamine. [Scan rate of 50 mV/s from -1.5V to +1V and rotation speed of 50 rpm.]

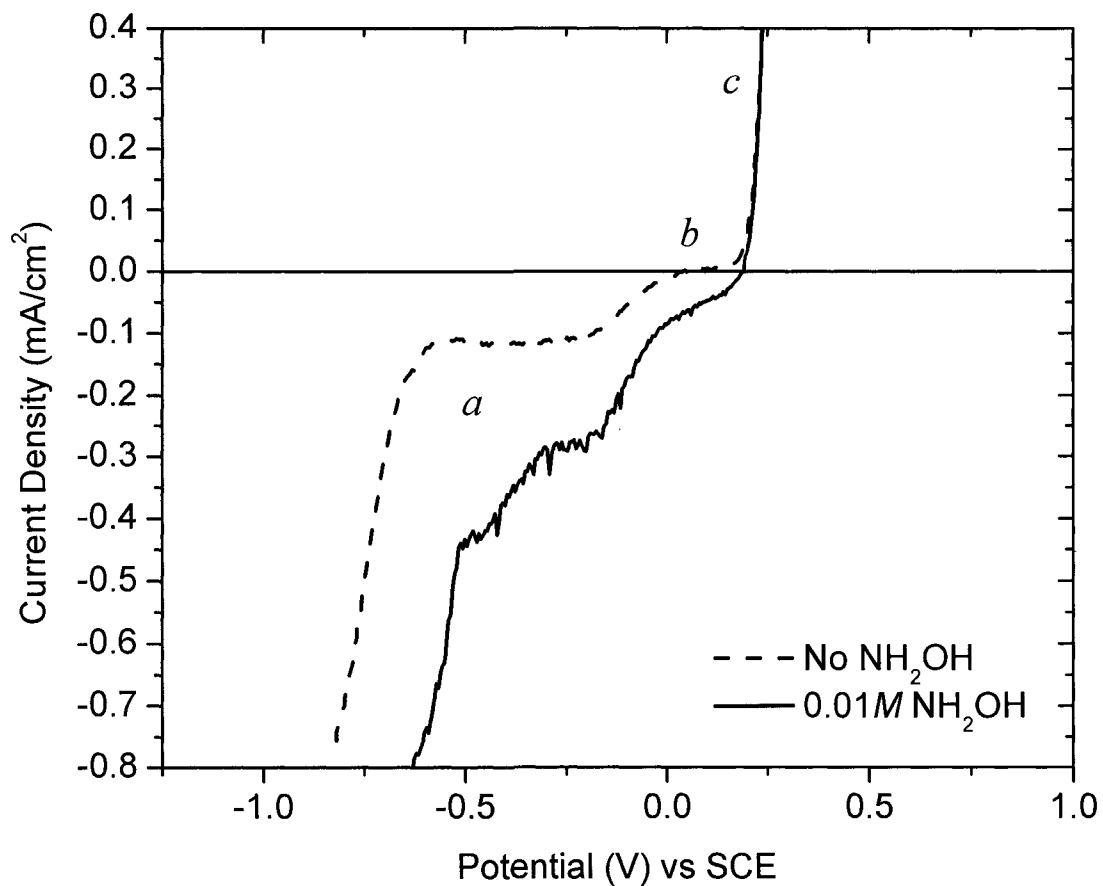


Figure 4.34. Voltammograms of copper film in pH 3 solutions with and without 0.01M hydroxylamine. [Scan rate of 50 mV/s from -1.5V to +1V and rotation speed of 50 rpm.]

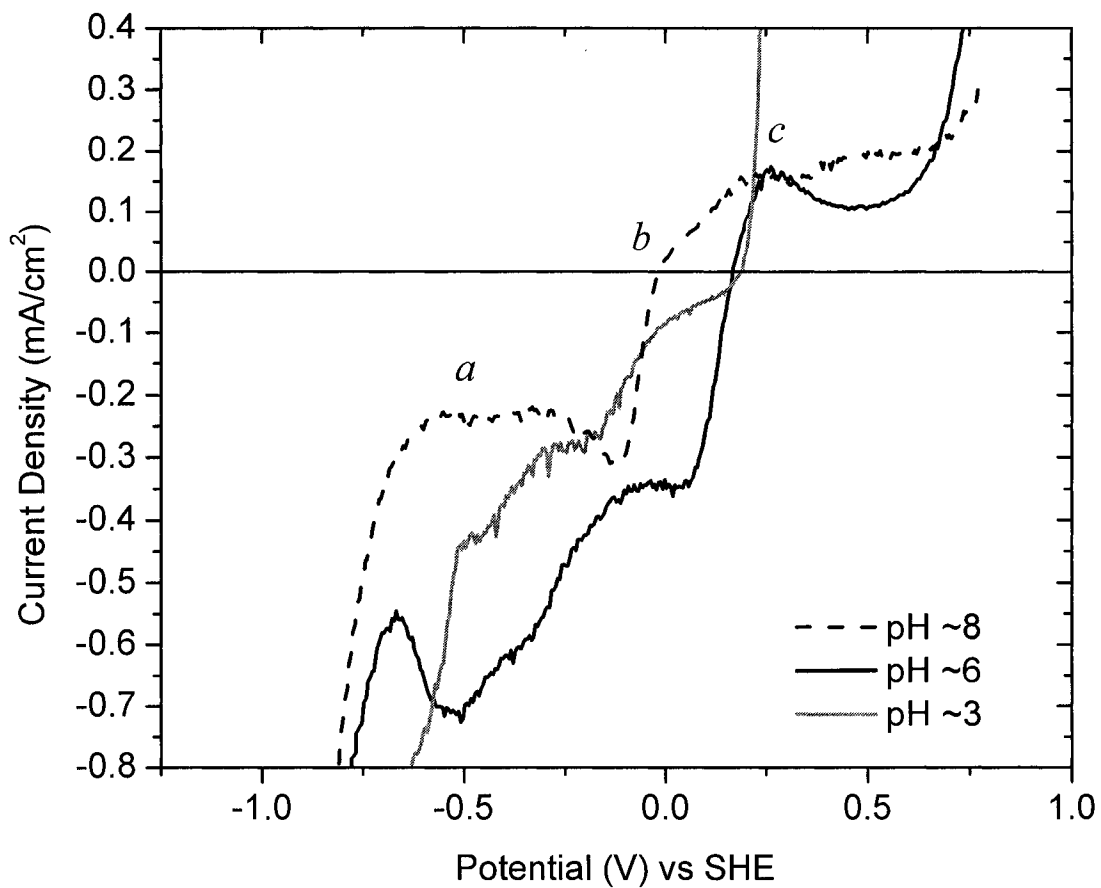


Figure 4.35. Voltammograms of copper film in 0.01M hydroxylamine based chemistries at pH values of 8, 6, and 3. [Scan rate of 50 mV/s from -1.5V to +1V and rotation speed of 50 rpm.]

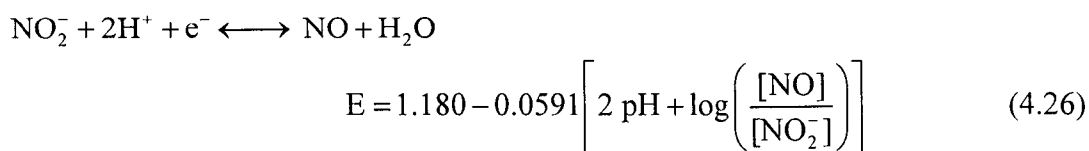
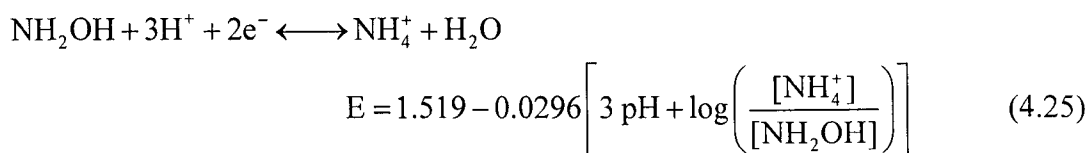
The magnitude of that cathodic peak is approximately 0.7 mA/cm^2 . The potential, at which reduction of hydrogen occurs, also shifts from -0.86V to -0.66V (SHE). With the addition of hydroxylamine at pH 6, the OCP shifts from -0.076V to $+0.165\text{V}$ (SHE), a difference of 0.241V . In region 'b', the R_p values determined from the two voltammograms are shown in Table 4.6. In region 'c', the anodic peak current density of copper in hydroxylamine containing solution is unexpectedly lower than the peak current density without hydroxylamine.

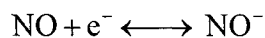
The voltammogram obtained in the 0.01 M hydroxylamine solution maintained at pH 3 is shown in Figure 4.34. As discussed in the background section, at this pH all the added hydroxylamine would be in the protonated form. Compared to the solution without hydroxylamine, the presence of hydroxylamine increases the cathodic current density, as was observed for solutions at pH 8 and 6. In region 'a', the shift in the potential for the onset of hydrogen reduction also behaves in the same manner as the potential shift for pH 8 and 6. In region 'b', the OCP shifts from 0.04V to 0.19V (SHE) with the addition of hydroxylamine, a difference of 0.15V . The R_p values determined from the two voltammograms are shown in Table 4.6. In the anodic portion of the voltammograms, region 'c', both curves show the same current-potential response. The anodic current densities from both voltammograms start to increase in an exponential fashion at potentials more oxidizing than $+0.19\text{V}$ (SHE). This is due to the dissolution of copper to copper ions.

Table 4.6. Calculated R_p and OCP values from the voltammograms of copper in solutions with pH values of 8, 6, and 3.

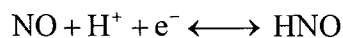
pH	No Hydroxylamine		0.01 M Hydroxylamine	
	R_p ($\Omega \cdot \text{cm}^2$)	OCP (V vs SHE)	R_p ($\Omega \cdot \text{cm}^2$)	OCP (V vs SHE)
8	2096 ± 231	-0.107	510 ± 33	-0.015
6	3294 ± 196	-0.076	298 ± 10	+0.165
3	8830 ± 670	+0.040	376 ± 45	+0.190

For comparison purposes, the voltammograms of copper in 0.01M hydroxylamine based chemistry at pH values of 8, 6, and 3 are plotted together in Figure 4.35. In region 'a' at -0.5V (SHE), there are noticeable cathodic peak current densities. This is very evident for pH 6 solution, and very subtle for pH 8 solution. For pH 3, the peak was not resolved due to the onset of hydrogen reduction. The magnitude of a cathodic peak at -0.5V (SHE) varied with pH. The highest peak with a current density of $\sim 0.7 \text{ mA/cm}^2$ occurred at pH 6. The cathodic peak current densities at -0.5V (SHE) for pH values of 8 and 3 were 0.23 and 0.45 mA/cm^2 , respectively. Several possible reduction reactions could explain the cathodic peak at -0.5V (SHE). These reactions and their corresponding Nernst equations are shown below.





$$E = -0.514 - 0.0591 \times \log \left(\frac{[\text{NO}^-]}{[\text{NO}]} \right) \quad (4.27)$$



$$E = -0.236 - 0.0591 \left[\text{pH} + \log \left(\frac{[\text{HNO}]}{[\text{NO}]} \right) \right] \quad (4.28)$$

The E^0 values for Reactions (4.25) and (4.26) are greater than 1V. Hence, the cathodic peak at -0.5V is not likely due to the reduction of either NH_2OH or NO_2^- . However, the E^0 values for Reactions (4.27) and (4.28), which involve the reduction of NO, are in the proximity of -0.5V. The equilibrium potentials for Reactions (4.27) and (4.28) at different pH and ion activity values are shown in Table 4.7.

Table 4.7. Calculated equilibrium potentials of reactions (4.27) and (4.28) in volts (vs SHE) at the corresponding pH values and ion activity ratios.

pH	Reaction (4.27)			Reaction (4.28)		
	$\left(\frac{[\text{NO}^-]}{[\text{NO}]} \right) =$			$\left(\frac{[\text{HNO}]}{[\text{NO}]} \right) =$		
	10^{-3}	1	10^{+3}	10^{-3}	1	10^{+3}
8	-0.337	-0.514	-0.691	-0.532	-0.709	-0.886
6	-0.337	-0.514	-0.691	-0.413	-0.591	-0.768
3	-0.337	-0.514	-0.691	-0.236	-0.413	-0.591

For example, in reaction (4.27) if $[\text{NO}^-] = 10^{-6}$ and $[\text{NO}] = 10^{-6}$ then the $\left(\frac{[\text{NO}^-]}{[\text{NO}]} \right)$ ratio becomes 1. If $[\text{NO}]$ is increased to 10^{-3} then the ratio would change to 10^{-3} . From Table

4.7, it is of interest to note that the reduction potentials of NO to NO⁻ are independent of pH. From Figure 4.35, the cathodic peak at -0.5V is also independent of pH. It is likely that the cathodic peak at -0.5V is due to the reduction of NO to NO⁻.

From the E^0 value of Reaction (4.26), it was determined that NO₂⁻ is not a likely reduction reaction at -0.5V. However, the discussion on the decomposition of hydroxylamine in the background section mentioned that a typical decomposition product of hydroxylamine is NO₂⁻. To further investigate the role of NO₂⁻, voltammetry experiments were carried out on copper in the absence and presence of KNO₂ in solution. Also the interaction of hydroxylamine with excess NO₂⁻ was investigated. The voltammograms from the investigation are plotted in Figure 4.36. The voltammogram of copper in solution containing only 0.01M KNO₂ shows a distinct cathodic peak at -0.6V (SHE). The E^0 for NO₂⁻ reduction is 1.18V, where as E^0 for NO reduction is -0.514V. Base on the E^0 values, the observed cathodic peak at -0.6V is likely not from the reduction of NO₂⁻, but rather from the reduction of NO. The presence of NO in the NO₂⁻ solution is probably due to the decomposition effects of HNO₂. At pH value of 9, NO₂⁻ is a stable ion. In a weakly acidic condition such as pH 6, the NO₂⁻ forms small amount of HNO₂ which is very unstable in aqueous solution. The HNO₂ formed in solution may undergo auto oxidation and reduction reactions to form NO₃⁻ and NO species. The feasibility of these reactions are shown below,



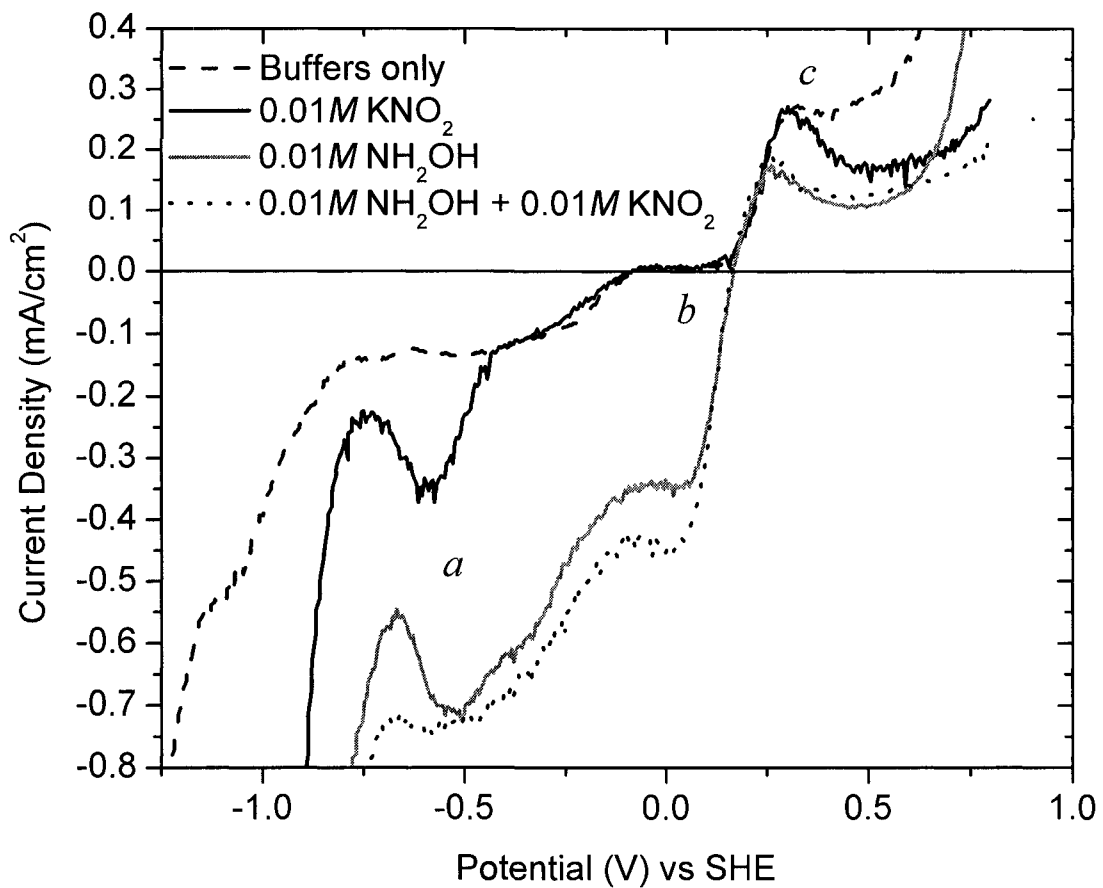
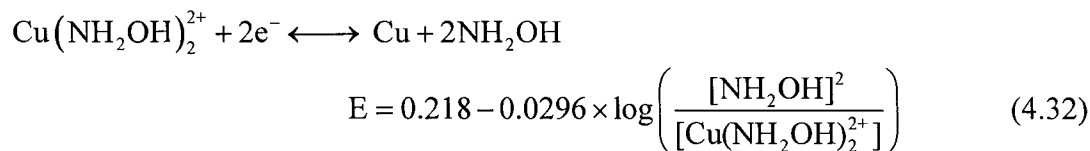
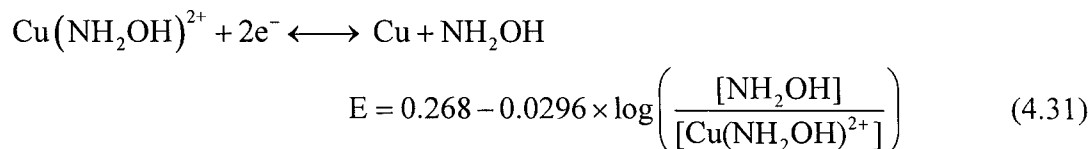


Figure 4.36. Voltammograms of copper film in pH 6 solutions containing only sulfate-phosphate buffers (---), buffers + 0.01M hydroxylamine (—), buffers + 0.01M KNO₂ (—), and 0.01M hydroxylamine + 0.01M KNO₂ (.....). Scan rate of 50 mV/s from -1.5V to +1V and rotation speed of 50 rpm.

Showing that the decomposition of HNO_2 forming NO specie is favorable; this would explain the presence of NO in a KNO_2 solution at pH 6. Interestingly, the voltammograms of copper in solutions with and without KNO_2 , were nearly identical from -0.4V to +0.3V (SHE).

Also plotted in Figure 4.36 is the voltammogram of copper in solution containing hydroxylamine at pH 6. The -0.5V (SHE) cathodic peak of copper in hydroxylamine solution clearly resembles the -0.6V (SHE) cathodic peak of copper in a solution containing KNO_2 . The slight discrepancy between the two reduction peaks is likely due to different NO concentrations and a different current-potential baseline. The voltammogram of copper in solution containing both hydroxylamine and NO_2^- seems to have a slightly higher current density in the cathodic portion of the curve than the voltammogram of copper in solution containing only hydroxylamine. Interestingly, for both voltammograms, the cathodic peak at -0.5V remains at the same current density value. Even though NO_2^- may introduce excess NO into the solution at pH 6, it is likely that the solution is already saturated with NO. The solubility of NO in aqueous solution is approximately 56 ppm (0.002 M). The presence of NO in hydroxylamine based solution was also confirmed from Carter and Small using electron spin resonance and Fourier-transformed infrared spectroscopy.^[97]

The anodic peak current density in region 'c' of Figure 4.35 and Figure 4.36 is likely due to the oxidation of copper through the formation of copper-hydroxylamine complexes. These reactions and their corresponding Nernst equations are shown in the following,



The calculated equilibrium potentials for reactions (4.31) and (4.32) are tabulated in Table 4.8. In Figure 4.35, the anodic peak at +0.25V (SHE) appears when copper is in an hydroxylamine solution at pH 8 and 6. At pH 3, no anodic peak was observed at +0.25V. It is also of interest to note that the anodic peak potential at +0.25V in Figure 4.35 seems to show no dependence on solution pH, especially between pH 8 and 6. As seen from the calculated equilibrium potentials in Table 4.8, the potentials also show no dependence on solution pH. The calculated equilibrium potentials for reactions (4.31) and (4.32) do not seem to coincide with the +0.25V anodic peak from the voltammograms of copper. It may be that this anodic peak at +0.25V is due to an accumulation of the copper-hydroxylamine complexes near the copper surface.

Table 4.8. Calculated equilibrium potentials for reactions (4.31) and (4.32) in volts (vs SHE) at the corresponding pH values and ion activity ratios.

pH	Reaction (4.31) $\left(\frac{[\text{NH}_2\text{OH}]}{[\text{Cu}(\text{NH}_2\text{OH})_2^{2+}]}\right)=$		Reaction (4.32) $\left(\frac{[\text{NH}_2\text{OH}]^2}{[\text{Cu}(\text{NH}_2\text{OH})_2^{2+}]}\right)=$	
	10^5	10^2	10^4	10
8	0.120	0.209	0.100	0.188
6	0.120	0.209	0.100	0.188
3	0.120	0.209	0.100	0.188

The polarization resistance (R_p) values identified in the linear region near the OCP typically provide insights to the corrosion behavior of a given system. Low R_p values represent a highly corrosive system and high R_p values represent lower a corrosive system. From the calculated R_p values shown in Table 4.6, the addition of hydroxylamine in solution significantly reduces the R_p value at all three pH conditions. This indicates that by adding hydroxylamine into the solution at any pH value ranging from 3 to 8, the corrosion of copper will increase. The lowest R_p value occurs at pH 6, and this corresponds with the maximum copper removal rate at pH 6, as shown in Figure 4.9.

In the voltammograms of copper (Figure 4.35) the transition from cathodic to anodic current densities starts from -0.25V and ends at +0.25V (SHE). It is also in this transition region (region 'b') near the OCP where values for R_p were determined. The transition toward OCP either from cathodic or anodic direction often looks linear. By fitting straight lines to these transition parts of the voltammogram, slopes on either side of OCP can be calculated and used to compare the rate at which either reduction or oxidation charge-

transfer takes place. The inverse of the slope would give units of $\Omega \cdot \text{cm}^2$ making the transition region pseudo-resistive. An example of this is shown in Figure 4.37 for the voltammogram of 0.01M hydroxylamine at pH 8. The cathodic pseudo-resistance value determined from Figure 4.37 is $\sim 253 \Omega \cdot \text{cm}^2$, and the anodic pseudo-resistance value is $\sim 1478 \Omega \cdot \text{cm}^2$. This shows that the cathodic reaction with lower pseudo-resistance value would have faster charge-transfer behavior than the anodic reaction. The pseudo-resistance values for each voltammogram in Figure 4.35 are shown in Table 4.9.

Table 4.9. Calculated pseudo-resistance values from the voltammograms of copper in 0.01M hydroxylamine based solution shown in Figure 4.35.

pH	Cathodic pseudo-resistance ($\Omega \cdot \text{cm}^2$)	Anodic pseudo-resistance ($\Omega \cdot \text{cm}^2$)
8	253 ± 7	1478 ± 25
6	298 ± 11	551 ± 23
3	1359 ± 50	20 ± 0.5

The determined pseudo-resistance values shown in Table 4.9 may provide some insight as to the interactions between reduction and oxidation charge-transfers near the OCP. Earlier discussions have shown that the maximum copper removal rate in hydroxylamine based solution at pH 6 corresponds to the minimum R_p value at that same pH. The cathodic and anodic pseudo-resistance values seem to have significant effects on the value of R_p near the OCP. At pH 6, the cathodic and anodic pseudo-resistance values have a difference of $\sim 253 \Omega \cdot \text{cm}^2$.

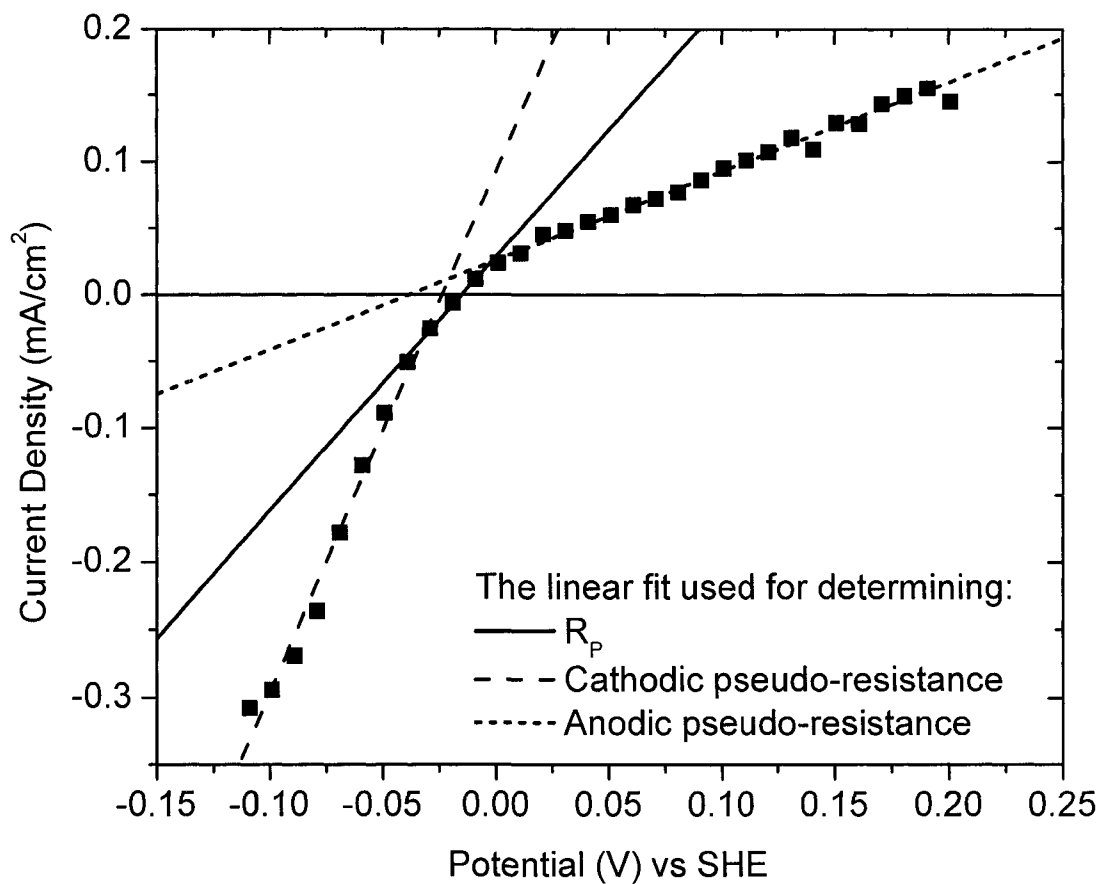


Figure 4.37. Voltammogram of copper in 0.01M hydroxylamine solution at pH 8. A linear fit of the cathodic portion of the curve determines the cathodic pseudo-resistance value (— — —). A linear fit of the anodic portion of the curve determines the anodic pseudo-resistance value (·····). A linear fit near the OCP determines the value for R_p (—).

At pH values of 8 and 3, the differences were $\sim 1,225 \Omega\cdot\text{cm}^2$ and $\sim 1,339 \Omega\cdot\text{cm}^2$, respectively. Small differences between the anodic and cathodic pseudo-resistance values would imply that the overall reaction may be limited by either the reduction or the oxidation process. At pH 8, because of the much higher anodic pseudo-resistance value over the cathodic pseudo-resistance value, oxidation reactions may be expected to control the overall redox process near OCP. The oxidation reaction at pH 8 that results in a high anodic pseudo-resistance value is likely due to the formation of a passive oxide. The behavior of decreasing anodic pseudo-resistance values toward an acidic pH indicates that the passive oxide layer breaks down or does not form under acidic conditions.

The behavior of the cathodic pseudo-resistance value with respect to pH shows an increasing pseudo-resistance value toward acidic pH. The reduction reactions that result in the cathodic pseudo-resistance value are dependent on the decomposition of hydroxylamine. It was mentioned earlier that in alkaline conditions, hydroxylamine is unstable and undergo auto-oxidation/reduction reactions. In acidic conditions, hydroxylammonium is very stable. The lack of hydroxylamine reactivity in solution at pH 3 explains why the cathodic pseudo-resistance value is high. The overall redox process at pH 3 is clearly limited by the reduction reactions.

4.6. Results from Capillary Electrophoresis Chromatography (CEC)

The analytical technique of capillary electrophoresis chromatography (CEC) was used to identify various anions and cations that were either initially present in hydroxylamine based solution or generated in solution after contacting with copper metal. The identification of these ionic species will reemphasize the likelihood of the proposed reaction mechanisms.

The chromatograms in Figure 4.38 are the ionic standards that were used. Chromatogram 'a' is the result from anionic standard while chromatograms 'b', 'c', and 'd' are from cationic standards. The anionic standard contained equal concentrations of KCl, KNO₂, K₂SO₄, and KNO₃ at 0.01 M. The first of the three cationic standards (chromatogram 'b') is for 0.01 M NH₄Cl. The second (chromatogram 'c') is for 0.002 M Cu(NO₃)₂. The third (chromatogram 'd') was obtained for a solution containing 0.1 M NH₄OH + 0.001 M CuSO₄ + HNO₃.

From chromatogram 'a', it is clear that the CEC technique can resolve anions clearly and sharply. It is important that NO₂⁻ is clearly resolved from other anions, because other anions will always be present in the solution due to inorganic acid that was used to acidify the solution. Sulfuric acid was predominantly used in the copper removal experiments, but nitric and hydrochloric acids were used periodically. Both chromatograms 'b' and 'c' show individual detection of NH₄⁺ and Cu²⁺ cations. However, in chromatogram 'd', a solution mixture containing NH₄⁺ and Cu²⁺ cations only shows a peak for NH₄⁺ and not Cu²⁺. The undetected Cu²⁺ cation in chromatogram 'd' is possibly due to the formation of Cu(NH₃)_x²⁺ complexes.

In Figure 4.39, anionic analyses of hydroxylamine based solutions have show signs of NO_2^- . The chromatogram at pH ~ 9 showed a small NO_2^- peak and also a fairly large SO_4^{2-} peak. The sulfate peak is due to the fact that the hydroxylamine based solutions were acidified using sulfuric acid. As the pH was adjusted to a value of 6 or 4 using sulfuric acid, the small NO_2^- peak disappeared and the SO_4^{2-} peak increased as expected. The disappearance of the NO_2^- peak is possibly due to the added H^+ ions into the solution that formed a neutral HNO_2 which quickly decomposed into NO and NO_3^- . It is important to note the presence of NO_2^- in the initial hydroxylamine solution prior to any exposure to copper metal.

The cationic analyses of hydroxylamine based solution are shown in Figure 4.40. In these analyses the hydroxylamine based solutions were also acidified using sulfuric acid. The chromatogram at pH 8 shows the presence of NH_4^+ . Also detected in the chromatogram were peaks of NH_3OH^+ and neutral NH_2OH . Since at pH 8 the majority of hydroxylamine is in its neutral form of NH_2OH , the chromatogram shows a much larger NH_2OH peak than the NH_3OH^+ peak. With decreasing pH values, the intensity of the NH_2OH peak decreases and the NH_3OH^+ peak increases. This is as expected due to the pK_a of 6 for hydroxylamine. In chromatograms at pH 6 and 3, the NH_4^+ ion was not detected.

Ion analyses were also performed on hydroxylamine based solutions at pH values of 8, 6, and 3 which were contacted with copper metal for 30 minutes. The results from anionic analyses before and after copper contact showed no difference in the chromatograms.

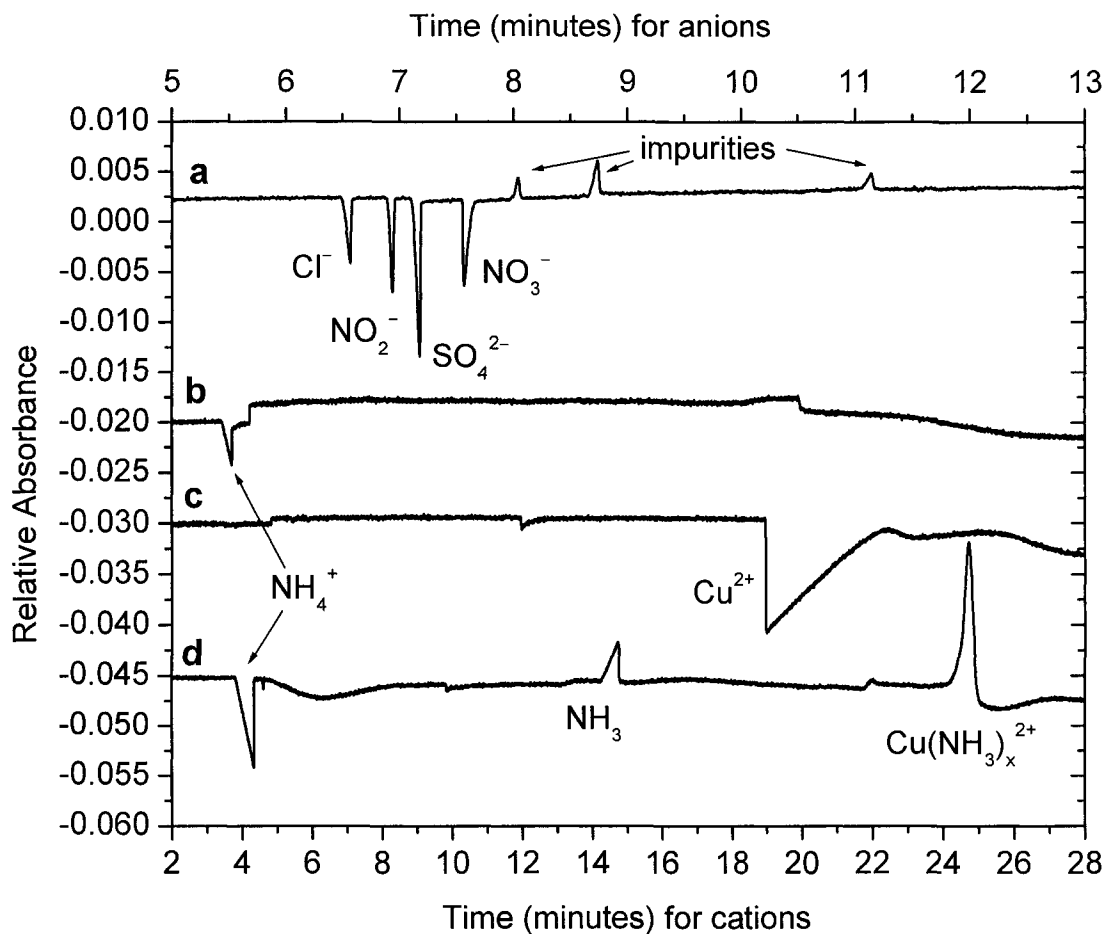


Figure 4.38. Chromatogram of ion analysis using CEC. Chromatogram 'a' is of equal concentrations of Cl^- , NO_2^- , SO_4^{2-} , and NO_3^- at 0.01 M. Chromatogram 'b' is of 0.01 M NH_4Cl . Chromatogram 'c' is 0.002 M $\text{Cu}(\text{NO}_3)_2$. Chromatogram 'd' is of 0.1 M NH_4OH + 0.001 M CuSO_4 + HNO_3 . [Electrokinetic injection for 5 second at 1kV. Applied voltage of 15kV (anions) and 30kV (cations). Capillary column was 75 μm in diameter, and 70 cm in length.]

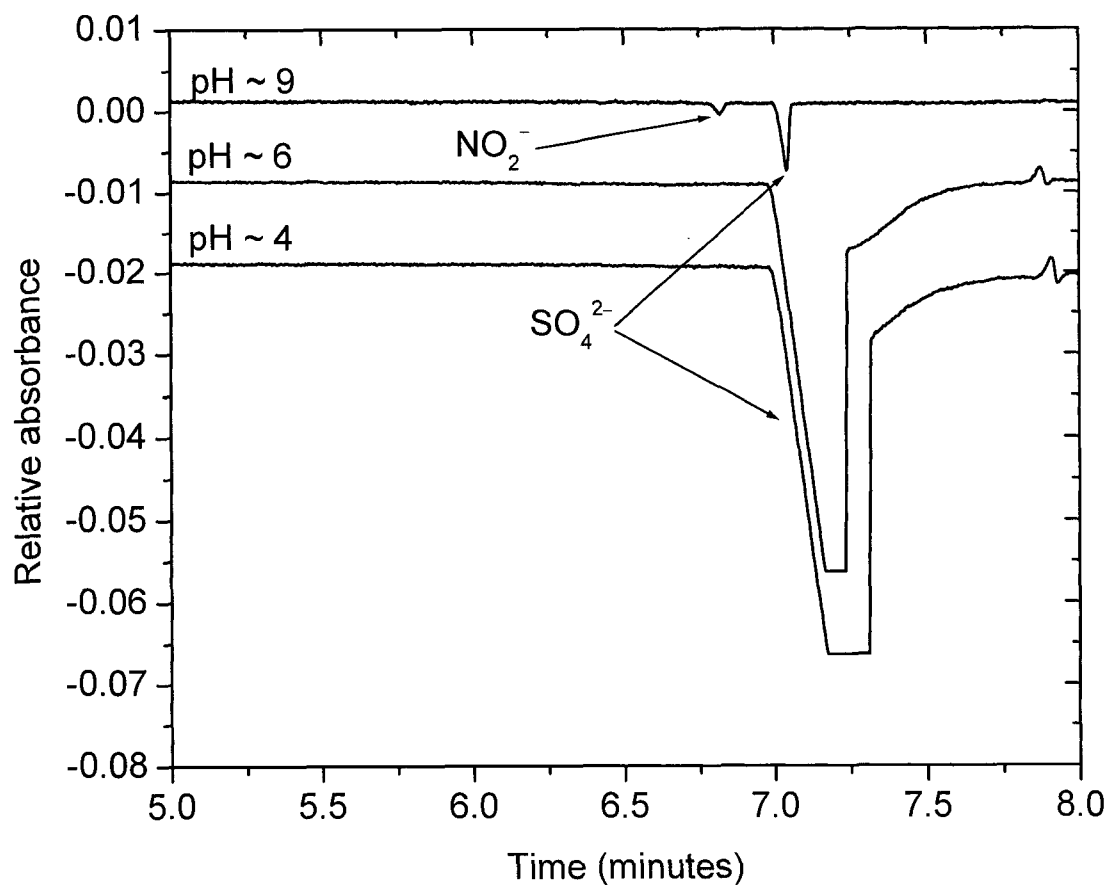


Figure 4.39. Chromatograph of anionic analysis using CEC. Analyte is 0.5 *M* hydroxylamine based solution prior to copper removal experiments. The solution also contains sulfuric acid for pH adjustments. [Electrokinetic injection for 5 second at 1 kV. Applied voltage of 15 kV. Capillary column was 75 μm in diameter, and 70 cm in length.]

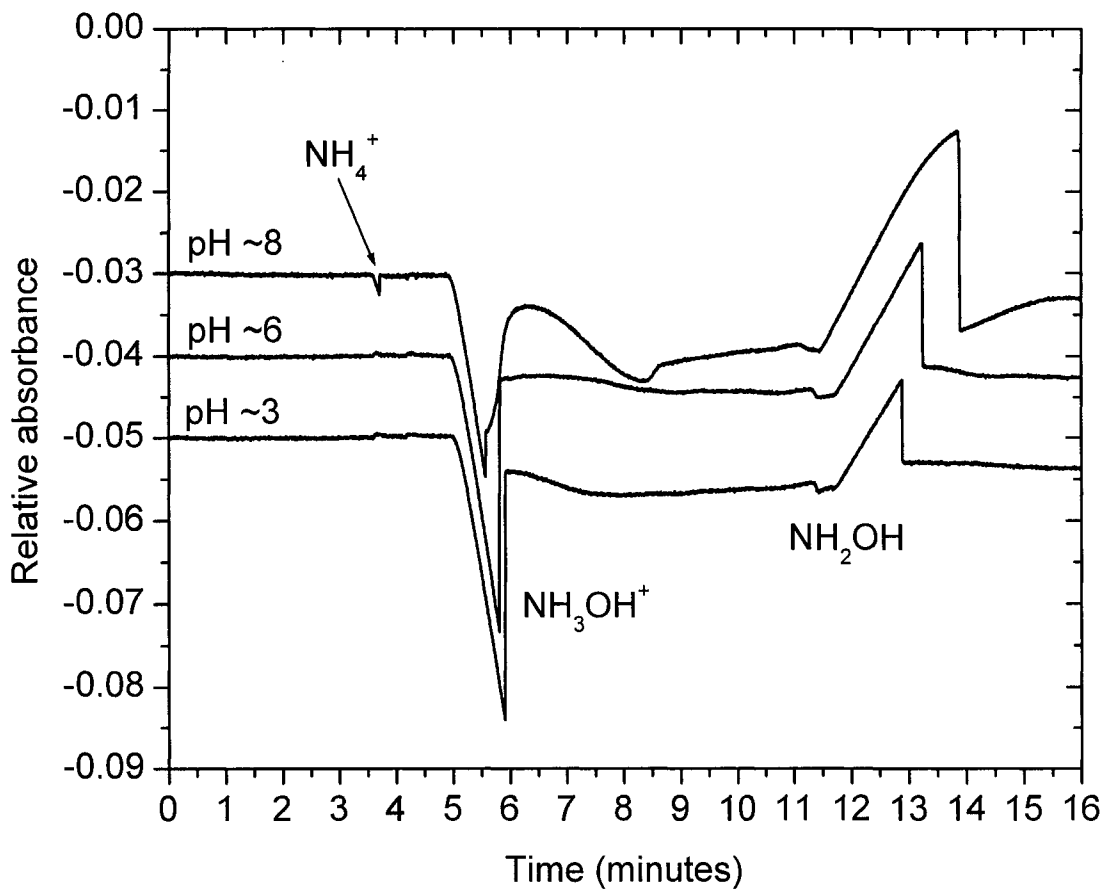


Figure 4.40. Chromatograph of cationic analysis using CEC. Analyte is 0.5 *M* hydroxylamine based solution prior to copper removal experiments. The solution also contains sulfuric acid for pH adjustments. [Electrokinetic injection for 5 second at 1 kV. Applied voltage of 30 kV. Capillary column was 75 μm in diameter, and 70 cm in length.]

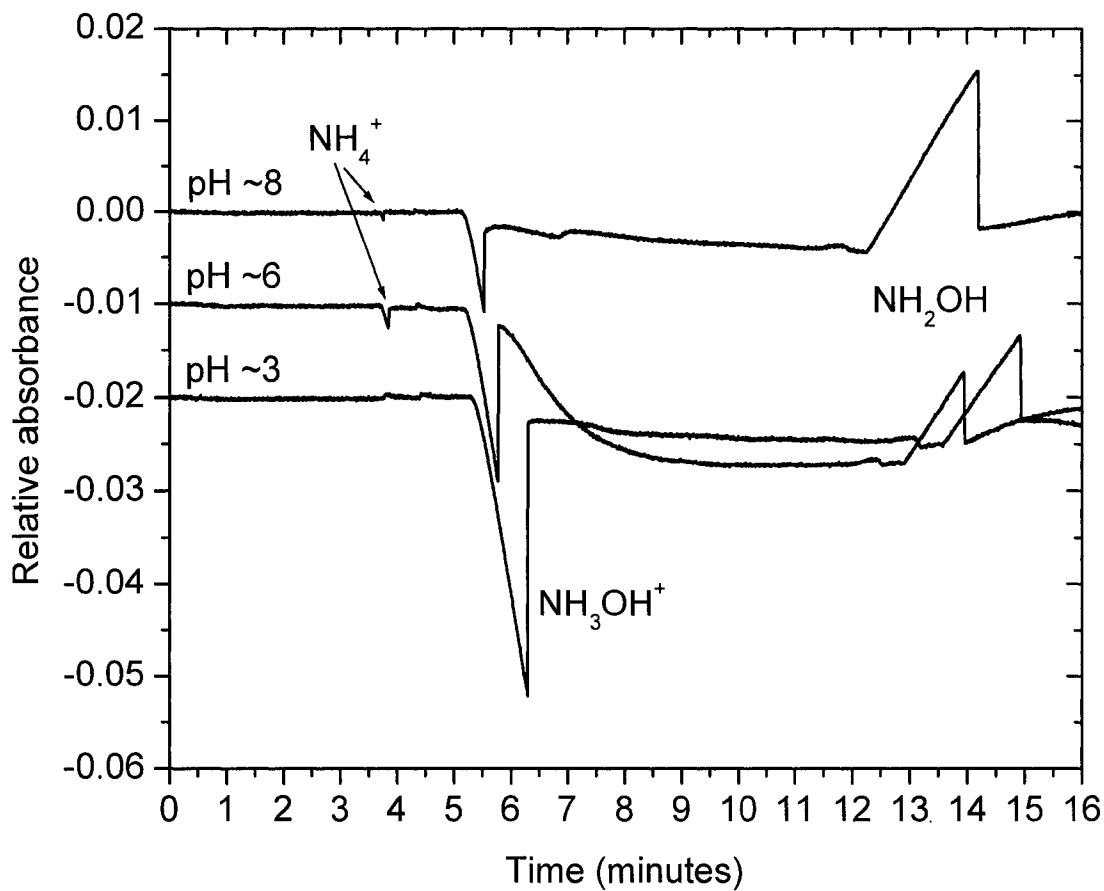


Figure 4.41. Chromatograph of cationic analysis using CEC. Analyte is 0.5 *M* hydroxylamine based solution after copper removal experiments. The solution also contains sulfuric acid for pH adjustments. [Electrokinetic injection for 5 second at 1 kV. Applied voltage of 30 kV. Capillary column was 75 μm in diameter, and 70 cm in length.]

However the cationic analyses did show some changes, as displayed in Figure 4.41. The NH_4^+ peak appears at both pH values of 8 and 6, but interestingly the peak intensity at pH 6 is larger than at pH 8. The cationic chromatogram of hydroxylamine prior to copper contact shows that NH_4^+ did not exist at pH 6. Also from Figure 4.41, the NH_3OH^+ peaks increased much more with decreasing pH than the NH_3OH^+ peaks in Figure 4.40. The NH_2OH peak at pH 6 in Figure 4.41 was actually smaller than that at pH 3. It was expected that the pH behavior of NH_2OH peaks after copper dissolution would be similar to Figure 4.40.

In order to examine the chemistry of hydroxylamine with respect to pH, the NH_3OH^+ and NH_2OH peaks from Figure 4.40 and Figure 4.41 were integrated. The results of the calculations are plotted with respect to pH in Figure 4.42. The integrated area is directly proportional to the concentration of hydroxylamine based species. Since the pK_a of hydroxylamine is approximately 6, the concentrations of NH_2OH and NH_3OH^+ are expected to be approximately the same at this pH. At pH values greater than 6, the concentrations of NH_2OH should be greater than NH_3OH^+ , and vice versa for pH values less than 6. Interestingly, the overall hydroxylamine concentration is lower after contact with copper. At pH 6, the overall hydroxylamine concentration dropped by half. This indicates that hydroxylamine is being consumed during copper dissolution.

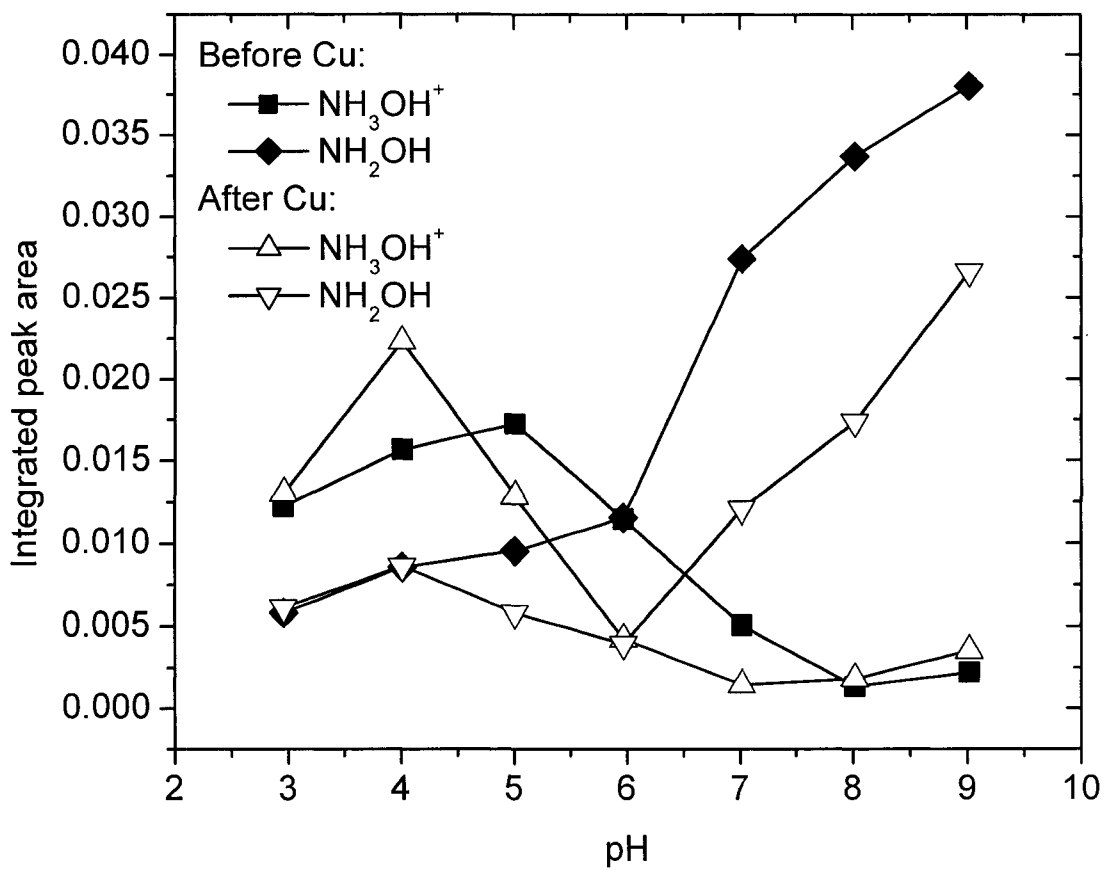


Figure 4.42. Integrated peak areas of NH_3OH^+ and NH_2OH species from chromatograms of cationic analysis (shown in Figure 4.40 and Figure 4.41) plotted with respect to pH.

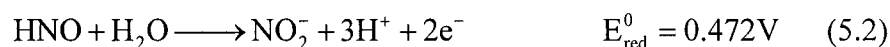
From the results in Figure 4.40, Figure 4.41, and Figure 4.42, it is evident that the reduction of hydroxylamine to ammonia does occur in solution. Not only does the reduction reaction occur during decomposition of hydroxylamine but it also occurs during the dissolution process of copper film. Using the chromatogram of a standard NH_4^+ ion analysis at pH 6, the measured NH_4^+ peak after copper dissolution is estimated to be 0.006 *M*. This is considerably small compared with the 50% of 0.5 *M* hydroxylamine that was consumed after copper dissolution. It is possible that the reduction of hydroxylamine to ammonia can influence the oxidation of copper metal, but the small amount of ammonia produced cannot account for the hydroxylamine that was consumed after copper dissolution.

The amount of hydroxylamine consumed was determined by subtracting the integrated area after copper contact from the area before copper contact. The consumption of hydroxylamine is an evidence that shows hydroxylamine does indeed participate in the oxidation process of copper. It is also possible that the hydroxylamine consumed is actually in the form of $\text{Cu}(\text{NH}_2\text{OH})_x^{2+}$ complex, which cannot be accurately determined with the current CEC cationic analyses.

CHAPTER 5. PROPOSED MECHANISM

At this juncture, a mechanism will be proposed for the removal of electroplated copper film in a hydroxylamine based chemical system maintained at different pH values. Since the removal behavior of copper film in a regular CMP tool (Figure 4.1) as well as the laboratory EC-AC tool (Figure 4.9), showed a maximum in removal rates at a pH value of 6, three pH values of 9, 6, and 3 will be used as a basis for discussion of copper removal mechanisms. Before the discussion on copper removal mechanisms, the chemistry of hydroxylamine from literatures and experimental results will be discussed. This will aid in the explanation of various nitrogen-based species other than hydroxylamine involved in the mechanism reactions.

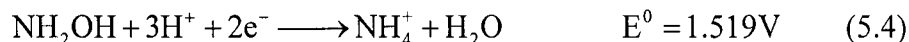
In the background section, some reaction mechanisms of hydroxylamine decomposition were discussed. A summary of these mechanisms is shown in Figure 2.8. The majority of the decomposition reactions involve oxidation of hydroxylamine into various intermediate chemical species. In alkaline conditions, the oxidation of hydroxylamine is coupled with the reduction of oxygen. This behavior is evident in Figure 4.18, where the levels of dissolved oxygen are plotted with respect to pH. The lack of oxygen in solution shows that hydroxylamine is oxidized at the expense of oxygen reduction reaction. The hydroxylamine will go through multiple-step oxidation reactions in conjunction with oxygen reduction. The oxidation reactions are shown as follows,



The reduction of oxygen is shown below.



Other reduction reactions besides oxygen are also possible, such as hydroxylamine to ammonia.



Analysis using capillary electrophoresis chromatography (CEC) showed the presence of NH_4^+ as well as NO_2^- (Figure 4.39 through Figure 4.41) at pH values above 6. Below pH 6, the presence of NO_2^- was not detectable by CEC. The E-pH diagram of a nitrogen-water system (Figure 4.15) shows that NO is more stable at pH 6 than NO_2^- . It is likely that the lack of NO_2^- at pH 6 is due to the oxidation of $\text{HNO} \rightarrow \text{NO}$. The levels of dissolved oxygen below pH 6 were constant at 7.4 ppm. The constant O_2 level near saturation signifies that hydroxylamine may be oxidized by oxygen at a much slower rate in acidic conditions. The hydroxylammonium cation (NH_3OH^+) appears to be much more stable and less reactive than hydroxylamine (NH_2OH) itself.

From the E-pH diagram of a nitrogen-water system (Figure 4.15), the measured redox potentials of hydroxylamine solution fall in the stability regions of $\text{H}_2\text{N}_2\text{O}_2$, HN_2O_2^- , and $\text{N}_2\text{O}_2^{2-}$. This shows that the fate of the nitroxyl (HNO or NO^-) intermediate is may be decided by the following reaction,



A summary diagram on the decomposition of hydroxylamine with respect to pH is shown in Figure 5.1.

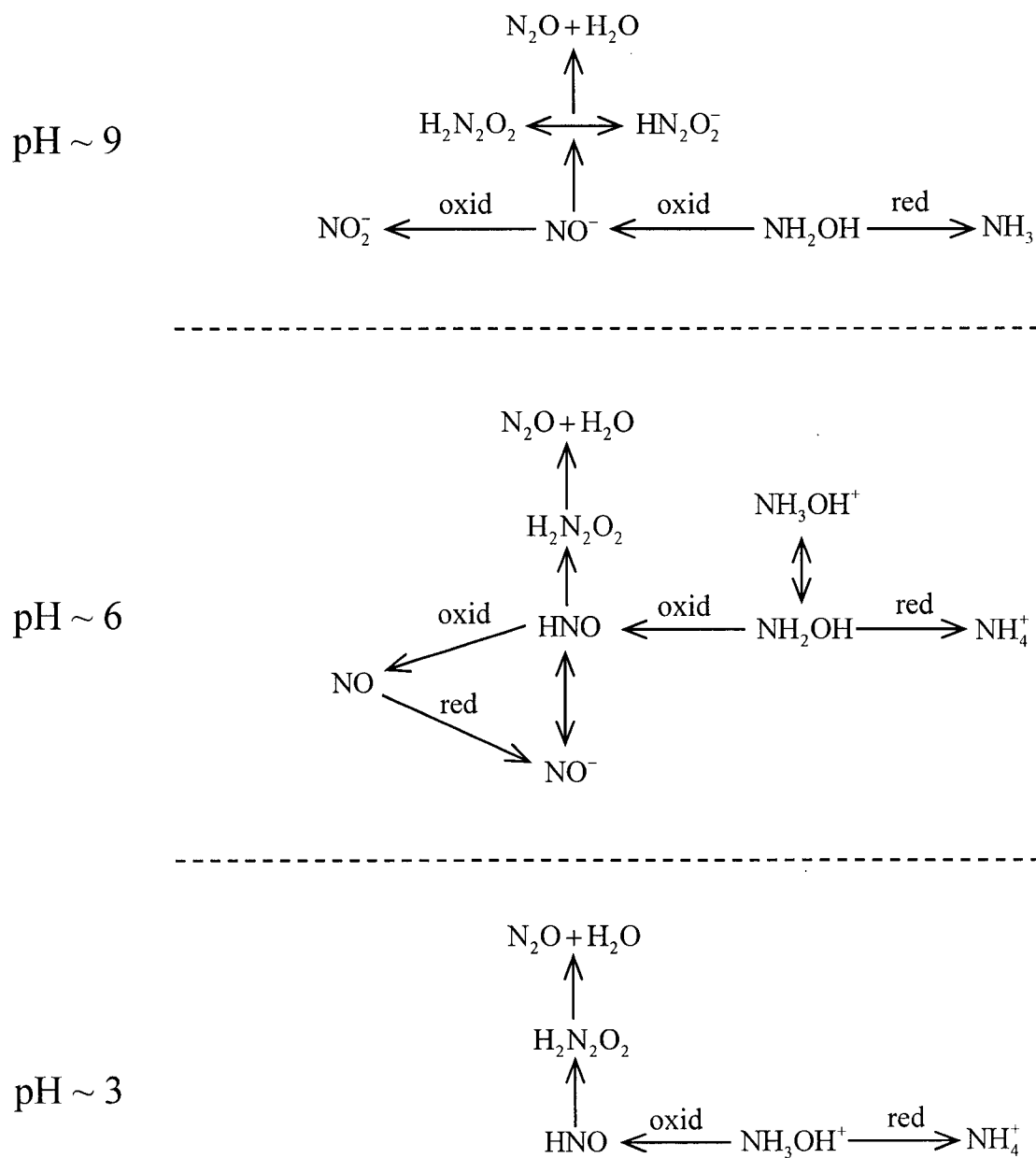
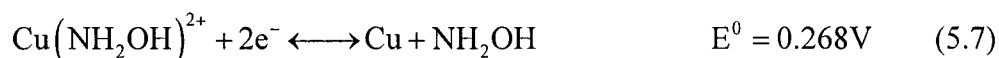
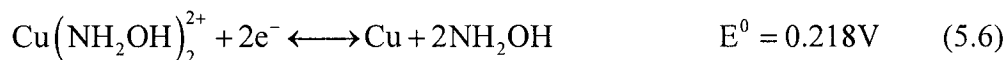


Figure 5.1. Summary diagram on the decomposition mechanisms of hydroxylamine at pH values of 9, 6, and 3. ["red" – reduction reactions and "oxid" – oxidation reactions.]

5.1. Proposed Mechanism for Copper Removal at pH Value of 6

The mechanism for the removal of copper in hydroxylamine based solution at pH 6 is due to oxidation of copper followed by hydroxylamine complexation coupled with the reduction of NO to H₂N₂O₂ via HNO intermediate.

- Oxidation reactions:



- Reduction reaction:



The E^0 values for Reactions (5.6) and (5.7) are lower than that of $\text{Cu}^{2+} \rightarrow \text{Cu}$. This shows that oxidation of copper metal through hydroxylamine complexation is more favorable.

It may be noted that the reduction reaction of hydroxylamine to ammonium ion has an $E^0 = 1.519\text{V}$ which is also favorable when coupled with Reaction (5.6) or (5.7). However, cationic analysis using capillary electrophoresis chromatography has shown that the amount of NH_4^+ produced after dissolution of copper does not equate with the amount of hydroxylamine consumed. Roughly a little more than 50% of 0.5M hydroxylamine was consumed, while only about 0.006 M NH_4^+ was produced.

Additionally, the electrochemical polarization curves (Figure 4.22) of copper in solution at different hydroxylamine concentrations held at pH 6 showed that an anodic portion of these curves were significantly affected, while the cathodic portion of the curve showed hardly any changes with hydroxylamine concentration. This lack of

dependency on hydroxylamine concentration shows that hydroxylamine was not directly involved in the reduction process at pH 6. Therefore, the reduction of $\text{NH}_2\text{OH} \rightarrow \text{NH}_4^+$ is not a dominant reaction.

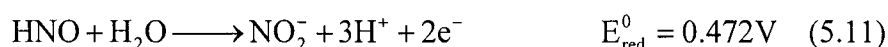
The voltammetry studies on copper showed a strong cathodic peak around -0.5 V (SHE) in the presence of hydroxylamine at pH 6, and this was identified as the reduction of $\text{NO} \rightarrow \text{NO}^-$ with an E^0 of -0.514V. Any NO^- produced were eventually converted to $\text{H}_2\text{N}_2\text{O}_2$. It is interesting to note that even though the reduction of $\text{NO} \rightarrow \text{NO}^-$ may not seem favorable, the E^0 value from the reduction reaction of $\text{NO} \rightarrow \text{H}_2\text{N}_2\text{O}_2$ shows that it is highly favorable. It may be that the copper ion catalyzes the reduction of NO to NO^- intermediate.

In Figure 4.17, where the copper-hydroxylamine-water and nitrogen-water E-pH diagrams are superimposed together, the measured redox potential of 0.5M hydroxylamine containing 0.001M Cu^{2+} at pH 6 are shown to fall in the region between the $\text{NO}/\text{H}_2\text{N}_2\text{O}_2$ and $\text{Cu}/\text{Cu}(\text{NH}_2\text{OH})_2^{2+}$ E-pH lines. This shows that the overall reaction between reduction of $\text{NO}/\text{H}_2\text{N}_2\text{O}_2$ and oxidation of $\text{Cu}/\text{Cu}(\text{NH}_2\text{OH})_2^{2+}$ is favorable.

5.2. Proposed Mechanism for Copper Removal at pH Value of 9

At pH 9, the measured redox potentials of solution without hydroxylamine fell in the stability region of CuO . With the addition of hydroxylamine into the solution, the solution redox potentials became more reducing and were close to the $\text{Cu}/\text{Cu}_2\text{O}$ E-pH line. The reducing nature of hydroxylamine appears to favor the formation of Cu_2O .

At this pH, the oxidation of hydroxylamine is coupled with O₂ reduction, shown in the following reactions,



As discussed earlier, the dissolved O₂ concentration was decreased at alkaline pH values. Since NO₂⁻ is stable in alkaline pH values, hydroxylamine decomposition is likely to yield NO₂⁻ rather than NO.

The observed copper removal rate at pH 9 is predominantly due to mechanical abrasion of the Cu₂O layer. The study on the effect of applied pressure and relative velocity during abrasion (Figure 4.5) showed that the copper removal rate is dependent on applied pressure. The ratio between RR_{Mechanical} and RR_{Chemical} shown in Figure 4.10 proves that, indeed, mechanical abrasion is the main contributing factor in copper removal rate. Once abrasion was stopped, the dissolution of copper was minimal at this pH.

5.3. Proposed Mechanism for Copper Removal at pH Value of 3

In acidic conditions hydroxylamine exists in its protonated form (NH₃OH⁺). Due to the unreactive nature of NH₃OH⁺, a majority of the decomposition reactions involving NH₂OH would likely cease. The Cu(NH₂OH)₂²⁺ and Cu(NH₂OH)²⁺ complexes are also not stable in acidic conditions. The measured redox potential of 0.5M hydroxylamine + 0.001M CuSO₄ solution at pH 3 fell in the stability region of Cu²⁺ (Figure 4.16). The

removal mechanism of copper is likely due to copper oxidation coupled with oxygen reduction, shown below,



The abrasion of copper in acidic hydroxylamine solution shows an increase in copper removal rate. The polarization curve (Figure 4.29) shows that this increase in copper removal rate is predominantly due to the increase in exchange current density of the cathodic reaction during abrasion. It is thus probable that the abrasion process creates a fresh copper surface that enables the reduction of oxygen to occur in a more efficient manner.

CHAPTER 6. CONCLUSIONS AND FUTURE WORK

6.1. Conclusions

The following conclusions can be made from this study:

1. The removal rates of copper in hydroxylamine based chemistries are highly dependent on solution pH. A maximum copper removal rate is achieved at pH 6 and a significantly lower removal rate occurs at pH values 3 and 9.
2. The constructed E-pH diagrams of copper-hydroxylamine-water and nitrogen-water systems identify that the reduction of NO to $\text{H}_2\text{N}_2\text{O}_2$ coupled with the oxidation of Cu to $\text{Cu}(\text{NH}_2\text{OH})_2^{2+}$ is favorable. The measured solution redox potentials plotted on the E-pH diagrams show that the coupled redox reaction is highly probable.
3. An electrochemical abrasion cell (EC-AC) was successfully designed and fabricated. Copper removal rates obtained using the EC-AC tool showed the same trend with respect to pH as the removal rates obtained on a regular CMP tool. Results obtained from the EC-AC tool can be used as a valid guideline to design new CMP slurries.
4. The electrochemical polarization of copper studied as a function of hydroxylamine concentration at a solution pH of 6 showed that the oxidation reaction is dependent on hydroxylamine, whereas the reduction reaction is not. The oxidation reaction is due to the oxidation of copper followed by hydroxylamine complexation.

5. Voltammetry studies of copper in hydroxylamine solution showed a reduction peak of NO to NO^- at -0.5V. This may explain the reduction of nitric oxide (NO) to hyponitrous ($\text{H}_2\text{N}_2\text{O}_2$) via nitroxyl (HNO or NO^-) intermediate at pH 6. The presence of NO in hydroxylamine solution is due to the auto-oxidation/reduction reactions of hydroxylamine.
6. Capillary electrophoresis chromatography detected NO_2^- and NH_4^+ ions initially present in hydroxylamine solutions due to decomposition of hydroxylamine. Detection of NH_2OH , and NH_3OH^+ molecules after contact with copper showed that hydroxylamine was consumed. The amount of NH_4^+ found in solution after contact with copper was considerably smaller than the amount of hydroxylamine that was consumed. This showed that the reduction process of NH_2OH to NH_4^+ is not dominant.

6.2. Future Work

To further understand the effects of hydroxylamine in the removal of copper, the following studies are suggested:

- An electrochemical and removal rate study of copper in hydroxylamine solution at pH 6 containing ruthenium(III) chloride. Ruthenium(III) chloride is a well-known nitric oxide scavenger. By decreasing the amount of nitric oxide in solution, the dissolution rate of copper should decrease. This will help in proving or disproving categorically whether the reduction reaction of nitric oxide is the cathodic reaction responsible for the dissolution of copper.

- Modifications to the electrochemical abrasion cell (EC-AC) for studying planarization issues, such as global and local planarity as well as non-uniformities, at different hydroxylamine based chemistries.
- Study the decomposition of hydroxylamine in more detail using the capillary electrophoresis chromatography. By measuring the amount of NH_2OH , NH_3OH^+ , NH_4^+ , and NO_2^- as a function of time, the rate of decomposition can be determined. This study would enable the understanding of the rate at which hydroxylamine decomposes in the CMP waste stream. The treatments of CMP waste stream will be more critical as CMP processes become more demanding.

APPENDIX

Relative Velocity Calculations Between Sample and Pad

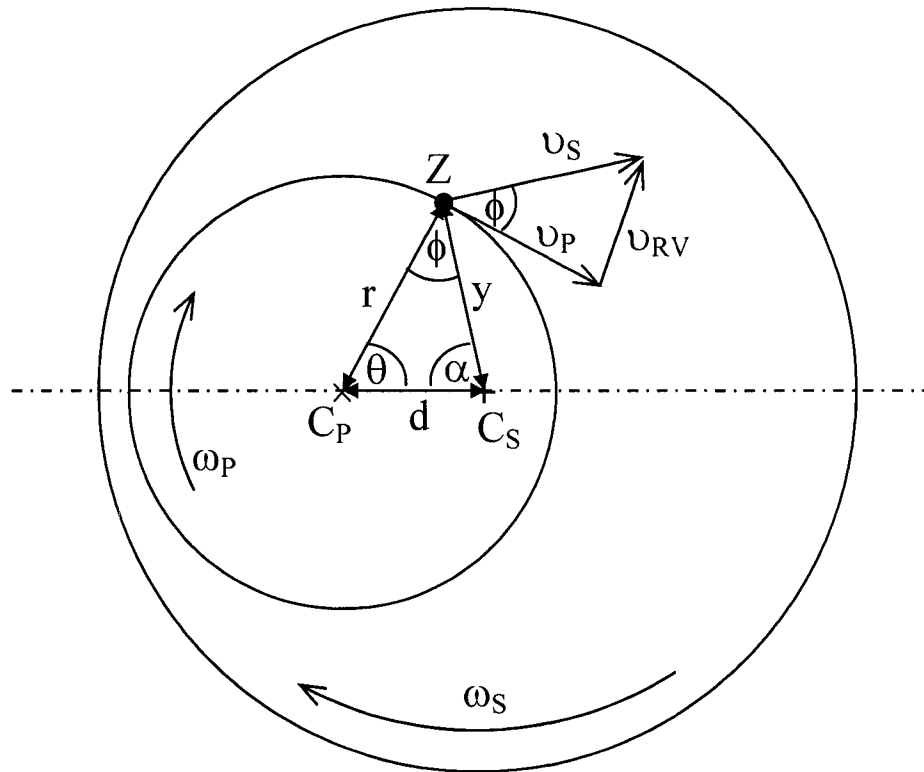


Figure A.1. Schematic diagram showing the relative velocity (v_{RV}) between the copper sample and the abrasion pad.^[98]

The relative velocity (v_{RV}) between the copper sample and the abrasion pad can be calculated using the law of cosine, as shown below,

$$|v_{RV}| = \sqrt{|v_P|^2 + |v_S|^2 - 2|v_P||v_S|\cos(\phi)} \quad (\text{A.1})$$

where v_p is the pad velocity and v_s is the copper sample velocity at point Z. The velocities of the pad and the sample are related to its rotational speeds shown in the following,

$$v_p = \omega_p y \quad \text{and} \quad v_s = \omega_s r \quad (\text{A.2})$$

where ω_p is pad rotational speed and ω_s is sample rotational speed. The distance between point Z and the center of the sample (C_s) is 'y'. The distance between point Z and the center of the pad (C_p) is 'r'. The distance between the two centers (C_s and C_p) is 'd'. The angle between v_p and v_s is ϕ . The angle ϕ can be expressed as $\phi = \pi - (\alpha + \theta)$. Using the law of sine, an expression for 'y' is determined, which are shown below.

$$\frac{r}{\sin \alpha} = \frac{d}{\sin \phi} = \frac{y}{\sin \theta} \quad (\text{A.3})$$

$$y = \frac{\sin \theta}{\sin(\theta + \alpha)} d \quad (\text{A.4})$$

Also using the law of sine, an expression for α as function of θ is shown below.

$$\alpha = \cot^{-1} \left[\frac{\left(\frac{d}{r} \right) - \cos \theta}{\sin \theta} \right] \quad (\text{A.5})$$

The averaged relative velocity is calculated using Equations (A.1), (A.2), (A.4), and (A.5). Throughout the calculation, only 'r' and θ will vary while the rest remain constant.

REFERENCES

1. G. Moore, "Cramming More Components Onto Integrated Circuits," *Electronics*, **38(8)** (1965)
2. *International Technology Roadmap for Semiconductors (ITRS)*, Semiconductor Industry Association (SIA), San Jose, CA, (2001).
3. K. L. Holland, *CMP Trends*, Techcet Group, LLC., Genoa, NV, (2000).
4. P. S. Lysaght, W. Mlynko, P. Lefevre and I. Ybarra, "Cost and initial performance observations of CMP vs. spin-etch processing for removal of copper metalization from patterned low-k materials," in *Proceedings of ISSM2000, the 9th International Symposium on Semiconductor Manufacturing* Tokyo, Japan, p. 161-164, (2000).
5. H. J. Kim, "Method for forming damascene-type metal wires in semiconductor devices using CMP and a spin etch process," KR Patent 2001003143, Hynix Semiconductor Inc., S. Korea, (2001).
6. S. Sivaram, H. Bath, R. Leggett, A. Maury, K. Monnig and R. Tolles, "Planarizing Interlevel Dielectrics by Chemical-Mechanical Polishing," *Solid State Technology*, **35(5)**, p. 87-91 (1992)
7. S. Sivaram, K. Monnig, R. Tolles, A. Maury and R. Leggett, "Overview of Planarization by Mechanical Polishing of Interlevel Dielectrics," in *Proceedings of the Third International Symposium on ULSI Science and Technology*, Editors: J. M. Andrews and G. K. Celler, The Electrochemical Society, p. 606-613, (1991).
8. *472 CMP Tool*, Novellus (formerly SpeedFam-IPEC), (2003).
9. *676 CMP Tool*, Novellus (formerly SpeedFam-IPEC), (2003).
10. *Teres CMP System*, Lam Research Corp., (2003).
11. *IC1000 CMP Pad*, Rodel Corporation, 451 Bellevue Rd, Newark, DE 19713, (2001).
12. *Suba™ Products*, Rodel Corporation, 451 Bellevue Rd, Newark, DE 19713, (2001).
13. *3M SlurryFree™ CMP*, Rodel Corporation, 451 Bellevue Rd, Newark, DE 19713, (2001).
14. *Fundamentals of Chemical Mechanical Planarization*, PTI Seminars, Inc.: Semiconductor & Electronic Training, 1749 Gilsinn Lane, Suite 250, Fenton, MO 63026, (2001).

15. F. W. Preston, "The theory and design of plate-glass polishing machines," *J. Soc. Glass Tech.*, **11**, p. 214-56 (1927)
16. N. J. Brown, "Preparation of Ultrasmooth Surfaces," *Annual Review of Materials Science*, **16**, p. 371-388 (1986)
17. N. J. Brown, P. C. Baker and R. T. Maney, "Optical polishing of metals," in *Optical, Electron, and Mass Spectroscopy and Other Related Properties*, Proceedings of SPIE-The International Society for Optical Engineering, p. 42-57, (1981).
18. N. J. Brown and L. Cook, "Paper TuB-A4, Tech Digest," in *Topical Meeting on the Science of Polishing*, Optical Soc. of America, (1984).
19. W.-T. Tseng and Y.-L. Wang, "Re-examination of Pressure and Speed Dependences of Removal Rate during Chemical-Mechanical Polishing Processes," *J. Electrochem. Soc.*, **144**(2), p. L15-L17 (1997)
20. S. R. Runnels and L. M. Eyman, "Tribology Analysis of Chemical-Mechanical Polishing," *Journal of the Electrochemical Society*, **141**(6), p. 1698-701 (1994)
21. L. M. Cook, "Chemical Processes In Glass Polishing," *Journal of Non-Crystalline Solids*, **120**(1-3), p. 152-71 (1990)
22. B. R. Lawn, T. R. Wilshaw, T. I. Barry and R. Morrell, "Hertzian Fracture of Glass Ceramics," *Journal of Materials Science*, **10**(1), p. 179-82 (1975)
23. S. R. Runnels, "Feature-Scale Fluid-Based Erosion Modeling for Chemical-Mechanical Polishing," *Journal of the Electrochemical Society*, **141**(7), p. 1900-4 (1994)
24. B. Zhao and F. G. Shi, "Chemical Mechanical Polishing: Threshold Pressure and Mechanism," *Electrochemical and Solid-State Letters*, **2**(3), p. 145-147 (1999)
25. D. J. Stein and D. Hetherington, "Review and Experimental Analysis of Oxide CMP Models," in *Chemical Mechanical Planarization in IC Device Manufacturing III*, Editors: R. L. Opila, I. Ali, Y. A. Arimoto, Y. Homma, C. Reidsema-Simpson and K. B. Sundaram, p. 217-233, (2000).
26. T. Izumitani, "Polishing, lapping, and diamond grinding of optical glasses," in *Treatise on Materials Science and Technology*, Editors: M. Tomozawa and R. Doremus, Academic Press, New York, p. 115-72, (1979).
27. R. Iler, *The Chemistry of Silica*, Wiley, New York, (1979).

28. D. M. Knotter, "Etching Mechanism of Vitreous Silicon Dioxide in HF-Based Solutions," *Journal of the American Chemical Society*, **122**, p. 4345-4351 (2000)
29. F. B. Kaufman, D. B. Thompson, R. E. Broadie, M. A. Jaso, W. L. Guthrie, D. J. Pearson and M. B. Small, "Chemical-Mechanical Polishing for Fabricating Patterned Tungsten Metal Features as Chip Interconnects," *Journal of the Electrochemical Society*, **138**(11), p. 3460-5 (1991)
30. D. J. Stein, D. Hetherington, T. Guilinger and J. L. Cecchi, "In situ electrochemical investigation of tungsten electrochemical behavior during chemical mechanical polishing," *Journal of the Electrochemical Society*, **145**(9), p. 3190-3196 (1998)
31. E. A. Kneer, *Electrochemical Aspects of Chemical Mechanical Polishing of Tungsten and Aluminum*, Ph.D., The University of Arizona, Tucson, AZ, (1998).
32. M. J. N. Pourbaix, *Atlas of Electrochemical Equilibriums in Aqueous Solutions. 2nd ed.*, 644 pp., (1974).
33. E. A. Kneer, C. Raghunath, V. Mathew, S. Raghavan and J. S. Jeon, "Electrochemical measurements during the chemical mechanical polishing of tungsten thin films," *Journal of the Electrochemical Society*, **144**(9), p. 3041-3049 (1997)
34. W. L. Guthrie, W. J. Patrick, E. Levine, H. C. Jones, E. A. Mehter, T. F. Houghton, G. T. Chiu and M. A. Fury, "A Four-Level VLSI Bipolar Metallization Design With Chemical-Mechanical Planarization," *IBM Journal of Research and Development*, **36**(5), p. 845-857 (1992)
35. M. B. Small and D. J. Pearson, "On-Chip Wiring for VLSI: Status and Directions," *IBM Journal of Research and Development*, **34**(6), p. 858 (1990)
36. R. Carpio, J. Farkas and R. Jairath, "Initial study on copper CMP slurry chemistries," *Thin Solid Films*, **266**(2), p. 238-44 (1995)
37. J. M. Steigerwald, *A Fundamental Study of Chemical Mechanical Polishing of Copper Thin Films*, Ph.D., Rensselaer Polytechnic Institute, Troy, New York, (1995).
38. P. Delahay, M. Pourbaix and P. Van Rysselberghe, "Potential-pH diagrams," *J. Chem. Education*, **27**, p. 683-8 (1950)
39. G. B. Shinn, V. Korthuis, A. M. Wilson, G. Grover and S. Fang, "Chemical-Mechanical Polish," in *Handbook of Semiconductor Manufacturing Technology*, Editors: Y. Nishi, R. Doering and T. Wooldrige, Marcel Dekker, Inc., (2000).

40. Q. Luo, D. R. Campbell and S. V. Babu, "Chemical-Mechanical Polishing of Copper in Alkaline Media," *Thin Solid Films*, **311**, p. 177-182 (1997)
41. A. J. Bard, R. Parsons and J. Jordan, *Standard Potentials in Aqueous Solution*, 1st ed, International Union of Pure and Applied Chemistry, Monographs in Electroanalytical Chemistry and Electrochemistry, M. Dekker, New York, (1985).
42. M. Hariharaputhiran, S. Ramarajan, Y. Li and S. V. Babu, "Mechanism of Cu removal during CMP in H₂O₂-glycine based slurries," in *Chemical-Mechanical Polishing--Fundamentals and Challenges*, Materials Research Society Symposium Proceedings, p. 129-134, (2000).
43. M. Hariharaputhiran, J. Zhang, S. Ramarajan, J. J. Keleher, Y. Li and S. V. Babu, "Hydroxyl radical formation in H₂O₂-amino acid mixtures and chemical mechanical polishing of copper," *Journal of the Electrochemical Society*, **147**(10), p. 3820-3826 (2000)
44. W. Huang, S. Raghavan, M. Peterson and R. Small, "Dissolution of Copper and Tantalum Films in Hydroxylamine Based Silica Slurries Under CMP Conditions," in *Chemical Mechanical Planarization in IC Device Manufacturing III*, Editors: R. L. Opila, I. Ali, Y. A. Arimoto, Y. Homma, C. Reidsema-Simpson and K. B. Sundaram, Proc. - Electrochem. Soc., p. 101-111, (2000).
45. S.-M. Lee, U. Mahajan, Z. Chen and R. K. Singh, "Study of Slurry Chemistry in Chemical Mechanical Polishing (CMP) of Copper," in *Chemical Mechanical Planarization in IC Device Manufacturing III*, Editors: R. L. Opila, I. Ali, Y. A. Arimoto, Y. Homma, C. Reidsema-Simpson and K. B. Sundaram, Proc. - Electrochem. Soc., p. 187-192, (2000).
46. M. Fayolle and F. Romagna, "Copper CMP evaluation: Planarization issues," *Microelectronic Engineering*, **37-38**, p. 135-41 (1997)
47. Y. Li, M. Hariharaputhiran and S. V. Babu, "Chemical-mechanical polishing of copper and tantalum with silica abrasives," *Journal of Materials Research*, **16**(4), p. 1066-1073 (2001)
48. J. Hernandez, P. Wrschka and G. S. Oehrlein, "Surface Chemistry Studies of Copper Chemical Mechanical Planarization," *Journal of The Electrochemical Society*, **148**(7), p. G389-397 (2001)
49. S. Tamilmani, W. Huang, S. Ragavan and R. Small, "Potential-pH Diagrams of Interest to Chemical Mechanical Planarization of Copper," *Journal of The Electrochemical Society*, **149**(12), p. G638-642 (2002)

50. R. J. Small, L. McGhee, D. J. Maloney and M. L. Peterson, "Redox slurries for chemical-mechanical polishing of semiconductor wafers and related circuit boards," Wo Patent 9804646, EKC Technology, Inc., 47 pp., (1998).
51. R. J. Small, L. McGhee, D. J. Maloney and M. L. Peterson, "Chemical Mechanical Polishing Composition and Process," US Patent 6313039, EKC Technology, Inc, (2001).
52. R. J. Small, L. McGhee, D. J. Maloney and M. L. Peterson, "Chemical Mechanical Polishing Composition and Process," US Patent 6117783, EKC Technology, Inc, (2000).
53. M. L. Peterson, R. J. Small, G. A. S. III, Z. J. Chen and T. Truong, "Investigating CMP and post-CMP cleaning issues for dual-damascene copper technology," *MICRO*, **17**(1), p. 27-34 (1999)
54. M. L. Peterson, R. J. Small, T. Truong and J.-Y. Lee, "Challenges of Electroplated Copper Film and Device Characteristics for Copper Slurry Design," *Semiconductor Fabtech*, **11**, p. 283-287 (2000)
55. J. Ritz, H. Fuchs and H. G. Perryman, "Hydroxylamine," in *Ullmann's Encyclopedia of Industrial Chemistry* Wiley-VCH Verlag GmbH, Weinheim, Germany, (2002).
56. W. Lossen, *J. Prake. Chem.*, **96**, p. 462 (1865)
57. C. A. Lobry de Bruyn, *Rec. Trav. Chim. Pays-Bas*, **10**, p. 100 (1891)
58. J. Ritz, H. Fuchs, H. Kieczka and W. C. Moran, "Caprolactam," in *Ullmann's Encyclopedia of Industrial Chemistry* Wiley-VCH Verlag GmbH, Weinheim, Germany, (2002).
59. M. van der Puy and J. H. Dimmit, *Hydroxylamine: Redox Properties of Hydroxylamines, Part 1, Inorganic Reactions*, AlliedSignal Inc., (1985).
60. E. A. MacWilliam, in *Kirk-Othmer Encyclopedia of Chemical Technology* Interscience, p. 371, (1968).
61. D. G. Harlow, R. E. Felt, S. Agnew, G. S. Barney, J. M. McKibben, R. Garber and M. Lewis, *Technical Report on Hydroxylamine Nitrate*, DOE/EH-0555, US Department of Energy: Office of Environment, Safety and Health. Office of Nuclear and Facility Safety, (1998).
62. W. M. Lee, "Stripping Compositions Comprising Hydroxylamine and Alkanolamine," US Patent 5279771, EKC Technology, Inc., (1994).

63. W. M. Lee, "Method of stripping resists from substrates using hydroxylamine and alkanolamine," US Patent 6242400, EKC Technology, Inc., (2001).
64. I. E. Ward, "Stripping with aqueous composition containing hydroxylamine and an alkanolamine," US Patent 5419779, Ashland Inc., (1995).
65. R. J. Small, "Post clean treatment composition comprising an organic acid and hydroxylamine," US Patent 5981454, EKC Technology, Inc., USA, 45 pp., (1999).
66. D. D. Wagman, W. H. Evans, V. B. Parker, I. Hallow, S. M. Baily and R. H. Schumm, *Selected Values of Chemical Thermodynamic Properties*, Notes 270-3, National Bureau of Standards and Technologies, Washington, D. C., (1968).
67. J. T. Maloy, "Nitrogen," in *Standard Potentials in Aqueous Solution*, Editors: A. J. Bard, R. Parsons and J. Jordan, Marcel Dekker, Inc., p. 127-139, (1985).
68. "Hydroxylamine," in *Comprehensive Inorganic Chemistry*, Editors: J. C. Bailar-Jr., H. J. Emeleus, S. R. Nyholm and A. F. Trotman-Dickenson, Pergamon Press, distributed by Compendium Publishers, Elmsford, NY, Oxford, (1973).
69. M. N. Hughes, H. G. Nicklin and K. Shrimanker, "Autoxidation of Hydroxylamine in Alkaline Solutions. Part II. Kinetics. The Acid Dissociation Constant of Hydroxylamine," *Journal of the Chemical Society, A. Inorganic, Physical, Theoretical*, p. 3485-3487 (1971)
70. W. M. Latimer, *The oxidation states of the elements and their potentials in aqueous solutions*, 2nd ed, Prentice-Hall, New York, (1952.).
71. A. Findlay and T. William, "Influence of colloids on the rate of reactions involving gases. I. Decomposition of hydroxylamine in the presence of colloidal platinum," *J. Chem. Soc.*, **119**, p. 170-6 (1921)
72. A. Kurtenacker and F. Werner, "Catalysis of hydroxylamine. III," *Z. anorg. allgem. Chem.*, **160**, p. 333-46 (1927)
73. N. Klein, *A Model for Reactions of the HAN-Based Liquid Propellants*, ARL-TR-405, Army Research Laboratory, (1994).
74. G. R. Rao and L. Meites, "Voltammetric Characteristics and Mechanism of Electrooxidation of Hydroxylamine," *The Journal of Physical Chemistry*, **70**(11), p. 3620-5 (1966)
75. M. N. Hughes and H. G. Nicklin, "Autoxidation of Hydroxylamine in Alkaline Solutions," *Journal of the Chemical Society, A. Inorganic, Physical, Theoretical*, p. 164-168 (1971)

76. P. C. Moews Jr and L. F. Audrieth, "The Autoxidation of Hydroxylamine," *Journal of Inorganic and Nuclear Chemistry*, **11**, p. 242-246 (1959)
77. J. H. Anderson, "The copper-catalyzed oxidation of hydroxylamine," *Analyst*, **89**(1058), p. 357-62 (1964)
78. J. R. Pembridge and G. Stedman, "Kinetics, Mechanism, and Stoichiometry of the Oxidation of Hydroxylamine by Nitric Acid," *Journal of the Chemical Society, Dalton Transactions*, p. 1657 (1979)
79. M. N. Hughes and G. Stedman, "Kinetics and Mechanism of the Reaction between Nitrous Acid and Hydroxylamine. Part I.," *Journal of the Chemical Society*, p. 2824 (1963)
80. A. A. Bothner-By and L. Friedman, "The reaction of nitrous acid with hydroxylamine," *J. Chem. Phys.*, **20**, p. 459-62 (1952)
81. V. Brusic, "Cu Corrosion Mechanisms and Control," in *Advanced Metallization Conference 2000, Proceedings of the Conference, San Diego, CA, United States, Oct. 2-5 and University of Tokyo, Tokyo, Japan, Oct. 19-20, 2000*, p. 127-135, (2000).
82. J. A. V. Butler, "Studies in heterogeneous equilibria. II. The kinetic interpretation of the Nernst theory of electromotive force," *Trans. Faraday Soc. (advance proof)*, (1924)
83. J. A. V. Butler, "Studies in heterogeneous equilibria. III. A kinetic theory of reversible oxidation potential at inert electrodes," *Trans. Faraday Soc. (advance proof)*, (1924)
84. T. Erdey-Gruz and M. Volmer, "The theory of hydrogen overvoltage," *Z. physik. Chem.*, **150**(Abt. A), p. 203-13 (1930)
85. C. M. A. Brett and A. M. O. Brett, *Electrochemistry: principles, methods, and applications*, Oxford science publications., Oxford University Press, Oxford ; New York, xxviii, 427, (1993).
86. J. Tafel, *Z. Phys. Chem. (Leipzig)*, **50**, p. 641 (1904)
87. M. G. Fontana, *Corrosion Engineering*, 3rd ed, McGraw-Hill, New York, (1986).
88. C. Wagner and W. Traud, *Z. Elektrochem.*, **44**, p. 391 (1938)
89. M. Stern and A. L. Geary, "Electrochemical polarization. I. A theoretical analysis of the shape of polarization curves," *Journal of the Electrochemical Society*, **104**, p. 56-63 (1957)

90. A. J. Bard and L. R. Faulkner, *Electrochemical Methods: Fundamentals and Applications*, Wiley, New York, 718, (1980).
91. L. Kiss, *Kinetics of electrochemical metal dissolution*, Studies in physical and theoretical chemistry ; v. 47., Elsevier, Amsterdam ; New York, 260, (1988).
92. B. H. Rosof and S. D. Emerson, *ROSOF*, Metallurgical Engineering, University of Arizona, Tucson, AZ, 85712, ver. PC DOS, (1977).
93. H.-H. Huang, *STABCAL*, Metallurgical Engineering, Montana Tech, Butte, MT 59701, ver. 2000, PC Windows, (2000).
94. V. Shafirovich and S. V. Lyman, "Nitroxyl and its anion in aqueous solutions: Spin states, protic equilibria, and reactivities toward oxygen and nitric oxide," *Proceedings of the National Academy of Sciences*, **99**(11), p. 7340-7345 (2002)
95. D. M. Stanbury, *Advanced Inorganic Chemistry*, **33**, p. 69-138 (1989)
96. M. Gratzel, S. Taniguchi and A. Henglein, *Ber. Bunsenges. Phys. Chem.*, **74**, p. 1003-1010 (1970)
97. M. K. Carter and R. J. Small, "Radical Formation in Hydroxylamine-Copper Chemical Mechanical Planarization Process," *Journal of The Electrochemical Society*, **150**(2), p. G107-G111 (2003)
98. W.-T. Tseng, J.-H. Chin and L.-C. Kang, "A Comparative Study on the Roles of Velocity in the Material Removal Rate during Chemical Mechanical Polishing," *J. Electrochem. Soc.*, **146**(5), p. 1952-1959 (1999)